Quantitative Structural and Compositional Studies of Catalyst Nanoparticles using Imaging and Spectroscopy in STEM.

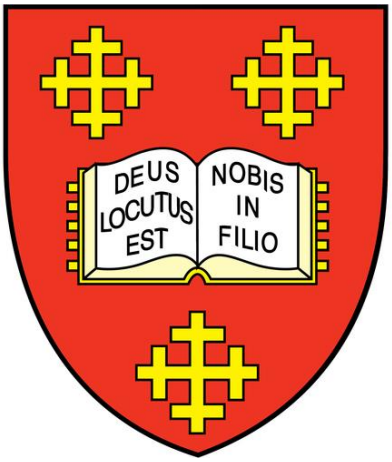

A thesis submitted for the degree of Doctor of Philosophy

Aakash Mahesh Varambhia

Mansfield College, University of Oxford

Hilary 2018

Abstract

The thesis aims to develop methods to explore how catalyst structure and composition affect catalytic performance of nanoparticles used in Proton Exchange Membrane Fuel Cell (PEMFC)applications. Using Scanning Transmission Electron Microscopy (STEM), the structure and composition of Pt and Pt-Co catalysts are explored with the intent of designing better catalysts. Catalysts such as pure Pt and alloyed Pt-Co ensembles are hugely popular in the PEMFC industry due to their catalytic activity and stability.

Out of the two ensembles, the bimetallic Pt-Co catalysts exhibit better performance and are cheaper to manufacture. The addition of a secondary element reduces the overall Pt loading making the catalyst cheaper. Introducing a secondary alloy also results in enhanced catalytic activity for reasons not well explained. To study the effects of enhanced activity, a thorough characterisation at the atomic scale is required. This means studying a catalyst's size, shape, strain and composition simultaneously, at high throughput, and linking this to catalytic activity.

Full characterisation of this detail is challenging, but not impossible. Using STEM, it is possible to obtain catalyst size, shape, strain and composition simultaneously. However due to the nature of the technique is it challenging to characterise industrially relevant materials at high throughput.

This thesis develops upon current methods for characterising nanoparticles in STEM to obtain nanoparticle size, shape, strain and composition at high throughput. In STEM, the size, shape and strain information is obtained from the Annular Dark Field (ADF) signal, whereas the composition information is obtained from Energy Dispersive X-ray Spectroscopy (EDS) and Electron Energy Loss Spectroscopy (EELS).

One of the challenges is combining the information from ADF, EDS and EELS signals into one quantifiable unit and building an analysis framework for catalyst nanoparticles. This can be achieved by converting the measured STEM signal into scattering cross-sections. The

scattering cross-section describes the effective area corresponding to the probability of scattering from a sample. With careful microscope calibration, the scattering cross-section can be converted to number of atoms.

Atom counts from the STEM signals provide the structure and composition information from a nanoparticle. The thesis will explore the minimum requirements needed to develop new automated methods to characterise structure and composition of nanoparticles using scattering cross-sections at high throughput. In addition, limitations and capabilities of current hardware and software are explored. The three-dimensional models obtained from the quantitative analysis can be used as inputs for Density Functional Theory (DFT) simulations to understand molecule adsorption mechanics better.

Combining high throughput technique development, STEM quantification and high scale DFT simulation together unlocks a detailed insight in understanding catalyst activity. Such detailed description of a system is the stepping stone towards reducing cost and time for better catalyst design.

List of Publications

Journal Articles

"Determining EDS and EELS partial cross-sections from multiple calibration standards to accurately quantify bi-metallic nanoparticles using STEM",
Aakash Varambhia, Lewys Jones, Andrew London, Dogan Ozkaya, Peter D Nellist, Sergio Lozano-Perez,
Micron, (2018), DOI: 10.1016/j.micron.2018.06.015.

"Managing dose-, damage- and data-rates in multi-frame spectrum-imaging", Lewys Jones, Aakash Varambhia, Richard Beanland, Demie Kepaptsoglou, Ian Griffiths, Akimitsu Ishizuka, Feridoon Azough, Robert Freer, Kazuo Ishizuka, David Cherns, Quentin M. Ramasse, Sergio Lozano-Perez, and Peter D. Nellist,
Microscopy, (2018), DOI:10.1093/jmicro/dfx125.

"Ideal vs real: Simulated annealing of experimentally derived and geometric platinum nanoparticles", Tom Ellaby, Jolyon Aarons, Aakash Varambhia, Lewys Jones, Peter Nellist, Doğan Özkaya, Misbah Sarwar, David Thompsett and Chris-Kriton Skylaris,
Journal of Physics: Condensed Matter, (2018), DOI:10.1088/1361-648X/aab251.

"An optical configuration for fastidious STEM detector calibration and the effect of the objective-lens prefield", Lewys Jones, Aakash Varambhia, Hidetaka Sawada, and Peter D. Nellist,
Journal of Microscopy, (2018), DOI:10.1111/jmi.12672.

"Predicting the oxygen binding properties of platinum nanoparticle ensembles by combining high-precision electron microscopy & DFT", Jolyon Aarons, Lewys Jones, Aakash Varambhia, Katherine E. MacArthur, Dogan Ozkaya, Misbah Sarwar, Chris-Kriton Skylaris, and Peter D. Nellist,
Nano Letters, **17**(7) (2017), DOI:10.1021/acs.nanolett.6b04799. – Joint first author.

"Electrochemical CO Oxidation at Platinum on Carbon Studied Through Analysis of Anomalous In Situ IR Spectra", Ian McPherson, Philip Ash, Lewys Jones, Aakash Varambhia, Robert Jacobs, and Kylie Vincent,
Journal of Physical Chemistry C (2017), DOI:10.1021/acs.jpcc.7b02166.

"Observation of metal nanoparticles at atomic resolution in Pt-based cancer chemotherapeutics"
Sheader A. A., Varambhia A.M., Fleck R. A., Flatters S. J. L. and Nellist P. D.,
Journal of microscopy 270, 92-97 (2017), https://doi.org/10.1111/jmi.12659

"Quantifying a Heterogeneous Ru Catalyst on Carbon Black Using ADF STEM", A. M. Varambhia, L. Jones, A. De Backer, V. T. Fauske, S. Van Aert, D. Ozkaya and P. D. Nellist,
Particle & Particle Systems Characterization **33**:7 (2016), DOI:10.1002/ppsc.201600067.

"A combined approach for deposition and characterization of atomically engineered catalyst nanoparticles". Q Yang, DE Joyce, S Saranu, GM Hughes, A Varambhia, MP Moody, PAJ Bagot.
Catalysis, Structure & Reactivity 1 (3), 125-131 (2015), DIO: 10.1179/2055075815Y.0000000006

Conference Proceedings

"From High-precision Imaging to High-performance Computing: Leveraging ADF-STEM Atom-counting and DFT for Catalyst Nano-metrology", Lewys Jones, Jolyon Aarons, Aakash Varambhia, Katherine E. MacArthur, Dogan Ozkaya, Misbah Sarwar, Chris-Kriton Skylaris, Peter D. Nellist,
Microscopy and Microanalysis, **23**(S1) (2017), DOI:10.1017/S1431927617010066.

"Quantitative STEM of Catalyst Nanoparticles using ADF Imaging with Simultaneous EDS and EELS Spectroscopy", Aakash M Varambhia, Lewys Jones, Annick De Backer, Sandra Van Aert, Dogan Ozkaya, Sergio Lozano-Perez, Peter D Nellist,
Microscopy and Microanalysis, **23**(S1) (2017), DOI:10.1017/S1431927617010108.

"New Opportunities in multi-frame STEM Spectroscopy & Fractional Beam-current EELS", Lewys Jones, Aakash Varambhia, Demie Kepaptsoglou, Quentin Ramasse, Robert Freer, Feridoon Azough, Sergio Lozano-Perez, Richard Beanland, and Peter Nellist,
16th European Microscopy Congress (2016),
DOI:10.1002/9783527808465.EMC2016.6336.

"Nano-scale strain measurements from high-precision ADF STEM", Lewys Jones, Aakash Varambhia, Sigurd Wenner, Magnus Nord, Per Harald Ninive, Ole Martin Løvvik, Randi Holmestad, and Peter Nellist,
16th European Microscopy Congress(2016), DOI:10.1002/9783527808465.EMC2016.6864.

"Experiment design for quantitative dark field imaging and spectroscopy of catalyst nanoparticles using Scanning Transmission Electron Microscopy (STEM)", Aakash Varambhia, Lewys Jones, Annick De Backer, Vidar Fauske, Sandra Van Aert, Dogan Ozkaya, Sergio Lozano-Perez, and Peter Nellist,
16th European Microscopy Congress (2016),
DOI:10.1002/9783527808465.EMC2016.6164.

"Atomic resolution electron microscopy of cobalt ferrite nanoparticles", Dominique Piché, Juan G Lozano, Aakash Varambhia, Frank Dillon, Lewys Jones, Peter D Nellist, Nicole Grobert,
16th European Microscopy Congress (2016),
DOI:10.1002/9783527808465.EMC2016.6724.

"Quantification of ADF STEM Image Data for Nanoparticle Structure and Strain Measurements", Peter Nellist, Lewys Jones, Aakash Varambhia, Annick De Backer, Sandra Van Aert, and Dogan Ozkaya,
Microscopy and Microanalysis, **22**(S3) p.896-897 (2016),

"Quantification of a Heterogeneous Ruthenium Catalyst on Carbon-black using ADF Imaging", Aakash Varambhia, Lewys Jones, Peter Nellist, Sergio Lozano-Perez, and Dogan Ozkaya,
Journal of Physics: Conference Series **644**:012035 (2015),
DOI:10.1088/1742-6596/644/1/012035.

Acknowledgements

I would like to extend my thanks to several people, in many academic institutions and departments who have generously contributed to the work and discussions presented in this thesis.

I would like to express my special gratitude to my supervisors Peter Nellist, Sergio Lozano-Perez and Dogan Ozkaya, who have been tremendous mentors for me. I would like to thank them for encouraging me to grow as a researcher and allowing me to explore several aspects of the project freely.

In particular, I would like to thank Peter for giving me to opportunity to travel to several domestic and international conferences during my DPhil; this number has now totalled to 23! I would like to thank Sergio for believing in my skills and his guidance during the difficult spectroscopic aspects of the project. I would like to thank Dogan for sacrificing several of his weekends to drive me to Harwell to perform time critical experiments.

A special mention goes to Lewys Jones. I owe my initial programming, analysis and microscope driving skills entirely to training provided by Lewys, and I am particularly indebted to him for this. Similarly, I would like to thank Hao Yang for supervising me on the microscope in the evenings during training and making sure I did not break anything. I would also like to thank Gerardo Martinez for useful simulation and experiment design discussions.

I am also hugely appreciative of close collaborators at several academic institutions and industry.

Starting with Thomas Aarholt, whose initial HyperSpy and Python discussions have been invaluable in helping me understand and perform spectroscopic analysis in my DPhil.

I would like to thank Sandra van Aert's group at the University of Antwerp, who have provided useful discussions during my visits to Antwerp and the ATOM workshops. My thanks go to Annick de Backer, Annelies de Wael, and Karel van den Bos. I would like to thank the group of Chris Skylaris at the University of Southampton, particularly, Jolyon Aarons and Tom Ellaby for useful electronic structure theory discussions. Finally, I would like to thank Ed Boyes, Pratibha Gai and Leonardo Larii for provision of and driving the ETEM during my visit to the University of York.

On the industry side, I would like to thank Hidetaka Sawada from JEOL for useful discussions on electron optics. I would also like to thank Manfred Schuster from Johnson Matthey for providing support when I was operating the microscope at Harwell.

I would like to thank my colleagues in Oxford for useful discussions and their constant support; Neil Young, Gareth Hughes, Yu-Jen Chou, Jack Haley, Andrew London, Alex Sheader, Colum O'Leary, Ian McPherson and Juan Lozano.

I would also like to thank my friends Trishant Umrekar, Daniel Man and Natanael Mota whom I coerced into proof reading my thesis for me.

For financial support, I acknowledge EPSRC and Johnson Matthey for funding my DPhil and Mansfield College for generously funding several conference expenses.

Finally, but by no means least, thanks go to my parents Mahesh and Mala Varambhia for their unbelievable support throughout the DPhil. They are the most important people in my world, and I dedicate this thesis to them.

List of Abbreviations

ADF – Annular Dark Field

APT – Atom Probe Tomography

CCD – Charge Coupled Device

DFT – Density Functional Theory

EDS – Energy Dispersive X-ray Spectroscopy

EELS – Electron Energy Loss Spectroscopy

ETEM - environmental-TEM

EXAFS - Extended X-Ray Absorption Fine Structure

MEMS - Micro Electro Mechanical System

MFSI – Multi Frame Spectrum Image

ORR – Oxygen Reduction Reaction

PEMFC – Proton Exchange Membrane Fuel Cell

SE - Secondary Electron

SEM – Scanning Electron Microscope

SNR – Signal to Noise Ratio

STEM – Scanning Transmission Electron Microscope

TEM – Transmission Electron Microscope

UV – Ultra Violet

ZLP – Zero Loss Peak

Table of Contents

1 Introduction to Catalysts

1.1 Chapter Overview

This chapter provides a short introduction to catalysis and sets the context for the project. A short introduction to PEMFC chemistry and its underlying mechanisms is presented. Building upon this, a review of current and previous literature linking catalysts activity and performance to nanoparticle morphology and composition is presented with additional emphasis made on heterogeneous Pt and Pt-alloy catalysts for PEMFCs applications. Moreover, a brief introduction to the effects the interface, structure and synthesis have on catalytic activity is presented.

1.2 Contextualising the Project

The hydrogen fuel cell concept has garnered a lot of the interest within the past decade. This growing interest is primarily due to water being the only by-product of the reaction. However, the hydrogen used within the fuel cell is sourced from non-renewable hydrogen reserves. Nevertheless, due to the relatively high efficiency of the hydrogen fuel cell compared to internal combustion engines makes it an attractive option to reduce our current carbon emissions (Hass, 2004).

For high turnover efficiency, fuel cells are designed using a proton exchange membrane configuration housing Pt-based catalysts (Holton and Stevenson, 2013; Jaksic et al., 1998; Nørskov et al., 2004). Pt-based catalysts require sufficiently low working temperatures (80°C), have a quick engine start-up time and possess high energy density output which outmatches the current battery-based technology(EERE of the U.S. Department of Energy, 2011; Fuel Cell Today and Matthey, 2013).

The Pt-based full cells have relatively simple reaction mechanics requiring pure hydrogen and oxygen (obtained from ambient air) as inputs on the anode and cathode ends of the fuel cell respectively. For the anode, substantial work has been done to improve the hydrogen exchange process, to the point where satisfactory efficiency has been achieved. In contrast, improving

efficiency on the cathode side has proved to be more challenging. The US department of energy analysis indicates that the fraction of Pt used in the fuel cell needs to be ~17% of the total cost of an 80kW fuel cell for this technology to be a viable replacement for the current combustion engines (EERE of the U.S. Department of Energy, 2011).

To reduce Pt cost, development is now geared towards synthesising hybrid catalysts based on cheaper metals as a substitute for pure Pt catalysts. Surprisingly, these hybrid bimetallic catalysts match or even exceed the performance of pure Pt systems (Z. Yu et al., 2012). Synthesis efforts range from developing alloyed metal nanoparticles to core-shell structures on an industrial scale and performance of these is measured by an iterative process (Saadatjou et al., 2014).

Measuring catalyst performance with this approach is quite time-consuming, especially when large quantities of the catalysts are synthesised daily. Ideally, an approach where the performance of catalysts can be quantified as quickly as possible after synthesis is required. For this approach to be successful simultaneous size, shape, strain, composition and stability of the catalyst nanoparticle ensemble at high throughput is required.

Catalyst nanoparticles are usually quantified using the following popular techniques: electron microscopy, x-ray powder diffraction, x-ray synchrotron methods, atom probe tomography, atomic force microscopy and cyclic voltammetry. Each technique has its advantages and disadvantages; these will be reviewed in the characterisation section.

This project focused on using scanning transmission electron microscopy for simultaneous size, shape, strain and composition of catalyst nanoparticles. Emphasis was made on developing high throughput techniques and combining simultaneously acquired structural and spectral signals from the various detectors within the electron microscope. The main aim is to develop a framework where nanoparticle synthesis can be directly correlated to industrial catalyst design, cutting production and testing time.

1.3 The Hydrogen Fuel Cell

Figure 1.1 is a simple schematic showing the concept of how a PEMFC functions. Hydrogen is fed on the anode side and oxygen, obtained from air, is fed on the cathode side. The adsorbed hydrogen atoms each lose an electron and are released as protons. The electrons and the hydrogen ions then flow towards the cathode, where the oxygen has been adsorbed onto the catalyst. Here the redirected hydrogen ions and their electrons combine with the adsorbed oxygen to produce water.

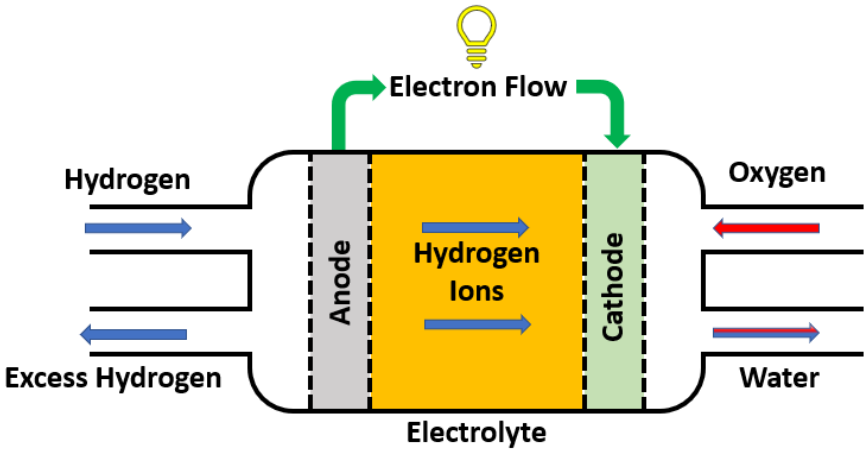

Figure 1.1 The PEMFC schematic

On the anode side, only a fraction of Pt is required compared to the cathode side. The reaction is also much more straightforward and is described by the equations below. The equations describe the adsorption of hydrogen onto a surface site, $*$, as it flows into the fuel cell. After the H-H bond is broken the spare electron and proton flow towards the cathode around and through the electrolyte respectively.

$$^1/_2 H_2 + * \rightarrow H^* \qquad (1)$$

$$H^* \rightarrow H^+ + * + e^- \qquad (2)$$

The kinetics of this reaction is simple and extremely efficient. Due to this the focus is to improve the ORR reactions on the cathode side. ORR reaction at the cathode is known for its poor efficiency and complicated mechanism (Gasteiger and Markovic, 2009). Stability is also

a major issue due to the corrosive environment around the cathode area, and the catalyst selectivity must be tuned for the desired reaction. Owing to the challenges in the ORR, the cathode requires a Pt loading several times higher compared to the anode (Appleby, 1993).

The cathode reaction is responsible for more than half of the voltage loss in a PEMFC fuel cell system (Sheng et al., 2010). The main reason for this is that there are two thermodynamic pathways known, with similar reaction probabilities, which can take place. These pathways are called the dissociative and associative pathways, shown below. The choice of reaction is highly sensitive to the catalyst type and directly linked to the synthesis method.

Dissociative pathway

$$^1/_2\, O_2 \rightarrow O^*$$
$$O^* + H^+ + e^- \rightarrow OH^*$$
$$OH^* + H^+ + e^- \rightarrow H_2O + *$$

Associative pathway

$$O_2 + * \rightarrow {O_2}^*$$
$${O_2}^* + H^+ + e^- \rightarrow {HO_2}^*$$
$${HO_2}^* + H^+ + e^- \rightarrow {H_2O_2}^*$$
$${H_2O_2}^* \rightarrow H_2O_2 + *$$

The dissociative pathway is the preferred mechanism where the adsorbed oxygen undergoes a 4-electron transfer process leading to the direct formation of water. In the dissociative mechanism, the oxygen-oxygen bond is broken, and the oxygen is adsorbed onto the Pt active site. The incoming hydrogen ions protonate these single oxygen atoms giving rise to surface-bound hydroxyl. The surface-bound hydroxyl is then further reduced to give water which is eventually desorbed from the catalyst surface (Jinnouchi, 2003).

The alternative pathway is the associative process, where the oxygen-oxygen bond does not break upon adsorption. This mechanism is known to produce hydrogen peroxide, which is an undesired product of the reaction as it diffuses into the polymer membrane of the fuel cell and causes radical degradation of the membrane.

1.4 Heterogeneous Catalysts

A catalyst is a substance that increases the rate of a chemical reaction, it is intimately involved in the reaction, but not consumed. Ideally, once the reaction is complete, the catalyst is regenerated out of the stoichiometric equation without any mass loss. Most synthesis process

requiring catalysts such as ammonia production, fuel cracking and pollutant removers remain fundamentally unchanged to this day.

Catalysts are usually grouped into two categories, heterogeneous and homogeneous. In the former group, the reactants, catalyst and the product are in different physical states. Whereas, in the latter case, the reactants, catalysts and products are in the same phase. Designs of PEMFCs are based on gas to solid reaction interfaces which have a high operating efficiency, are clean and lightweight in operation(Liu et al., 2013). In this design, the catalyst is either in a meta-stable or solid-state form and is usually supported on carbon black. The carbon black support consists of crumpled graphite with low-range ordering and helps maintain the structural integrity of the nanoparticles.

The chemical reaction occurs on the nanoparticle interface exposed to vacuum or air, where the probability of a reaction is dependent on 'active sites'. These are sites with specific crystallographic orientation and structure that have the highest probability to induce a chemical reaction. The mechanisms of these sites are poorly understood and are an active area of research (Gontard et al., 2007; Natesakhawat et al., 2012; Yates, 1995).

To link catalyst synthesis and performance quantitatively, four main characteristics of the catalyst must be considered:

Activity – the ability to absorb the reactants just strongly enough to facilitate a reaction between the adsorbates and release them once the reaction is finished.

Selectivity – the ability to create the desired product at the end of the reaction.

Stability- to be able to withstand the reaction and the operating environment in a fuel cell (acidity, strong oxidants and fluctuating temperatures).

Poisoning resistance – the ability to resist poisoning from impurities most likely found in a fuel cell from the feed gases.

The relationship of these characteristics to catalytic activity requires a thorough study of a nanoparticle's size, shape, strain and composition at high throughput. As a case-study, Pt and Pt-Co catalysts were quantified in this project, with a generalised framework in mind that can be extended to several other materials.

1.5 Pt Group Metals

Pt group metals are a set of metals in the VIII group of the periodic table and are known the exhibit similar physical and chemical properties. Group VIII metals are particularly good at resisting corrosion, have a high melting point and offer good structural stability.

The performance of these materials is best represented using "volcano plots", where the catalytic activity is plotted as a function of adsorption energy, Figure 1.2 (Jaksic et al., 1998). The plot covers most of the group VIII metals, and Pt exhibits one of the highest current densities for an O-reduction reaction from the selection.

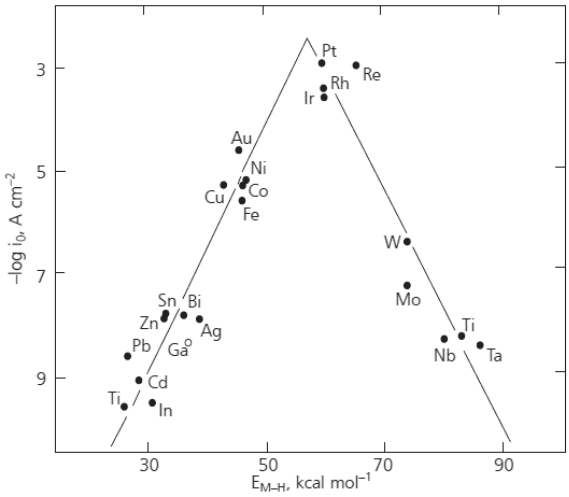

Figure 1.2 logarithm of exchange current density vs the bonding adsorption strength for hydrogen oxidation reaction, figure reprinted from (Jaksic et al., 1998)

Unfortunately, Pt is an expensive metal and to meet the requirements set by US department of energy that Pt should consist of 17% of the cost of a PEMFC(EERE of the U.S. Department of Energy, 2011), an alloying material is usually used to reduce the Pt loading (Oezaslan and Strasser, 2011).

The introduction of a secondary element enhances the activity considerably, Figure 1.3. Reasons for activity enhancement are not well known. Extensive research within the field has indicated that optimising the stability and shape by adopting certain alloy stoichiometry and material loadings is key(Boyes and Gai, 2014; Raróg-Pilecka et al., 2005; Schulenburg et al., 2009). Activity enhancement is known to be correlated to size, shape, structure, strain and synthesis of the catalyst, and is discussed in the next sections.

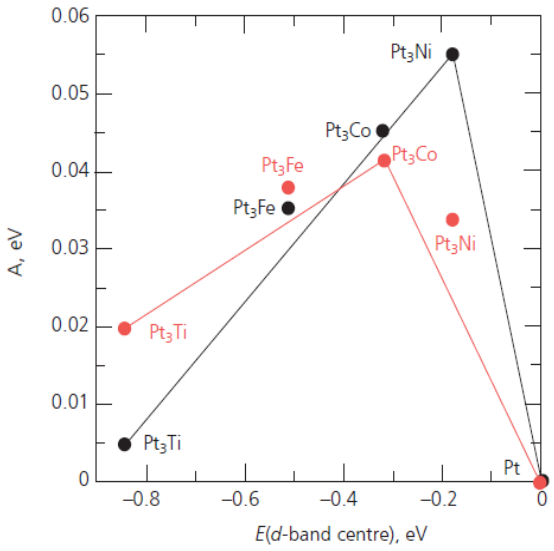

Figure 1.3 current output as a function of the d-band centre for alloyed catalysts with Pt as the benchmark, figure reprinted from (Stamenkovic et al., 2006). *The red curve shows predicted catalytic activity from simulations, whereas the black curve shows the experimental approximations.*

1.5.1 The Reactive Interface

To increase the probability of a reaction, a high Pt surface area that is exposed to the vacuum or air is required. Catalysts such as these take common forms such as the one shown in Figure 1.4. The catalyst shown in Figure 1.4 is a pure Pt industrial catalyst manufactured by Johnson Matthey and is in powder form. Subsequent STEM images of the nanoparticles indicate a size range between 2nm and 20nm. Each nanoparticle varies widely in size and shape, as shown by Figure 1.4b and c. When one of these nanoparticles is viewed along a zone axis, crystalline features are observed, Figure 1.4d. These features give 2D projection information of the crystalline facets present and ordering of the nanoparticle.

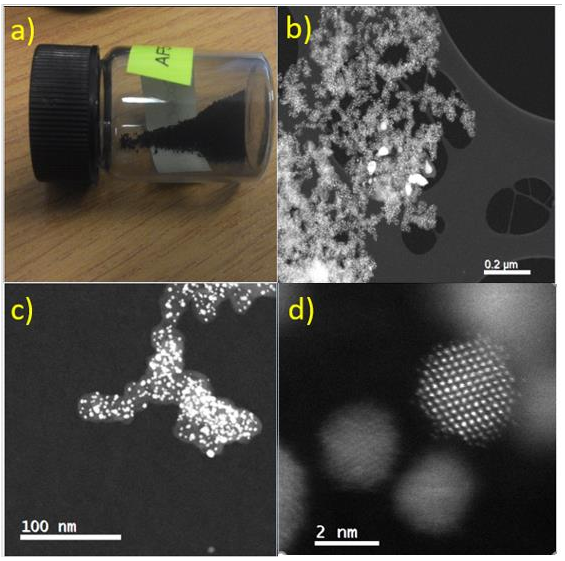

Figure 1.4 a) Pure Pt industrial catalyst after synthesis in powder form, b) STEM image of the catalyst, the image gamma has been enhanced to show the TEM carbon grid. c) a closer look at the catalyst and its carbon-black support, d) Atomic resolution image of an on-zone catalyst nanoparticle.

3D structure inversions of nanoparticles, such as Figure 1.4d, have been performed using quantitative STEM, Figure 1.5, (Jones et al., 2014) and tomography (Goris et al., 2013b). The reconstructed models show that the nanoparticles have different coordination at the surface, which in turn affects their binding potential with the gas adsorbates. Termination sites on the surface are believed to be the 'active sites', but this remains a popular topic for debate and depends on the catalyst composition. For example for Ru catalysts, the most active site is believed to be the 'B5' site (Saadatjou et al., 2014), whereas for Pt this may not be the case (Yates, 1995).

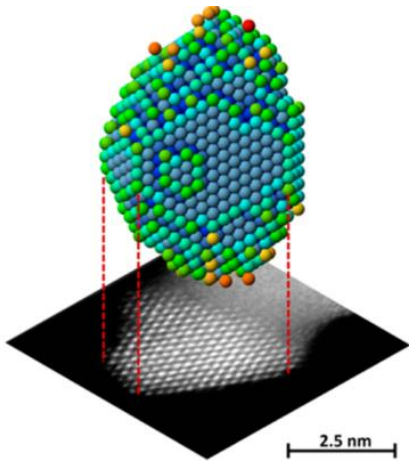

Figure 1.5 3D reconstruction of a pure Pt nanoparticle using ADF scattering cross-sections, reprinted from (Jones et al., 2014). The nanoparticle atoms are colour coded as a function of coordination number.

Gas molecule Interactions on the surface of nanoparticles such as in Figure 1.5 are usually studied using slab models in DFT. This approach assumes periodic structures and does not account for major steps and defects at the surface layer. However, this approach is popular because full nanoparticle calculations are time-consuming and the time required scales as the cube of the number of atoms (Haynes et al., 2006). Recently, a linearly time-scaling code was developed that now makes full nanoparticle calculations viable (Skylaris et al., 2005). With this new capability, it is possible to simulate O and H interactions at each surface site of a nanoparticle and calculate the surface averaged binding energy and correlate this to catalytic activity (Aarons et al., 2017).

Figure 1.6 shows a schematic of O and H molecules at the catalyst surface as a function of potential energy. Incoming particles diffuse in the gas phase onto the metal surface where they may bond to the surface. On the surface, diffusion may occur and thus disassociating the molecule into atoms, followed by a surface reaction where the atoms combine to form a new molecule. Finally, desorption occurs, and the surface bond is broken, and the newly formed molecule is released from the catalyst.

In a perfect catalyst reaction, the initial energy barrier for the reaction is high as energy must be expended to break the molecules bonds. Once the molecule is anchored and stabilised on the surface of the catalyst, as shown in Figure 1.6, splitting of the molecular bonds occurs. Then through several reaction pathways on the surface of the nanoparticle, a new molecule is formed by reducing the overall energy of the reaction (Bowker, 1998). The new molecule is then released from the nanoparticle in the gas phase.

Figure 1.6 is a thermodynamically downhill process for transition metals, the energetics of adsorption, in simple cases, can be understood with a Lennard-Jones type potential. Ultimately, the effectiveness of this process is determined by the nature of the particle surface structure and size.

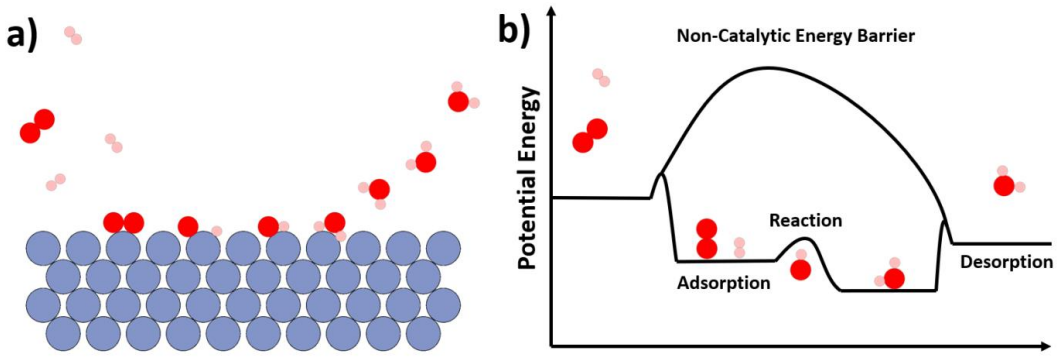

Figure 1.6 Simplified molecular and atomic events during a catalytic reaction. b) A simplified energetics plot of a catalytic reaction (y-axis: adsorbate potential energy).

1.5.2 Effect of Surface Structure and Size

The previous section highlighted the importance of surface dynamics in catalytic reactions, the basis of which was first developed by (Langmuir, 1918). Building upon this (Taylor, 1925), proposed the concept of the 'active site' as the optimal areas on the surface where the desired reaction is most probable. Taylor's approach proposed that atoms with the lowest coordination, often found at abrupt termination sites on a crystalline surface, exhibit enhanced catalytic activity. The abrupt termination of a crystal plane at the surface exposes the atoms to an asymmetric environment where on one side the atoms are exposed to the surface and its neighbours, and in the opposite direction the bulk.

With modern developments in computational software and hardware, it is now possible to calculate binding energies at each termination to study active sites. Most literature studying the electronic structure indicates that the catalytic activity for Pt-group metal catalysts depends on the d-band centre of the electronic density of states as a function of coordination number (Falicov and Tersoff, 1981).

Sometimes, depending on the electronic potentials used, it is difficult to determine where the active site is. For example, work by (Falicov and Tersoff, 1981) using a Ni surface model based on self-consistent atomic orbitals calculations predict that the optimum active site for a catalyst are sites c and d in Figure 1.7. However, other work either supports or contradicts this

claim and the topic is an area of ongoing research (Falicov and Tersoff, 1981; Taylor, 1925; Xin et al., 2014; F. Yang et al., 2015; Zhang et al., 2015).

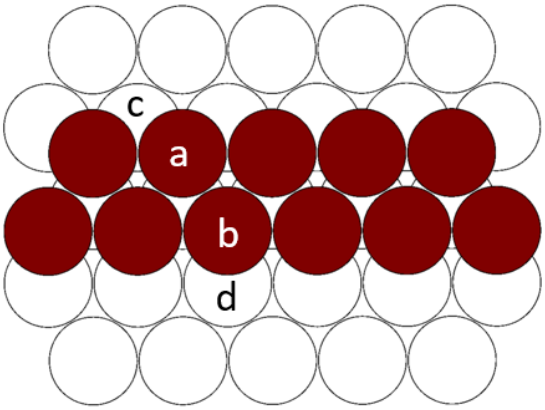

Figure 1.7 geometry of a (111) fcc metal with active sites a, b, c and d.

However, what is well known is that, depending on the surface plane, e.g. [110] or [100], the activity and binding energy varies considerably. For example, experiments with pure Pt samples indicate that the activation energy for CO desorption is about 20% higher for the [112] planes when compared to the [111] plane(Yates, 1995).

Therefore, as the first step towards understanding reaction sites, calculating the binding energy provides a simpler explanation for a complex problem. This is routinely simulated for small 'magic number' nanoparticles with (<200 atoms). The fraction of the total atoms identified as an active site from the nanoparticle is then plotted as a function of crystal size, Figure 1.8. The general conclusion from such studies is that as the nanoparticle size decreases, the surface to volume ratio increases and the catalytic activity increases. This is true up to a certain crystallite size, after this the molecule over binds to the nanoparticle and poisoning occurs.

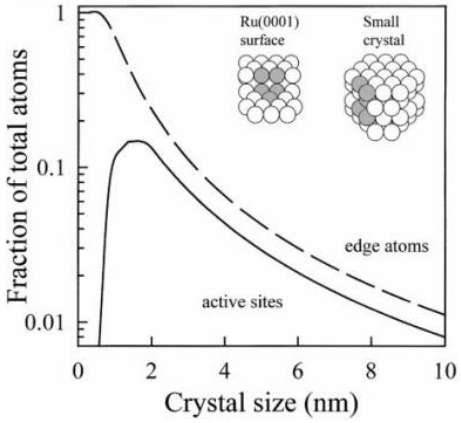

Figure 1.8 fraction of edge atoms and active sites on small Ru crystals relative to the total number of atoms as a function of crystal size, figure reprinted from (Jacobsen et al., 2000).

A balance must be achieved between optimal nanoparticle size and stability for a reaction. Additionally, as demonstrated by (Aarons et al., 2017), industrially relevant samples are far from perfect. The results of this study are described in more detail in chapter 4.5. Furthermore, to reduce the monetary cost of the catalyst, industrially relevant catalysts are often alloyed. This changes the surface reactivity substantially (Figure 1.3) and only recently software and hardware capabilities have been developed at the level to start probing bimetallic nanoparticles (Deepak et al., 2011; Koh and Strasser, 2007; Wang et al., 2015).

By determining the activity of a catalyst with a combination of microanalysis experiments and simulation, the iterative design and testing process can be reduced significantly. Ultimately the chemist must then decide on how to synthesise the perfect catalyst.

1.5.3 Catalyst Synthesis and Design

Figure 1.9, shows some of the popular routes used for synthesising catalysts. Metal and oxide nanoparticles can be prepared by either a ‘bottom-up’ or a ‘top-down process, making them versatile catalysts. Colloidal nanoparticles are obtained from routes 2, 3 and 7. Usually, the bottom-up approach is preferred as it requires less energy to synthesise catalysts and is the industry standard.

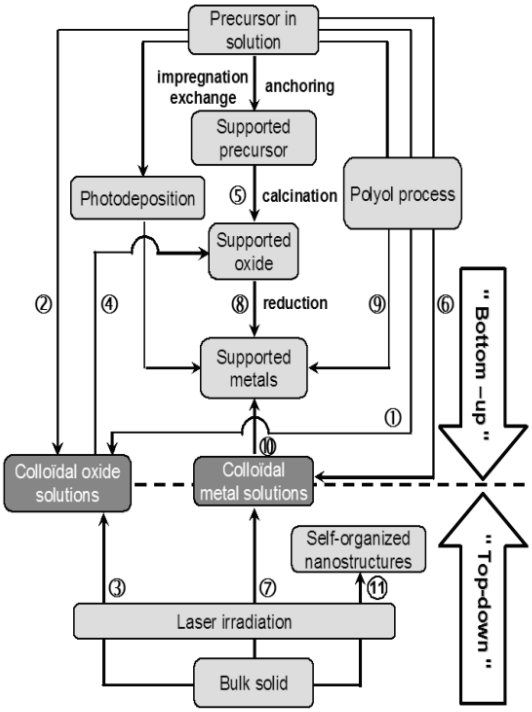

Figure 1.9 The catalyst design process, figure reprinted from (Bozon-Verduraz et al., 2008).

However, with the bottom-up approach, the nanoparticles vary widely in size, shape, composition and stability. The alternative top-down approach usually produces optimal nanoparticles but is difficult to scale up. Much effort has been put towards scaling up this process since this allows for fine tuning several nanoparticle parameters predicted by simulations and microanalysis (Wang et al., 2011; Young et al., 2008).

Since upscaling the top-down process is still a work in progress, the catalyst industry tries to perfect the bottom-up approach through trial and error. In some cases, this has proven to be successful, and in others, not much progress is made. From iterative synthesis and testing routines, the primary approaches to improve catalytic activity are alloying, surface coating large particles and synthesising core-shell nanoparticles. Often the only way to directly visualise what has been synthesised requires the sample to be probed by electron microscopy.

Mixed Pt-X binary alloys, where element X is a substitute material like Co, Ni, Fe, Rh, show enhanced activity towards ORR(Kinoshita, 1990). While these alloys are highly active, they are also often structurally unstable during or post reaction. Both theoretical and experimental observations indicate that severe leaching of the substitute element takes place (Kinoshita,

1990; Toda, 1999). The acid in the fuel cell environment induces a dissolution of the substitute element during oxidation leading to nanoparticle instability.

In the case of Pt-Ni, Pt-Co and Pt-Fe, the secondary element is known to easily migrate onto the surface of the nanoparticle during the ORR reaction (Toda, 1999). The migrating ions from the nanoparticles provide sites for radical peroxide formation because of the ORR mechanism. To prevent the secondary element from migrating onto the surface, a balance in composition between the primary and secondary elements is required. This is often achieved iteratively by changing the loading ratio of the primary and secondary element.

Further activity enhancement can be achieved by layering Pt onto or just below a surface of the secondary metal. This is a new research area that is attracting considerable interest, where the idea is to create an ideal surface layer with the desired crystallographic orientation for the gas molecule to bind onto.

However, the most popular approach used to enhance catalytic activity is synthesising core-shell nanoparticles. Here, ideally, the primary element (Pt) covers the surface of the nanoparticle whereas the bulk is formed of the cheaper secondary element (Ni, Co). When compared to the alloyed and layering approaches, the core-shell approach has proven more promising in enhancing nanoparticle stability and activity.

Industrial core-shell nanoparticles are synthesised in a similar approach to alloyed nanoparticles. Usually, a bottom-up approach is implemented, and the most popular synthesis pathway is to prepare a supported precursor in solid or solution form which can be turned into an alloy. The precursor is anchored onto a support material, heat treated and reduced to obtain alloyed nanoparticles. The nanoparticles are then acid leached, where the secondary element is leached away from the surface of the nanoparticle leaving a Pt enriched surface. Finally, the resultant catalyst is deposited onto a polymer exchange membrane and installed onto a hydrogen fuel cell.

1.6 Conclusions

A summary of the fuel cell design and synthesis process was presented. The literature review in this chapter indicates that an efficient catalyst must fulfil four crucial requirements. These are activity, selectivity, stability and poisoning resistance. Iterative design and testing has indicated that platinum group VIII metals can meet these requirements. For PEMFCs, pure Pt and Pt-based alloys exhibit the highest performance-to-efficiency ratio. However, the fundamental reason for this is not well known.

Significant work has been undertaken to study the electronic structure and defining active sites for various catalysts. This work usually indicates that there is a correlation between the structure and composition of a catalyst and its performance. Additionally, some work indicates that there is an optimal size range where the nanoparticles have optimal catalytic performance. Further modifications to the nanoparticle by introducing an alloy has also been shown to increase performance significantly. However, this approach is highly sensitive to the synthesis pathway used.

Therefore, to make a direct connection between nanoparticle synthesis and performance, where the trial and error performance testing cycle is reduced, a high throughput characterisation of size, shape strain and composition that feeds into modelling is required.

1.7 References

Aarons, J., Jones, L., Varambhia, A., MacArthur, K.E., Ozkaya, D., Sarwar, M., Skylaris, C.K., Nellist, P.D., 2017. Predicting the Oxygen-Binding Properties of Platinum Nanoparticle Ensembles by Combining High-Precision Electron Microscopy and Density Functional Theory. Nano Lett. 17, 4003–4012. doi:10.1021/acs.nanolett.6b04799

Appleby, A. J., 1993. Electrocatalysis of aqueous dioxygen reduction. J. Electroanal. Chem. 357, 117–179. doi:10.1016/0022-0728(93)80378-U

Bowker, M., 1998. The basis and applications of heterogeneous catalysis. Oxford Science Publications.

Boyes, E.D., Gai, P.L., 2014. Aberration corrected environmental STEM (AC ESTEM) for dynamic in-situ gas reaction studies of nanoparticle catalysts. J. Phys. Conf. Ser. 522, 12004. doi:10.1088/1742-6596/522/1/012004

Bozon-Verduraz, F., Fiévet, F., Piquemal, J.-Y., Brayner, R., El Kabouss, K., Soumare, Y., Viau, G., Shafeev, G., 2009. Nanoparticles of metal and metal oxides: some peculiar synthesis methods, size and shape control, application to catalysts preparation. Brazilian J. Phys. 39, 134–140. doi:10.1590/S0103-97332009000200002

Deepak, F.L., Casillas-Garcia, G., Esparza, R., Barron, H., Jose-Yacaman, M., 2011. New insights into the structure of PdAu nanoparticles as revealed by aberration-corrected STEM. J. Cryst. Growth 325, 60–67. doi:10.1016/j.jcrysgro.2011.04.026

EERE of the U.S. Department of Energy, 2011. Fuel Cell technologies program [WWW Document]. U.S. Dep. Energy.

Falicov, M., Tersoff, J., 1981. Electronic structure and local atomic configurations of flat and stepped (111) surfaces of Ni and gu 24.

Fuel Cell Today, Matthey, J., 2013. The Fuel Cell Industry Review.

Gasteiger, H.A., Markovic, N.M., 2009. Just a Dream—or Future Reality? 324, 48.

Gontard, L.C., Chang, L.Y., Hetherington, C.J.D., Kirkland, A.I., Ozkaya, D., Dunin-Borkowski, R.E., 2007. Aberration-corrected imaging of active sites on industrial catalyst nanoparticles. Angew. Chemie - Int. Ed. 46, 3683–3685. doi:10.1002/anie.200604811

Goris, B., Roelandts, T., Batenburg, K.J., Heidari Mezerji, H., Bals, S., 2013. Advanced reconstruction algorithms for electron tomography: from comparison to combination. Ultramicroscopy 127, 40–7. doi:10.1016/j.ultramic.2012.07.003

Hass, H., 2004. Well-to-wheels analysis of alternative fuels and powertrains in the European context, VDI Berichte. doi:10.2788/79018

Haynes, P.D., Mostofi, A. A., Skylaris, C.-K., Payne, M.C., 2006. ONETEP: linear-scaling density-functional theory with plane-waves 26, 78–91. doi:10.1088/1742-6596/26/1/034

Holton, O.T., Stevenson, J.W., 2013. The role of platinum in proton exchange membrane fuel cells. Platin. Met. Rev. 57, 259–271. doi:10.1595/147106713X671222

Jacobsen, C.J.H., Dahl, S., Hansen, P.L., Törnqvist, E., Jensen, L., Topsøe, H., Prip, D. V., Møenshaug, P.B., Chorkendorff, I., 2000. Structure sensitivity of supported ruthenium catalysts for ammonia synthesis. J. Mol. Catal. A Chem. 163, 19–26. doi:10.1016/S1381-1169(00)00396-4

Jaksic, J.M., Ristic, N.M., Krstajic, N. V., Jaksic, M.M., 1998. Electrocatalysis for hydrogen electrode reactions in the light of fermi dynamics and structural bonding FACTORS—I. individual electrocatalytic properties of transition metals. Int. J. Hydrogen Energy 23, 1121–1156. doi:10.1016/S0360-3199(98)00014-7

Jinnouchi, R., 2003. New Insight Into Microscale Transport Phenomena in Pefc By Quantum Md. Microscale Thermophys. Eng. 7, 15–31. doi:10.1080/10893950390150421

Jones, L., MacArthur, K.E., Fauske, V.T., van Helvoort, A.T.J., Nellist, P.D., 2014. Rapid estimation of catalyst nanoparticle morphology and atomic-coordination by high-resolution z-contrast electron microscopy. Nano Lett. 14, 6336–41. doi:10.1021/nl502762m

Kinoshita, K., 1990. Particle Size Effects for Oxygen Reduction on Highly Dispersed Platinum in Acid Electrolytes. J. Electrochem. Soc. 137, 845. doi:10.1149/1.2086566

Koh, S., Strasser, P., 2007. Electrocatalysis on bimetallic surfaces: Modifying catalytic reactivity for oxygen reduction by voltammetric surface dealloying. J. Am. Chem. Soc. 129, 12624–12625. doi:10.1021/ja0742784

Langmuir, I., 1918. The Adsorption of Gases on Plane Surfaces of Glass, Mica and Platinum. J. Am. Chem. Soc. 40, 1361–1403. doi:doi: 10.1021/ja02242a004

Liu, Z., Ma, L., Zhang, J., Hongsirikarn, K., Goodwin, J.G., 2013. Pt Alloy Electrocatalysts for Proton Exchange Membrane Fuel Cells: A Review. Catal. Rev. 55, 255–288. doi:10.1080/01614940.2013.795455

Natesakhawat, S., Lekse, J.W., Baltrus, J.P., Paul, R., Howard, B.H., Deng, X., Matranga, C., 2012. Active Sites and Structure-activity Relationships of Copper- based Catalysts for Carbon Dioxide Hydrogenation to Methanol Active Sites and Structure-activity Relationships of Copper-based Catalysts for Carbon Dioxide Hydrogenation to Methanol. ACS Catal 2, 1667–1676. doi:10.1021/cs300008g

Nørskov, J.K., Rossmeisl, J., Logadottir, A., Lindqvist, L., Kitchin, J.R., Bligaard, T., Jónsson, H., 2004. Origin of the overpotential for oxygen reduction at a fuel-cell cathode. J. Phys. Chem. B 108, 17886–17892. doi:10.1021/jp047349j

Oezaslan, M., Strasser, P., 2011. Activity of dealloyed PtCo3 and PtCu3 nanoparticle electrocatalyst for oxygen reduction reaction in polymer electrolyte membrane fuel cell. J. Power Sources 196, 5240–5249. doi:10.1016/j.jpowsour.2010.11.016

Raróg-Pilecka, W., Miśkiewicz, E., Szmigiel, D., Kowalczyk, Z., 2005. Structure sensitivity of ammonia synthesis over promoted ruthenium catalysts supported on graphitised carbon. J. Catal. 231, 11–19. doi:10.1016/j.jcat.2004.12.005

Saadatjou, N., Jafari, A., Sahebdelfar, S., 2014. Ruthenium Nanocatalysts for Ammonia Synthesis: A Review. Chem. Eng. Commun. 202, 420–448. doi:10.1080/00986445.2014.923995

Schulenburg, H., Müller, E., Khelashvili, G., Roser, T., Bönnemann, H., Wokaun, A., Scherer, G.G., 2009. Heat-Treated PtCo3 Nanoparticles as Oxygen Reduction Catalysts. J. Phys. Chem. C 113, 4069–4077. doi:10.1021/jp808134j

Sheng, W., Gasteiger, H. a., Shao-Horn, Y., 2010. Hydrogen Oxidation and Evolution Reaction Kinetics on Platinum: Acid vs Alkaline Electrolytes. J. Electrochem. Soc. 157, B1529. doi:10.1149/1.3483106

Skylaris, C.K., Haynes, P.D., Mostofi, A. A., Payne, M.C., 2005. Introducing ONETEP: Linear-scaling density functional simulations on parallel computers. J. Chem. Phys. 122, 1–10. doi:10.1063/1.1839852

Stamenkovic, V., Mun, B.S., Mayrhofer, K.J.J., Ross, P.N., Markovic, N.M., Rossmeisl, J., Greeley, J., Nørskov, J.K., 2006. Changing the activity of electrocatalysts for oxygen reduction by tuning the surface electronic structure. Angew. Chemie - Int. Ed. 45, 2897–2901. doi:10.1002/anie.200504386

Taylor, H.S., 1925. A Theory of the Catalytic Surface. Proc. R. Soc. A Math. Phys. Eng. Sci. 108, 105–111. doi:10.1098/rspa.1925.0061

Toda, T., 1999. Enhancement of the Electroreduction of Oxygen on Pt Alloys with Fe, Ni, and Co. J. Electrochem. Soc. 146, 3750. doi:10.1149/1.1392544

Wang, D., Yu, Y., Zhu, J., Liu, S., Muller, D.A., Abruña, H.D., 2015. Morphology and activity tuning of Cu3Pt/C ordered intermetallic nanoparticles by selective electrochemical dealloying. Nano Lett. 15, 1343–1348. doi:10.1021/nl504597j

Wang, Z.W., Li, Z.Y., Park, S.J., Abdela, A., Tang, D., Palmer, R.E., 2011. Quantitative Z-contrast imaging in the scanning transmission electron microscope with size-selected clusters. Phys. Rev. B - Condens. Matter Mater. Phys. 84, 73408. doi:10.1103/PhysRevB.84.073408

Xin, H., Vojvodic, A., Voss, J., Nørskov, J.K., Abild-Pedersen, F., 2014. Effects of d-band shape on the surface reactivity of transition-metal alloys. Phys. Rev. B 89, 115114. doi:10.1103/PhysRevB.89.115114

Yang, F., Deng, D., Pan, X., Fu, Q., Bao, X., 2015. Understanding nano effects in catalysis.

Yates, J.T., 1995. Surface chemistry at metallic step defect sites. J. Vac. Sci. Technol. A Vacuum, Surfaces, Film. 13, 1359. doi:10.1116/1.579564

Young, N.P., Li, Z.Y., Chen, Y., Palomba, S., Di Vece, M., Palmer, R.E., 2008. Weighing supported nanoparticles: Size-selected clusters as mass standards in nanometrology. Phys. Rev. Lett. 101, 246103. doi:10.1103/PhysRevLett.101.246103

Yu, Z., Zhang, J., Liu, Z., Ziegelbauer, J.M., Xin, H., Dutta, I., Muller, D. a., Wagner, F.T., 2012. Comparison between dealloyed PtCo 3 and PtCu 3 cathode catalysts for proton exchange membrane fuel cells. J. Phys. Chem. C 116, 19877–19885. doi:10.1021/jp306107t

Zhang, L., Anderson, R.M., Crooks, R.M., Henkelman, G., 2015. Correlating Structure and Function of Metal Nanoparticles for Catalysis. Surf. Sci. 640, 65–72. doi:10.1016/j.susc.2015.03.018

2 Introduction to Characterisation Methods

2.1 Chapter Overview

This chapter reviews the current characterisation methods, along with their strengths and weaknesses. The available characterisation methods have been grouped into bulk averaging methods and single-particle methods. To achieve meaningful and high-throughput characterisation a review of recent capabilities of each technique is presented.

2.2 The Available Characterisation Methods

Catalyst characterisation methods can be grouped into two main categories, the bulk averaging methods and precise single-particle methods. Figure 2.1 shows the grouping of popular techniques used within the field for both categories. Each technique has its strengths and weaknesses which can be further classed by analysis speed.

For instance, bulk averaging methods are labelled as “fast”, these techniques usually require time frames between minutes and hours to characterise the properties of a catalyst. However, these methods only provide an average of the whole ensemble and detailed information about active sites and bonding is washed out by the resolution of the technique.

In contrast, few particle methods are labelled “slow”, these techniques take several hours and sometimes days to analyse a single nanoparticle. These techniques provide detailed information of single or few nanoparticles, but the bulk information is lost.

Ideally, a balanced characterisation method is required, this would be a method where detailed information of a nanoparticle is obtained in a reasonable amount of time encompassing the whole ensemble. The following sections briefly review the popular catalyst characterisation techniques used within the field and highlight their strengths and weaknesses for analysing ultra-small PEMFC nanoparticles.

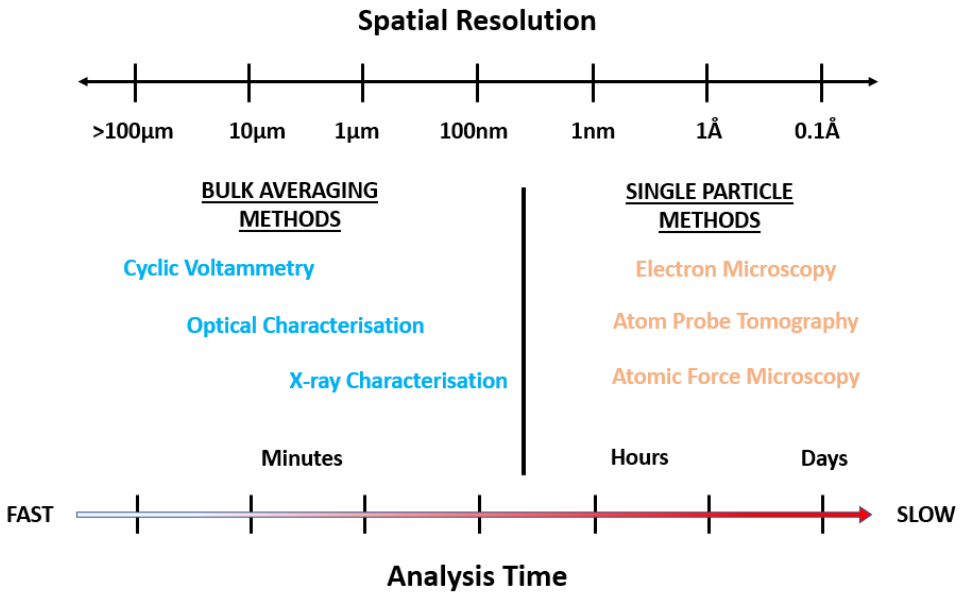

Figure 2.1 Popular catalyst nanoparticle characterisation methods grouped within their respective categories. The separation line indicates the gap between the analysis time and resolution limits of the two categories.

2.3 Optical Characterisation

Optical spectroscopic methods such as Raman, infra-red and UV-vis spectroscopy can provide measurements of inelastic and elastic scattering of a particular wavelength of light. This can provide information about the electronic structure of the catalyst nanoparticles, from which oxidation state and bonding information of a particle can be determined (Hammes, 2005).

Typically, this is done by illuminating a sample with a laser beam, where the inelastically scattered beam is measured by a detector. The difference in frequency, wavelength and energy of the scattered beam provides an indication of the electronic state of the sample. Since the vibrational frequencies of the scattered beam are chemically unique, a molecular fingerprint of the sample can be obtained (Butler et al., 2016).

In solid state physics, optical spectroscopy has been used to measure temperature and find the bulk crystalline orientation of samples, whereas in nanotechnology this method has been used to measure bulk crystallite size (Khanna et al., 1981; X. Li et al., 2015).

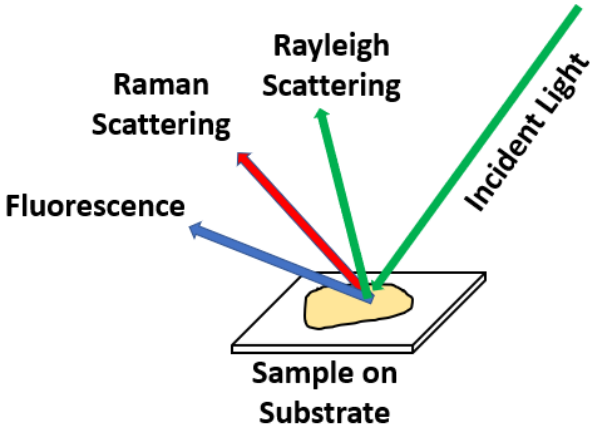

Figure 2.2 Simple Raman spectroscopy schematic

The main advantage of this characterisation method is that it is inexpensive and fast. This makes it ideal for bulk chemical characterisation of a wide variety of samples in the physical and biological sciences. Additionally, it is ideal for confirming bulk element composition and phonon configuration in a non-invasive manner.

However, the principal disadvantage of this method is its wavelength limited resolution. The limit at which two objects can be resolved as separate entities is determined by the Rayleigh criterion, equation *3*.

$$\sin(\theta_R) = 1.22 \times {}^{\lambda}/_{d} \qquad (3)$$

Where θ_R is the angular position of the first order diffraction minimum, λ is the wavelength of the incident photon and d is the separation between two diffracting objects. At 633nm photon wavelength of the laser, the typical Raman spectroscopy resolution is quoted of being in the order of 1 micron (Butler et al., 2016; Khanna et al., 1981; Khavrus et al., 2012; Kumar et al., 2015).

Most PEMFC catalyst nanoparticles have a size range of 2-10nm, which means that optical characterisation cannot provide the detailed atomic structural information required to study size, shape, strain and composition at the atomic level.

2.4 Cyclic Voltammetry

Cyclic voltammetry is a miniature test rig that determines a samples catalytic performance, Figure 2.3. Here a working electrode's potential is increased proportionally with time and after a set maximum is reached the potential is ramped in the opposite direction. The ramp cycles are repeated several times and the current of the working electrode is measured and plotted as a function of applied voltage.

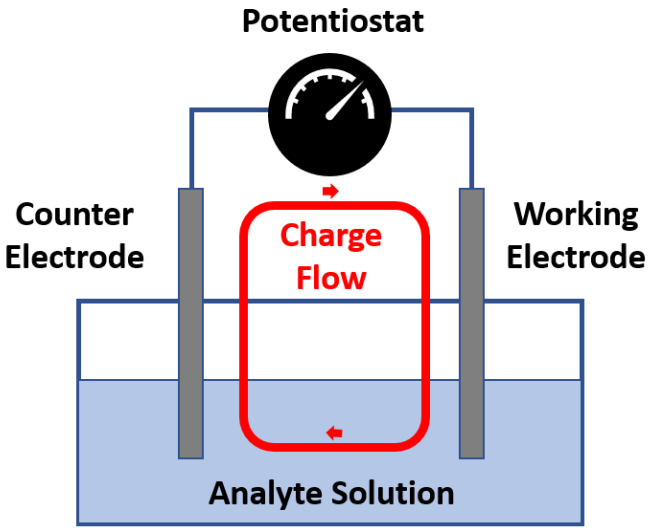

Figure 2.3 Simple schematic of a cyclic voltammeter.

This technique is particularly useful for measuring the performance of fuel cell catalysts after synthesis or during life cycles of a cell. Several research papers often incorporate some correlative cyclic voltammetry results alongside other characterisation techniques (Crabb et al., 2000; Khan et al., 2009). Even though the performance measured is of the bulk sample, the results are often enough to give a definite indication whether the synthesis was successful.

However, it is not possible to obtain conclusive information of interactions at the atomic level and often a "single/few" particle method from Figure 2.1 is required to supplement for this (Schulenburg et al., 2009). Other approaches have also tried emulating voltammetry experiments at the micron scale using X-rays and electron microscopy. However here care must be taken to mitigate the effect of the incoming beam flux for perturbing the experiment (Chenna and Crozier, 2012).

2.5 X-ray Characterisation

X-ray characterisation allows the determination of crystal and molecular structure of a sample. Here an incident beam of X-rays illuminates the sample, and by measuring the intensity and scattering angles of the diffracted beam properties such crystal structure, strain and size can be determined. By rotating and moving the sample around it is also possible to map the three-dimensional structure of a large enough sample.

Figure 2.4 shows the simple schematic for a general X-ray diffraction experiment. The information content obtained from this is dependent on the source and size of the X-ray beam. Also depending on the technique, the sample or the detector is moved during analysis.

The most common technique used for analysis is the powder diffraction technique, where the sample is in powder form and is rotated. The diffraction from the poly-crystalline sample is recorded by the detector, and the overall crystallography of the bulk sample is determined. By analysing the diffraction peaks, it is possible to obtain bulk average information about crystallite size and strain (Patterson, 1939).

Another popular technique is synchrotron x-ray diffraction. In this method the x-rays, which penetrate through the sample are recorded using fixed detectors. To obtain a scanning image, the sample is mounted on a stage and rastered along a defined path. The resulting diffraction pattern is recorded, and a sample image is inverted from this to obtain a real space projection.

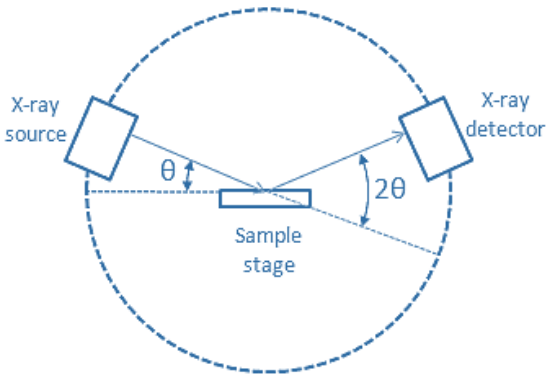

Figure 2.4 X-ray diffraction schematic, usually either the detector or the sample is rotated on an axis. Schematic adapted from https://chem.libretexts.org /Core/Analytical_Chemistry/Instrumental_Analysis/Diffraction_Scattering_Techniques

In addition to this, the scattered x-ray energy loss can also be measured, thus providing chemical and bonding information about a sample. The x-ray absorption fine structure can provide location information such as coordination number, ordering and nearest neighbour distances (Ravel and Kelly, 2007). Whereas, x-ray absorption near edge spectra can provide chemical, oxidation state and bonding transition information(Jones, 1988).

X-ray diffraction techniques are one of the dominant methods for analysing catalyst nanoparticles due to the wealth of information obtained. However, limitations on the incident beam size (~20nm) mean that analysis of ultra-small PEMFC nanoparticles with this method is challenging. Additionally, scanning a sample with respect to a fixed x-ray beam means that sample loading may sometimes be difficult and time-consuming.

2.6 Atom Probe Tomography

In atom probe tomography, the sample is usually mounted onto a needle and subjected to a bias voltage. The atoms from the needle are flung off onto characteristic trajectories and deposited on a screen, Figure 2.5. Deposited atoms on the screen create interpretable patterns, which provide chemical and structural information about the sample.

Atom probe tomography can provide chemical and structural information about a sample at atomic resolution making it one of the few techniques that can study catalyst nanoparticles. However, currently, the main limitation of the technique is experiment time and sample preparation. A typical experiment lasts a few hours for a few samples, which means low throughput. Plus difficult sample preparation, to make sure that the nanoparticles deposited on the needle are an accurate representation of the sample, is time-consuming (Q. Yang et al., 2015).

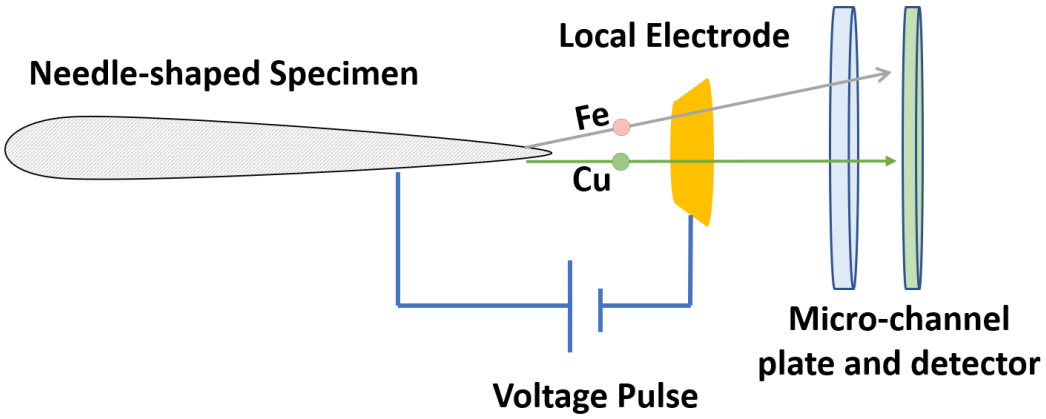

Figure 2.5 Schematic of an atom probe, where ions from the needle-shaped specimen are evaporated by applying a voltage pulse.

2.7 Atomic Force Microscopy

In atomic force microscopy, a metallic needle tip is scanned across the sample surface, and the displacement of the needle caused by the field around the sample is measured (Figure 2.6). The atomic force microscope has popular uses in imaging and manipulating a sample. The tip can be scanned along the sample to measure the forces (electrostatic, magnetic or van der Waals) and image the sample under different configurations. Alternatively, sample manipulation can be performed by either direct contact or by applying a potential across the tip.

The key strength of this technique lies in the ability to measure and change a sample in a desired manner. Recent efforts have aimed at integrating nanotechnology and biological research for in-situ analysis of drug responses of live cells (De Jong and Borm, 2008). Additionally, it is one of the few techniques that can image nanoparticles at atomic resolution and provide three-dimensional structure and compositional information.

However, there are a few limitations of this technique; the slow scan speed means that the technique in its current state cannot provide high throughput analysis (Lapshin, 2007). The slow scan will also draw concern towards the sample's thermal stability. To mitigate this the microscope is usually operated under ultra-high vacuum conditions on an air table or in an isolated room.

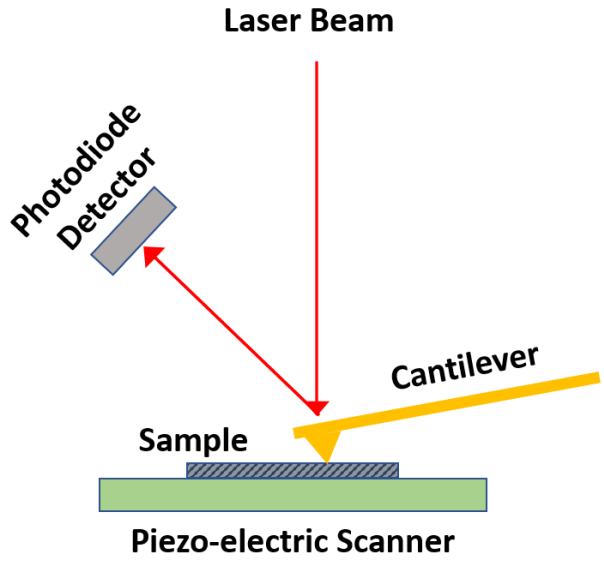

Figure 2.6 Atomic force microscopy schematic.

2.8 Electron Microscopy

In electron microscopy, the sample is illuminated by electrons, and a two-dimensional projection of the diffraction or image of the sample is obtained. There are two types of electron microscope modes, surface-scanning and transmission.

In a conventional SEM, an electron probe is focused by an electromagnetic lens onto the specimen's surface. The probe is scanned in a raster across the surface, and the scattered electrons and signals are collected by a detector for analysis. Current SEMs have typical electron accelerating voltages of 1-30keV, with a probe sizes ranging from sub-nm to 10nm. This means that the SEM is not suitable for characterising ultra-small PEMFC nanoparticles at atomic resolution. However, it is well suited for studying macroscopic properties such as clustering of nanoparticles and support metal interactions on a grid.

In contrast to the SEM, an electron in TEM passes through the sample, and various pre-and post-specimen detectors measure the interaction. The TEM can usually be operated in either parallel illumination mode or scanning mode.

In parallel illumination mode, the beam interacts over a large sample area, and an image can be observed on the imaging plane. This mode routinely provides two-dimensional atomic

resolution images but deriving quantitative information from this is difficult. This is mainly due to the interference electron wave giving rise to phase contrast, making images difficult to interpret (Cowley, 1969; Lee et al., 2012).

In the scanning mode, also known as STEM, a scanning convergent beam forms a raster over the sample. Current aberration-corrected microscopes have sub-angstrom probe sizes which means that the electron beam interaction with the sample is localised. This means that, with the right detectors, simultaneous structural and chemical information of a sample can be obtained.

The primary disadvantage of STEM is low throughput and sample damage. However, recent developments in quantitative STEM demonstrate that rapid inversion of two-dimensional data into three-dimensional structures is routinely possible (Jones et al., 2014). This means that STEM has the potential to perform detailed catalysts analysis at high throughput. The next chapter highlights the basics of STEM and recent developments in the field.

2.9 Conclusions

A review of some of the popular characterisation techniques shows that they can be grouped into either “bulk averaging” or “few particle” methods. The optical, voltammetry and x-ray techniques provide a bulk average measurement of the sample’s overall chemical and structural information. Whereas, atom probe tomography, atomic force and electron microscopy provide detailed information about the sample at low throughput.

A brief overview of the advantages and disadvantages of each technique indicates that for high throughput atomic resolution characterisation of industrial PEMFC catalyst nanoparticles, STEM is a valuable tool. Much of this is due to recent developments in techniques to directly interpret two-dimensional images from STEM and invert them into three-dimensional structures.

2.10 References

Butler, H.J., Ashton, L., Bird, B., Cinque, G., Curtis, K., Dorney, J., Esmonde-White, K., Fullwood, N.J., Gardner, B., Martin-Hirsch, P.L., Walsh, M.J., McAinsh, M.R., Stone, N., Martin, F.L., 2016. Using Raman spectroscopy to characterize biological materials. Nat. Protoc. 11, 664–687. doi:10.1038/nprot.2016.036

Chenna, S., Crozier, P.A., 2012. Operando transmission electron microscopy: A technique for detection of catalysis using electron energy-loss spectroscopy in the transmission electron microscope. ACS Catal. 2, 2395–2402. doi:10.1021/cs3004853

Cowley, J.M., 1969. IMAGE CONTRAST in a TRANSMISSION SCANNING ELECTRON MICROSCOPE. Appl. Phys. Lett. 15, 58–59. doi:10.1063/1.1652901

Crabb, E.M., Marshall, R., Thompsett, D., 2000. Carbon Monoxide Electro-Oxidation Properties of Carbon-Supported PtSn Catalysts Prepared Using Surface Organometallic Chemistry. J. Electrochem. Soc. 147, 4440. doi:10.1149/1.1394083

De Jong, W.H., Borm, P.J.A., 2008. Drug delivery and nanoparticles:applications and hazards. Int. J. Nanomedicine 3, 133–49.

Hammes, G.G., 2005. Spectroscopy for the Biological Sciences. John Wiley & Sons, Inc., Hoboken, NJ, USA. doi:10.1002/0471733555

Jones, L., MacArthur, K.E., Fauske, V.T., van Helvoort, A.T.J., Nellist, P.D., 2014. Rapid estimation of catalyst nanoparticle morphology and atomic-coordination by high-resolution z-contrast electron microscopy. Nano Lett. 14, 6336–41. doi:10.1021/nl502762m

Jones, R.G., 1988. X-ray absorption: Principles, applications, techniques of EXAFS, SEXAFS, and XANES, Endeavour. John Wiley and Sons,New York, NY. doi:10.1016/0160-9327(88)90177-9

Khan, A S. A, Ahmed, R., Mirza, M.L., 2009. Evaluation of Catalytic Activity of Pt and Pt-Ru Catalysts for Electro-oxidation of Methanol in Acid Medium by Cyclic Voltammetry. Port. Electrochim. Acta 27, 429–442. doi:10.4152/pea.200904429

Khanna, R.K., Stranz, D.D., Donn, B., 1981. A spectroscopic study of intermediates in the condensation of refractory smokes: Matrix isolation experiments of SiO. J. Chem. Phys. 74, 2108–2115. doi:10.1063/1.441393

Khavrus, V.O., Ibrahim, E.M.M., Bachmatiuk, A., Rümmeli, M.H., Wolter, A. U.B., Hampel, S., Leonhardt, A., 2012. High-pressure catalytic chemical vapor deposition of ferromagnetic ruthenium-containing carbon nanostructures. J. Nanoparticle Res. 14. doi:10.1007/s11051-012-0914-5

Kumar, N., Stephanidis, B., Zenobi, R., Wain, A.J., Roy, D., 2015. Nanoscale Mapping of Catalytic Activity Using Tip-enhanced Raman Spectroscopy. Nanoscale. doi:10.1039/C4NR07441F

Lapshin, R. V., 2007. Automatic drift elimination in probe microscope images based on techniques of counter-scanning and topography feature recognition. Meas. Sci. Technol. 18, 907–927. doi:10.1088/0957-0233/18/3/046

Lee, Z., Meyer, J.C., Rose, H., Kaiser, U., 2012. Optimum HRTEM image contrast at 20kV and 80kV-Exemplified by graphene. Ultramicroscopy 112, 39–46. doi:10.1016/j.ultramic.2011.10.009

Li, X., Lin, M.-W., Puretzky, A.A., Idrobo, J.C., Ma, C., Chi, M., Yoon, M., Rouleau, C.M., Kravchenko, I.I., Geohegan, D.B., Xiao, K., 2015. Controlled Vapor Phase Growth of Single Crystalline, Two-Dimensional GaSe Crystals with High Photoresponse. Sci. Rep. 4, 5497. doi:10.1038/srep05497

Patterson, A.L., 1939. The Scherrer Formula for X-Ray Particle Size Determination. Phys. Rev. 56, 978–982. doi:10.1103/PhysRev.56.978

Ravel, B., Kelly, S.D., 2007. The difficult chore of measuring coordination by EXAFS. AIP Conf. Proc. 882, 150–152. doi:10.1063/1.2644458

Schulenburg, H., Müller, E., Khelashvili, G., Roser, T., Bönnemann, H., Wokaun, a., Scherer, G.G., 2009. Heat-Treated PtCo3 Nanoparticles as Oxygen Reduction Catalysts. J. Phys. Chem. C 113, 4069–4077. doi:10.1021/jp808134j

Yang, Q., Joyce, D.E., Saranu, S., Hughes, G.M., Varambhia, a., Moody, M.P., Bagot, P. a. J., 2015. A combined approach for deposition and characterization of atomically engineered catalyst nanoparticles. Catal. Struct. React. 2055075815Y.000. doi:10.1179/2055075815Y.0000000006

3 The Basics of STEM

3.1 Chapter Overview

This chapter covers the basics of STEM and the various detectors available to quantify catalyst nanoparticles. A brief overview of how ADF and spectroscopic detectors can be used to study catalyst morphology and shape is presented. A brief overview how the ADF and spectroscopic detectors work is presented along with their strengths and limitations. Finally, a proposed workflow technique of how STEM can be used to quantify catalyst nanoparticles to simplify the catalyst development cycle is presented.

3.2 Using STEM to Probe Catalysts

Images in STEM are formed by scanning a focused electron probe across a sample (Cowley, 1969), Figure 3.1. For atomic resolution, a finite probe of less than, or approximately, one angstrom is used as this ensures sufficient sampling to resolve atomic lattice planes. As the electron probe interacts with the sample, various signals are produced, which can be measured using detectors, Figure 3.1. The key advantage of STEM is that a sample can be probed locally. Due to this, thermal damage caused by the electron beam is dissipated locally when compared to conventional parallel illumination methods (Williams and Carter, 2009). As the sample is probed locally, chemical information can be measured using x-ray and electron energy loss detectors, whereas, structural information can be measured using ADF and SE detectors, Figure 3.2.

When using STEM to image catalysts, there are three main causes structural damage caused by the electron beam, these are heating, knock-on and radiolysis. Heating is caused by excitations of phonons within the sample as it interacts with the electron beam. Knock-on damage is defined as the displacement of atoms from their lattice sites by the incoming electron beam, and the damage caused is proportional to beam energy. Radiolysis is defined as the breaking of chemical bonds in a sample by mainly electron-electron interactions, such as ionization. The cause of each damage mechanism depends on a combination of conditions

such as type of material and beam energy. For Pt-based catalysts, previous studies in the thesis of (MacArthur., 2014) have shown that structural damage is predominantly caused by knock-on effects.

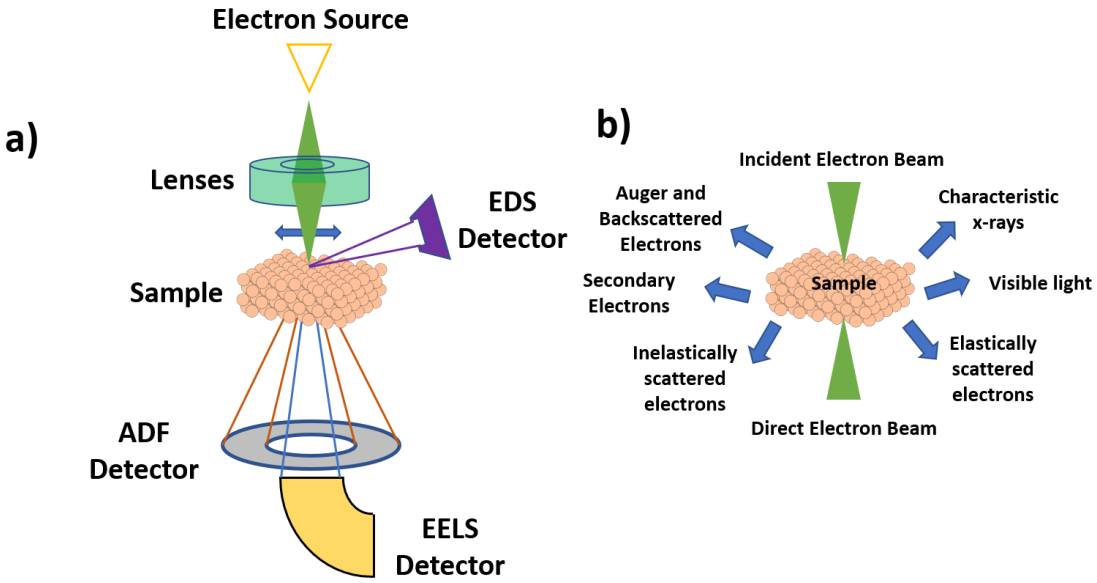

Figure 3.1 a) STEM schematic, with a focused probe in green scanning over a sample and the available detectors for imaging and spectroscopy, b) Some of the signals generated from the electron beam interaction which can be detected using various detectors.

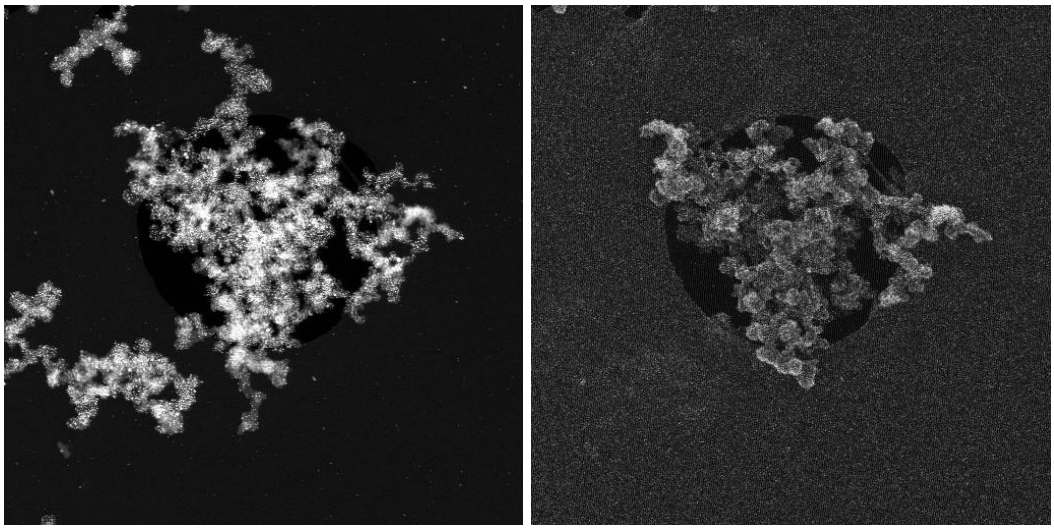

Figure 3.2 Simultaneous annular dark field (left) and secondary electron image (right) recorded on a JEOL ARM 200CF electron microscope, providing the catalyst structure and support material shape.

With the introduction of aberration correctors in the past decade (Krivanek et al., 2008), STEM now routinely provides atomic resolution ADF images, Figure 3.3. The primary trait of the ADF imaging mode is that the scattered signal measured is Z^n dependent where Z is the atomic number and n is between 1.2 and 1.7, as mentioned in Chapter 2 of (Nellist, 2011). This type

of scattering is known as Rutherford scattering (Rutherford 1911; Egerton, 2011). As the scattering angle becomes larger, the electron beam becomes less and less coherent. The intensity of the scattering is strongly dependent on the atom number Z in the specimen.

By tuning the ADF collection angle, the *Z*-dependence can be tuned selectively to image the catalyst and (or) the support material, Figure 3.3. This selectivity makes the ADF mode ideal for imaging catalyst nanoparticles which are supported on lighter element materials (Nellist and Pennycook, 1996).

In ADF imaging, the scattering from the sample that falls onto the detector is integrated over an annular ring. This means that the measured signal is incoherent (Nellist and Pennycook, 2000) and is described by a convolution of the probe intensity profile $P(\boldsymbol{r_0} - \boldsymbol{r})$ with a discrete object function $O(\boldsymbol{r})$, equation 4 (Pennycook and Jesson, 1990). Here $\boldsymbol{r}$ is a two-dimensional position vector in the sample illuminated by the STEM probe located at $\boldsymbol{r_0}$.

$$I(\boldsymbol{r_0}) = \int P(\boldsymbol{r_0} - \boldsymbol{r}) O(\boldsymbol{r}) d^2\,\boldsymbol{r} \qquad (4)$$

With the appropriate microscope calibrations, the resultant ADF images are quantifiable. This is discussed in more detail in the next chapter. The image intensities in the image can be quantified to obtain the number of atoms along a crystal column. From the atomic columns in the image two-dimensional x-y coordinate information about the column positions can be obtained and the z-height information can be obtained through tomography (Bals et al., 2011) or quantitative STEM with energy minimization (Jones et al., 2014).

Quantitative ADF STEM is great for obtaining three-dimensional structures of pure element samples. However, if more than one atom type is present in the sample, the measured image intensity will then depend on both element number and specimen thickness. Decoupling composition and thickness effects quantitatively from the ADF signal is difficult. Therefore, spectroscopic signals such as EDS and EELS are more suited for this purpose (Egerton, 2011; Watanabe and Williams, 2006).

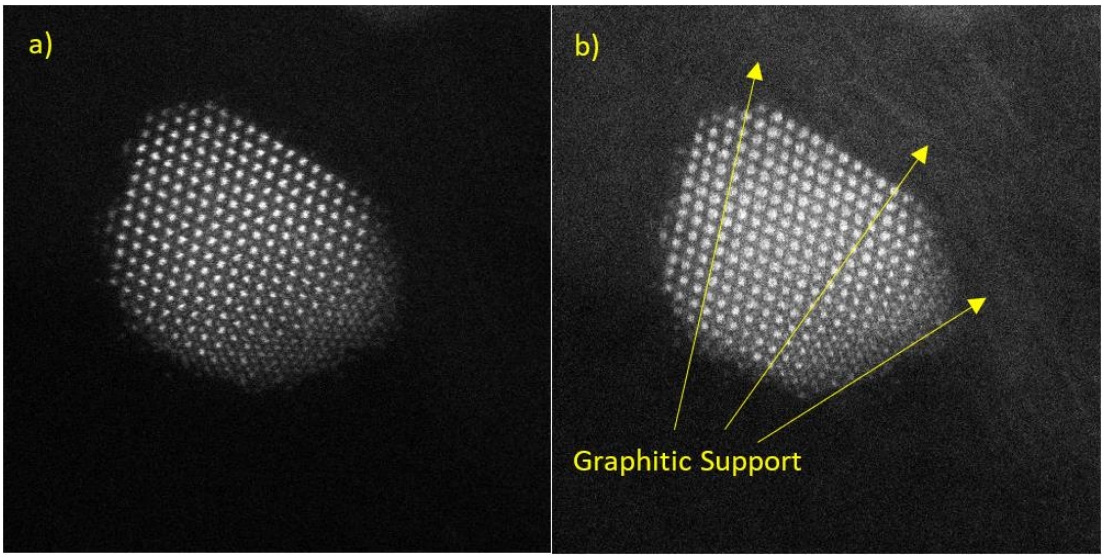

Figure 3.3 An on-axis Pt nanoparticle recorded at two different ADF collection angles, the image on the left shows a stronger Z dependence than the image on the right. However, the image on the right contains more detailed information about the catalyst support.

EDS and EELS signals can be recorded simultaneously alongside the ADF signal as the probe interacts with the sample. These spectroscopic signals are produced by interactions of the incident electron with atoms in the sample, Figure 3.4. In some cases, when an incident electron interacts with an atom, an inner shell ionisation event occurs. Here, the incident beam electron knocks out an inner shell electron leaving a void which can be filled by an electron from a higher state (Williams and Carter, 2009). The incident electron loses energy (ΔE) and promotes the interacting atom to an excited state. When the atom eventually relaxes back to its ground state, excess energy is released in the form of fluorescence yield, (one example is x-ray). The excitation and relaxation energies are characteristic for each element and can be detected using appropriate EDS and EELS detectors.

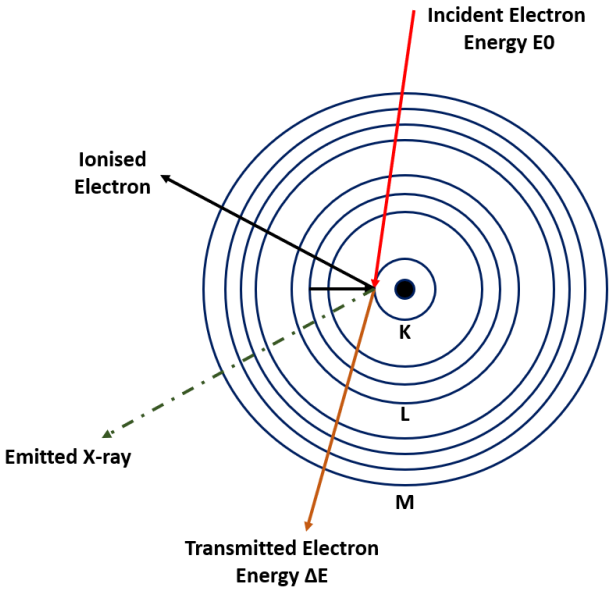

Figure 3.4 Emission of a characteristic Kα X-ray by momentum transfer from an incident electron with energy E_0. The energies of the X-ray and transmitted electron are measured using the EDS and EELS spectrometers respectively.

For EDS signal detection, the detector is usually made up of either Si or Ge material. X-rays generated from the sample (Figure 3.4) hit the detector and are converted into a charged pulse. The pulse is then processed into an energy readout by a pulse processor and relayed to a computer. The most common detectors are Si-based, but recently Si Drift Detectors (SDDs) have been gaining popularity (Lechner et al., 2001).

Figure 3.5 shows the X-ray ionisation data obtained from a Pt-Co nanoparticle on a JEOL ARM 200CF microscope. The main drawback of x-ray spectroscopy is the lack of sufficient counts from thin samples such as nanoparticles. This is due to the x-ray ionisation cross-section being several orders of magnitude lower than that of ADF and EELS cross-sections (MacArthur et al., 2015).

Furthermore, the EDS detector collection solid angle is limited; only a small fraction of the x-rays generated are collected. This is being improved by better sample holder modifications and detector technology (Zaluzec, 2013). Even with this limitation, EDS quantification is a popular method of quantifying bimetallic nanoparticles because data processing is straightforward and easy due to the low noise background in the signal.

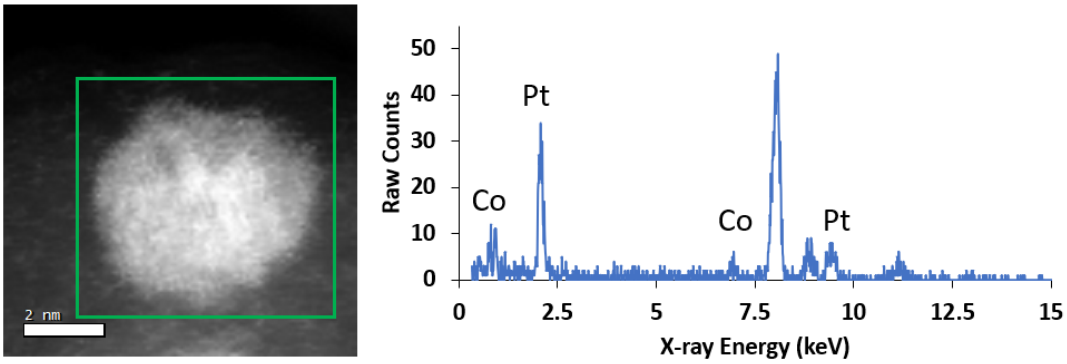

Figure 3.5 Pt and Co X-ray intensities detected from a Pt-Co nanoparticle using an EDS detector. The Pt and Co signals originate from within the green region of interest selected around the nanoparticle.

The alternative spectroscopic characterisation method is EELS. Here the chemical signal originates not from x-rays, but from the transmitted electron, Figure 3.4. The transmitted electrons from the sample are dispersed as a function of energy using a magnetic prism-filter system (Gubbens et al., 2010), and focused on a CCD or counting detector coupled to an array detection system. The EELS signal provides more detailed chemical information from about a sample such as valence and conduction band electronic properties, and oxidation state information. Additionally, the Co-L ionisation cross-section is three orders of magnitude higher than EDS Co-K corresection (MacArthur et al., 2015).

However, the EELS signal is sometimes more complicated to interpret compared to EDS signal. The energy around 0eV is known as the zero-loss peak. The zero-loss peak contains all the elastically scattered electron components and gives an indication of the energy spread of the electron source. Usually, for thin samples, more than 90% of the measured EELS signal is contained in the zero-loss peak as most electrons pass through the sample without interacting (Hofer, 1991).

The low-loss region is typically defined from >0eV and 50eV and is dominated by plasmon oscillations of the valence electrons and interband transitions from valence to conduction bands. For example, with this technique, the plasmonic and electronic structure of catalysts such as Au and Pd has been probed (Ringe et al., 2015).

The high-loss region is defined for energies higher than 50eV and corresponds to the excitation of electrons from localised orbitals on a single atomic site to extended unoccupied electron energy levels just above the Fermi level of the sample. This means that the high-loss can describe bonding and oxidation state information in detail from the sample by measuring peak energy shifts and ionisation peak intensity ratios (Ni et al., 2011; Z. Yu et al., 2012).

The main issue with processing EELS signals is the removal of the background from the data. In the low-loss spectrum, the background originates from a combination of phonon and plasmon oscillations and is challenging to model. Whereas, in the high-loss, the measured chemical signal of interest is superimposed on a background that dominated by single and collective low energy electron excitations (Liu and Brown, 1987).

Figure 3.6 shows a Co and Pt EELS spectra, from a Pt-Co nanoparticle, recorded on a JEOL ARM 200CF microscope. A decaying background exhibiting inverse power-law behaviour can be seen in the Co spectrum. As shown by the Pt spectrum in Figure 3.6, for increasing energy-losses, the signal to noise ratio becomes worse, and for small nanoparticles, the background becomes challenging to model because of low SNR. Furthermore, the ionisation edge shape sometimes complicates the quantification procedure. For example, in Figure 3.6, the Co signal has sharp peaks compared to the Pt signal, which is a delayed double hump.

Due to the involved quantification, EELS remains less popular compared to EDS, even though the latter provides more chemical information about the sample and the signal count is three orders of magnitude larger. The ideal approach would be to record the EDS and EELS data simultaneously to build up signal statistics and exploit the advantage of both techniques.

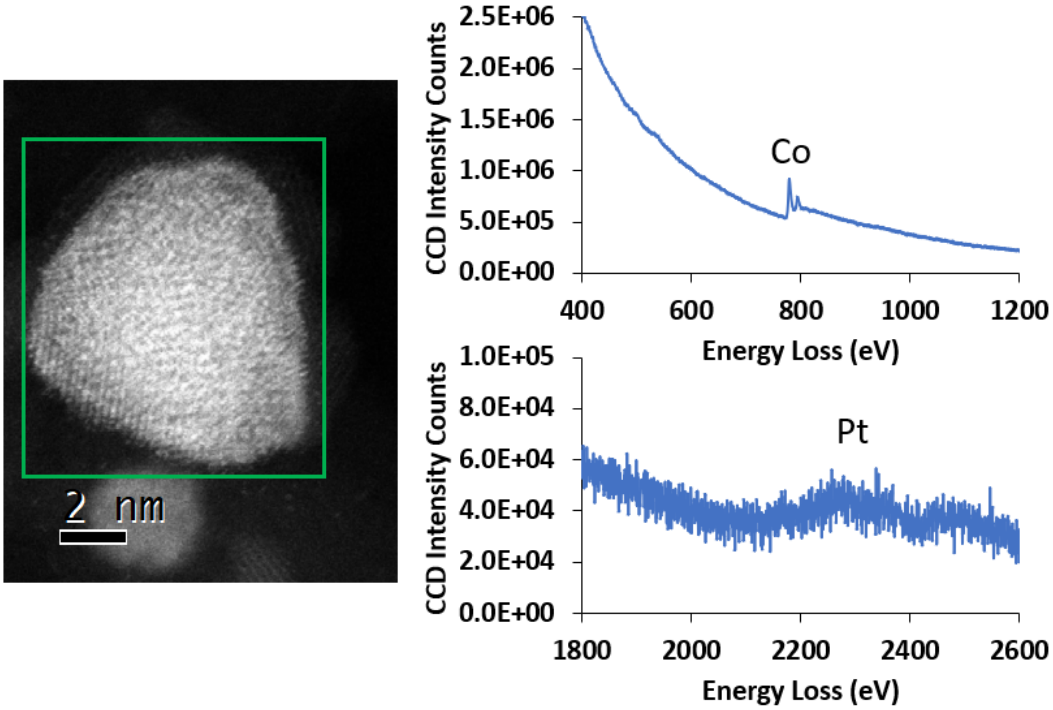

Figure 3.6 Pt and Co electron energy loss signal from a bimetallic nanoparticle. The Pt and Co signals originate from within the green region of interest selected around the nanoparticle.

3.3 Using STEM for Better Catalyst Design

With new hardware and software capabilities such as faster EDS and dual-EELS detectors, recording ADF, EDS and EELS data simultaneously is becoming more routine (Kothleitner et al., 2014). In this thesis a method of characterising a catalyst's size, shape and strain information was explored using ADF, EDS and EELS signals. Structural information can be quantified using the ADF signal, whereas the composition information can be quantified using EDS and EELS signals. With this in mind, a workflow can be envisioned to characterise catalyst nanoparticles at high throughput, Figure 3.7.

In Figure 3.7, nanoparticles synthesised by industry can be characterised into three-dimensional structures using STEM. The three-dimensional structures obtained from STEM can be used as inputs for electronic structure codes such as DFT. Catalyst activity and bonding information as a function of nanoparticle size can be used to predict catalyst performance. Moreover, the information can be relayed to the synthesisers and improve upon the catalyst design.

To build the design pipeline an optimisation of the software and technique development to characterise catalyst nanoparticles at high throughput is required. This is demonstrated in more detail in the next chapters in the form of case studies for different catalyst materials.

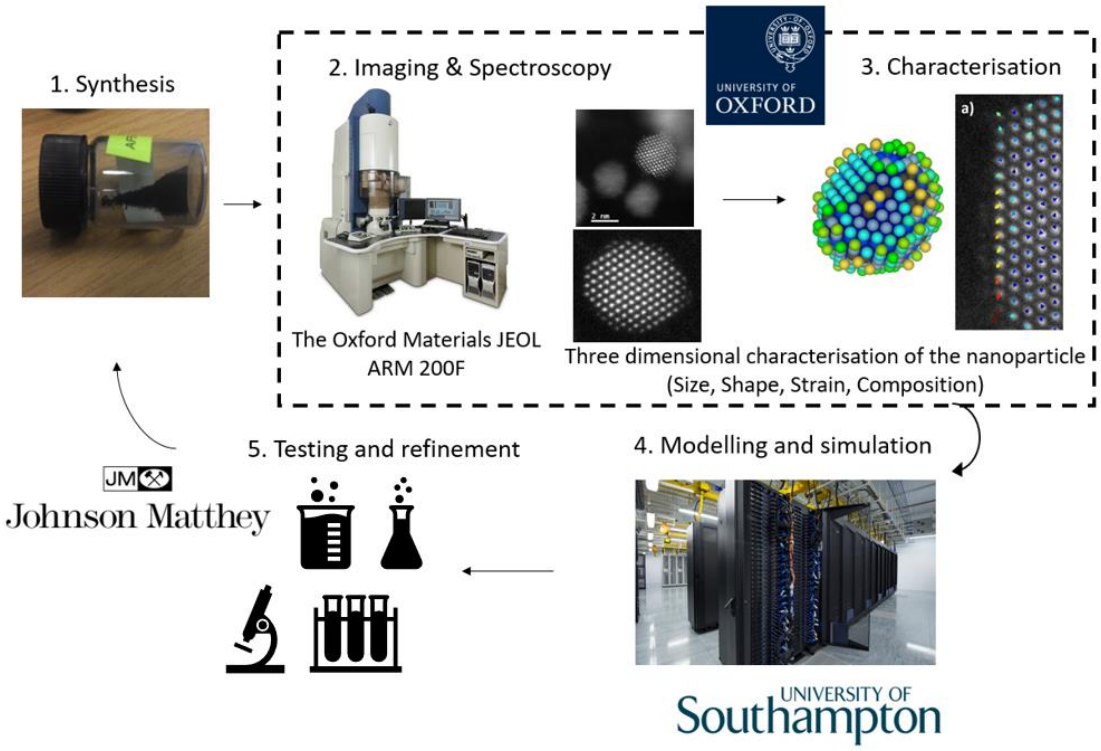

Figure 3.7 The catalyst design process and the collaborators involved in the project. Ranging from synthesis to characterisation, to simulations, and finally, testing and refinement.

3.4 Conclusions

STEM offers a broad range of signals that can provide structural and compositional information about a sample. For example, the ADF detector can be used to obtain structure information and the spectroscopic (EDS and EELS) detectors can be used to obtain composition information. These detectors can be run simultaneously and provide (generate) a wealth of information. Additionally, the simultaneous recording data using different detectors mitigates each detector's disadvantages as well. With recent developments in microscope hardware, it is now becoming routinely possible to acquire multivariate (ADF, EDS and EELS) datasets. Thus, a workflow can be developed to characterise catalyst nanoparticles at high throughput for simplifying the design process.

3.5 References

Bals, S., Casavola, M., Van Huis, M. A., Van Aert, S., Batenburg, K.J., Van Tendeloo, G., Vanmaekelbergh, D., 2011. Three-dimensional atomic imaging of colloidal core-shell nanocrystals. Nano Lett. 11, 3420–3424. doi:10.1021/nl201826e

Brydson, R. (Ed.), 2011. Aberration-Corrected Analytical Transmission Electron Microscopy, First Edit. ed. Wiley.

Cowley, J.M., 1969. IMAGE CONTRAST in a TRANSMISSION SCANNING ELECTRON MICROSCOPE. Appl. Phys. Lett. 15, 58–59. doi:10.1063/1.1652901

Egerton, R.F., 2011. Electron Energy-Loss Spectroscopy in the Electron Microscope, Springer, New York. doi:10.1007/978-1-4419-9583-4

Gubbens, A., Barfels, M., Trevor, C., Twesten, R., Mooney, P., Thomas, P., Menon, N., Kraus, B., Mao, C., McGinn, B., 2010. The GIF Quantum, a next generation post-column imaging energy filter. Ultramicroscopy 110, 962–970. doi:10.1016/j.ultramic.2010.01.009

Hofer, F., 1991. Determination of inner-shell cross-sections for EELS-quantification. Microsc. Microanal. Microstruct. 2, 215–230. doi:10.1051/mmm:0199100202-3021500

Jones, L., MacArthur, K.E., Fauske, V.T., van Helvoort, A.T.J., Nellist, P.D., 2014. Rapid estimation of catalyst nanoparticle morphology and atomic-coordination by high-resolution z-contrast electron microscopy. Nano Lett. 14, 6336–41. doi:10.1021/nl502762m

Kothleitner, G., Grogger, W., Dienstleder, M., Hofer, F., 2014. Linking TEM Analytical Spectroscopies for an Assumptionless Compositional Analysis. Microsc. Microanal. 20, 678–86. doi:10.1017/S1431927614000130

Krivanek, O.L., Corbin, G.J., Dellby, N., Elston, B.F., Keyse, R.J., Murfitt, M.F., Own, C.S., Szilagyi, Z.S., Woodruff, J.W., 2008. An electron microscope for the aberration-corrected era. Ultramicroscopy 108, 179–195. doi:10.1016/j.ultramic.2007.07.010

Lechner, P., Fiorini, C., Hartmann, R., Kemmer, J., Krause, N., Leutenegger, A., Soltau, H., Stotter, D., Stotter, R., Struder, L., Weber, U., 2001. Silicon drift detectors for high count rate X-ray spectroscopy at room temperature. Ultramicroscopy 458, 281–287.

Liu, D.-R., Brown, L.M., 1987. Influence of some practical factors on background extrapolation in EELS quantification. J. Microsc. 147, 37–49. doi:10.1111/j.1365-2818.1987.tb02816.x

MacArthur, K.E., Slater, T.J.A., Haigh, S.J., Ozkaya, D., Nellist, P.D., Lozano-perez, S., 2015. Quantitative EDX Analysis of Catalyst Nanoparticles Using a Partial Scattering Cross Section Approach. Microsc. Microanal. In press, 1–23. doi:10.1017/S1431927615015494

Nellist, P.D., Pennycook, S.J.J., 2000. The principles and interpretation of annular dark-field Z-contrast imaging, Advances in Imaging and Electron Physics. doi:10.1016/S1076-5670(00)80013-0

Nellist, P.D., Pennycook, S.J., 1996. Direct Imaging of the Atomic Configuration of Ultradispersed Catalysts. Science (80-.). 274, 413–415. doi:10.1126/science.274.5286.413

Ni, N., Lozano-Perez, S., Sykes, J., Grovenor, C., 2011. Quantitative EELS analysis of zirconium alloy metal/oxide interfaces. Ultramicroscopy 111, 123–130. doi:10.1016/j.ultramic.2010.10.020

Pennycook, S.J., Jesson, D.E., 1990. High-Resolution Incoherent Imaging of Crystals. Phys. Rev. Lett. 64, 938–942.

Ringe, E., Desantis, C.J., Collins, S.M., Duchamp, M., Dunin-, R.E., Dunin-Borkowski, R.E., Skrabalak, S.E., Midgley, P.A., 2015. Near-Field Plasmonic Behavior of Au/Pd Nanocrystals with Pd-Rich Tips. arXiv Prepr. 5, 1506.

E. Rutherford, The Scattering of α and β Particles by Matter and the Structure of the Atom, Philosophical Magazine. Series 6, vol. 21. May 1911

Watanabe, M., Williams, D.B., 2006. The quantitative analysis of thin specimens: A review of progress from the Cliff-Lorimer to the new ζ-factor methods. J. Microsc. 221, 89–109. doi:10.1111/j.1365-2818.2006.01549.x

Williams, D.B., Carter, C.B., 2009. Transmission Electron Microscopy, 2nd ed. Springer.

Yu, Z., Zhang, J., Liu, Z., Ziegelbauer, J.M., Xin, H., Dutta, I., Muller, D. a., Wagner, F.T., 2012. Comparison between dealloyed PtCo 3 and PtCu 3 cathode catalysts for proton exchange membrane fuel cells. J. Phys. Chem. C 116, 19877–19885. doi:10.1021/jp306107t

Zaluzec, N.J., 2013. Direct Comparison of X-ray Detector Solid Angles in Analytical Electron Microscopes. Microsc. Microanal. 19, 1262–1263. doi:10.1017/S1431927613008301

4 Catalyst Structure Determination using STEM ADF Quantification

4.1 Chapter Overview

This chapter covers a brief review of ADF quantification techniques. A short comparison between two popular structural inversion techniques, tomography and single projection, is made. From this comparison, the single projection techniques are favoured because of higher throughput. A more in-depth review of single projection techniques to invert images of pure element nanoparticles to their structures using ADF STEM is presented. Finally, these techniques were applied to quantify two catalyst systems as case studies.

The first system is a pure Ru catalyst used for ammonia synthesis and the second system is pure Pt catalysts used for PEMFC applications. For the Ru catalyst case study, the experimental data was acquired by Dr Lewys Jones and the analysis was performed by the author. For the Pt case study, the experimental data, the STEM simulations and the atom counting was performed by the author. The structural inversion and DFT simulations were performed by Dr Lewys Jones and Dr Jolyon Aarons respectively.

The results in this chapter present work from the following peer-reviewed publications:

- First Author: "Quantifying a Heterogeneous Ru Catalyst on Carbon Black Using ADF STEM", A. M. Varambhia, L. Jones, A. De Backer, V. T. Fauske, S. Van Aert, D. Ozkaya and P. D. Nellist, *Particle & Particle Systems Characterization* **33**:7 (2016), DOI:10.1002/ppsc.201600067.
- Joint First Author: "Predicting the oxygen binding properties of platinum nanoparticle ensembles by combining high-precision electron microscopy & DFT",Jolyon Aarons, Lewys Jones, Aakash Varambhia, Katherine E. MacArthur, Dogan Ozkaya, Misbah Sarwar, Chris-Kriton Skylaris, and Peter D. Nellist, *Nano Letters*, **17**(7) (2017), DOI:10.1021/acs.nanolett.6b04799.
- Second Author: "An optical configuration for fastidious STEM detector calibration and the effect of the objective-lens prefield", Lewys Jones, Aakash Varambhia, Hidetaka Sawada, and Peter D. Nellist, *Journal of Microscopy*, (2018), DOI:10.1111/jmi.12672.

4.2 Brief Review of ADF Quantification Techniques

There are two popular methods of characterising catalyst nanoparticles as three-dimensional models using STEM. The first method is tomography; this method allows for a three-dimensional model to be computed from a series of images taken at several tilt angles. The greater the number of projection images, the better the reconstruction. Typically 70 images are required for a reliable reconstruction (Zewail et al., 2010), and the accuracy depends on the reconstruction algorithm used (Batenburg and Sijbers, 2011).

Tomography is ideal for large samples where electron beam damage does not affect the morphology of the sample. Small nanoparticles usually cannot withstand the electron beam for longer than a few minutes without sustaining structural damage (De Backer et al., 2015b; Egerton, 2014; Jones et al., 2014; MacArthur et al., 2016). Moreover, since electron tomography experiments range in the time span of hours for a single nanoparticle (Yang et al., 2017), it is not an ideal for high throughput analysis.

To improve upon this, discrete tomography methods have been recently developed. In discrete tomography, only two projections of an object are required, and a statistical decomposition method is deployed to obtain a three-dimensional reconstruction of a nanoparticle (De Backer et al., 2017). This however, is still not high throughput as experiments may take time spans of several minutes/hours to scan a nanoparticle along two ideal zone axes. The reason for this is mainly due to the difficulty in rotating the sample to a desired zone-axis and then tilting it along a projection plane, whilst hoping minimal damage occurs to it.

The second method is a single projection inversion technique based on quantifying ADF image intensities into number of atoms from a single sample orientation. Here, the microscopist images nanoparticles that are found along a low-order zone axis on the support grid, thus reducing the time required to tilt along a desired axis. Much work has been done in this field by several research groups and there are two main approaches to obtain three-dimensional

structures. These two methods are simulation matching and statistical decomposition. They are described in more detail in the next section.

4.2.1 Obtaining Atom Counts from an ADF Image Using Simulation and Statistical Decomposition

In the simulation-matching approach, the experimental image intensities are converted into scattering cross-sections and compared to STEM image simulations. The simulated image intensities are in the form of "fractional beam current". This means that the image intensity is represented by the scattered signal with respect to the incident electron beam. Therefore, to compare the experiment to simulations, the experimental image intensities must also be represented units of fractional beam current.

With the appropriate microscope calibrations, the ADF image intensities can be fractionated with respect to the incident electron beam (Lebeau et al., 2010; Wang et al., 2011). This can be done using the expression given by equation 5. Here, I represents the measured intensity of either the experiment, detector or vacuum and is illustrated by Figure 4.1. The $I_{detector}$ is the full electron beam, in vacuum, illuminating the detector. I_{vacuum} is the vacuum intensity, which can often be non-zero due to experiment dependent amplifier offset. Thus, it is critical that the experiment and the detector scans are performed under the same amplifier settings and preferably the same experimental session. Usually the incident current i is dropped by a factor to avoid damaging and saturating the detector. The atomic column intensities of the nanoparticle shown in Figure 4.1, could then be integrated using Voronoi cells, which can be defined as being equivalent to a 2D Wigner-Seitz cell in this case (Rosenauer et al., 2011). Alternatively the atomic column intensity can be integrated by fitting two-dimensional Gaussians and calculating the volume under the fit (Van Aert et al., 2013).

$$fractional\ intensity = \frac{I_{experiment} - I_{vacuum}}{I_{detector} - I_{vacuum}}\left(\frac{i_{detector}}{i_{experiment}}\right) \qquad (5)$$

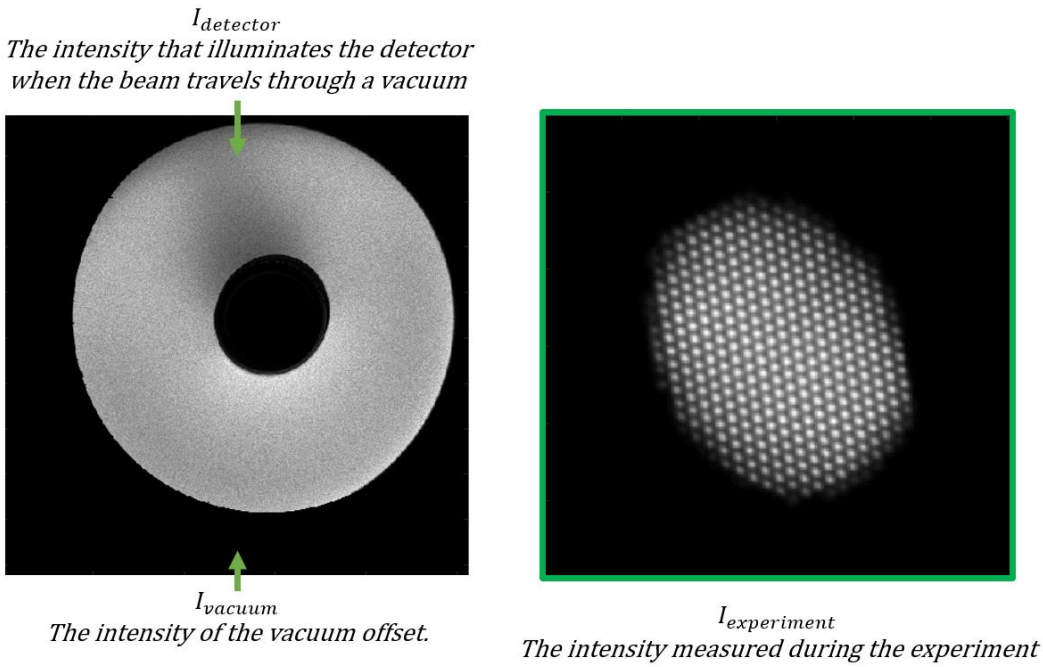

Figure 4.1 Illustration of where each term in equation 5 *originates from to fractionate the intensity from an experimental STEM image of a nanoparticle. The I detector and I vacuum values are dependent on the amplifier offsets during the experiment.*

With precise calibrations and image fractionation, the measured atomic column intensities can be converted into a "scattering cross-section". The mathematical framework of this technique is described in more detail in (E et al., 2013). In summary, the scattering cross-section in a fractionated ADF image can be measured by integrating the ADF image intensity and multiplying it by the pixel area.

The idea of scattering cross-sections was first proposed by (Retsky, 1974) and then further developed by (E et al., 2013). The concept of cross sections is used widely in scattering physics for x-rays, neutrons (Sears and Shelley, 1991) and electrons (Egerton et al., 1987). It describes the effective area corresponding to the probability of scattering (or absorption). This can be measured by multiplying the ratio of the measured scattered beam and the incoming flux by the pixel area. The scattering cross-section is robust to several microscope parameters such as magnification, defocus, convergence angle, source size, astigmatism, scan noise and sample mis-tilt (E et al., 2013).

Once the scattering cross-section has been measured, atom counts for a nanoparticle ADF image, such as Figure 4.1, are obtained through by reference simulation-library comparisons (Jones et al., 2014). The reason a simulation library is required is due to the electron channelling effects, which is described in more detail in section 4.2.2.

For Figure 4.1 to provide an accurate representation of the measured cross-section, well calibrated measurements of the incident probe current, detector sensitivity and ADF collection angles are required (E et al., 2013; Jones et al., 2017; MacArthur et al., 2014; G. T. Martinez et al., 2015). Mis-calibrations of these parameters can lead to errors of up to 20% in the quantification (Jones, 2015). This is a major drawback of the simulation approach, because a simulation will always provide an answer with a given set of microscope parameters. Obtaining accurate detector calibrations is discussed in more detail in section 4.3.

Fortunately, an alternative method exists to decouple the intensities in a STEM image into the number of atoms. In this method the intensities in the image are statistically decomposed into an underlying grouping, sorted by atomic thickness (De Backer et al., 2013; Van Aert et al., 2011). However, the drawback of this approach is the need for many observations per unit thickness to get a reliable estimate of the number of atoms in a column. To mitigate the drawbacks of both the simulation and statistical techniques, a hybrid method has recently been developed to combine the strengths of the respective methods for reliable atom counting (De wael et al., 2017). As this method is still in its infancy, most quantitative ADF work in this thesis uses simulation matching techniques.

Figure 4.2 summarises the methodology of using the simulation method to obtain three-dimensional atomic column information from a two-dimensional image STEM image. The fractionated intensity in the image is converted into a scattering cross-section by integrating the intensity around each atomic column the image and multiplying it by the pixel area (E et al., 2013).

Then the experimental scattering cross-section is simulation matched or, alternatively, statistically decomposed to obtain the number of atoms for each atomic column. In the statistical decomposition method, the measured scattering cross-sections are grouped into a histogram and the intensities are regarded as independent statistical draws from a Gaussian mixture model (Van Aert et al., 2011). The cross-sections are grouped as a superposition of Gaussians describing the probability that a specific intensity value will be observed using a classification criterion. The number of atoms within the decomposition is obtained by plotting the score of the classification criterion as a function of number of atoms and selecting a minimum. The model from this minimum determines the thickness in atoms for each measured cross-section (Van Aert et al., 2013).

Both the simulation matching and statistical decomposition workflows have been automated with the use of software such as Absolute Integrator (Jones et al., 2014) or statSTEM (De Backer et al., 2016). The largest error during nanoparticle quantification in Figure 4.2 comes from the calibration of the ADF detector collection angles.

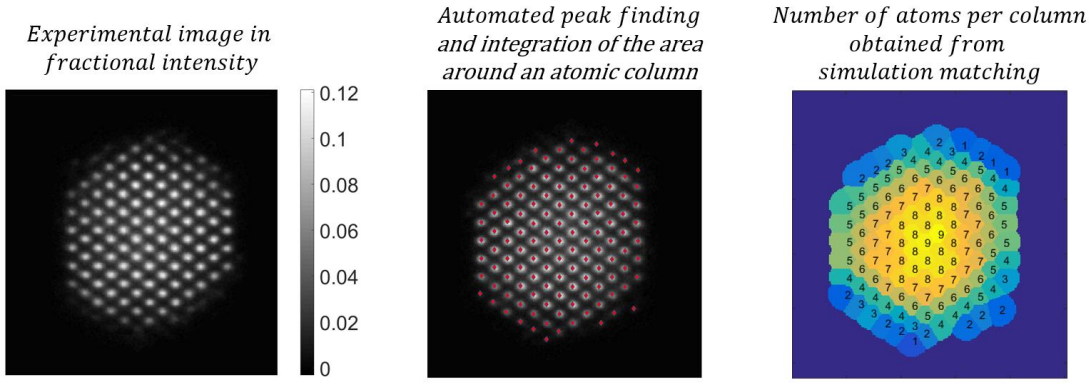

Figure 4.2 ADF quantification workflow for catalyst nanoparticles, from integrated intensities to atom counts for each atomic column.

4.2.2 Electron Channelling

To accurately quantify and directly interpret ADF images such as Figure 4.2 on a column by column basis, a simulation library comparison is required. When atoms are aligned along a low order zone axis such as Figure 4.2, they provide a small lensing effect on the beam (Van Dyck and Op De Beeck, 1996), shown in Figure 4.3. The scattering from the subsequent atoms is stronger because of this focusing effect, resulting a higher detected intensity. For high-angle

ADF, the measured intensity in this configuration increases monotonically with atomic column thickness. The maximum specimen thickness to saturate the ADF signal depends on the collection angle and can range in the order of a few 100nm to a few microns as the collection angle is increased.

Furthermore, this effect is more profound for heavier atoms, such as Pt, as heavier atoms provide a stronger lensing effect compared to lighter atoms. In the case of bimetallic Pt-Co nanoparticles, this effect becomes even more complicated and thus spectroscopy is often required. However, in some circumstances channelling has been exploited to map the height of dopant atoms within atomic columns based on their contributions to the image intensity (Allen et al., 2003; Voyles et al., 2003). The effect of multielement columns and ordering is briefly discussed in more detail in Chapter 7.9

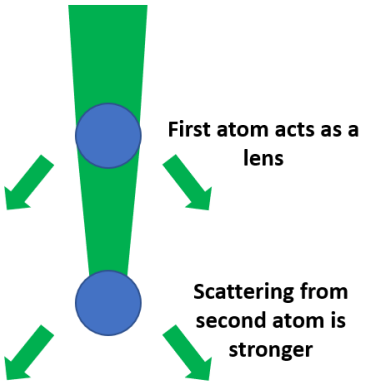

Figure 4.3 Simple schematic of electron channelling, the first atom acts as a lens and focuses the STEM probe producing a stronger scattering from the second atom. Thus, a higher intensity is produced when compared to individual atoms.

4.2.3 STEM Simulations

In STEM simulations, electron propagation through the sample is emulated for a given specimen. One of the most popular methods used to describe this electron propagation is the multislice approach, because of its fast computation speed (Kirkland et al., 1987). In a multislice calculation, the sample is partitioned into thin slices perpendicular to the electron beam.

Once the incident wavefunction for a multislice calculation has been described, the interaction of the wave within the crystal needs to be understood. The scattering of electrons to higher angles from the specimen at a reasonable temperature needs to be understood as well. The thermal effects within the sample will cause a dampening of the Bragg scattering. A popular method to deal with the thermal effects is a semi-classical approach where the thermal diffuse scattering from a crystal is modelled by approximations first proposed by (Kirkland, 1998; Loane et al., 1991). This approach estimates that due to the atomic movements in the crystal lattice being several orders of magnitude smaller than the speed of the incident electron, each electron will "see" a slightly different lattice deviated by a random amount. This is called the frozen phonon approximation and the lattice deviation is controlled by a temperature factor.

The interaction between the incident electron and the atom is based on several semi-classical parameterisations obtained from structure factor theory (Allen et al., 2014; Lobato and Van Dyck, 2015). Finally, with descriptions of the incident wave, thermal effects and the atomic potential, a multislice propagation of the electron can be performed through the sample. In the multislice, the crystal is segmented by finite slices along the z-direction and the propagation of the wavefunction is summed for all the slices to form an image. For the STEM simulations, the μSTEM (Allen et al., 2014) and MULTEM (Lobato and Van Dyck, 2015) software were used in this thesis.

4.3 Detector Calibrations

In STEM, accurate knowledge of the detector angles is very important for simulation-matching quantification. Recently, a new method ('swung beam') has been developed, where a parallel pencil beam is formed in STEM to map the ADF detector in angle space, Figure 4.4. This method allows for the direct observation of the distortions caused by the post specimen lenses in the microscope and allows for greater accuracy when measuring the outer collection angle of the detector. This method also has another key advantage, being able to measure the EELS spectrometer collection angle directly. This collection angle is usually not well known and nominal values are used during EELS cross-section simulations

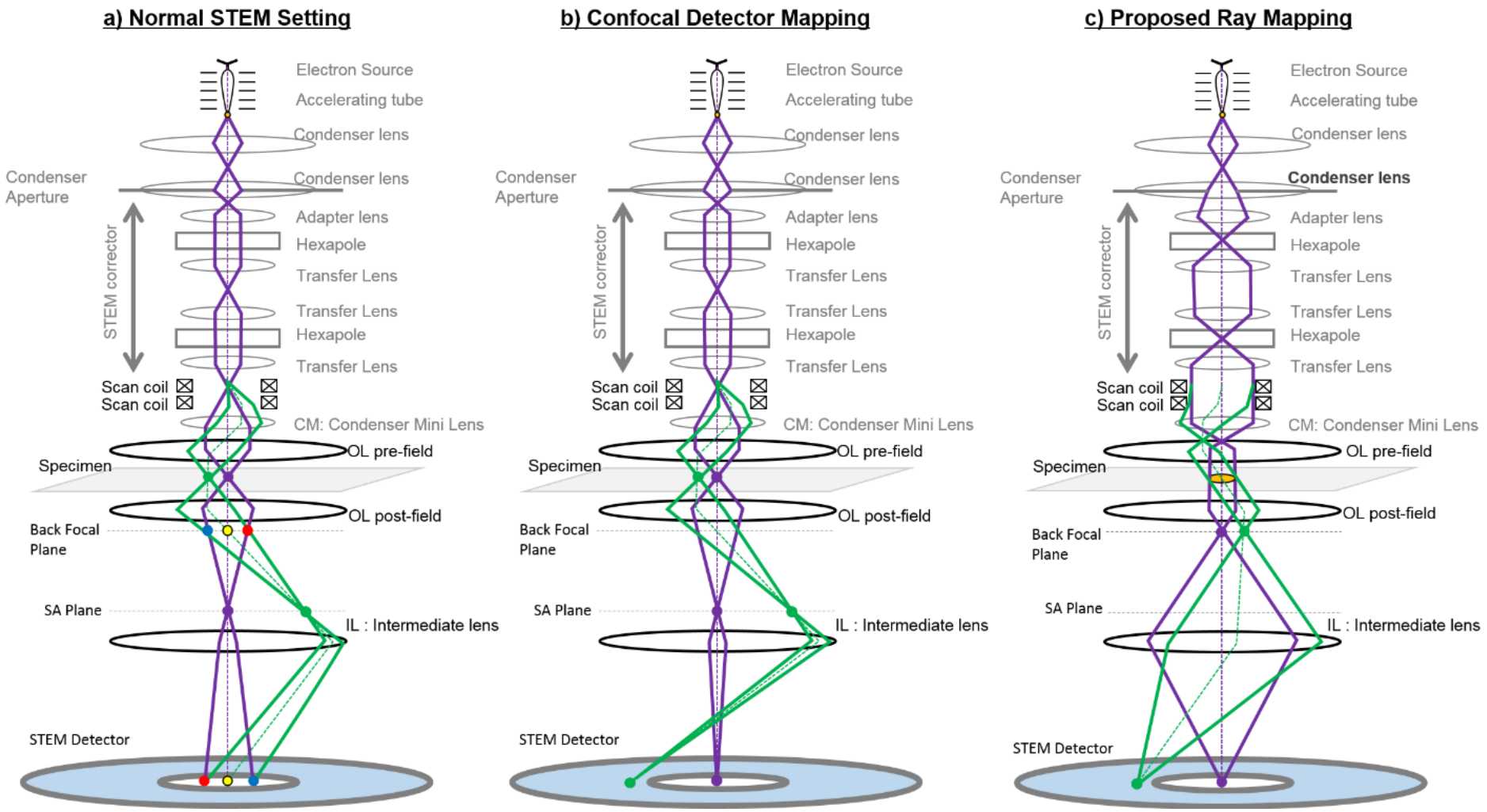

Figure 4.4 Optical ray diagrams to illustrate a) regular STEM imaging, b) the conventional (confocal) detector scanning approach, and c) the proposed mapping procedure. Reprinted from (Jones et al., 2017)

Before the development of the swung beam method, most published ADF detector calibrations and response maps were recorded using a confocal optical geometry (Scott D. Findlay and LeBeau, 2013; Fritz et al., 2011; Katz-Boon et al., 2013; LeBeau and Stemmer, 2008; MacArthur et al., 2014; G. T. Martinez et al., 2015). This method owes its popularity to being incorporated as an option in most microscope control software and can be configured with the press of a button. In this approach the pre-specimen lenses are configured to be in focused probe mode, whereas, the post specimen lenses are configured to be in TEM-imaging mode, Figure 4.4.

This introduces a disparity between the calibration and the actual STEM experiment, as the post specimen lenses during the experiment are configured to be in diffraction mode. Because of this disparity, an abrupt high-angle truncation at shorter camera lengths can be observed and therefore the measured outer angles will be mis-calibrated(Jones et al., 2017). This truncation also depends on the accelerating voltage and various other configurations used during the measurement.

However the largest source of error lies in the measurement of the detector inner-angle (Jones, 2016). The source of this error is due to the liner drift-tube around the inner part of ADF detectors, Figure 4.5. Previous methods to calibrate the inner angle have included observing the shadow of the ADF detector hole on the CCD or use a deflected bright-field disc to determine the start of the active layer of the liner tube. However, both methods cannot directly determine where the active layer begins for measuring the inner angle.

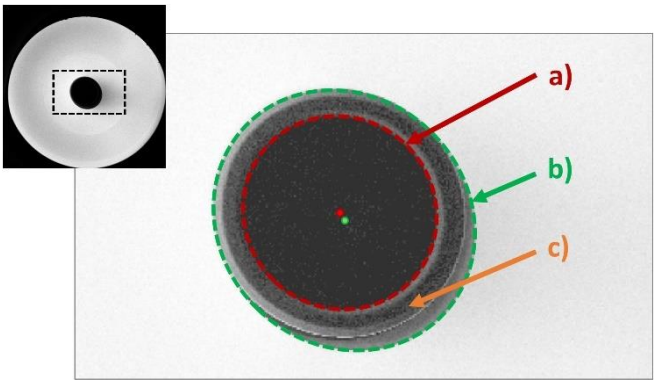

Figure 4.5. Centre portion of the upper dark-field detector showing a) the inner edge of the drift-tube, b) the start of the active area of the scintillator, and c) the 'dead layer' between a) and b).

The swung beam setup rectifies this problem by leaving the post specimen lenses in diffraction mode and creating a pencil beam using the pre-specimen lenses to map the entire active area of the ADF

detector. Detector calibrations performed in this manner are more reliable and directly comparable to the STEM experiment.

The full details of how this is performed on the microscope are available in the publication by (Jones et al., 2017) and a manual is provided in the appendix. For the purposes of this project, this method was used to measure the collection angles of ADF detector configurations at various camera lengths and the EELS collection angle. A tabulated chart of collection angles and detector scans for the Oxford JEOL ARM 200CF are presented in Table 4.1 and Figure 4.6.

With this new detector calibration technique and simulation matching, nanoparticles can be quantified accurately. The rest of the sections in this chapter go through applications of quantitative STEM to study pure element industrial catalysts.

	Upper ADF		**Lower ADF**			**Gatan DF**			**BF / ABF**		**EELS Aperture (outer angle)**	
CL	**Inner**	**Outer**	**Inner**§	**Outer** (behind ADF1)	**Outer** (solo)	**Inner**	**Outer** (behind ADF2)	**Outer** (solo)	**Inner**	**Outer**	**5mm**	**2.5mm**
1.5 cm						109.07 ± 0.58	176.30 ± 1.54 *	176.30 ± 1.54 *			101.69 ± 0.14	51.15 ± 0.14
2 cm			155.24 ± 3.80		271 *	82.30 ± 0.21	135.93 ± 0.39	194.15 ± 2.21			77.37 ± 0.43	38.12 ± 0.89
2.5 cm			127.13 ±1.94		271 *	67.63 ± 0.59	111.31 ±1.09	153.60 ± 4.64	27.06 ± 0.07	58.79 ± 0.37	62.38 ± 0.29	32.14 ± 0.11
3 cm			100.91 ± 1.06	150.55 ± 5.76	271 *	53.06 ± 0.53	88.51 ± 0.98	117.90 ± 2.66	21.96 ±0.18	46.53 ±0.28	49.19 ± 0.43	24.94 ± 0.18
4 cm	166.55 ± 1.03	271 *	77.43 ± 0.88	117.77 ± 4.46	271 *	40.96 ±0.15	67.39 ± 0.28	90.52 ± 2.69	16.96 ± 0.01	35.70 ± 0.21	37.94 ± 0.33	19.28 ± 0.02
5 cm	111.80 ± 0.22	271 *	52.37 ± 0.29	79.31 ± 2.04 †	198.01 †	27.64 ± 0.38	46.17 ± 0.70	61.48 ± 1.68	10.99 ± 0.05	24.41 ± 0.23		
6 cm	97.14 ± 0.87	271 *	44.40 ± 0.02	69.58 ± 0.89 †	164.47 ± 7.32 †	24.04 ± 0.04	39.02 ± 0.07	52.75 ± 0.81	9.45 ± 0.03	20.65 ± 0.30		
8 cm	72.80 ± 1.08	271 *	33.01 ± 0.36	51.37 ± 0.91 †	120.77 ± 4.32 †	17.48 ± 0.36	29.35 ± 0.66	39.02 ± 0.47	6.71 ± 0.01	15.62 ± 0.20		
10 cm	61.72 ± 1.61	244.84	28.13 ± 0.07	44.24 ± 0.72	104.36 ± 3.76 †	15.35 ± 0.05	24.82 ± 0.09	33.53 ± 0.64	6.03 ± 0.09	13.20 ± 0.28		
12 cm	50.39 ± 1.29	199.89 †	22.85 ± 0.02	36.00 ± 0.36	84.72 ± 3.22 †	12.25 ± 0.12	19.94 ±0.22	27.38 ± 0.52	4.82 ± 0.01	10.98 ± 0.12		
20 cm	30.33 ± 0.76	114.38 ± 4.33 †	13.57 ± 0.08	22.02 ± 0.25	50.95 ± 1.44 †	7.32 ± 0.13	11.79 ± 0.24	16.29 ± 0.36				
40 cm	14.75 ± 0.13	58.74 ± 2.30	6.64 ± 0.10	11.04 ± 0.16	25.78 ± 0.92	3.07 ± 0.01	6.01 ± 0.02	8.60 ± 0.07				
	§ Average measurement of observed inner-angles from both solo and shadowed scans. * Detector outer angle truncated by projector-lens flux-cut-off. † Caustic folding yields anomalous extra ring.											

Table 4.1 Effective detector angles measured using the swung mapping approach on the JEOL Oxford ARM 200CF electron microscope. Reprinted from (Jones et al., 2017)

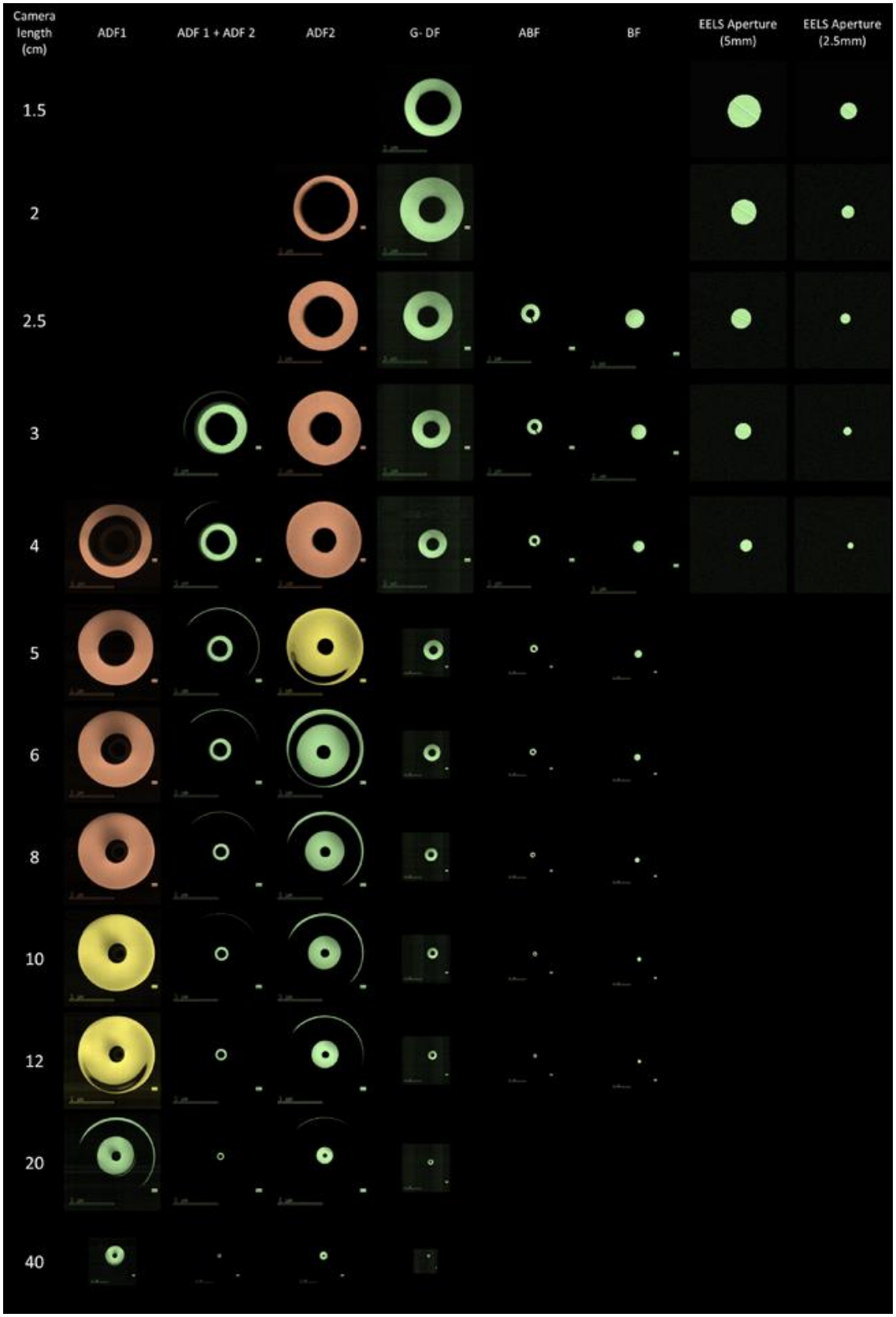

Figure 4.6 Detector response maps using the swung beam technique, response maps such as these were used for the quantitative catalyst experiments in the following chapters. Reprinted from (Jones et al., 2017)

4.4 Case Study: Quantifying an Industrial Ru Catalyst

Ru-based catalysts are used in many applications such as ammonia production, catalytic converters and fuel cells (Saadatjou et al., 2014). Theoretical modelling shows that ammonia synthesis over Ru is an even more surface sensitive reaction compared to alternative catalysts such as iron (Jacobsen et al., 2000; Raróg-Pilecka et al., 2005).

Over the years, there has been increasing emphasis on commercial Ru/C catalysts (Benner et al., 1986; BP, 1979; Kusada et al., 2013; Raróg-Pilecka et al., 2005). Such catalysts show promising potential over the current common industrial catalysts (Abo-Hamed et al., 2014; Kusada et al., 2013; Saadatjou et al., 2014). Similarly, discoveries of the potential of Ru catalysts have been extended to other areas (such as CO oxidation (Alayoglu et al., 2008; Kusada et al., 2013)).

The activity of catalyst nanoparticles depends on the morphology of their exposed surface, which itself can strongly depend on the support material (Jacobsen et al., 2000). However, determining their morphology is a severe characterisation challenge.

There are several papers that have presented theoretical and experimental studies of Ru nanoparticles(García-García et al., 2009; Liu et al., 2003; Saadatjou et al., 2014; Zhao et al., 2014). Two-dimensional raft-like structures in supported heterogeneous Ru catalysis were first reported using conventional TEM image contrast by Prestridge et al.(Prestridge et al., 1977). In their paper it was concluded that due to the uniformly low contrast from the Ru crystals, the crystals observed were rafts. It was later pointed out that this method of determining particle thickness can be misleading (Datye et al., 1988; Treacy and Howie, 1980) because contrast is dependent on the orientation of the metal crystal with respect to the electron beam.

Additionally, a microdiffraction study of Au-Ru nanoparticle patterns showed that some patterns could not be attributed to any known structure (Cowley and Plano, 1987). For these patterns, agreement could be found if a raft-like morphology was assumed.

To investigate the rafting phenomenon, recently developed ADF quantification techniques were used, including both the simulation matching approach from (E et al., 2013) and a statistical analysis approach from (De Backer et al., 2013) for atom counting.

4.4.1 Ru Catalyst Synthesis

The carbon supported Ru catalyst was supplied by Johnson Matthey Technology Centre and prepared using an adaptation of an established deposition precipitation method (Theobald et al., 2011) starting with $RuCl_3$. The final product was achieved by reducing in $5\%H_2/N_2$ at 100 ^oC for 1 h.

4.4.2 Imaging Parameters

The catalyst was imaged using ADF STEM on a JEOL ARM 200F, at the University of Trondheim, Norway. The camera length for the ADF detector was set up with collection angles spanning 69 mrad to 138 mrad. Three areas of the Ru catalyst were imaged. These areas, named as R1, R2 and R3, are shown in Figure 4.7. Initially regions R1 and R2 were observed as being amorphous, whereas R3 had crystalline and amorphous parts. As the regions were further exposed to the electron beam, they crystallised. Movies were recorded to observe any possible changes; 33 frames were recorded for R1 and R2, and 44 frames were recorded for R3.

Both areas were imaged for approximately 15 minutes each with a beam current of approximately 35pA. After applying various corrections (listed in the next section, 4.4.3), the three areas in Figure 4.7 were then quantified for two key features: crystal lattice system and thickness.

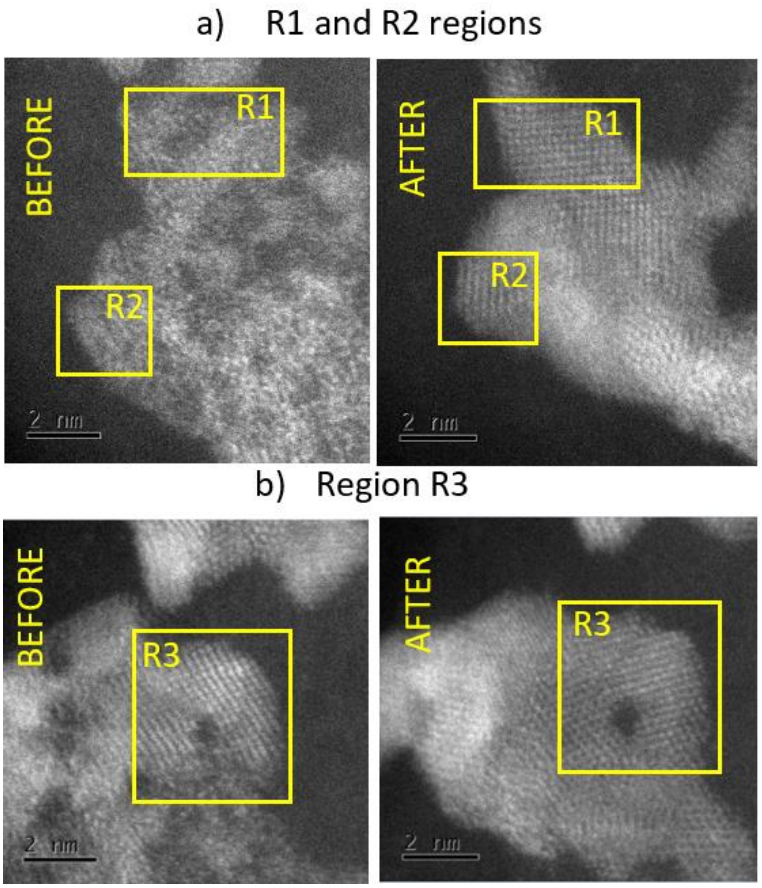

Figure 4.7 Wide field of view images of the Ru catalyst on carbon black, before and after ~15 minutes total imaging time, using a 35pA beam and 38µs pixel dwell time. The analysis regions are highlighted in yellow. The R1 and R2 were initially amorphous and R3 was partially amorphous. The catalysts had been morphing before the acquisition process started, and hence do not represent the catalyst's initial state. Reprinted from (Varambhia et al., 2016)

4.4.3 Correcting Experimental Parameters for Quantification

To quantify the images accurately, some experimental calibrations were made before acquiring the data. The general procedure applied to these images is summarised as follows. First an image of the detector sensitivity is acquired(MacArthur et al., 2014). This is done to measure variations in the detector sensitivity. Most simulation software assume a perfectly uniform detector, whereas, in an experimental situation, detector sensitivity varies greatly(MacArthur et al., 2014). To correct for this, an approach proposed by (Martinez et al., 2014) was used to normalise the images using an electron flux weighting. With effective uniform detector linearity, the measured intensities can then be directly correlated to atom counts using a previously published method (Findlay and LeBeau, 2013; LeBeau et al., 2010; LeBeau and Stemmer, 2008).

After the detector sensitivity was normalised, the images were recorded, and further corrections were applied. One of these corrections is normalisation of the electron current at the detector. The current of

cold field emission guns decay throughout the imaging process. Due to this, a decrease in the image intensity is seen, thus giving an incorrect estimation of the atomic columns during quantification. The current was recorded at different intervals and then factored into the quantification to compensate for this decay.

Finally the images were scan-drift corrected using a technique developed by(Jones et al., 2015). Scanning distortions can lead to errors such as imprecisely mapping peak positions and incorrectly correlating peak positions between sets of images for comparisons. They can also lead to incorrect intensity quantification. The correction ensured that the relative areas within the analysis regions remained consistent between frames.

4.4.4 Determining the Crystal Lattice System

Structure type (nanoparticle, cluster, rafts, porous etc), crystal lattice system (fcc, bcc, amorphous etc), particle size and support are some of the parameters that affect the performance of a catalyst. For Ru nanocatalysts the performance appears to strongly depend on the crystallography and the exposed surface plane, even more so than conventional catalysts (Jacobsen et al., 2000; Raróg-Pilecka et al., 2005; Saadatjou et al., 2014). Additionally, the type of support material also plays a key role in determining particle crystallography (Monosmith and Cowley, 1983) and also morphology(Jacobsen et al., 2000).

Determining the crystal lattice system of a catalyst is important as it affects catalyst performance. However, it is also a parameter that is required for the thickness quantification process. To explore this further, a set of frames from the recorded sequence were chosen and analysed. Three consecutive frames for each region, with a maximum drift rate of 1 pixel between the three frames, were chosen and averaged. The frames that were chosen to originate from the latter stages of the movie, where drift was fairly stable ensuring that the column positions were relatively drift free and the atomic column positions could be labelled reliably for structural analysis.

A map of vectors linking the atomic column locations with their respective bond angles was created using in-house software (Figure 4.8). In the figure, the measured angles between the yellow and blue

vectors are labelled. From examination of the distribution of angles in Figure 4.8d, it can be seen that for R1 the distribution peaks close to 90º, with a mean of 88.13º and a standard error of 1.12º, whereas for R2 and R3 the angles peak at just under 110°, with means of 106.11° ± 1.21° and 103.52° ± 0.98° respectively where the ± quotes the standard error. Such angles are characteristic of projections of a face-centred cubic (fcc) structure, with the <100> projection giving 90º and the <110> projection giving 109º, however given the angle distributions in Figure 4.8, other projections are also possible.

To investigate the relationship between the fcc <100> and <110> projections, the modulus of the blue and yellow vectors were measured (Figure 4.8e). In an fcc structure the vector modulus of R2 and R3 (assuming <110> orientations) should be related to R1 (<100> orientation) by a factor of $\sqrt{6}/2$. The mean vector moduli and standard deviations were 2.08Å ± 0.02Å, 2.26Å ± 0.03Å, and 2.31Å ± 0.02Å for regions R1, R2, and R3 respectively. The expected inter-peak spacing using the fcc Ru lattice parameters from refs (Abo-Hamed et al., 2014) (Zhao et al., 2014), which are refs [7] and [11] in (Varambhia et al., 2016), for both orientations are also shown in Figure 4.8e.

However, it can be noted that the distance measurements in particular show significant deviation from the expected values. Deviations from the expected angle and vector moduli may be explained by a number of factors such as the inclination of the carbon support surface to the incoming beam direction, the nearest neighbour chosen by the peak assignment algorithm(Jones et al., 2014) and defects in the Ru structure. The structures are clearly still somewhat from equilibrium and may be influenced significantly by the C support.

The angle and peak distance measurements are suggestive of an fcc structure, which is surprising as bulk Ru is known to have a hcp structure. Several papers that have presented theoretical and TEM micro-diffraction studies of hcp Ru (García-García et al., 2009; Liu et al., 2003; Saadatjou et al., 2014; Zhao et al., 2014). However other studies have reported fcc structures (Datye et al., 1988; Treacy and Howie, 1980). To complicate things further, a microdiffraction study of Au-Ru nanoparticle patterns showed that some patterns could not be attributed to any known structure (Cowley and Plano, 1987). This indicates that whilst diffraction techniques can be used to obtain the structure of a sample easily

without the need for aberration correction, it is not possible to easily observe the change caused by the electron beam as shown in Figure 4.7.

Upon further investigation in the literature, Ru can exhibit an fcc structure under certain conditions. The proposal of fcc Ru is supported by theoretical calculations and experiments performed by a number of groups. One of the first reports of fcc Ru synthesis was by (Kusada et al., 2013). Additionally; DFT calculations, experiments and fcc Ru nanoparticle synthesis by (Zhao et al., 2014) show that under certain pressure-temperature conditions it is possible to form fcc Ru. Furthermore, recent synthesis of meta-stable Ru nanoparticles without a support material by Abo-Hamed et al(Abo-Hamed et al., 2014) also indicates that crystalline phase observed in Figure 4.7 may be fcc.

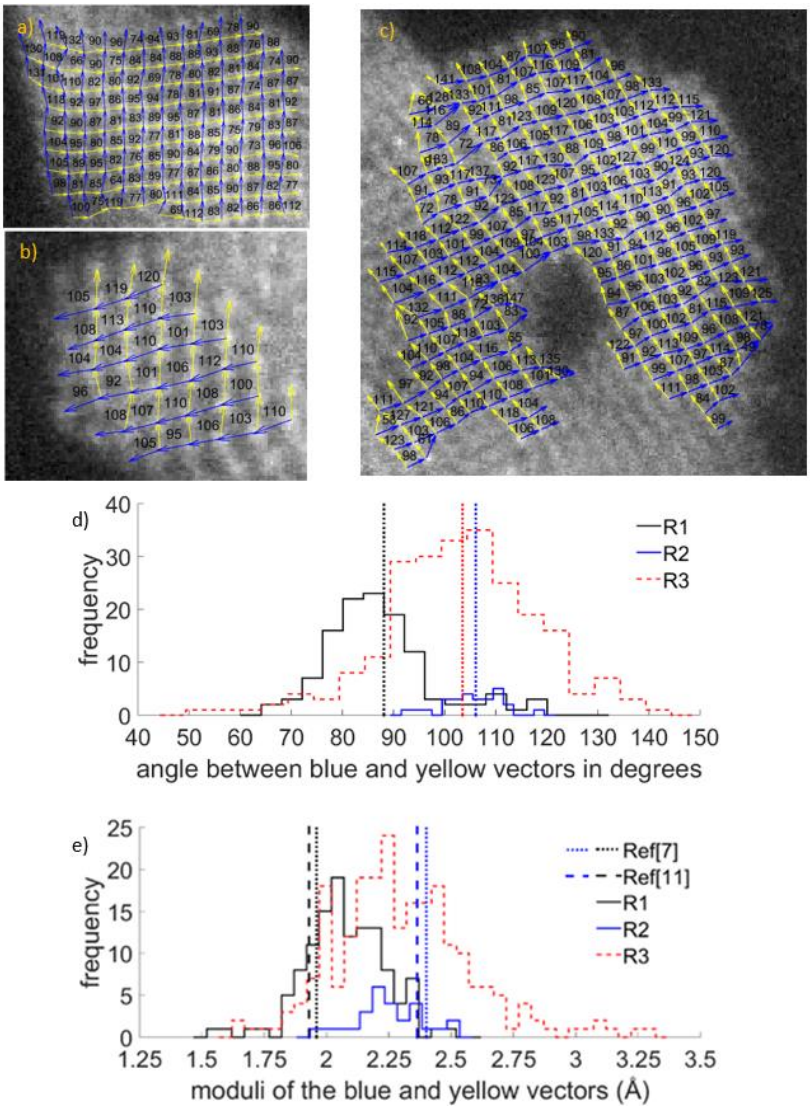

Figure 4.8 a), b) and c) Enlargements of the areas shown in Figure 1 with atomic-column nearest-neighbour pairings and vector angles annotated. d) Histogram showing the measured angles and indicated means (vertical dashed lines). e) Histogram of vector lengths with indicated literature lengths for fcc Ru. Reprinted from (Varambhia et al., 2016)

4.4.5 Quantifying the Thickness within the Regions of Interest

Once the observed regions have been determined as fcc, the image intensities can be used to measure the thickness of the nanostructures. The thickness of the catalyst within the regions of interest (Figure 4.7) was quantified using two methods: comparison to simulations and statistical decomposition. In the comparison to simulations method, the total intensity of atomic columns within the images were integrated using Voronoi cells (Rosenauer et al., 2011). The integrated intensity can be shown to be a scattering cross-section for the column, and this quantity is robust to many imaging parameters (E et al., 2013).

The measured cross-sections were then compared to a reference simulation library of a Ru crystal using the method described in (E et al., 2013; Jones et al., 2014). A Ru crystal was simulated using the multislice method with the μSTEM software(Allen et al., 2014) at increasing column thicknesses, for up to 10 atom column thickness, using 30 phonons and a 2048x2048pix supercell tiled 8 times in x and y. Figure 4.9 shows that the simulated cross-section plotted as a function of number of atoms in a column is relatively insensitive up to 5 atoms to whether a <100> or <110> viewing direction is used for the fcc lattice.

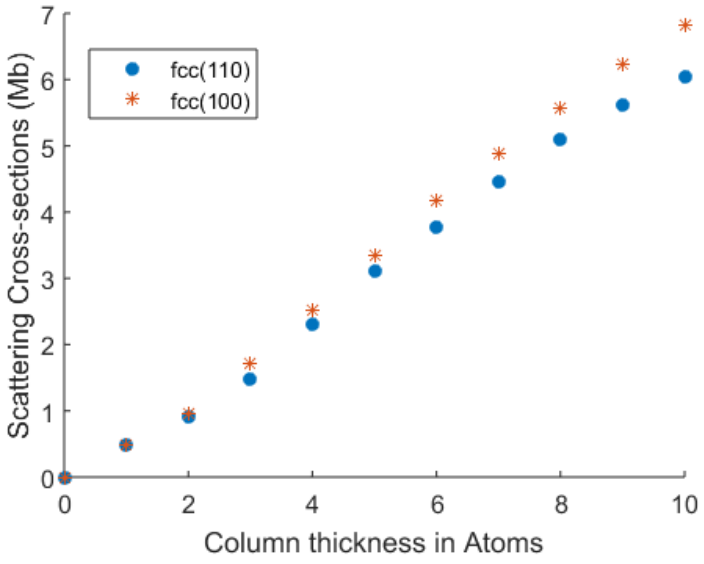

Figure 4.9 Simulated cross-sections for different Ru crystal orientations. The comparison shows that different orientations of fcc provide similar cross-sections up to 5 atoms. Reprinted from (Varambhia et al., 2016)

The scattering cross-sections from the simulation were then compared to the measured cross-sections of the atomic columns within the regions of interest using Absolute integrator software(Jones et al.,

2014). Previous work has demonstrated that this type of quantification method can have a typical error of ±1 atom sensitivity for columns up to 20 atom thicknesses (Lebeau et al., 2010; Van Aert et al., 2013).

In the statistical decomposition approach, the distribution of scattering cross-sections is decomposed into a small number of overlapping Gaussian distributions, where the optimal number of Gaussian components is selected using an Integrated Classification Likelihood (ICL) approach (Van Aert et al., 2013). This statistical decomposition is used to assign atom counts to the atom columns. This technique relies only on the relative intensities from the experimental images and thus does not depend on accurate calibration of microscope parameters. It does, however, require a sufficiently large number of measurements combined with a sufficiently high precision in measurements that could be limited by noise, microscope instabilities etc(De Backer et al., 2013). Here, both approaches have been used to provide a consistent picture of sample thickness.

For the ICL analysis, cross-sections from a combined set of 3 frames (1 from each region) were used. The fitted Gaussians (and the optimal order selection criterion) from the Gaussian Mixture Model are shown in Figure 4.10**.** The arrow indicates that the optimal number of components was 7.

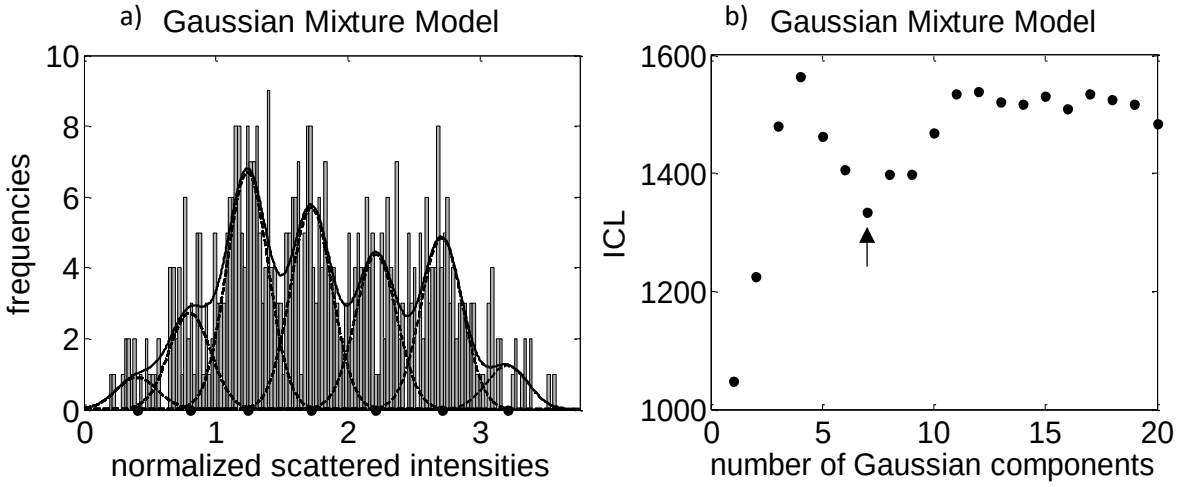

Figure 4.10 a) Histogram of integrated column intensities from 3 frames (1 frame from each region) with a fitted Gaussian Mixture Model. b) The order criterion selection from the Gaussian Mixture Model. The arrow shows the optimal number of components needed for the Gaussian fitting. The three frames from each region were chosen from the movie at t = 680s, 702s, 392s for R1, R2 and R3 respectively. Reprinted from (Varambhia et al., 2016)

Having assigned a number of atoms to a particular Gaussian component using the ICL approach, the mean cross-section for that Gaussian can be compared with the cross-section derived from an image

simulation approach, as shown in Figure 4.11 which shows a discrepancy between the two methods. The scattering cross-sections from ICL increase linearly with thickness whereas the room temperature Ru image simulation does not. The non-linearity in the simulated cross-sections seen in Figure 4.11 arises because of the channelling of electrons along atomic columns(Nellist and Pennycook, 2000a). As the Ru atoms were constantly moving due to recrystallization, it is likely that they are significantly displaced from perfect alignment, decreasing the channelling. Such displacements can be included in scattering cross-section simulations. By increasing the RMS displacement within simulation to model the disorder of the sample, slight better agreement between the two techniques was obtained (also shown in Figure 4.11). This approach demonstrates how using both simulation matching, and statistical analysis can provide a consistent and convincing analysis of sample thickness.

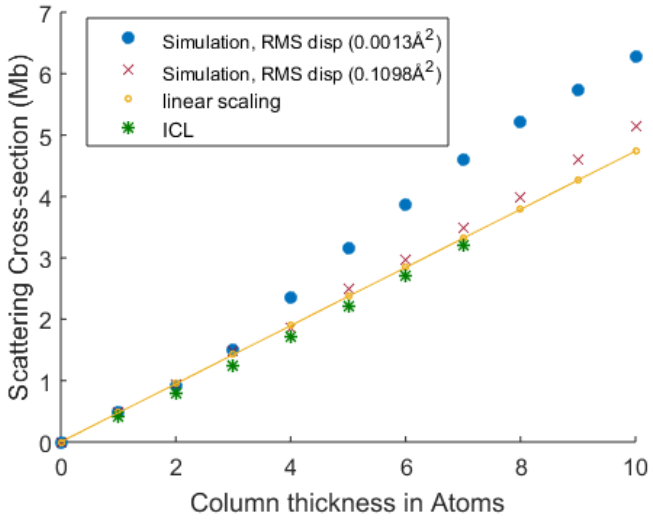

Figure 4.11 ICL analysis of the integrated intensity as a function of atomic column thickness. The analysis was performed using components from one frame from each of the analysis regions. The figure shows a simulation library (fcc <110>) corresponding to room temperature (Root Mean Squared (RMS) displacement of 0.0013Å^2), a fictitious high temperature (Root Mean Squared (RMS) displacement of 0.1098Å^2), and a linear model where the number of atoms multiplied by the cross-section for a single atom is used. Reprinted from (Varambhia et al., 2016)

Using a linear scaling of cross-section with respect to thickness as a good compromise between the library matching and statistical techniques, the cross-sections from the observed areas were converted into three-dimensional surface plots, Figure 4.12. The linear scaling model is insensitive to whether a <100> or <110> orientation is observed since the cross-section is simply proportional to the number of atoms when channelling is not considered. Some gaps within the plots e.g. R1, t = 121 s, indicate that not all columns could be quantified using peak labelling as the regions at the beginning were still amorphous. The latter plots indicate a raft-like topology for the all regions. This observation confirms

a similar hypothesis made by Prestridge et al(Prestridge et al., 1977), but here a robust image quantification approach is used, rather than making qualitative use of conventional TEM contrast which was later criticized by Treacy and Howie(Treacy and Howie, 1980) as likely to be misleading.

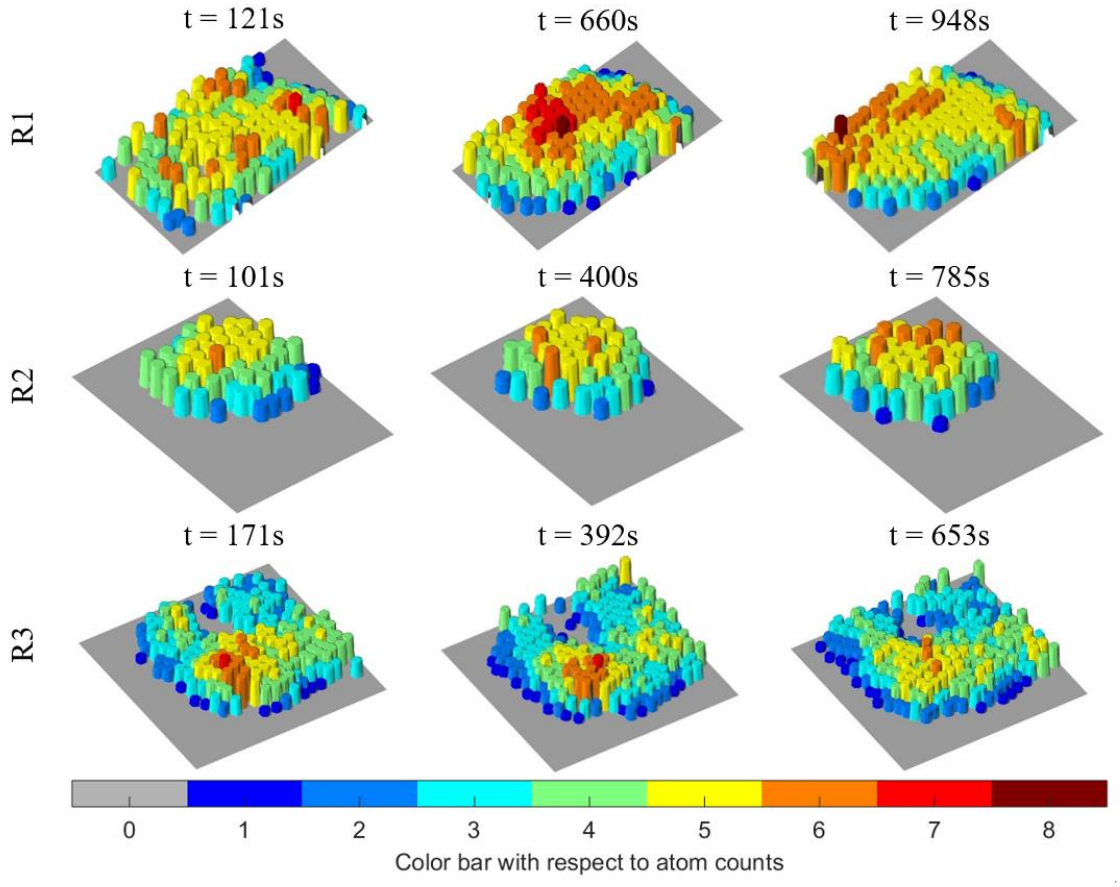

Figure 4.12 Surface plots created using the linear library from Figure 4.11. These plots and the average thickness measurements from Figure 4.13 indicate that structures of stable thicknesses were formed after a few minutes of imaging. Reprinted from (Varambhia et al., 2016)

Additionally, the thickness of the observed regions stabilised after a certain imaging time (Figure 4.13). For frames (mostly the initial frames) where the thickness could not be resolved due to amorphous regions, the mean thickness was quantified using the mean cross-section of the whole sample.

Figure 4.13 shows that whilst imaging, the nanoparticle changes from an amorphous to a crystalline state forming a structure that does initially increase in thickness before the thickness stabilises but is still raft-like in nature having a thickness that is much smaller than the lateral extent. The stabilisation of the structure may be due to the carbon support as Ru is known to interact strongly with the support material(Jacobsen et al., 2000; Raróg-Pilecka et al., 2005; Saadatjou et al., 2014). The support can play a role in not only particle stability but also morphology(Jacobsen et al., 2000) (Datye et al., 1988). DFT

calculations by (Zhao et al., 2014) for a slab of Ru crystal that is 6 atoms thick show that an fcc structure can be obtained if some of the carbon atoms from the support occupy the interstitial sites within the Ru structure(Zhao et al., 2014).

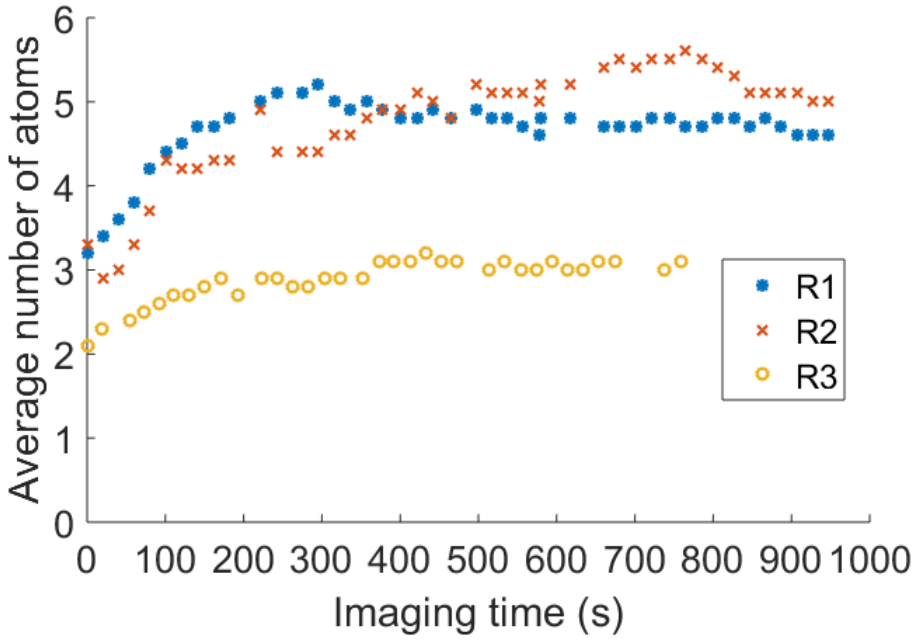

Figure 4.13 Mean thickness plot as the catalyst was being imaged. All regions stabilised in thickness after being exposed to the electron beam for a while. Time t = 0s represents the start of the acquisition process but the materials had been subjected to some electron irradiation ahead of this time. Reprinted from (Varambhia et al., 2016)

4.4.6 Conclusions

Utilising the latest quantification techniques in ADF microscopy, a Ru catalyst on carbon black support was analysed. Three regions were recorded for approximately 15 minutes. These regions showed that the Ru particle started off as an amorphous agglomeration (or both crystal/amorphous agglomeration) of atoms and then fully crystallised. After applying scan-drift correction and current normalisation, the images were quantified. From the vector mapping and angle measurements the crystal structure was suggested to be fcc with a lattice parameter close to those observed previously for fcc Ru. Using two established methods of quantifying thickness it was seen that assuming the absence of electron channelling was important to get agreement between the approaches, which is justified by the large amount of disorder in the particle. It was seen that the regions observed form stable rafts of up to 6 atoms in thickness. This could have interesting implications for catalytic performance as fcc Ru nanoparticles have been synthesised previously, but Ru rafts have not previously been conclusively demonstrated.

4.5 Case Study: Quantifying an Industrial Pt Catalyst using STEM Metrology and DFT

Several studies of catalyst nanoparticles make use of idealised structures such as surfaces or 'magic number' polyhedral nanoparticles. Often this means that morphological diversity present in real industrial catalysts is neglected. Because of the wide morphological variability, nanoparticles with a wide morphological variability need to be characterised across the whole ensemble.

Some of the first attempts to understand and connect the coordination number and chemical activity of catalysts was with the use of x-ray absorption fine structure techniques (EXAFS) (Ishiguro et al., 2012; Takao et al., 2014). But the nature of broad beam x-ray techniques means that nanoparticles cannot be probed individually, and therefore an average measurement of an ensemble is obtained.

To probe individual nanoparticles in detail at high throughput, methods such as quantitative STEM are required. Following this, a reduced-scaling density functional theory method can be used to determine the electronic structure of the nanoparticles, and a prediction of the binding energy across several surface sites can provide an estimation of the optimal nanoparticle as a function of size. This information can then be used to optimise synthesis routes and reduce the testing cycle of industrial catalysts.

High resolution ADF images can routinely be recorded with aberration correctors in STEM. Determining structures from these images is an inversion problem that is either tackled by using tomography or ADF image quantification. Here, for throughput, the experimental ADF intensities were converted to scattering cross-sections and the number of atoms were determined from simulated cross-sections. The reference data were calculated via careful calibrations and the structures were experimentally verified by plotting a 'master weighing curve', shown as a blue curve in Figure 4.14 and described in more detail in section 4.6.

To solve the electronic structure of catalysts with DFT, calculations are often performed on surfaces or idealised structures (Mavrikakis et al., 1998; Nørskov et al., 2009; Stamenkovic et al., 2006; Stephens et al., 2011). In conventional DFT approaches, the computational burden scales as the cube of the number of atoms. Hence, several studies have utilised periodic structures where a single crystal plane

is modelled or ultra-small ‘magic number’ polyhedra are modelled. These models exhibit only a fraction of the morphological surface range present in experimental nanoparticles.

Fortunately, the development of a new generation of linear-scaling DFT calculation methods, such as the ONETEP program (Skylaris et al., 2005), allows for computation on larger systems (Wilkinson et al., 2014). This development bridges a boundary between quantitative STEM of realistic nanoparticles, which were often too large for simulation, with high scale DFT to calculate catalytically relevant sizes of nanoparticles.

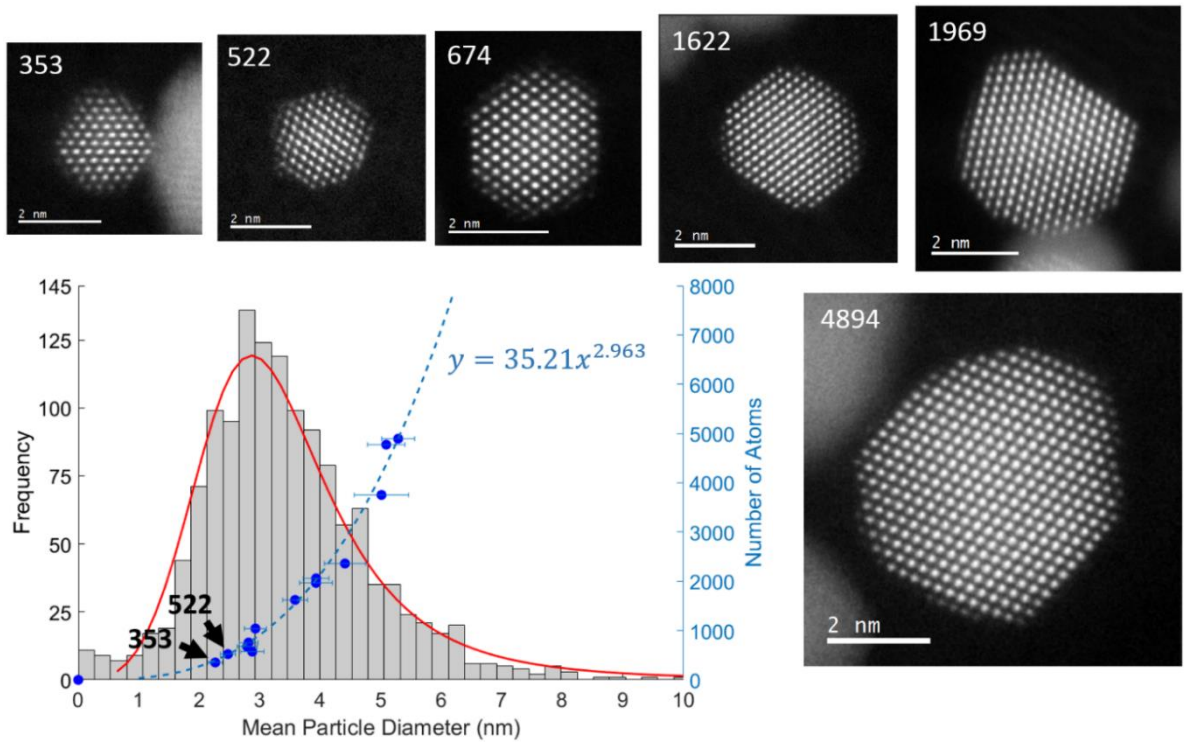

Figure 4.14 Particle size distribution from 1342 measurements with a mean and median diameter of 3.46nm and 3.25nm respectively. The representative STEM images are labelled by total atom count and the overlaid scatter plot (blue points) shows the number of atoms as a function of mean particle diameter. Nanoparticles 353 and 522 are highlighted as the nanoparticles that were used as inputs for DFT. Reprinted from (Aarons et al., 2017)

4.6 Obtaining the Master Weighing Curve

After atom counting the ADF STEM images and creating the models, 13 sufficiently on zone nanoparticles spanning the ensemble size range were plotted as a function of average nanoparticle diameter, Figure 4.14. From the plot (blue dashed line), the number of atoms follow a cubic relation, as expected. The measured pre-factor of 35.21 is within 0.2% agreement with the value of bulk-like number density of Pt if the nanoparticles are assumed to be spherical.

This pre-factor can be derived as follows

$$Number\ of\ Atoms = Volume\ .\ Number\ Density$$

$$Number\ of\ Atoms = \frac{4}{3}\pi r^3 . \frac{Atoms\ per\ Unit\ Cell}{Unit\ Cell\ Volume}$$

FCC Pt has 4 atoms per unit cell and a nanoparticle lattice parameter of ~0.3902nm (Solliard and Flueli, 1985)

$$Number\ of\ Atoms = \frac{4}{3}\pi r^3 . \frac{4}{(0.392)^3}$$

Re-expressing the expression in terms of diameter and simplifying gives

$$Number\ of\ Atoms = \frac{4}{3}\pi \left(\frac{d}{2}\right)^3 . \frac{4}{(0.392)^3}$$

$$Number\ of\ Atoms = \ 35.25\ .\ d^3$$

This confirms that the number of atoms, i.e. the nanoparticle 'weighing', is accurate and thus providing confident atom count estimates for each column in the image.

4.6.1 Why Nanoparticle Shape is Important

Many previous studies have focused on 'magic number' nanoparticles such as cuboctahedra, or icosahedra. Industrial nanoparticles are rarely ideal shaped, and this introduces a risk of mismatches when trying to link simulations to experiment, especially at the nanoparticle surface.

Investigating the surface effects is challenging, and as a test case, the cathode side Oxygen Reduction Reaction (ORR) was studied for both perfect cuboctahedra and experimentally observed pure Pt nanoparticles. According to the Sabatier principle, catalytic activity is determined by the binding and disassociating strength of the atom-surface interaction (Stamenkovic et al., 2006). As mentioned in chapter 1.3, once the oxygen and hydroxyl are bound to the metal surface, the reaction can proceed in two pathways. If the oxygen molecule binds too weakly, the molecule won't be able to disassociate properly. Whereas, if the oxygen or hydroxyl bind too strongly, smothering at the active sites occurs, preventing further reactions from occurring.

Thus, to understand the surface effects, the binding energy of the reactants to the nanoparticle's surfaces have been used as the catalytic activity descriptor. The aim is to use this descriptor to understand catalytic activity of a widely varying size range of nanoparticles, similar to a method proposed by (Shao et al., 2011).

4.6.2 Experimental Methods

The sample investigated was a pure Pt catalyst used on the ORR cathode side of a PEMFC fuel cell. The sample was prepared by grinding, followed by sonication for half an hour in pure ethanol and then drop cast onto a holey carbon TEM grid. The loading was baked at 80°C before the experiment. The nanoparticles are supported on a carbon-black support and to contextualize the ensemble, the particle size was measured. To evaluate the size of the distribution, ADF STEM images at several magnifications were recorded using a JEOL 3000F microscope, Figure 4.15. The resolution of the images is low, but it is enough for a sizing analysis using automated thresholding. A total of 1342 nanoparticles were measured for the particle analysis, Figure 4.14.

Additionally, high resolution STEM images were recorded across the wide size range to obtain a representative population of the sample Figure 4.14. Following a study by (De Backer et al., 2015), a 12cm camera length with ADF collection angles spanning 51.7-248.4mrad was chosen. To minimise sample damage and correct scan distortions a series of images were recorded and aligned (Jones et al., 2015). The electron dose per ADF frame was evaluated at 1.38 10^4 $e^-Å^{-2}$ which is above the minimum dose required to achieve reliable atom count of ±1 atom precision(De Backer et al., 2015a).

From several high-resolution nanoparticle images, 13 were sufficiently close to a crystallographic zone axis for accurate atom counting. These are represented across a size range and some of the nanoparticles are shown in Figure 4.14 and further images are shown in Figure 4.18.

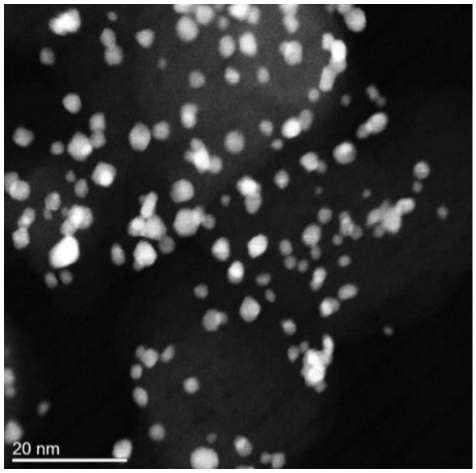

Figure 4.15 Low magnification STEM image from a Pt catalyst sample. Reprinted from (Aarons et al., 2017)

4.6.3 Atom Counting and Three-dimensional Model Reconstruction

After the image alignment, the image intensity was fractionated in Absolute Integrator(Jones et al., 2014) using an ADF detector scan, Figure 4.16, following an electron flux weighting approach(Martinez et al., 2014). A correction was made for the amorphous carbon support by locally subtracting the background intensity using a method from (De Backer et al., 2015) and the calculated cross-sections were converted into atom counts using the μSTEM software (Allen et al., 2014). The ADF STEM image simulations were calculated using the quantum excitations of phonons model provided through the μSTEM software developed at the University of Melbourne. An 8x8 Pt unit cell was sampled along the <110> or <100> zone axis, with a 2048x2048 reciprocal mesh. The atomic root mean square displacement was calculated using the parametrization from (Gao and Peng, 1999) at 300K temperature. 30 atomic phonon configurations were generated to obtain a reliable scattering cross-section to create a simulation library.

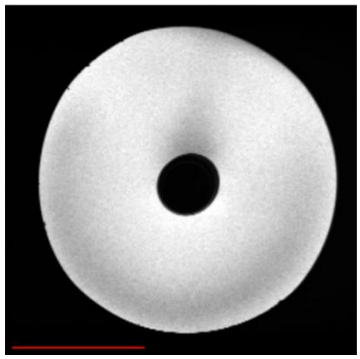

Figure 4.16 ADF detector efficiency scan, Reprinted from (Aarons et al., 2017)

Three dimensional nanoparticle structures were obtained fixing atomic column coordinates and displacing the z-column counts using the method from (Jones et al., 2014) . Initially, the column atoms were placed equatorially about the mid plane and then relaxed along the z-direction using a Lennard-Jones potential for Pt. A genetic algorithm was used to search a wide possible energy landscape. For more details of this see, (Aarons et al., 2017; Jones et al., 2014).

Structures obtained in this manner are computationally efficient though a somewhat simplified approach to determining the optimum structure. Therefore, the structure optimisation was followed up by a more computationally intensive, unconstrained, geometry relaxation using the Sutton-Chen force field within the DL_POLY4 software(Sutton and Chen, 1990). During this relaxation, a small ~0.1Å atomic separation was observed around the periphery of the nanoparticle models.

Importantly, three-dimensional nanoparticle models determined in this way may not be the 'ground truth' solution, but rather are 'a solution', given the prior knowledge and estimates made in the assumption. Instead, the models provide the most probable experimentally determined structure in a probability space.

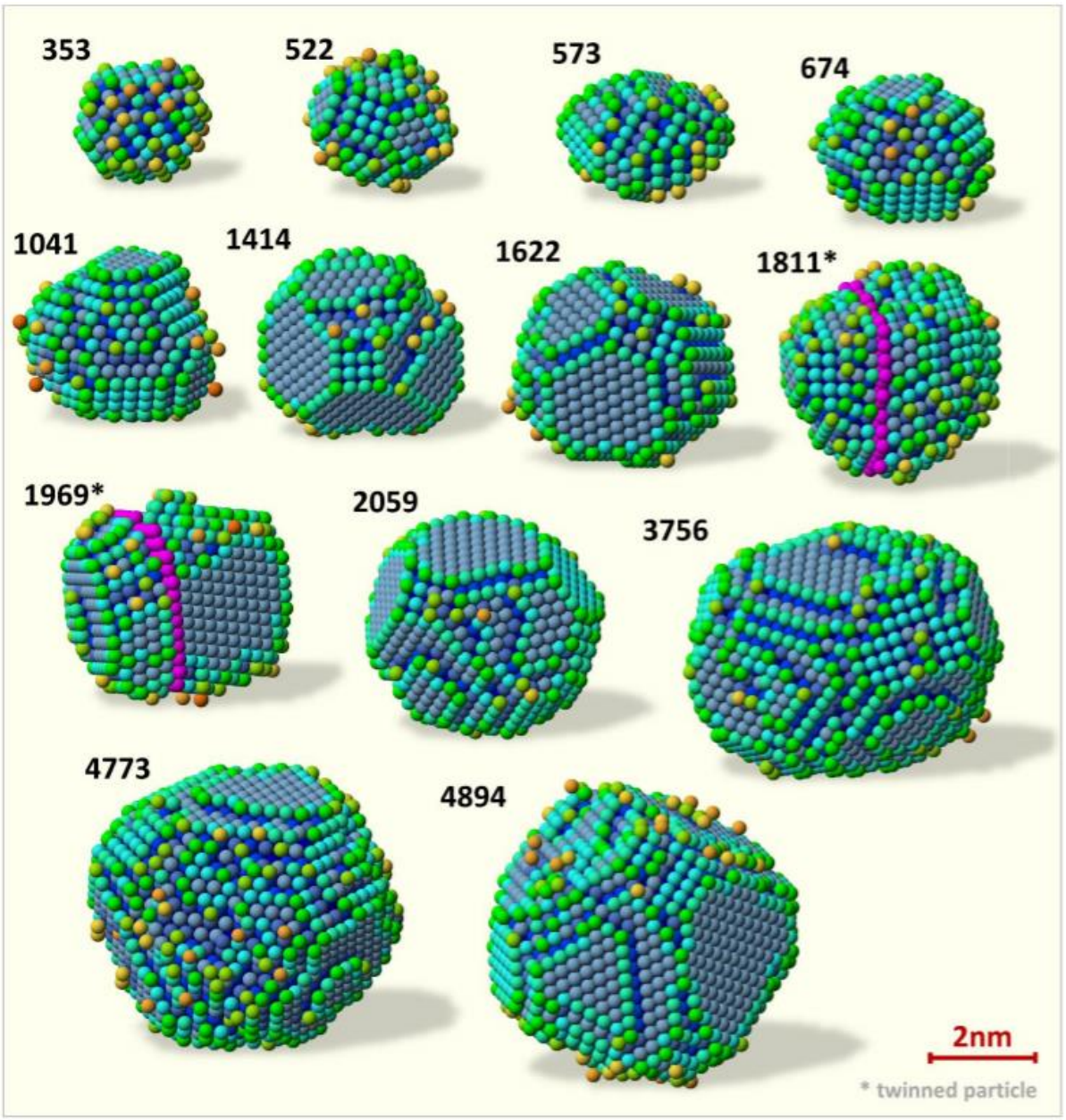

Figure 4.17 Experimentally determined models. Particles 353 and 522 were used as inputs for DFT simulations. The pink line presents twinning of the nanoparticle, whereas, the rest of the colours represent the coordination number. Reprinted from (Aarons et al., 2017)

4.6.4 DFT Calculations

After the unconstrained geometry relaxation, Nanoparticle 353 and 522 were used as inputs for the ONETEP DFT program (Skylaris et al., 2008) by Dr Jolyon Aarons. ONETEP allows calculations of non-periodic structures such as nanoparticles using a Coulomb cut-off approach when calculating all the electrostatic interactions in the energy functional (Hine et al., 2011). This cut-off is implemented by a spherical truncation to the electrostatic potential. Provided that the truncation covers almost the entire electronic density of the nanoparticle, the calculations can be approximated to a nanoparticle

isolated in space. Estimates on how large the spheres were obtained by rigorously converging the electron exchange potential with respect to radius of the nanoparticle. More details of this can be found in the appendix of the publication by (Aarons et al., 2017).

4.6.5 Correlating Nanoparticle Metrology to Electronic Structure

Of the nanoparticles observed a few were close to the 'magic number' cuboctahedral structures, Figure 4.18. By plotting the coordination number as a function of nanoparticle size, a classic surface area to volume effect is observed. As the particle size increases the proportion of bulk-like coordination increases as well.

Additionally, clear surface roughness can be observed in the experimental nanoparticles with significantly more atoms of lower coordination than cuboctahedral nanoparticles of equivalent size. The low coordination sites, with 6 or fewer atoms, are presented by the dashed line in Figure 4.18d. And for nanoparticles such as 353, 20% of the atoms have <6 atom coordination. This percentage rises to 46% if other facets that are not bulk-like are considred.

DFT calculations were then performed on the nanoparticles with 353 and 522 atoms. Owing to DFT calculations being computationally demanding, it was only possible to compute the electronic energies of the smallest two nanoparticles within a reasonable time frame. Further details of the DFT calculations can be found in (Aarons et al., 2017).

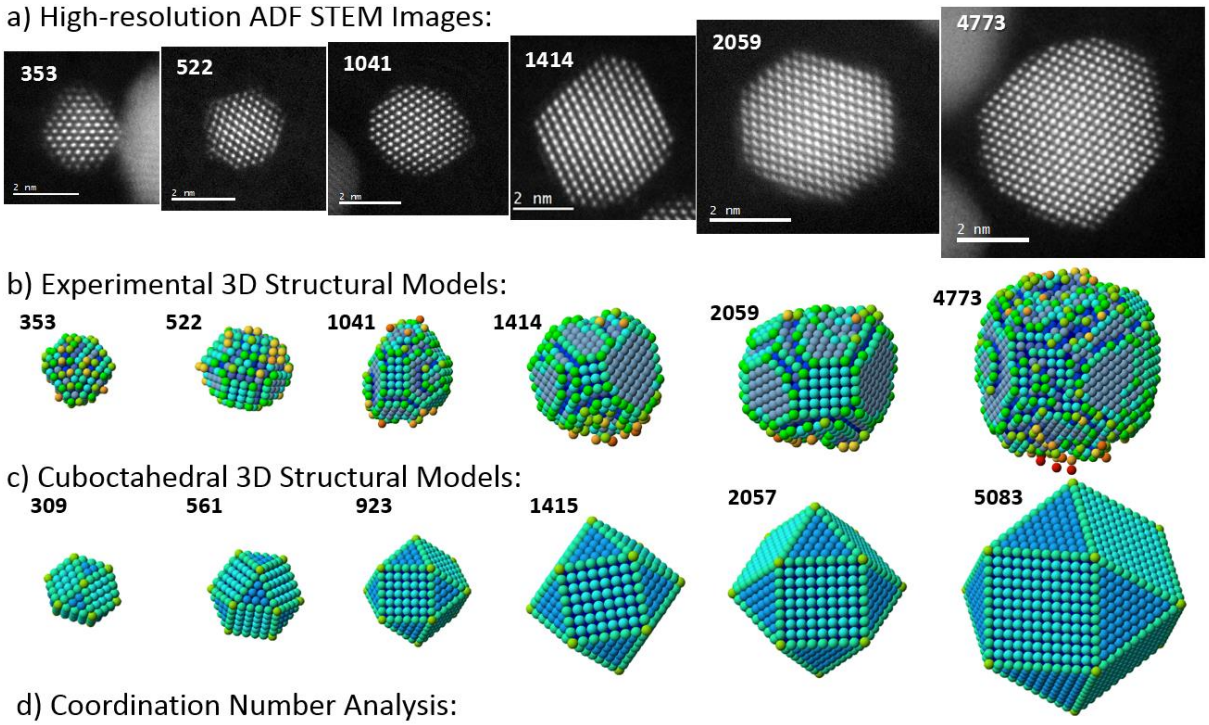

Figure 4.18 a) HR-STEM images and b) the accompanying hard-sphere models. The atoms are coloured by coordination number and rotated to show the dominant facest with respect to the cuboctahedra models c). Populations histograms in d) show the cuboctahedral (left) and experimental (right) coordination numbers as a function of number of atoms. The coordination corresponding to the facets (111), (110), (100) and edges are labelled within the coordination figure respectively. Whereas coordination above or equal to 10 atoms is represented as the bulk. Reprinted from (Aarons et al., 2017)

With these two nanoparticles, a descriptor can be obtained to describe and predict the chemical properties across the observed ensemble of nanoparticles. To achieve this, the local electronic density was mapped as an isosurface of the total electrostatic potential of the nanoparticle, Figure 4.19. By comparing the electronic charge density maps and the coordination number of the experimental and cuboctahedral nanoparticles, the experimental structures show a greater number of sites with low electron density.

The atoms with low coordination exhibit lower electron density at the surface due to the Smoluchowski effect (Smoluchowski, 1941). This effect describes the spreading out of the electronic charge density at sharp, surface corrugations and defects causing a loss in electronic density above low coordination sites, this has also been observed in several other works as well(Han and Weiss, 2012; Ibach, 2010; Vladimirova et al., 2007).

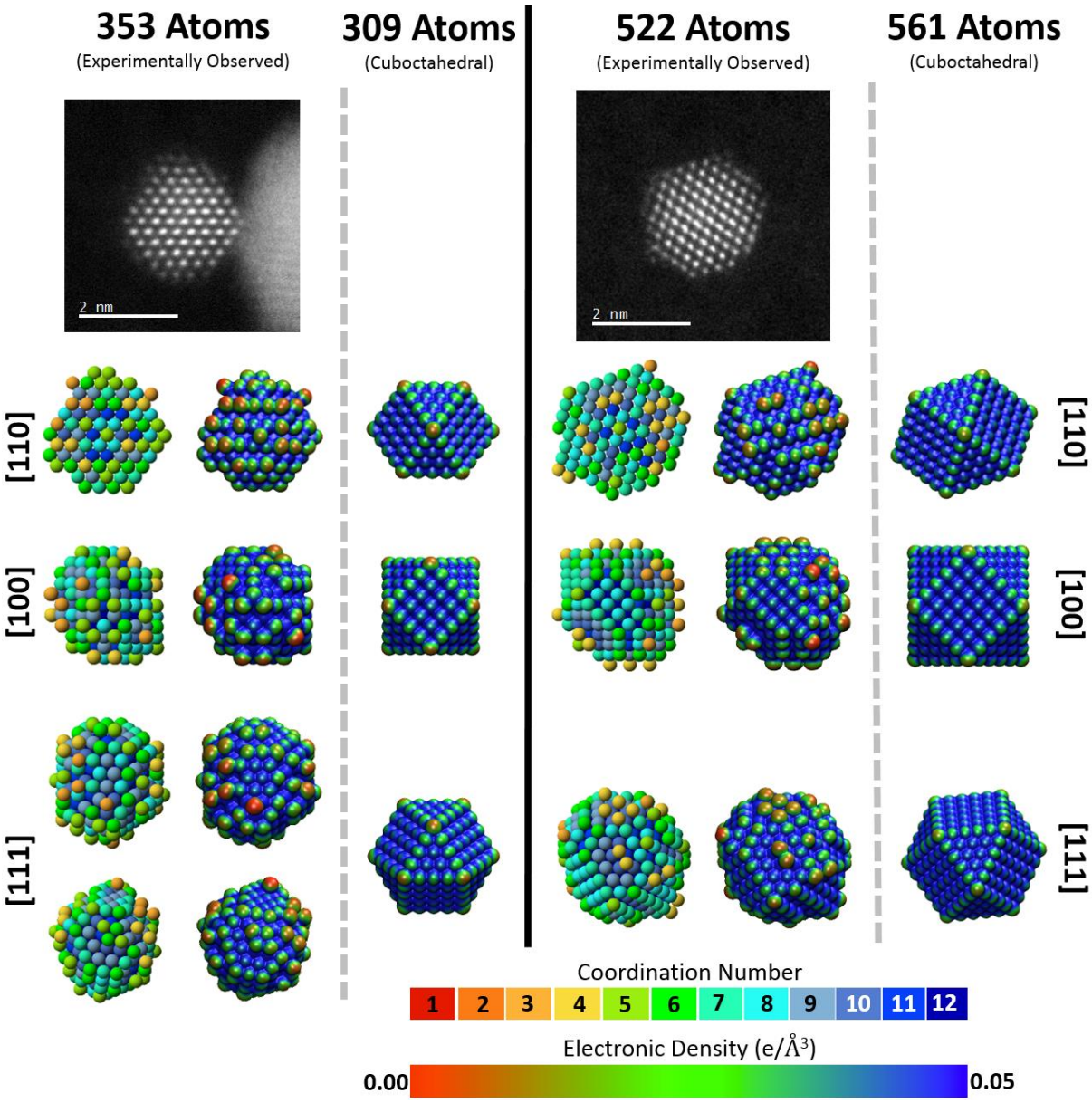

Figure 4.19 Coordination number and DFT analyses for the smaller (left) and larger (right) nanoparticles studied. Hard-sphere structural models were calculated from the ADF data and are coloured according to their coordination number; these are shown rotated to various viewing directions to highlight their morphology. Alongside the structural models, the DFT results showing isovalue surfaces of total electrostatic potential at 0.0 Ha colourised by the local electronic density. Size analogue cuboctohedra DFT results are shown for comparison. Reprinted from (Aarons et al., 2017)

The coordination sites and electronic density iso-surfaces highlight a diverse range of surface sites between the magic number and experimental models. To evaluate this systematically (Aarons et al.,

2017) developed an algorithm to systematically identify all the atop, bridge, and hollow sites across the nanoparticle surface. With this code a generalised coordination number of every possible site for an oxygen adsorbate was calculated using a formula from (Calle-Vallejo et al., 2014)

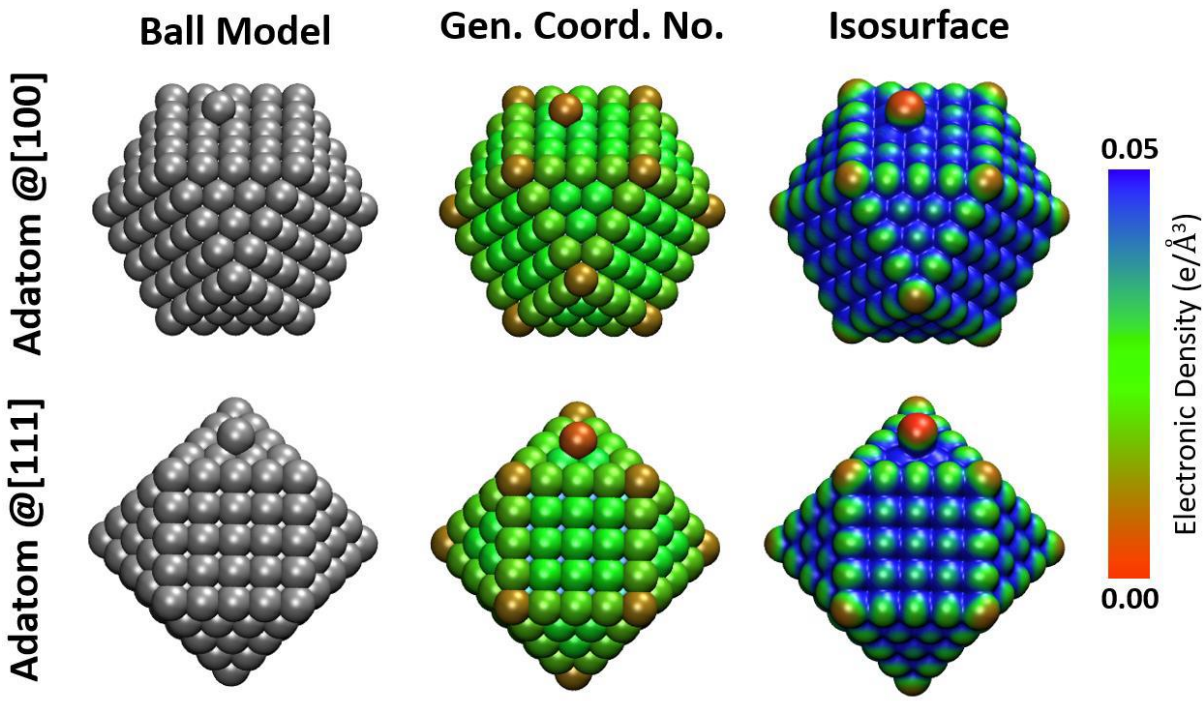

Figure 4.20 Structural models representing the ball model, generalised coordination and iso-surface models on a Pt309 cuboctahedral nanoparticle. Reprinted from (Aarons et al., 2017)

When the generalised coordination is plotted as a function of all possible surface sites, several features present within the experimental nanoparticles can be seen when compared to the cuboctahedral models, Figure 4.21. Firstly, the magic number Pt309 nanoparticle exhibits a small portion of the uniquely coordinated oxygen bindings sites and a total of 25 unique sites are required to describe every possible symmetry-related adsorption site and thus, making a systematic DFT study relatively tractable. The experimental nanoparticles, on the other hand, have a far greater number of unique site geometries and the largest nanoparticle (4894 atoms) within the ensemble, Figure 4.17, exhibits ~8300 unique surface adsorption sites.

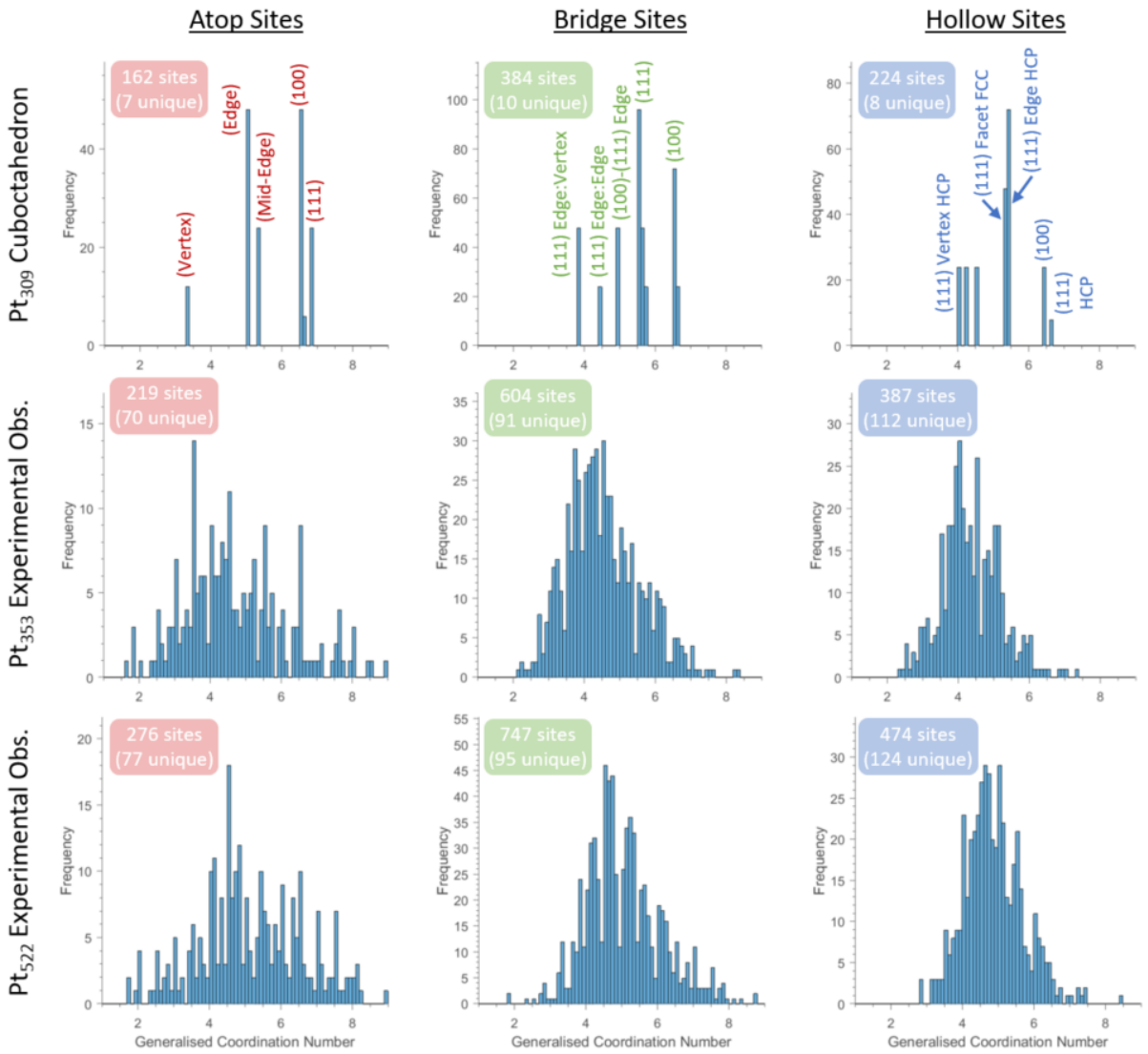

Figure 4.21 Histograms of the generalised coordination number as a function of all possible surface sites for the Pt 309 cuboctahedral and the experimental, Pt353 and Pt522 nanoparticles. Reprinted from (Aarons et al., 2017)

Figure 4.22 shows the oxygen binding across a variety of sites from a Pt309 cuboctahedron as a function of the electron density value on the isosurface, and as a function of generalised coordination number. Electronic density values from each binding site (atop, bridge or hollow) are used as descriptors of O binding strength. The linear relationships provide a straightforward link between each binding energy as a function of electron density value. The advantage of using electronic descriptors is that they can be extended to study alloyed nanoparticles as well.

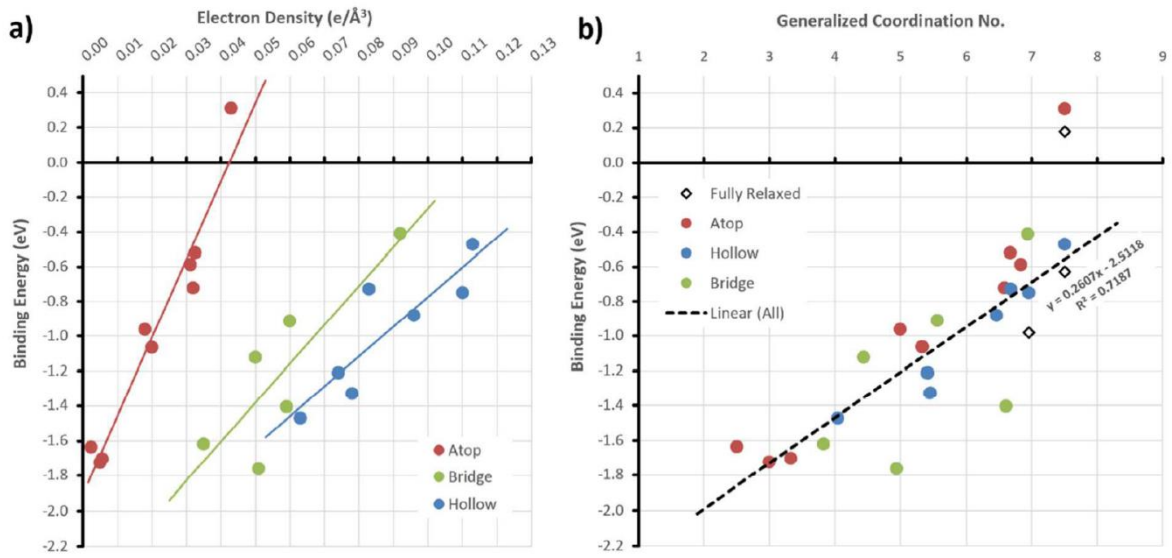

Figure 4.22 Calculated oxygen binding energies for various atop, bridge and hollow sites covering a Pt309 cuboctahedral nanoparticle. Reprinted from (Aarons et al., 2017)

Using this descriptor and the master curve from Figure 4.22 an 'averaged binding energy' can be predicted for each coordinated atom. The linear trend in Figure 4.22b allows for extrapolation from the computationally expensive individual DFT calculations, onto many thousand unique sites across the experimental observations, thus, predicting a binding energy for every surface site.

As an 'ideal' anchoring metric, the fraction of sites within 0.2eV of the optimum binding strength of -0.52eV was calculated using the linear fit in Figure 4.22b for each nanoparticle. While this does not describe a quantitative relationship to catalytic activity explicitly, it does offer a rapidly estimated metric for comparing any given nanoparticle with a reference with the rest of the ensemble.

The fraction of sites within the 0.2eV metric is sensitive to particle size, shape and roughness and can therefore be used to evaluate and compare catalytic performance of nanoparticles from a real catalyst sample. This metric was measured for the 13 observed nanoparticles, truncated and non-truncated cuboctahedron (Wulff) nanoparticles, and randomly generated quasi spherical nanoparticles. Out of the two structures mentioned, the comparison to Wulff is more important as this represents the thermodynamic equilibrium shape of a truncated octahedral crystal.

For the truncated, Wulff-shape, nanoparticles a monotonic relationship is observed, and is dominated by size effects. Even though the Wulff shape nanoparticles have similar {111}/{110} face ratios, at small nanoparticle sizes (~2nm) the excess low coordinated edges and vertices result in a small fraction

of sites within 0.2eV from the optimal. This trend matches well with work by (Shao et al., 2011) for nanoparticles smaller than 2nm. However, imaging nanoparticles <2nm is experimentally difficult due to beam damage and were not investigated in this study. However, for all the nanoparticles in Figure 4.23 a similar trend is observed, though with sharper tips and troughs for sizes under 2nm.

The fraction of sites <0.2eV for the experimental nanoparticles was always lower than the Wulff shape structures, but higher than the cuboctahedra. Thus, the experimental nanoparticle shape is kinetically bound between the ideal Wulff shape and the cuboctahedral shape. From Figure 4.17 and the generalised coordination histogram analysis Figure 4.21, an increase in roughness as a function of nanoparticle size is observed for the experimental nanoparticles. A lowering of the generalised coordination number is also observed and because the lowest coordination sites are so strongly over bound, rough ad-atom sites effectively poison the surface locally and block the high coordination sites below. The downward shift of the experimental curve at ~3nm from the Wulff trend have various topographic effects, thus reducing the fraction of active sites <0.2eV from the optimal binding energy.

As an additional comparison, a series of 1,600 randomly generated quasi spherical models were generated and the fraction of sites <0.2 from the optimum were evaluated. These nanoparticles were created from a single FCC Pt crystal and the spheres were truncated with various radius thresholds.

In summary, from the 13 experimentally observed ensemble, the nanoparticles reach the most closely to Wulff in the size range of 2.7-3.5nm. The location of the minimum is consistent with the industrially optimised synthesis process and activity operation previously reported(Shao et al., 2011). As the nanoparticles get larger the experimental and quasi spherical curves plateau. This is because the very largest nanoparticles are more spherical suggesting that they are further from their thermodynamic optimum shape and the surface facets are truncated as size increases.

Two twinned nanoparticles were also observed but were not included in the study as these are rarely observed in this sample. Additional study of twinned nanoparticles would require a wider range of twinned nanoparticles to draw any conclusions.

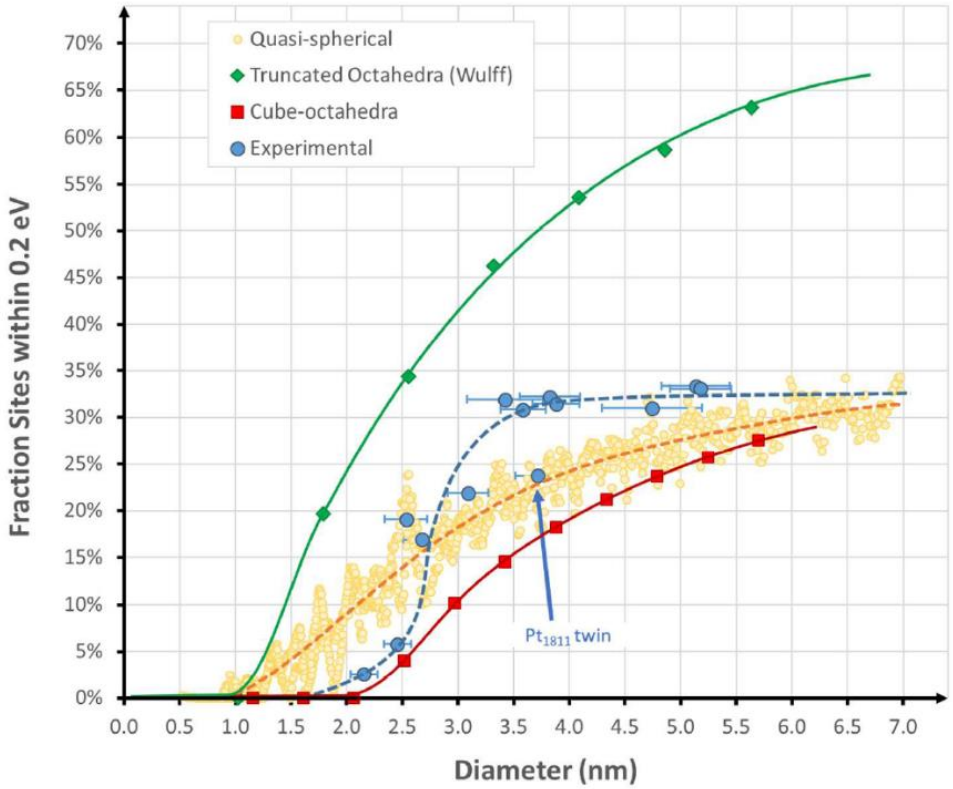

Figure 4.23 Fraction of the surface sites within 0.2eV of the optimal binding energy of -0.52 eV for the 13 observed nanoparticles. The truncated octahedra, cuboctahedra and quasi spherical nanoparticles are shown with their respective labels as well. Reprinted from (Aarons et al., 2017)

4.6.6 Conclusions

The three-dimensional models presented here can be obtained from a single day of microscope time. Then with a with a few hours of data process structural models of up to 5000 atoms can be created on a standard desktop computer. These structural models can be used as inputs for DFT calculations to yield their electronic structure.

As the experimental nanoparticle size increased, the roughness increased compared to the Wulff structures. This leads to more sites with lower electron density and therefore higher O-binding reducing activity. Using a DFT calibrated master curve, an estimate of the fraction of sites within 0.2eV of the optimum binding energy can be calculated in a few seconds and used to rapidly predict the catalytic activity of experimentally determined structures. Additionally, this dramatically reduces the need to do a DFT calculation of the adsorption energy at each distinct site.

This high throughput approach agrees well with experimentally and theoretically determined findings for the pure Pt nanoparticle system(Calle-Vallejo et al., 2015; Lima et al., 2007). While quantitative

structural inversion of bi-metallic catalysts is difficult with ADF images, the use of quantitative spectroscopic techniques in STEM discussed in the next chapter aim to tackle this. Then with bimetallic models, the electronic descriptor methodology described in this chapter could easily be extended to study such models.

4.7 References

Aarons, J., Jones, L., Varambhia, A., MacArthur, K.E., Ozkaya, D., Sarwar, M., Skylaris, C.K., Nellist, P.D., 2017. Predicting the Oxygen-Binding Properties of Platinum Nanoparticle Ensembles by Combining High-Precision Electron Microscopy and Density Functional Theory. Nano Lett. 17, 4003–4012. doi:10.1021/acs.nanolett.6b04799

Abo-Hamed, E.K., Pennycook, T., Vaynzof, Y., Toprakcioglu, C., Koutsioubas, A., Scherman, O.A., 2014. Highly active metastable ruthenium nanoparticles for hydrogen production through the catalytic hydrolysis of ammonia borane. Small 10, 3145–3152. doi:10.1002/smll.201303507

Allen, L.J., D'Alfonso, A.J., Findlay, S.D., 2014. Modelling the inelastic scattering of fast electrons. Ultramicroscopy 151, 1–12. doi:10.1016/j.ultramic.2014.10.011

Allen, L.J., Findlay, S.D., Oxley, M.P., Rossouw, C.J., 2003. Lattice-Resolution Contrast From a Focused Coherent Electron Probe. Part II. Ultramicroscopy 96, 65–81. doi:10.1016/S0304-3991(02)00381-9

Batenburg, K.J., Sijbers, J., 2011. DART: A Practical Reconstruction Algorithm for Discrete Tomography. IEEE Trans. Image Process. 20, 2542–2553. doi:10.1109/TIP.2011.2131661

Calle-Vallejo, F., Loffreda, D., Koper, M.T.M., Sautet, P., 2015. Introducing structural sensitivity into adsorption–energy scaling relations by means of coordination numbers. Nat. Chem. 7, 403–410. doi:10.1038/nchem.2226

Calle-Vallejo, F., Martínez, J.I., García-Lastra, J.M., Sautet, P., Loffreda, D., 2014. Fast prediction of adsorption properties for platinum nanocatalysts with generalized coordination numbers. Angew. Chemie - Int. Ed. 53, 8316–8319. doi:10.1002/anie.201402958

Cowley, J.M., Plano, R.., 1987. A Microdiffraction Study of Gold-Ruthenium Catalyst Particles. J. Catal. 108, 199–207.

Datye, A.K., Logan, A.D., Long, N.J., 1988. Transmission Electron Microscopy of Ru Supported on Model Oxide Surfaces. J. Catal. 109, 76–88.

De Backer, A., De wael, A., Gonnissen, J., Van Aert, S., 2015a. Optimal experimental design for nano-particle atom-counting from high-resolution STEM images. Ultramicroscopy 151, 46–55. doi:10.1016/j.ultramic.2014.10.015

De Backer, A., Jones, L., Lobato, I., Altantzis, T., Goris, B., Nellist, P.D., Bals, S., Van Aert, S., 2017. Three-dimensional atomic models from a single projection using Z-contrast imaging: verification by electron tomography and opportunities. Nanoscale 9, 8791–8798. doi:10.1039/C7NR02656K

De Backer, A., Martinez, G.T., MacArthur, K.E., Jones, L., Béché, A., Nellist, P.D., Van Aert, S., Backer, A. De, Aert, S. Van, 2015b. Dose limited reliability of quantitaive ADF STEM for nano-particle atom-counting. Ultramicroscopy 151, 56–61. doi:10.1016/j.ultramic.2014.11.028

De Backer, A., Martinez, G.T., Rosenauer, A., Van Aert, S., 2013. Atom counting in HAADF STEM using a statistical model-based approach: Methodology, possibilities, and inherent limitations. Ultramicroscopy 134, 23–33. doi:10.1016/j.ultramic.2013.05.003

De Backer, A., van den Bos, K.H.W., Van den Broek, W., Sijbers, J., Van Aert, S., 2016. StatSTEM: An efficient approach for accurate and precise model-based quantification of atomic resolution electron microscopy images. Ultramicroscopy 171, 104–116. doi:10.1016/J.ULTRAMIC.2016.08.018

De wael, A., De Backer, A., Jones, L., Nellist, P.D., Van Aert, S., 2017. Hybrid statistics-simulations based method for atom-counting from ADF STEM images. Ultramicroscopy 177, 69–77. doi:10.1016/j.ultramic.2017.01.010

E, H., MacArthur, K.E., Pennycook, T.J., Okunishi, E., D'Alfonso, a. J., Lugg, N.R., Allen, L.J., Nellist, P.D., 2013. Probe integrated scattering cross sections in the analysis of atomic resolution HAADF STEM images. Ultramicroscopy 133, 109–119. doi:10.1016/j.ultramic.2013.07.002

Egerton, R.F., 2014. Choice of operating voltage for a transmission electron microscope. Ultramicroscopy 145, 85–93. doi:10.1016/j.ultramic.2013.10.019

Egerton, R.F., Crozier, P.A., Rice, P., 1987. Electron energy-loss spectroscopy and chemical change. Ultramicroscopy 23, 305–312. doi:10.1016/0304-3991(87)90240-3

Findlay, S.D., LeBeau, J.M., 2013. Detector non-uniformity in scanning transmission electron microscopy. Ultramicroscopy 124, 52–60. doi:10.1016/j.ultramic.2012.09.001

Findlay, S.D., LeBeau, J.M., 2013. Detector non-uniformity in scanning transmission electron microscopy. Ultramicroscopy 124, 52–60. doi:10.1016/j.ultramic.2012.09.001

Fritz, R., Beyer, A., Stolz, W., Müller, K., Schowalter, M., Rosenauer, A., Häusler, I., Kirmse, H., Mogilatenko, A., Neumann, W., Volz, K., 2011. Quantitative Analysis of Chemical Composition Using HAADF-STEM in a JEOL 2200FS. Microsc. Microanal. 17, 1410–1411. doi:10.1017/S1431927611007926

Gao, H.X., Peng, L.-M., 1999. Parameterization of the temperature dependence of the Debye–Waller factors. Acta Crystallogr. Sect. A Found. Crystallogr. 55, 926–932. doi:10.1107/S0108767399005176

García-García, F.R., Guerrero-Ruiz, a., Rodríguez-Ramos, I., 2009. Role of B5-type sites in Ru catalysts used for the NH3 decomposition reaction. Top. Catal. 52, 758–764. doi:10.1007/s11244-009-9203-7

Han, P., Weiss, P.S., 2012. Electronic substrate-mediated interactions. Surf. Sci. Rep. 67, 19–81. doi:10.1016/j.surfrep.2011.11.001

Hine, N.D.M., Dziedzic, J., Haynes, P.D., Skylaris, C.-K., 2011. Electrostatic interactions in finite systems treated with periodic boundary conditions: Application to linear-scaling density functional theory. J. Chem. Phys. 135, 204103. doi:10.1063/1.3662863

Ibach, H., 2010. Vibration spectroscopy of water on stepped gold surfaces. Surf. Sci. 604, 377–385. doi:10.1016/j.susc.2009.11.034

Ishiguro, N., Saida, T., Uruga, T., Nagamatsu, S., Sekizawa, O., Nitta, K., Yamamoto, T., Ohkoshi, S., Iwasawa, Y., Yokoyama, T., Tada, M., 2012. Operando Time-Resolved X-ray Absorption Fine Structure Study for Surface Events on a Pt 3 Co/C Cathode Catalyst in a Polymer Electrolyte Fuel Cell during Voltage-Operating Processes. ACS Catal. 2, 1319–1330. doi:10.1021/cs300228p

Jacobsen, C.J.H., Dahl, S., Hansen, P.L., Törnqvist, E., Jensen, L., Topsøe, H., Prip, D. V., Møenshaug, P.B., Chorkendorff, I., 2000. Structure sensitivity of supported ruthenium catalysts for ammonia synthesis. J. Mol. Catal. A Chem. 163, 19–26. doi:10.1016/S1381-1169(00)00396-4

Jones, L., 2016. Quantitative ADF STEM: acquisition, analysis and interpretation. IOP Conf. Ser. Mater. Sci. Eng. 109, 12008. doi:10.1088/1757-899X/109/1/012008

Jones, L., 2015. Quantitative ADF STEM : acquisition , analysis and interpretation 1–16. doi:10.1088/1757-899X/109/1/012008

Jones, L., MacArthur, K.E., Fauske, V.T., van Helvoort, A.T.J., Nellist, P.D., 2014. Rapid estimation of catalyst nanoparticle morphology and atomic-coordination by high-resolution z-contrast electron microscopy. Nano Lett. 14, 6336–41. doi:10.1021/nl502762m

Jones, L., Varambhia, A., Sawada, H., Nellist, P.D., 2017. An optical configuration for fastidious STEM detector calibration and the effect of the objective lens pre-field Manuscript. J. Microsc. submitted.

Jones, L., Yang, H., Pennycook, T.J., Marshall, M.S.J., Van Aert, S., Browning, N.D., Castell, M.R., Nellist, P.D., 2015. Smart Align—a new tool for robust non-rigid registration of scanning microscope data. Adv. Struct. Chem. Imaging 1, 8. doi:10.1186/s40679-015-0008-4

Katz-Boon, H., Rossouw, C.J., Dwyer, C., Etheridge, J., 2013. Rapid Measurement of Nanoparticle Thickness Profiles. Ultramicroscopy 124, 61–70. doi:10.1016/j.ultramic.2012.08.009

Kirkland, E.J., 1998. Advanced Computing in Electron Microscopy, 1st Edition. New York.

Kirkland, E.J., Loane, R.F., Silcox, J., 1987. Simulation of annular dark field stem images using a modified multislice method. Ultramicroscopy 23, 77–96. doi:10.1016/0304-3991(87)90229-4

Kusada, K., Kobayashi, H., Yamamoto, T., Matsumura, S., Sumi, N., Sato, K., Nagaoka, K., Kubota, Y., Kitagawa, H., 2013. Discovery of face-centered-cubic ruthenium nanoparticles: Facile size-controlled synthesis using the chemical reduction method. J. Am. Chem. Soc. 135, 5493–5496. doi:10.1021/ja311261s

Lebeau, J.M., Findlay, S.D., Allen, L.J., Stemmer, S., 2010. Standardless atom counting in scanning transmission electron microscopy. Nano Lett. 10, 4405–4408. doi:10.1021/nl102025s

LeBeau, J.M., Stemmer, S., 2008. Experimental quantification of annular dark-field images in scanning transmission electron microscopy. Ultramicroscopy 108, 1653–1658. doi:10.1016/j.ultramic.2008.07.001

Lima, F.H.B., Zhang, J., Shao, M.H., Sasaki, K., Vukmirovic, M.B., Ticianelli, E.A., Adzic, R.R., 2007. Catalytic Activity−d-Band Center Correlation for the O 2 Reduction Reaction on Platinum in Alkaline Solutions. J. Phys. Chem. C 111, 404–410. doi:10.1021/jp065181r

Liu, P., Logadottir, a., Nørskov, J.K., 2003. Modeling the electro-oxidation of CO and H2/CO on Pt, Ru, PtRu and Pt3Sn. Electrochim. Acta 48, 3731–3742. doi:10.1016/S0013-4686(03)00538-3

Loane, R.F., Xu, P., Silcox, J., 1991. Thermal vibrations in convergent-beam electron diffraction. Acta Crystallogr. Sect. A Found. Crystallogr. 47, 267–278. doi:10.1107/S0108767391000375

Lobato, I., Van Dyck, D., 2015. MULTEM: A new multislice program to perform accurate and fast electron diffraction and imaging simulations using Graphics Processing Units with CUDA. Ultramicroscopy 156, 9–17. doi:10.1016/j.ultramic.2015.04.016

MacArthur, K.E., Jones, L., Nellist, P.D., 2014. How flat is your detector? Non-uniform annular detector sensitivity in STEM quantification. J. Phys. Conf. Ser. 522, 12018. doi:10.1088/1742-6596/522/1/012018

MacArthur, K.E., Slater, T.J.A., Haigh, S.J., Ozkaya, D., Nellist, P.D., Lozano-Perez, S., 2016. Compositional quantification of PtCo acid-leached fuel cell catalysts using EDX partial cross sections. Mater. Sci. Technol. 32, 248–253. doi:10.1080/02670836.2015.1133021

Martinez, G.T., Jones, L., Backer, A. De, 2014. Quantitative STEM normalisation : the importance of the electron flux.

Martinez, G.T., Jones, L., Backer, A. De, Béché, A., Verbeeck, J., Aert, S. Van, Nellist, P.D., 2015. Quantitative STEM normalisation: the importance of the electron flux. Ultramicroscopy. doi:10.1016/j.ultramic.2015.07.010

Mavrikakis, M., Hammer, B., Nørskov, J.K., 1998. Effect of Strain on the Reactivity of Metal Surfaces. Phys. Rev. Lett. 81, 2819–2822. doi:10.1103/PhysRevLett.81.2819

Monosmith, W.B., Cowley, J.M., 1983. Electron microdiffraction from very small gold particles. Ultramicroscopy 12, 177–183. doi:10.1016/0304-3991(83)90257-7

Nellist, P.D., Pennycook, S.J., 2000. The Principles and Interpretation of Annular Dark-Field Z-Contrast Imaging. Adv. Imaging Electron Phys. 148–203.

Nørskov, J.K., Bligaard, T., Rossmeisl, J., Christensen, C.H., 2009. Towards the computational design of solid catalysts. Nat. Chem. 1, 37–46. doi:10.1038/nchem.121

Prestridge, E.B., Via, G.H., Sinfelt, J.H., 1977. Electron microscopy studies of metal clusters: Ru, Os, Ru-Cu, and Os-Cu. J:Catal. 50, 115–123.

Raróg-Pilecka, W., Miśkiewicz, E., Szmigiel, D., Kowalczyk, Z., 2005. Structure sensitivity of ammonia synthesis over promoted ruthenium catalysts supported on graphitised carbon. J. Catal. 231, 11–19. doi:10.1016/j.jcat.2004.12.005

Retsky, M., 1974. Observed single atom elastic cross sections in a scanning electron microscope. Optik (Stuttg). 41, 127–142. doi:10.2172/4239746

Rosenauer, A., Mehrtens, T., Müller, K., Gries, K., Schowalter, M., Venkata Satyam, P., Bley, S., Tessarek, C., Hommel, D., Sebald, K., Seyfried, M., Gutowski, J., Avramescu, A., Engl, K., Lutgen, S., 2011. Composition mapping in InGaN by scanning transmission electron microscopy. Ultramicroscopy 111, 1316–1327. doi:10.1016/j.ultramic.2011.04.009

Saadatjou, N., Jafari, A., Sahebdelfar, S., 2014. Ruthenium Nanocatalysts for Ammonia Synthesis: A Review. Chem. Eng. Commun. 202, 420–448. doi:10.1080/00986445.2014.923995

Sears, V.F., Shelley, S. A., 1991. Debye–Waller factor for elemental crystals. Acta Crystallogr. Sect. A Found. Crystallogr. 47Sears, V, 441–446. doi:10.1107/S0108767391002970

Shao, M., Peles, A., Shoemaker, K., 2011. Electrocatalysis on Platinum Nanoparticles: Particle Size Effect on Oxygen Reduction Reaction Activity. Nano Lett. 11, 3714–3719. doi:10.1021/nl2017459

Skylaris, C.-K., Haynes, P.D., Mostofi, A. A, Payne, M.C., 2008. Recent progress in linear-scaling density functional calculations with plane waves and pseudopotentials: the ONETEP code. J. Phys. Condens. Matter 20, 64209. doi:10.1088/0953-8984/20/6/064209

Skylaris, C.K., Haynes, P.D., Mostofi, A. A., Payne, M.C., 2005. Introducing ONETEP: Linear-scaling density functional simulations on parallel computers. J. Chem. Phys. 122, 1–10. doi:10.1063/1.1839852

Smoluchowski, R., 1941. Anisotropy of the electronic work function of metals. Phys. Rev. 60, 661–674. doi:10.1103/PhysRev.60.661

Solliard, C., Flueli, M., 1985. Surfaces stress and size effect on the lattice parameter in small particles of gold and platinum. Surf. Sci. Lett. 156, A321. doi:10.1016/0167-2584(85)90434-7

Stamenkovic, V., Mun, B.S., Mayrhofer, K.J.J., Ross, P.N., Markovic, N.M., Rossmeisl, J., Greeley, J., Nørskov, J.K., 2006. Changing the activity of electrocatalysts for oxygen reduction by tuning the surface electronic structure. Angew. Chemie - Int. Ed. 45, 2897–2901. doi:10.1002/anie.200504386

Stephens, I.E.L., Bondarenko, A.S., Perez-Alonso, F.J., Calle-Vallejo, F., Bech, L., Johansson, T.P., Jepsen, A.K., Frydendal, R., Knudsen, B.P., Rossmeisl, J., Chorkendorff, I., 2011. Tuning the Activity of Pt(111) for Oxygen Electroreduction by Subsurface Alloying. J. Am. Chem. Soc. 133, 5485–5491. doi:10.1021/ja111690g

Sutton, A.P., Chen, J., 1990. Long-range Finnis–Sinclair potentials. Philos. Mag. Lett. 61, 139–146. doi:10.1080/09500839008206493

Takao, S., Sekizawa, O., Nagamatsu, S., Kaneko, T., Yamamoto, T., Samjeské, G., Higashi, K., Nagasawa, K., Tsuji, T., Suzuki, M., Kawamura, N., Mizumaki, M., Uruga, T., Iwasawa, Y., 2014. Mapping Platinum Species in Polymer Electrolyte Fuel Cells by Spatially Resolved XAFS Techniques. Angew. Chemie Int. Ed. 53, 14110–14114. doi:10.1002/anie.201408845

Theobald, B.R.C., Ball, S.C.B., O'malley, R.L., Thompsett, D., Hards, G.A., 2011. Catalyst. WO20120117226 A1.

Treacy, M.J., Howie, A., 1980. Contrast Effects in the Transmission Electron-Microscopy of Supported Crystalline Catalyst Particles. J. Catal. 63, 265–269.

Van Aert, S., Batenburg, K.J., Rossell, M.D., Erni, R., Van Tendeloo, G., 2011. Three-dimensional atomic imaging of crystalline nanoparticles. Nature 470, 374–377. doi:10.1038/nature09741

Van Aert, S., De Backer, A., Martinez, G.T., Goris, B., Bals, S., Van Tendeloo, G., Rosenauer, a., 2013. Procedure to count atoms with trustworthy single-atom sensitivity. Phys. Rev. B - Condens. Matter Mater. Phys. 87, 64107. doi:10.1103/PhysRevB.87.064107

Van Dyck, D., Op De Beeck, M., 1996. A simple intuitive theory for electron diffraction. Ultramicroscopy 64, 99–107. doi:10.1016/0304-3991(96)00008-3

Varambhia, A.M., Jones, L., De Backer, A., Fauske, V.T., Van Aert, S., Ozkaya, D., Nellist, P.D., 2016. Quantifying a Heterogeneous Ru Catalyst on Carbon Black Using ADF STEM. Part. Part. Syst. Charact. 33, 438–444. doi:10.1002/ppsc.201600067

Vladimirova, M., Stengel, M., Vita, A. De, Baldereschi, a, Böhringer, M., Morgenstern, K., Berndt, R., Schneider, W.-D., 2007. Supramolecular self-assembly and selective step decoration on the Au(111) surface. Europhys. Lett. 56, 254–260. doi:10.1209/epl/i2001-00514-3

Voyles, P.M., Grazul, J.L., Muller, D.A., 2003. Imaging individual atoms inside crystals with ADF-STEM. Ultramicroscopy 96, 251–273. doi:10.1016/S0304-3991(03)00092-5

Wang, Z.W., Li, Z.Y., Park, S.J., Abdela, A., Tang, D., Palmer, R.E., 2011. Quantitative Z-contrast imaging in the scanning transmission electron microscope with size-selected clusters. Phys. Rev. B - Condens. Matter Mater. Phys. 84, 73408. doi:10.1103/PhysRevB.84.073408

Wilkinson, K.A., Hine, N.D.M., Skylaris, C.-K., 2014. Hybrid MPI-OpenMP Parallelism in the ONETEP Linear-Scaling Electronic Structure Code: Application to the Delamination of Cellulose Nanofibrils.

Yang, Y., Chen, C.C., Scott, M.C., Ophus, C., Xu, R., Pryor, A., Wu, L., Sun, F., Theis, W., Zhou, J., Eisenbach, M., Kent, P.R.C., Sabirianov, R.F., Zeng, H., Ercius, P., Miao, J., 2017. Deciphering chemical order/disorder and material properties at the single-atom level. Nature 542, 75–79. doi:10.1038/nature21042

Zewail, A.H., Thomas, J.M. (John M., World Scientific (Firm), 2010. 4D electron microscopy : imaging in space and time. Imperial College Press.

Zhao, Z., Meng, C., Li, P., Zhu, W., Wang, Q., Ma, Y., Shen, G., Bai, L., He, H., He, D., Yu, D., He, J., Xu, B., Tian, Y., 2014. Carbon coated face-centered cubic Ru–C nanoalloys. Nanoscale 6, 10370. doi:10.1039/C4NR02632B

5 Catalyst Composition Determination using STEM Spectroscopic Quantification

5.1 Chapter Overview

This chapter discusses the current spectroscopic quantification methods and recent developments in spectra acquisition. First, a brief review of quantification techniques using known element standards is presented. Quantification methods using a needle and nanoparticle quantification standard is compared and discussed. Scattering cross-sections measured from the standards were then used to quantify Pt3Co and PtCo3, leached and unleached, catalyst nanoparticle ensembles. Elemental composition plots from over 200 nanoparticles as a function of nanoparticle size were produced and compared to two-dimensional strain plots. Linking nanoparticle strain and composition is briefly discussed, and prospects for three-dimensional structure inversion are reviewed.

In this chapter, most of the work was performed by the author including all the experiments and data analysis. The needle samples were prepared by Dr Andrew London, and the image alignment was performed by Dr Lewys Jones.

The results in this chapter present work from the following manuscripts:

- First Author: Determining EDS and EELS partial cross-sections from multiple calibration standards to accurately quantify bi-metallic nanoparticles using STEM,
  Aakash Varambhia, Lewys Jones, Andrew London, Dogan Ozkaya, Peter D Nellist, Sergio Lozano-Perez, Micron, 113 (2018), 69-82.
- First Author: "Quantitative ADF STEM and spectroscopy of Pt-Co catalyst nanoparticles",
  Aakash Varambhia, James Sode, Dogan Ozkaya, Sergio Lozano-Perez, Peter D Nellist, Micron, (2018), in prep.

5.2 Spectroscopic Quantification Methods

Spectroscopic signals such as EDS and EELS provide an effective way of characterising multi-element samples such as Pt-Co nanoparticles in STEM. The advantage of spectroscopy over imaging is the ability to decouple composition and mass-thickness effects for thin samples, into the number of various types of atoms in a sample. This is currently not possible for multi element samples using conventional ADF quantification techniques alone. With recent developments in microscope hardware and software, it is now possible to acquire the ADF, EDS and EELS signals simultaneously and at high speed. However, the methods of quantifying the signals emitted from the sample vary greatly. Most approaches

use pure-element standards in the form of needles, nanoparticles and wedges to quantify the spectroscopic signal into either partial scattering cross-sections, zeta-factors or k-factors. But self-consistency between the different methods has not been verified and the units of the quantification are not standardised. This chapter presents a robust approach for measuring and combining ADF, EDS and EELS signals using needle and nanoparticle standards in units of the partial scattering cross-section. The partial scattering cross-section allows an easy interpretation of the signals emitted from the sample and enables accurate atom-counting of the sample.

5.2.1 Brief Review of Spectroscopic Quantification Techniques

To quantify industrially relevant materials such as bimetallic Pt-Co catalyst nanoparticles, a thorough characterisation of their size, shape and composition is required. Catalyst systems such as Pt-Co are of particular interest in the fuel cell industry due to their enhanced activity compared to pure element catalyst counterparts (Koh and Strasser, 2007; Liu et al., 2013; Xin et al., 2012).

Currently, quantitative size and shape information can be routinely obtained from pure element nanoparticles using quantitative Annular Dark Field (ADF) Scanning Transmission Electron Microscopy (STEM) (Aarons et al., 2017). Composition information is also visible in ADF imaging (Liu and Cowley, 1990), but for bimetallic nanoparticle systems, the ADF signal alone is not sufficient in decoupling the intensity variations caused by composition and thickness changes. To decouple these effects, a spectroscopic approach such as Energy Dispersive X-ray Spectroscopy (EDS) or Electron Energy Loss Spectroscopy (EELS) is required. In both spectroscopic approaches, the intensity obtained can be interpreted by observation of the strength of the signals at characteristic excitation energies for a given element. In principle, measured intensities from ADF, EDS and EELS can all be interpreted in terms of an appropriate partial scattering cross-section (E et al., 2013; Egerton, 2008; MacArthur et al., 2015; Martinez et al., 2015). Here a method is presented for experimentally determining EDS and EELS cross-sections, and, more importantly, verify their accuracy by demonstrating consistency of counting atoms in nanoparticles across measurements made using ADF, EDS and EELS.

The cross-section we measure is described as partial because it depends on factors such as the collection-angle, collection-efficiency, and the size and shape of the detectors in question. Additionally,

due to detection reliability and counting statistics, sometimes not all ionization edges of the sample are incorporated in the measurement. Since most of these factors are microscope dependent, the partial cross-section is an excellent parameter to benchmark detector performance between microscopes (MacArthur et al., 2015).

Multiple attempts have been made at performing quantification using standards in the past (Cliff and Lorimer, 1975; Watanabe et al., 1996). However, for small nanoparticles, detector and software limitations have made this quantification difficult and time consuming. With the recent increase in EDS collection-efficiency using new silicon drift detectors (Phillips et al., 2014) and improvements to the Gatan Image Filter (GIF) (Gubbens et al., 2010) it is now possible, with sufficient speed and counting statistics, to obtain both EDS and EELS signals simultaneously alongside the ADF signal (Kothleitner et al., 2014). Our aim is, that by collecting signals simultaneously from ADF and spectroscopic detectors, thickness and composition effects can be decoupled completely for the highest precision quantification of nanoparticles composition and structure.

The measurement of ADF cross-sections has become well established (Aarons et al., 2017; E et al., 2013; Jones et al., 2014) and relies on careful detector calibration (Jones et al., 2017) and conversion to atom counts through simulation matching techniques (Aarons et al., 2017), statistical decomposition (De Backer et al., 2013; Van Aert et al., 2011) or a hybrid of the two (De wael et al., 2017).

In contrast, spectroscopic quantification has made use of the following methods: k-factor(EDS)(Cliff and Lorimer, 1975), ζ (zeta)-factor(EDS)(Watanabe and Williams, 2006) or a partial scattering cross-section (EELS and EDS) (Craven et al., 2016; MacArthur et al., 2015). Within these approaches the most popular quantification techniques are the k-factor approach for EDS and the Hartree Slater cross-section approach for EELS. These techniques owe their popularity to out-of-the-box incorporation within commercially available software. As these techniques rely on theoretically calculated models, they may contain systematic errors of up to 10% in some cases (Watanabe et al., 2003).

The alternative but more tedious approach is to measure the k-factor and the scattering cross-section experimentally. Here difficulties emerge due to sample preparation, as the k-factor approach requires a

thin well-characterised binary sample and the cross-section approach requires a pure element sample thin enough for minimal multiple scattering. In order to tackle the binary sample problem, (Watanabe et al., 1996) proposed the pure element zeta factor method to quantify the EDS signal. Building upon this, (Kothleitner et al., 2014) proposed a method to quantify the EDS and EELS signal using a pure element needle standard. Here the thickness of the needle can be directly measured by physically tilting the needle by 90°. Here the EDS signal was quantified using a zeta factor and the EELS signal was quantified using a partial scattering cross-section. The zeta-factor and the partial cross-section were then linked by a conversion factor for multivariate elemental analysis. However, no attempt was made at representing the zeta-factor as a scattering cross-section.

To standardise the ADF, EDS and EELS units, (MacArthur et al., 2015) proposed a wedge sample approach to convert the zeta factor into a EDS partial scattering cross-section. But determining the z-thickness for a wedge sample is difficult, and may lead to systematic errors in quantification (MacArthur et al., 2015). While a standard-less simulation matching based technique has been demonstrated for EDS signals, it is difficult to implement (Chen et al., 2016). In this technique, all parameters of the microscope must be characterised meticulously for a good agreement with theory, but even here, some discrepancies remain (Chen et al., 2016; Findlay et al., 2017). Because of the tedious nature of this technique, standard-based techniques remain popular as the microscope calibrations required are fewer and easier.

Recently, (Zanaga et al., 2016) proposed a method to quantify the EDS signal in zeta-factors using tomography and nanoparticles as a known standard. But no verification was made to check the accuracy of the quantification against established methods using wedge or needle standards. In the same year, (Craven et al., 2016) proposed a method of determining EELS partial cross-sections using experimentally measured electron mean free paths, but no comparison to EDS cross-sections was made.

Here the aim is to aim to validate and verify the accuracy of measured partial scattering cross-sections using both needle and nanoparticle standards. Not only does this increase the accuracy of the quantification, but also allows for quantification of samples where the known element standard is difficult to synthesise. For example, to quantify the Co concentration in Pt-Co nanoparticles a pure Co

standard is required. However, synthesising a pure Co nanoparticle standard is difficult due to Co readily oxidising when exposed to air. Alternatively, ion-milling a bulk material Co needle is much easier and a single atom Co partial cross-section can be measured. Thus, the accuracy between needle and nanoparticle known element standards needs to be verified.

Additionally, representing the ADF, EDS and EELS signals as partial scattering cross-sections simplifies quantification and allows for benchmarking of different microscopes. Here a benchmark is presented of the measured EDS cross-section on two JEOL ARM 200CF microscopes, one with a single EDS detector and the other with a double EDS detector.

This chapter also shows how the EDS and EELS signals can be linked through a constant when the spectroscopic signal is represented in partial scattering cross-section. Then with the measured partial cross-sections, the concentration within a sample can be quantified using independent, but simultaneously acquired, signals. As an example, an on-axis nanoparticle was atom counted using ADF and EDS cross-sections and for the first time. The validity of the two methods was verified for a ~5nm nanoparticle and future acquisition and analysis approaches are proposed utilising multiframe spectroscopy.

5.2.2 Calibration Standards and Acquisition Methods

In the method presented here, the key to measuring a spectroscopic cross-section is having a sample with varying thickness. A fraction of the scattered intensity from the sample and electron probe interaction is recorded as a function of various sample thicknesses. From this, a single atom partial scattering cross-section can be calculated (Craven et al., 2016; MacArthur et al., 2015). Here nanoparticles of varying size and atom probe needle samples were used for comparison and cross-section measurements.

The pure element Pt nanoparticles used for the partial cross-section measurement were a commercially produced oxygen reduction reaction catalyst from Johnson Matthey. The nanoparticles were supported on carbon black and have a median size range of 3.25nm. The same batch of nanoparticles were used in a previous study atom counting study, (Aarons et al., 2017), where one of the findings linked the

number of atoms in the nanoparticles to the nanoparticle diameter to demonstrate the accuracy of ADF-based atom counting. A Pt EELS partial cross-section was not measured for the Pt nanoparticles due to difficulties in obtaining sufficient signal from the available edges for small samples. Additionally, Co EELS partial cross-sections from nanoparticles were also omitted from the study due to the difficulty in synthesising pure element Co nanoparticles due to oxidation.

The carbon-supported Pt nanoparticle sample was crushed using mortar and pestle, drop-cast on a carbon grid, and mounted onto a JEOL Be double-tilt holder for the partial cross-section measurements. For the single EDS detector microscope, the holder was tilted towards the EDS detector by 20° in the +x direction. The EDS detector in this microscope is placed at right angles (on the right-hand side) with respect to the sample holder. Whereas, for the double EDS detector microscope, the holder was tilted by 15° in in the +x and +y directions, as the second detector is front placed. Nanoparticles from the centre of the copper grid were chosen for analysis to minimise shadowing. Additionally, the Be holder varied for the single and double EDS systems. For the single EDS detector microscope, the holder has a machine-thinned side for optimal X-ray collection at 20° +x tilt. Whereas, the Be holder on the double EDS detector microscope is machined even more thinly on both the front and the side for optimal X-ray collection.

As an alternative, to measuring both the Pt and Co spectroscopic EDS and EELS partial cross-sections, a needle calibration standard was prepared using a Zeiss Nvision 40 dual-beam Focused Ion Beam (FIB) instrument. The Pt and Co needle standards were prepared by electropolishing wire and then finally sharpened using FIB (Miller and Russell, 2007). The needles were mounted onto a Fischione 2050 tomography holder for the experiment. With this approach both Pt and Co cross sections can be measured with sufficient EDS and EELS signals. The maximum thickness of the needle can be measured by tilting the needle by 90°. However, to measure the entire needle surface thickness, an accurate measurement of the mean free path (λ) is required. Using a method proposed by (Craven et al., 2016) the mean free path was measured and compared to the Malis and Iakoubovskii parameterisations (Iakoubovskii et al., 2008; Malis et al., 1988).

Table 5.1 summarises the signals obtained using the two calibration standards. The spectroscopic partial cross-sections were obtained using methods described here and building upon work from (Craven et al., 2016; MacArthur et al., 2015). For Pt, the Lα, Lβ, Mα+Mβ and their total partial cross-sections were measured. Whereas for Co, the Kα, Kβ and their total partial cross-sections were measured.

The Pt EDS partial cross-section measurements between the needle and nanoparticle methods were compared for consistency. Then, atom counts from the measured Pt EDS partial cross-section were compared to an independent ADF quantification for an on-axis pure Pt nanoparticle. The ADF quantification was performed using Voronoi integration and simulation matching (Jones et al., 2014). In this approach, the intensity around an atomic column is integrated by segmenting the atomic columns into 'Voronoi' cells based on the distance between neighbouring atomic columns (Rosenauer et al., 2011). The integrated intensity from the Voronoi cell is converted into a scattering cross-section and the number of atoms in each atomic column are obtained by simulation matching. Similarly, the EDS quantification also used Voronoi integration, but the atom counts were obtained by dividing the total cross-section of a given column by the single atom Pt partial cross-section.

		Nanoparticle		*Needle*	
		Pt	Co	Pt	Co
Partial cross-section (σ)	EDS	✓		✓	✓
	EELS			✓	✓

Table 5.1 summary of the spectroscopic calibration standards and the partial cross-sections obtained.

Experimental data was acquired on a JEOL ARM 200CF microscope operated at 200kV acceleration voltage with a probe size of ~0.8-1 Å. For the EDS partial cross-section benchmark test, EDS partial cross-sections were measured using nanoparticle standards on a single, and double EDS detector system. The acquisition parameters for the different samples are listed in Table 5.2, where the probe convergence α, EELS collection angle β and ADF detector collection angles were directly measured, with 99% accuracy, using a method from (Jones et al., 2017). Additionally, ray tracing and projector lens optimisation was performed, with the help of JEOL, using a method proposed by (Craven et al., 2017). This ensures that the effect of chromatic aberrations from the electrons entering the GIF are minimised.

The probe current was calibrated using the EELS drift tube for each spot size and microscope indicated emission. For the Pt and Co needle in Table 5.2, the needle experiments were performed at various beam currents ranging from 74 – 412pA. As both microscopes in this experiment were equipped with cold field emission guns, the probe current in such systems would gradually decay during the experiment. For the microscopes used in this experiment, the current decayed by about 1% - 2% every 15 minutes. Thus, the beam current was constantly monitored by noting the indicated emission throughout the experiment day.

Sample	*Experiment probe current (pA)*	*Approximate dose ($e^-Å^2$)*	*Pixel dwell time*	*EELS collection angle β (mrad)*	*Probe convergence angle α (mrad)*	*ADF detector collection angle (mrad)*
Pt Needle	74 - 412	2.9 - 4.7 x 10^7	0.02s	37.94	22.48	40.96-90.52
Co Needle	74 - 397	2.9 - 4.5 x 10^7	0.02s	37.94	22.48	40.96-90.52
Pt off-axis NP 1 EDS detector	186	3.7 x 10^6	0.001s	N/A	22.48	50.39-242.03
Pt off-axis NP 2 EDS detectors	67	1.34 x 10^6	0.001s	N/A	22	~50-240
Pt on-axis NP	85	8.47 x 10^4	50μs	N/A	22.48	50.39-242.03

Table 5.2 summary of acquisition parameters used during the experiment. NP = nanoparticle.

5.2.3 Partial Spectroscopic Scattering Cross-section Theory

In the same way that the ADF scattering cross-section can be calculated from the image intensity (E et al., 2013; Retsky, 1974), it is possible to calculate an EDS (MacArthur et al., 2015) and EELS (Egerton, 2011; Hofer, 1991) partial scattering cross-section. The scattering cross-section has been shown to be robust to several parameters such as tilt, defocus, field of view, source size and astigmatism(E et al., 2013).

For thin samples such as nanoparticles, where absorption, fluorescence, multiple scattering and channelling (Nellist, 2011) can be neglected, the EDS partial scattering cross-section for a single atom of element x is given by (MacArthur et al., 2015):

$$\sigma_x^{EDS} = \frac{I_x e}{i\tau n_x t} \qquad (6)$$

Where n_x is the volumetric number density of the elemental species being detected, t is the sample thickness, I_x is the raw x-ray counts detected from the sample, i is the probe current, τ is the exposure time and e is the electronic charge. Here it is assumed that the sample in projection can be regarded as homogeneous on the scale of the illuminating probe. For atomic-resolution studies, an integration of

the counts over a Voronoi cell in the EDX map gives a partial cross-section for that column, by analogy with the approach for ADF cross-sections (E et al., 2013). For comparison, the popularly used ζ-factor method defined by (Watanabe et al., 2003) is:

$$\zeta_x^{EDS} = \frac{\rho t}{I_x} \times C_x D_e \qquad (7)$$

Where I_x is the raw x-ray counts, ρ is the sample density in kg/m^3, t is the sample thickness, C_x is the weight fraction of element *x*. And D_e is the total number of electrons the sample is exposed to during the experiment, expressed by equation 8.

$$D_e = i\tau/e \qquad (8)$$

In equation 7, the definition of sample density in the zeta-factor approach is in kg/m^3 which makes absolute quantification of nanoparticles, in terms of "number of atoms", cumbersome. Nonetheless, partial cross-section is very similar to the ζ-factor and can be equated to it using equation 9. Where M is the molar mass (in kg/mol) and N_A is Avogadro's constant.

$$\sigma_x^{EDS} = \frac{M}{N_A \zeta_x} \qquad (9)$$

Similarly, the EELS partial cross-section can be obtained by normalisation of the core-edge intensity by the zero-loss peak I_0, which is approximated as the total incoming electron beam. In the single scattering case, the EELS partial cross-section for element x is given by (Egerton, 2011):

$$\sigma_x^{EELS} = \frac{I_x}{I_0 n_x t} \qquad (10)$$

The first attempt at linking EDS and EELS signals was by (Kothleitner et al., 2014), where the zeta factor and the EELS cross-section were linked to their respective measured intensities as follows:

$$\sigma_x^{EELS} = \left(\frac{I_x^{EELS}}{I_0} \times \frac{i\tau e^{-1}}{I_x^{EDS}} \right) \frac{A_r}{N_A \zeta_x}$$

$$\sigma_x^{EELS} \times \zeta_x \left(\frac{N_A}{A_r} \times \frac{I_0}{i\tau e^{-1}} \right) = \frac{I_x^{EELS}}{I_x^{EDS}} \qquad (11)$$

Once again, this expression is rather cumbersome to deal with, as a number density conversion from kg/m^3 to atoms/m^3 is required. This can be simplified by representing the EDS signal in scattering cross-section notation resulting in:

$$\sigma_x^{EELS} = \left(\frac{I_x^{EELS}}{I_0} \times \frac{i\tau e^{-1}}{I_x^{EDS}} \right) \sigma_x^{EDS} \qquad (12)$$

For thin samples, if I_0 and $i\tau/e$ are represented by the same total number of electrons interacting with the sample (derived from the full beam current), I_0 and $i\tau/e$ cancel out. Thus, an obvious relationship between the scattering cross-section and the measured intensity is obtained:

$$\frac{\sigma_x^{EELS}}{\sigma_x^{EDS}} = \frac{I_x^{EELS}}{I_x^{EDS}} \qquad (13)$$

The choice of I_0 is discussed in more detail in the discussion section 5.2.9.2 of the chapter. For thin samples <10nm, equation 13 allows for an easy switch between the EDS and EELS signal intensities using a linear relationship which is a ratio of their partial scattering cross-sections.

By combining spectroscopic data in this manner, processing of multivariate datasets becomes much easier and increases data throughput when analysis several nanoparticles. In the case of bimetallic Pt-Co nanoparticles, signals can be collected simultaneously for a hybrid elemental map depending on the difficulty of processing a spectroscopic edge in either method. For example, high energy EELS edges such as the Pt M5 - M4 have low signal to background ratio, making it difficult to process. This element could alternatively be quantified using EDS, where the Pt L and M signals are easier to acquire. Whereas, the Co $L_{2,3}$ edges could be quantified using EELS because of easier acquisition and well-defined white lines.

5.2.4 Experimental Quantification Procedure

Figure 5.1 summarises the quantification procedure that was used for the needle and nanoparticle standards with the general workflow for each technique. The needle method determined the partial cross-section from the sample thickness whereas, the nanoparticle method determines the partial cross-section from the number of atoms. The key to get both methods to converge to obtain similar results is in determining the thickness and number of atoms accurately. Each processing step is discussed in more detail in the upcoming subsections.

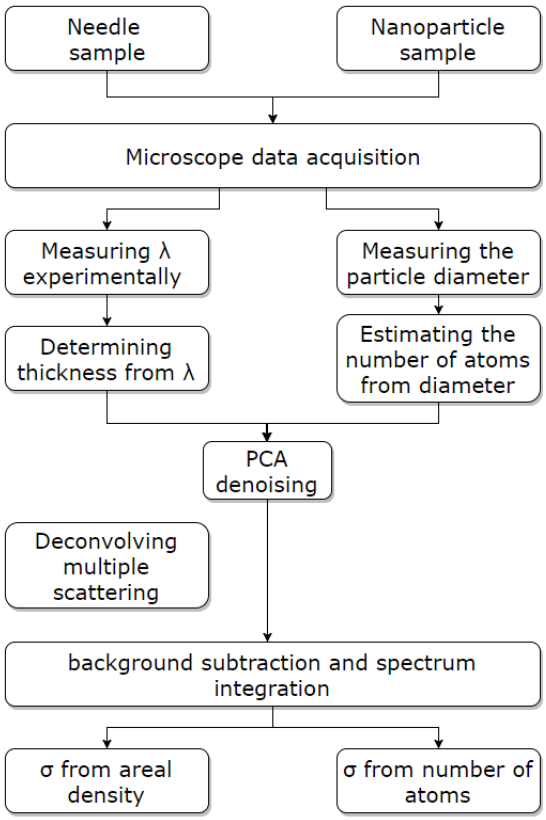

Figure 5.1 the spectroscopic data acquisition workflow for the needle and nanoparticle standards, from microscope acquisition and data analysis to partial cross-section measurements. A deconvolution step can be performed to remove the effects of multiple scattering. In the results presented in 5.2.9.1 deconvolution was not performed, the implications of this are discussed in 5.2.9.2.

5.2.5 Background Subtraction and Integration Parameters.

Table 5.3 shows the spectral integration and background-subtraction windows that were used, these windows were applied consistently throughout both the needle and nanoparticle analyses. Ensuring

consistency between the partial cross-section calculations also allowed for benchmark comparison between microscopes.

For the EDS quantification a two-window background subtraction was used. For integrating the EDS signal, the integral limits were defined conventionally as 1.2× full width half maximum of the peak. For the EELS background subtraction, an inverse power-law subtraction was used. Modelling the signal peaks and correlating the fitting coefficients to the peak integral was also considered, but this would mean that the partial cross-section obtained would be defined with a new fitting reference. Additionally, the time taken to fit a model over several spectra using the currently established algorithm in Hyperspy is computationally intensive for a large spectrum image. Future implementations within Hyperspy, such as Smart Adaptive Multi-Dimensional Fitting (SAMFire) (Ostaševičius et al., 2016), aim to rectify this.

The choice of using a narrow 30eV EELS Co integration window in Table 5.3 was determined with Pt-Co nanoparticle experimental conditions in mind, which will be explored in a future study. To sample composition variation across the nanoparticle accurately, the EELS spectra should be recorded at low enough doses without causing significant structural damage to the nanoparticle. Sometimes in this situation, a smaller integration window is more favourable due to low signal to noise (SNR) (Kothleitner and Hofer, 1998). For example, a narrow 30eV Co signal integration window provides better SNR compared to a larger integration window. The larger integration window in this instance would worsen the SNR as the post edge signal is weak.

		Background windows(keV)	***Integration windows(keV)***	***Theoretical peak /edge maxima(keV)***
EDS	**Co Kα**	6.51-6.65, 7.21-7.35	6.65-7.21	6.93
	Co Kβ	7.21-7.36, 7.94-8.09	7.40-7.86	7.65
	Pt Lα	9.08-9.15, 9.65-9.72	9.15-9.65	9.44
	Pt Lβ	10.64-10.71, 11.43-11.50	10.71-11.43	11.07
	Pt Mα + Mβ	1.77-1.85, 2.40-2.49	1.85-2.24	2.05, 2.12
EELS	**Co L3 & L2**	60eV width before peak	30eV width	779eV, 794eV
	Pt M5 -M4	150eV width before peak	300eV width	2122eV, 2202eV

Table 5.3 The integration and background subtraction windows for the EDS and EELS partial cross-sections.

5.2.6 Needle Quantification.

For the data acquisition step in Figure 5.1, an appropriate 0° tilt for the needle was determined and the spectroscopic data was recorded. Care was taken to ensure that the needle was tilted away from a major zone axis by observing the Kikuchi lines. To measure the thickness across the needle, the mean free path must be determined accurately. For further details on how this is performed, the reader should refer to the publication by (Craven et al., 2016). The advantage of this approach is that a pixel-wise thickness determination can be obtained for the sample. The following paragraph summarises this procedure for context.

A low loss Spectrum Image (SI) of the needle was recorded and the maximum t/λ was plotted as a function of axial position from a determined 0° needle tilt, Figure 5.2a. The needle was then tilted by 90° so that the maximum thickness (t) could be determined by image thresholding, Figure 5.2b. Following subsequent alignment of the 0° and 90° needle tips, the t/λ profile followed the absolute thickness profile very closely for most axial positions except at the tip due to oxidation, Figure 5.2c. Points where the t/λ was less than 1 and followed the absolute thickness profile closely were used for the λ calculation. The λ was obtained from the gradient of a linear plot of t^2 against $(t/\lambda)^{2}$. Figure 5.2d. The thickness was then determined by multiplying λ to the t/λ map.

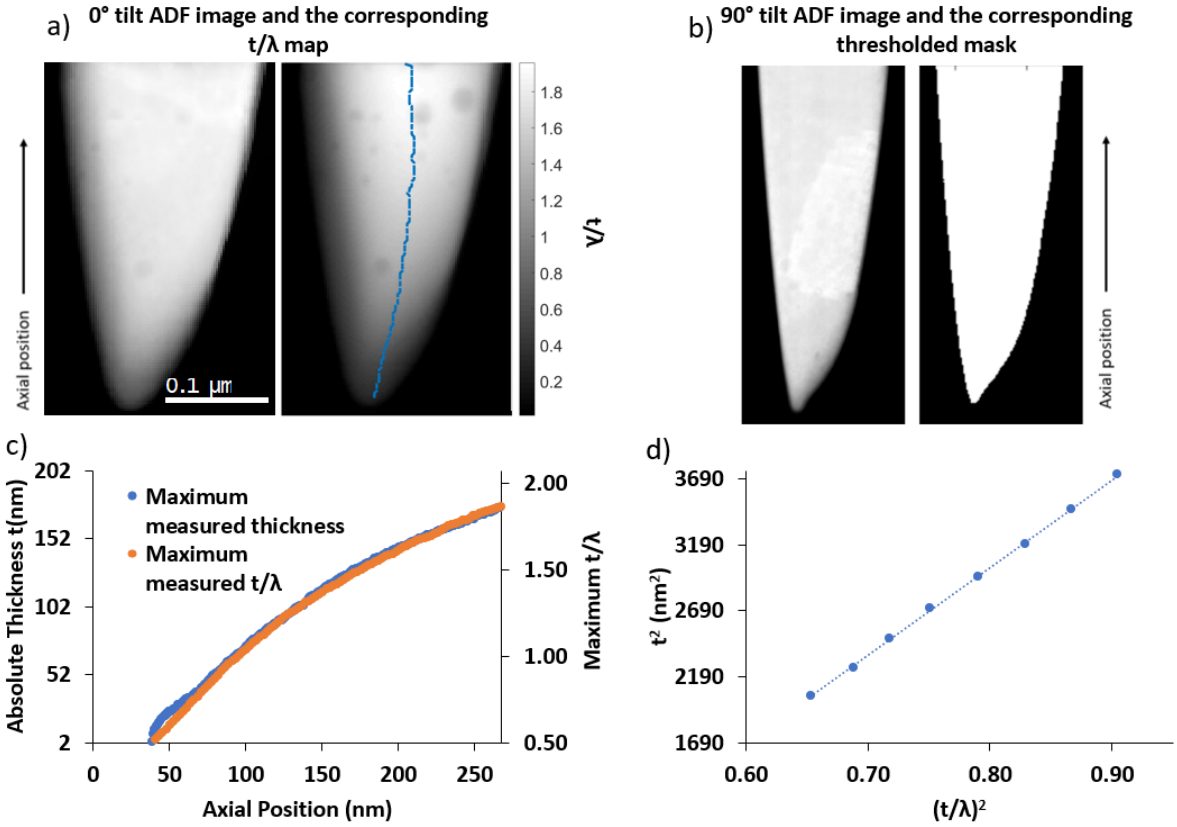

Figure 5.2 a) 0° tilt ADF image with a corresponding t/λ map, with the maximum t/λ annotated by the blue line, for a Co needle, b) 90° ADF image of the needle with a thresholded mask that was used to determine the absolute thickness of the needle, c) plot of absolute thickness against maximum t/λ for each axial position; and d) plot of t^2 against $(t/\lambda)^2$ with a linear fit from which the mean free path was measured.

The data for the spectroscopic partial cross-section measurements was recorded using a combination of spectrum images (SI) and linescans across the needle. Spectrum images were recorded with a step size of ~2nm, whereas the linescans were recorded with a ~0.5Å step size. The EELS partial cross-section was measured from the SI so that a broad range of thicknesses could be covered from the needle. The EDS partial cross-section was measured using finely sampled linescans with a ~0.5Å step size. Due to the low X-ray yield, finely sampled linescans ensured that the spectrum could be binned appropriately while sufficiently sampling the sample morphological changes across the needle as the probe scanned the specimen.

It is also possible to collect a finely sampled SI map of the needle but due to the large field of view, the file size (hundreds of gigabytes) and time (several hours) required to record this data cube is not justified. In contrast, line scans and less finely sampled SI maps have a smaller file size and require less

time to record. Acquiring spectra in this way also mitigates any afterglow effects that would affect the EELS dark reference correction and the partial cross-section measurements. Additionally, the EELS "bleed through" effect was addressed using a similar method proposed by (Bobynko et al., 2015).

The low-loss and the high-loss EELS spectra were binned, aligned and denoised using Hyperspy (de la Pena et al., 2017). Principal Component Analysis (PCA) was used for denoising and the processed spectra were checked to ensure that there were no artefacts from missing components. A comparison of the raw and denoised spectra for a selected pixel is shown in Figure 5.3. Since only the thin regions of the needle were analysed, deconvolution was not necessary. For the EDS fractionation in equation 6, the probe current was measured using the EELS drift tube and for the EELS fractionation the zero-loss peak intensity in equation 10 was scaled using a CCD linearity test. The Pt and Co number densities were calculated geometrically using lattice parameters from (Davey, 1925) and (Owen and Jones, 1954) for Pt and Co respectively. The spectroscopic partial cross-sections were then calculated using the measured beam current, ZLP, number density and the sample thickness as shown by the flow chart, Figure 5.1.

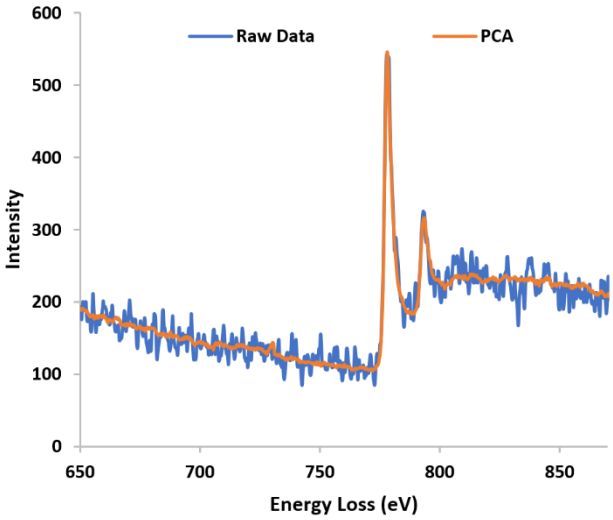

Figure 5.3 Comparison of the EELS spectra before and after PCA denoising from a ~30nm thickness region of the Co needle.

5.2.7 Nanoparticle Quantification.

For the nanoparticle partial cross-section calibration, spectrum images for the particles were taken. An area on the specimen grid containing up to 12 non-overlapping nanoparticles was selected and the SI was taken in a burst of 4 sequential frames so that particle drift could be observed (Jones et al., 2018).

To measure the nanoparticle diameter and number of atoms, the ADF image in each frame was thresholded and segmented using a watershed transform, Figure 5.4. The definition of the watershed transform is given in the appendix, chapter 8.2. The diameter of each labelled segment was estimated by equating the segment area of the nanoparticle to the area of a circle and averaged across the frames. The number of atoms for each nanoparticle was determined by estimating the diameter of the nanoparticles as a sphere with an fcc lattice. This approximation was validated in a previous study on the same nanoparticles were the number of atoms were found to increase with $\sim r^3$, with a number density pre-factor matching bulk Pt (Aarons et al., 2017). As the previous on axis study in (Aarons et al., 2017) has highlighted that most of the pure Pt particles are quasi-spherical, it is assumed that ellipticity in Figure 5.4 is due to nanoparticle tilt on the carbon support. In the case of elliptical nanoparticles "long" and "short" diameter axes would have to be defined, which would cause either an overestimation or underestimation in the number of atoms (when compared to the sphere assumption). The error associated with this would depend on the crystal structure of the nanoparticles resulting in a different cross-section measurement.

The EDS intensities within each mask were summed as the collective nanoparticle intensity and normalised by the intensity of the incident electron beam (i.e. $I_x/i\tau e^{-1}$). Then fractional intensity was multiplied by the pixel area to obtain a total nanoparticle cross-section in units of barns. From this, the single-atom partial EDS cross-section was obtained by dividing the total partial cross-section by the number of atoms in the nanoparticle. This method is analogous to the method used by (E et al., 2013) where the sum of the measured ADF intensity is multiplied by the pixel area to obtain a scattering cross-section.

Figure 5.4 (left) size selected non-channelling Pt nanoparticles used for the partial cross-section measurements, (centre) the thresholded and segmented imaged that was used to mask the EDS spectrum and (right) the raw Pt EDS signal from each nanoparticle before binning.

5.2.8 On-axis ADF and EDS Nanoparticle Quantification.

For the final test of verifying the EDS partial cross-section obtained from standards, an on-axis Pt nanoparticle was atom counted using both EDS and ADF quantification techniques. In the ADF quantification approach, data was collected using multiframe acquisition and non-rigid aligned (Jones et al., 2015). To measure the ADF collection angles accurately and precisely, a recently developed calibration technique was employed (Jones et al., 2017). The column peak intensities from the aligned data were Voronoi integrated and quantified using simulation matching (Jones et al., 2014; Rosenauer et al., 2009). The ADF image simulations were performed using the μSTEM software (Allen et al., 2014).

Similarly, the EDS signal was collected using a multi-pass approach (Jones et al., 2018), where the column peaks and Voronoi integration areas were obtained from the simultaneously acquired ADF image. The integrated EDS intensity was subsequently converted into atom counts using the single atom Pt partial cross-section calibration. Due to this, channelling was not considered and would contribute to the error by overestimating the number of atoms in the on-axis EDS quantification and is discussed later in the results section.

5.2.9 Results and Discussion

5.2.9.1 Measurement of the mean free path and the partial cross-sections.

Table 5.4 compares the measured experimental mean free path with the Malis and the Iakoubovskii parametrisations. For the convergence and collection angles used, the data shows good agreement with the Malis parameterisation, which is surprising. Analysis performed by (Craven et al., 2016) for high convergence and collection angles in modern aberration corrected STEMs also leans towards similar conclusions. This measurement shows that determining an accurate mean free path is key to obtaining an accurate partial cross-section measurement as choosing the wrong parameterisation could lead to errors of up to 20%. However, it is still not clear as to which parameterization to use universally as it has been shown to depend on the collection angle and element in question (Zhang et al., 2012).

The number density of the needles was derived by assuming a fcc structure for both elements with their respective lattice parameters from (Davey, 1925) and (Owen and Jones, 1954). However, Co is also well known to have hcp structure (Owen and Jones, 1954), this was also calculated, and the number density does not change significantly (90.28 atoms/nm^3) compared to the fcc structure shown in Table 5.4. Both Co and Pt number density values agree well with previous calculations by (MacArthur et al., 2015).

	Pt	***Co***
Density(atoms/nm^3)	66.41	90.16
Malis mean free path(nm)	59.53	81.40
Iakoubovskii mean free path(nm)	88.40	109.10
Experimental mean free path(nm)	57.57	81.55

Table 5.4 the calculated and measured mean free path parameters for both Pt and Co needles. The mean free path agrees with at least one of the calculated parameterisations.

Once the number density and the mean free path is determined accurately, the thickness per binned pixel can be plotted against a "fraction of the incident beam", i.e. $I_x/i\tau e^{-1}$ for EDS and I_x/I_0 for EELS, using equations 6 and 10 respectively, Figure 5.5. This quantity represents the fraction of the incident beam that is scattered and gives rise to the detected spectroscopic signal. By representing the detected spectroscopic signal in terms of its fraction of the incident beam, a direct comparison of the signal efficiency can be made between EELS and EDS signals.

The I_0 EELS fractionation in Figure 5.5 was performed using a zero-loss peak from the low-loss spectrum integrated over a 30eV window. The choice and errors arising from a different definition of I_0 are discussed in more detail in section 5.2.9.2. Data points from the thinner regions of the needle ~<5nm – 10nm were removed from the analysis because these regions would be dominated by oxide layers. Additionally, thicker regions of the needle which are more susceptible to errors from deconvolution and absorption effects were also removed. Only the most linear part of the dataset, from the thin regions, was used for the EELS partial cross-section measurement.

It is also possible to pick out background fitting and thickness systematic errors in Figure 5.5. The plots should extrapolate to zero (or be close to zero) fractional intensity at lower thicknesses or number of atoms. This can be seen for all the plots hence the edge intensity integration and thickness determination were processed correctly.

A systematic error from the mean free path determination would also get washed out during the subsequent composition analysis (Craven et al., 2016) if the elemental quantification is done using the same mean free path and oxide removal process. In this situation, the gradient of the plot can still be used the determine a partial scattering cross-section, with an offset. Thus, the main EELS error contribution arises from the background modelling and integration, especially for very high energy loss edges such as Pt. This is where EDS acquisition would be more favourable to quantify the Pt composition within a nanoparticle sample.

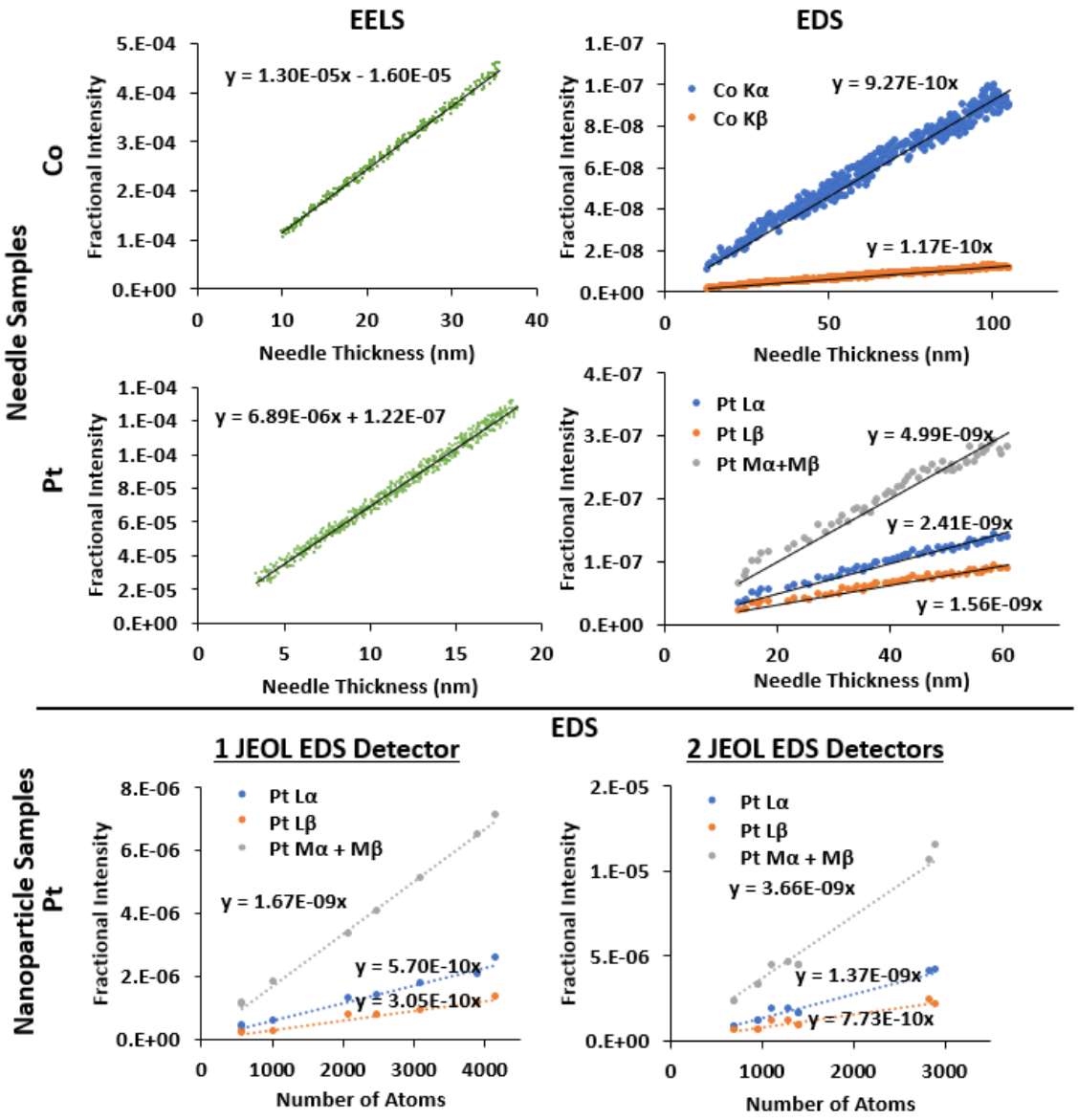

Figure 5.5 the EELS and EDS signals plotted in fractionalised intensity as a function of either the needle thickness or nanoparticle number. Normalising the spectroscopic intensity as fractional intensity allows for an easy visual comparison between the EELS and EDS signals for selected integration windows. The 'y' value in the linear fit represents fractional intensity, whereas the 'x' value represents the thickness or number of atoms. The intercept of the fit was set to zero for the EDS measurement.

5.2.9.2 Effects of multiple scattering at higher thicknesses

This section discusses the implications of choosing various definitions of the zero-loss peak to measure the EELS partial scattering cross-section to quantify nanoparticles. Most nanoparticles analysed in this thesis have a thickness range between 1nm and 10nm. At larger thicknesses the effects of multiple scattering can become significant.

There are two effects of multiple scattering that need to be considered: 1) multiple inelastic-elastic scattering causing electrons to scatter outside the GIF entrance aperture; and 2) multiple inelastic scattering which enters the GIF but scatters outside the 30eV integration windows used in the previous section. Figure 5.6 shows both these effects in action as a function of increasing thickness for a Co $L_{2,3}$ edge recorded using a ~65mrad collection angle and 30eV integration window.

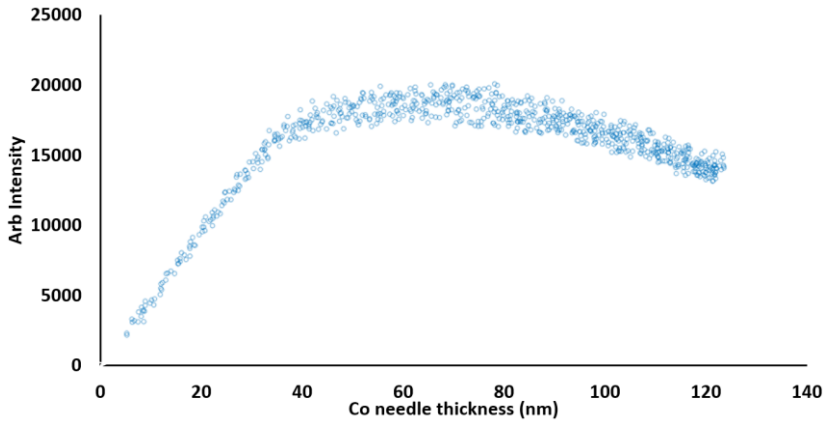

Figure 5.6 Integrated Co $L_{2,3}$ edge intensity without deconvolution (using a 30eV integration window) as a function of increasing thickness for a ~65mrad collection angle, recorded on the Harwell ARM 200CF.

A key feature in Figure 5.6 is the curvature of the plot at higher thicknesses, the cause of this is multiple scattering causing electrons to scatter outside the GIF entrance aperture. Figure 5.7 represents the multiple inelastic-elastic scattering entering the GIF for $t/\lambda = 0.5$ with increasing collection angle. To mitigate the effects of multiple inelastic-elastic scattering which falls outside the GIF entrance aperture the collection angle could be increased. For Co, increasing the collection angle above 30mrad means that more than 80% of the inelastic scattering and 60% of the elastic scattering would enter the GIF. Experimentally, this means that the core-loss intensity of a, 30eV integration window, Co $L_{2,3}$ edge will increase linearly as a function of thickness for a greater range of thicknesses. The consequence of

increasing the collection angle significantly is an increase in chromatic aberration effects distorting the peak shape. This would not have a significant effect on the integrated edge intensity for atom counting, but it would certainly affect any oxidation state measurements.

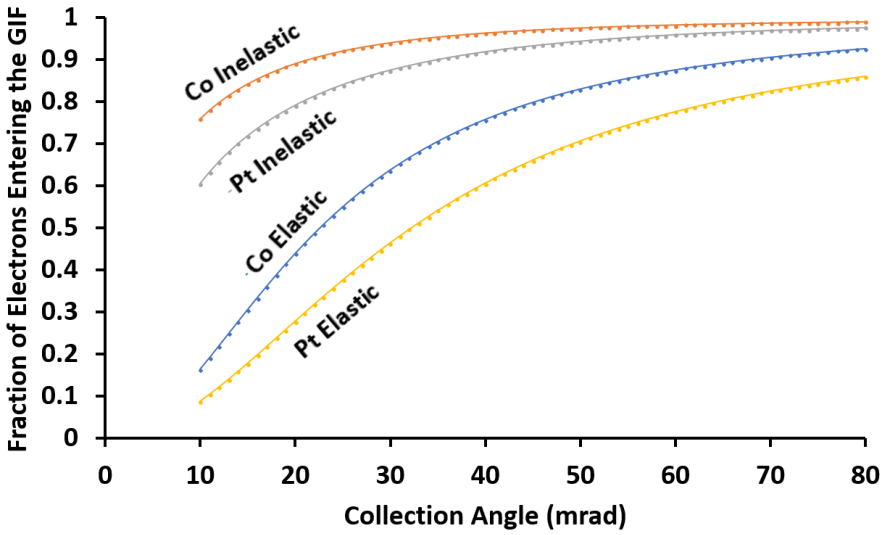

Figure 5.7 Fraction of the elastic and inelastic intensity entering the GIF for a given collection angle for Pt and Co atoms at t/λ= 0.5 (i.e. Pt thickness of ~30nm and Co thickness of ~41nm), calculated using the code from (Bergen and Egerton, 2015).

For experiments where both oxidation state measurements and accurate atom counting are desired, a restricted aperture collection angle is required. In this situation it is more favourable to use the ZLP from the low-loss spectrum for the normalisation. By using a low-loss from the same pixel location as the core-loss (recorded using dual EELS) for the I/I_0 fractionation, a partial, first order compensation for the scattering outside the aperture is obtained (Egerton, 2008). Experimentally, this means that a larger thickness range can be accessed to measure the scattering cross-section as shown by Figure 5.8 for a ~38mrad collection angle.

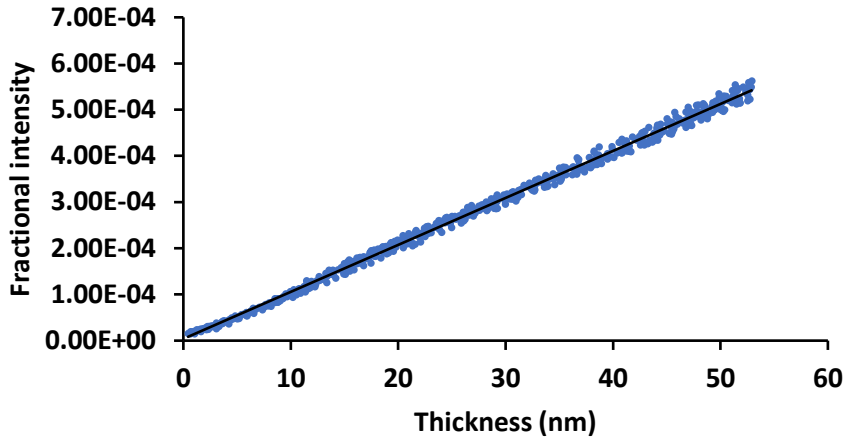

Figure 5.8 Fractional Co intensity where the Co $L_{2,3}$ edge has been normalised using an I_0 from the low-loss spectrum. By using the zero-loss from the low-loss spectrum, a greater thickness range can be accessed for linear fitting for a smaller (~38mrad) collection angle when compared to Figure 5.6.

Once scattering outside the GIF has been compensated, the effects of multiple inelastic scattering entering the GIF need to be mitigated. For thicker samples, multiple scattering would increase the intensity distribution in both the low-loss and high-loss parts of the spectra when compared to the single scattering case; i.e. an increase in intensity across the spectrum is observed in the post ZLP, plasmon, core-loss and post edge regions.

This effect can be partially mitigated by 1) increasing both the core-loss and low-loss the integration windows used for the fractionation, or 2) deconvolving the multiple scattering using Fourier-Log (FL) or Fourier-Ratio (FR) deconvolution.

Figure 5.9 shows various intensity fractionation (I/I_0) plots for a Co dataset with a ~38mrad collection angle. The orange line represents intensity fractionation using no deconvolution. The grey plot represents intensity fractionation of the high-loss that has been deconvolved using Fourier Ratio (FR) deconvolution with a ZLP from the low-loss spectrum. The blue plot shows intensity fractionation using a 30eV integration window on both the low-loss and high-loss spectra. The black plot represents intensity fractionation after splicing the low and high loss spectra; and applying Fourier-Log (FL) deconvolution. The green plot represents intensity fractionation using a ZLP recorded in vacuum.

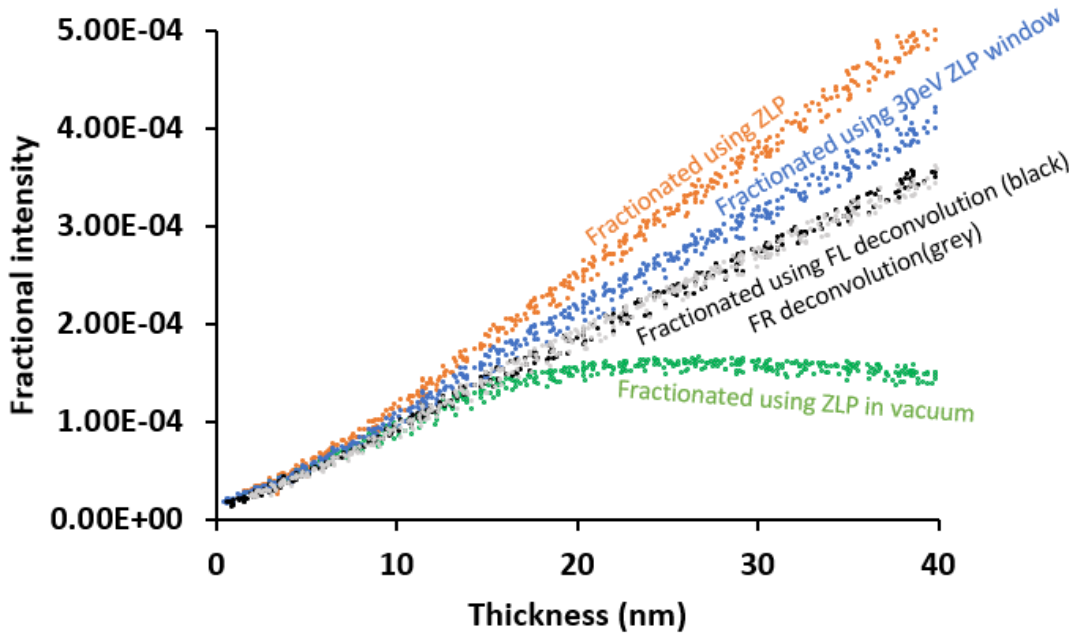

Figure 5.9 Fractional intensity (I/I_0) from a Co $L_{2,3}$ edge plotted as a function of thickness with different definitions of I_0 that can be used in equations 10 and 12.

A compensation on the inelastic multiple scattering can be partially obtained by using similar integration windows for the low-loss ZLP and core-loss Co edge. This can be seen in Figure 5.9, where the orange plot lies above the 30eV integration window method. However, as the 30eV integration method trends above the deconvolved plots, this method does not fully compensate for multiple scattering unless very large integration windows are used.

For the 30eV integration window method, complications arise if an alloy or oxide sample is being quantified as the plasmon mean free path and multiple scattering within the sample will change. The advantage of this approach is the processing is simpler compared to the deconvolution methods, which is discussed next.

From Figure 5.9 it can be seen that the ideal option is to obtain a single scattering spectrum using FR and FL deconvolution methods, where all multiple scattering effects have been deconvolved from both the low-loss and high-loss spectra. One way to obtain the single scattering fractionation plot is by splicing the low loss and high loss spectra together and applying FL deconvolution, i.e. the black line shown in Figure 5.9 using a method proposed by (Craven et al., 2016). Similarly, FR deconvolution can also be used to deconvolve multiple scattering. In this method the low-loss and high-loss spectra are taken serially or with dual EELS and then the deconvolution is performed. A closer comparison

between the FL and FR methods is shown in Figure 5.10 where both methods provide comparable results.

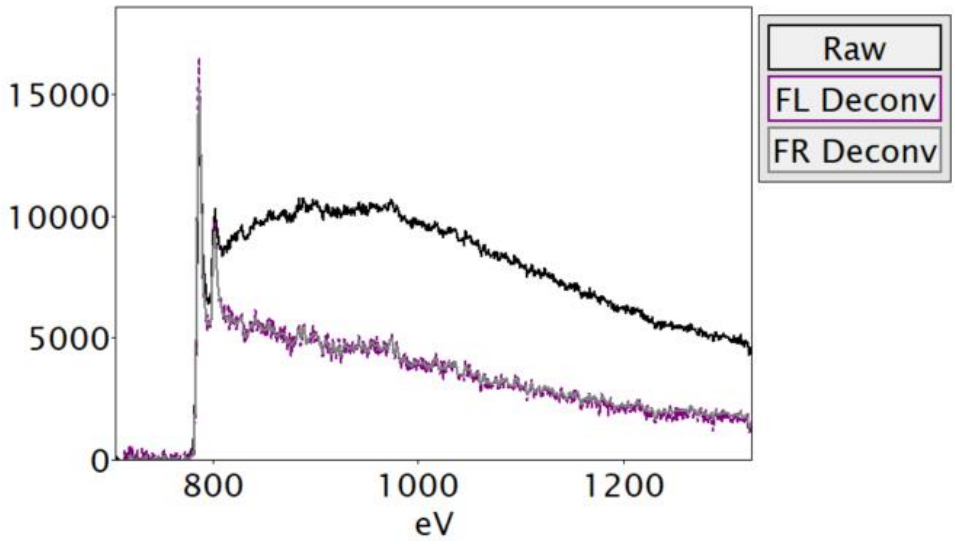

Figure 5.10 A Comparison between the raw, FR and FL deconvolved spectra. The y-axis is arbitrary intensity and the FR deconvolved spectra is shown in grey, whereas the FL deconvolved spectra is shown in purple. The spectra were taken from the same region with a ~25×25nm area and ~35nm thickness of the Co needle.

The different cross-sections obtained from the slopes of Figure 5.9 are shown in Table 5.5. From the table, FL and FR deconvolution provide the closest match to the Hydrogenic model when white-lines are incorporated within the calculation. It can also be seen that for the Co sample, a systematic error of ~11% could be present if a deconvolution is not performed to remove multiple scattering during the fractionation using the 30eV integration method (for slopes in the 10-40nm thickness range).

ZLP fractionation method	**Measured Co $L_{2,3}$ cross-section (kb)**
ZLP from low-loss (no deconvolution)	1.81
30eV ZLP integration window for low and high loss	1.43
FR deconvolution	1.28
FL deconvolution	1.28
ZLP vacuum (from linear region up to 10nm)	0.88
Calculated Co $L_{2,3}$ cross-sections using Digital Micrograph (kb)	
Hartree Slater Model	0.88
Hydrogenic Model with White-Lines	1.18

Table 5.5 Measured Co EELS cross-sections using different definitions of I_0. The first four measured cross-sections were obtained from the linear thickness range between 10nm and 40nm in Figure 5.9. The ZLP vacuum cross-section was measured from a ~0.5nm – 10nm linear thickness range.

The main drawback of the FR and FL deconvolution methods is a significant increase in processing time. With this approach, data is often collected using dual-EELS, where the EELS low-loss signal is

prone to the 'bleed-through' effect (Bobynko et al., 2015). In the bleed-through effect, the stray scattering in the GIF enhances the ZLP intensity in a non-linear manner, Figure 5.11. This can be corrected by subtracting the offset present before the ZLP, or by fitting a model over the underlying spectrum and subtracting the spectrum from this model.

Additionally, the low-loss and high-loss are corrected using the same dark reference value, acquired at the end of the SI scan. This would have an adverse effect on the intensity fractionation if the ZLP afterglow is not processed correctly. The effects of this will be pursued in the future by taking independent dark and gain refences via a "Fractional EELS" approach, discussed in more detail in section 7.8. Once both the low-loss and high-loss spectra have been recorded, they can be spliced together. The optimal splice ratio between the low-loss and the high-loss is reported to be within 20-30 (Craven et al. 2016) but the author has not tested this on the Oxford ARM, however. Additionally, the lower the splice ratio, the larger the core-loss dwell time has to be for nanoparticles (as the SNR is poor). The longer scan time means greater structural changes, thus the elemental composition distribution within the nanoparticle is no longer representative of the original state before exposure to the electron beam.

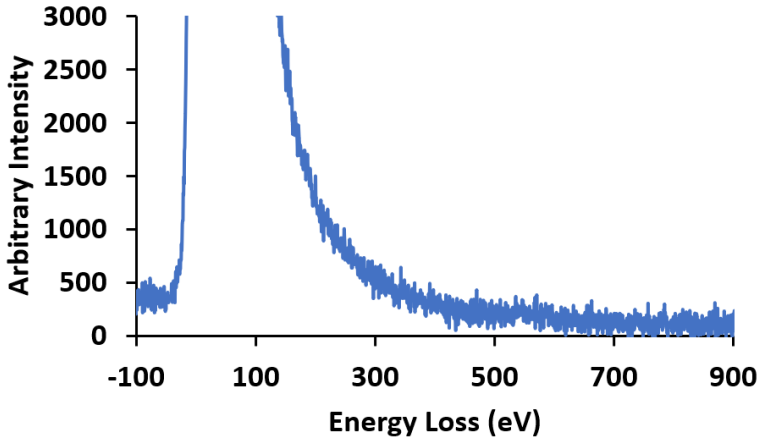

Figure 5.11 The EELS bleed-through effect on the Oxford University ARM 200CF. Enhanced intensity offset before the ZLP edge can be observed, this intensity decays in a non-linearly with increasing energy loss.

After correcting the bleed through effect, ensuring that the gain and dark reference correction is processed properly, optimising the splice ratio, and or splicing the data, the spectra can be deconvolved.

All these parameters add significant processing time to the spectra, and one of the aims of this thesis is to increase processing throughput for industry.

As most of the nanoparticles studied in this thesis were <10nm in size, a closer comparison at the smaller thickness range in shown in Figure 5.12. In this plot, the FL-deconvolved line (black) matches closely to the ZLP in vacuum line (green) up to 10nm thickness, with the slope (from 1-10nm) deviating by ~ 2%. The lines without any deconvolution start diverging as early as ~1nm thickness. The linear-fit slopes of all the methods are comparable within 10nm, however the 30eV integration window and no deconvolution plots have curvature at these thickness ranges. The slopes of 30eV ZLP normalisation method has a ~7% deviation, whereas the slope of the data where no deconvolution was performed was ~10% due to curvature in the plots.

However, as the ZLP in vacuum and FL deconvolution lines closely match at lower thicknesses, the ZLP in vacuum can provide faster processing and comparable results to the FL deconvolution method for thin samples such as Co for <10nm thickness (and ~38mrad collection angle in this case).

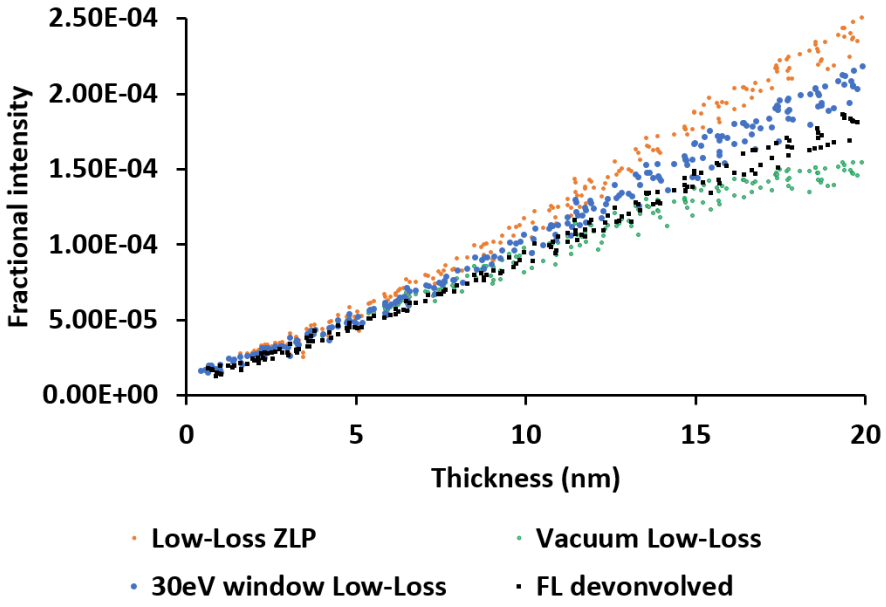

Figure 5.12 Enlarged plot of Figure 5.9 for fractional intensity as a function of thickness up to 20nm. The FR deconvolution dataset has been removed to remove clutter when comparing between the different multiple and single scattering scenarios.

The largest drawback of quantifying the Co cross-section within the <10nm thickness range for nanoparticles is the oxide layer contribution. The oxide error from the thin region is difficult to quantify

as the oxide structure of the needle and nanoparticles would have to be determined. As shown by Table 5.5 ,if a pure Co number density is assumed, the cross-section from the ZLP in vacuum from a region <10nm is ~30% less than the FL cross-section from the 10-40nm thickness region. To reduce the error on the number of Co atoms within this thickness range, a quantification of Co number density using a combination of ADF, EDS and EELS signals simultaneously would be required. Therefore, as most nanoparticles studied in the next chapter are in an oxidised state, the Co cross-section from a ZLP in vacuum was used for quantification.

If a cross-section measured using the ZLP in vacuum is used to quantify nanoparticles on a carbon support, the thickness of the carbon support will contribute to the multiple scattering as well. This can be minimised by selecting nanoparticles that are over-hanging from the support or have a very thin carbon support. The error limit for this was not investigated in this thesis. One way to check this upper limit would require investigating how the integrated core-loss intensity changes before and after deconvolution for nanoparticles surrounded by a carbon support with varying thickness. Here a plot of spectrum integrated edge intensity as a function of the mean free path with and without deconvolution would have to be plotted to obtain an error estimate. This will be investigated in the future.

5.2.9.3 A note on deconvolutions when using Hyperspy

Most of the EELS processing in this thesis was done using Hyperspy. Whilst the denoising, background subtraction and integration routines are well developed within the package, it appears that Richardson-Lucy (RL) deconvolution (Hyperspy Version 1.3.0) incorrectly processes high-loss data.

In the RL deconvolution routine, the Co white-lines intensities were enhanced significantly when compared to the raw data, Figure 5.13. Most of the intensity on either side of the white-lines was reduced significantly and added to the Co $L_{2,3}$ peaks, but the total integral of the entire spectrum was equal to the total integral of the raw data spectrum. This resulted in what appears to be an artefact that increases the linearity of the integrated Co edge for larger thicknesses, Figure 5.14.

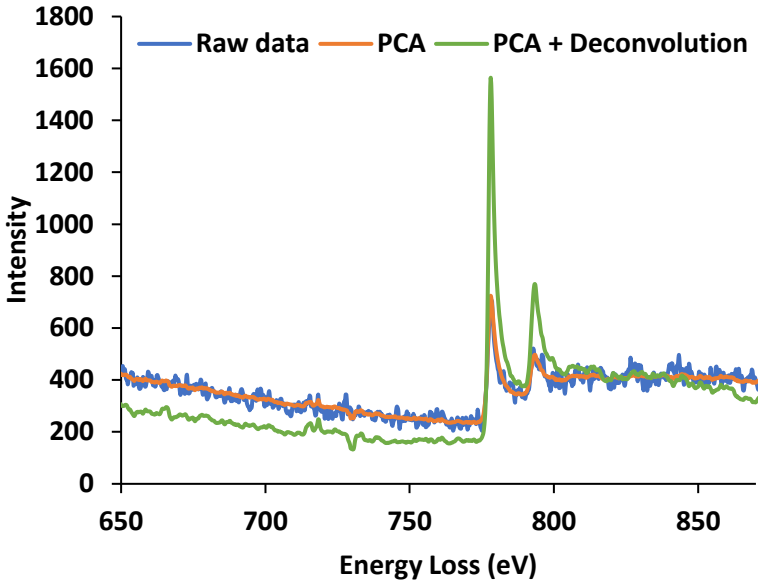

Figure 5.13 Comparison of the EELS spectra before and after PCA denoising and Richardson-Lucy deconvolution.

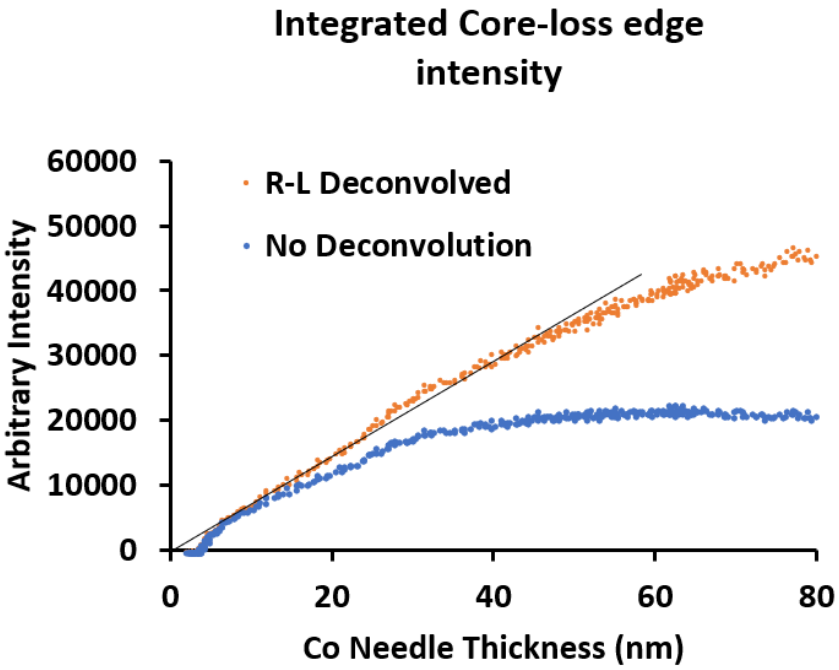

Figure 5.14 Comparison of the integrated core-loss intensity as a function of increasing thickness from a Co needle line-scan. The Richardson-Lucy deconvolution increased the integrated intensity of the Co $L_{2,3}$ edge significantly.

5.2.10 Partial Cross-section Measurements.

Finally, by using the slopes in Figure 5.5, the measured λ, and number density in Table 5.4, the needle EDS and EELS partial cross-sections were calculated. The calculated values are summarised in Table 5.6, where the needle and nanoparticle Pt EDS partial cross-sections for the L-lines agree quite well and the M lines differ by more than 30%. The discrepancy in the M-line quantification may be explained from the difficulty in the M line detection, which is more sensitive to absorption effects, which could cause significant errors in its quantification (Lábár and Salter, 1991).

Absorption effects due to the EDS signal acquisition and detector geometry were also considered, by measuring the EDS partial cross-section from the right and left halves of the needle. This seemed to have little impact on the overall M line partial cross-section. The author did not expect this to be ~30% and is not sure what the cause of this is. This discrepancy reaffirms the need to cross-check cross-sections measured using multiple standards, which are then used to quantify materials with different stoichiometries. However, the characteristic K and L lines agree well between the two samples and can be used for quantification.

As stated previously, the conversion of EDS partial cross-sections into units of barns, allows for an easier comparison with the simultaneously acquired EELS and ADF signals. For example, a direct comparison of the EDS signal shows that the EDS partial cross-section is 2 orders of magnitude smaller than the EELS and 6 orders of magnitude smaller than the collected ADF signal (typically Mb range) (Figure 5.16 and Table 5.6). For the two EDS detectors system, the Pt EDS partial cross-section is slightly more than double. The EDS partial cross-section gives a direct comparison of the efficiency between the two microscopes, which cannot be obtained from just measuring the solid angle. Here the stated nominal solid angles from JEOL would be up to 0.89Sr for a single EDS detector and 1.25Sr for a double EDS detector. It should also be noted that the microscope fitted with the double EDS detectors uses the current state of the art detector offered by JEOL and hence this comparison is not completely identical. The microscopes equipped with the double EDS system have an updated design compared to the single EDS detector system. Furthermore, as mentioned before, the Be holders between the

microscopes were different and therefore would also contribute towards the partial cross-section measurements.

When the measured EELS partial cross-sections are compared to the Hartree Slater and hydrogenic models (Leapman et al., 1980), using the quantification tool in Digital Micrograph, they show relatively good agreement with one another (i.e. the values are within the same order of magnitude). However, the aim here is not to obtain a perfect match between the measured as the HS partial cross-sections do not take into account the white-lines in the calculation. For a more thorough comparison the measured partial cross-section should be compared to a multislice (Allen et al., 2014) and DFT simulation (Tait et al., 2016).

A key point that should be noted when correlating the ADF, EDS and EELS signals is that if any of the microscope settings, such as detector placements (ADF, EDS or EELS) or post specimen optics (ADF and EELS) change drastically, the cross-sections in Table 5.6 would have to be remeasured. However, the calibration experiment is easy and software automation using Hyperspy (de la Pena et al., 2017), AtoMap (Nord et al., 2017), Absolute Integrator (Jones et al., 2014) and StatSTEM (De Backer et al., 2016) can in principle make this type of analysis routine.

EDS partial cross-sections	Pt EDS partial cross-section with a single EDS detector					
	EDS lines	Lα	Lβ	Lα + Lβ	Mα+Mβ	L + M
	Needle	5.55b	3.58b	9.13b	11.47b	20.60b
	Nanoparticles	5.69b	3.05b	8.74b	16.67b	25.41b
	Pt EDS partial cross-section with double EDS detectors					
	EDS lines	Lα	Lβ	Lα + Lβ	Mα+Mβ	L + M
	Nanoparticles	13.68b	7.73b	21.41b	36.61b	58.02b
	Co EDS partial cross-section with a single EDS detector					
	EDS lines	Kα	Kβ	Kα + Kβ		
	Needle	5.88b	0.76b	6.64b		
EELS partial cross-sections	Pt EELS partial cross-section					
	EELS edges	M5, M4 (300eV window)				
	Needle	Measured: 1.02kb		Calculated Hartree Slater:		1.26kb
				Calculated Hydrogenic:		---
	Co EELs partial cross-section					
	EELS edges	L3, L2 (30eV window)				
	Needle	Measured: 1.43kb		Calculated Hartree Slater:		0.88kb
				Calculated Hydrogenic:		0.80kb

Table 5.6 Summary of the EDS and EELS single atom partial cross-sections (in barns) obtained from the needle and nanoparticle calibration standards. The standard % errors are provided in Table 5.7 in the error analysis section.

The measured EDS cross-sections can now be used to provide a method for counting of the number of atoms in a nanoparticle as an alternative method to using ADF intensities. Although the lower cross-section will lead to lower precision, EDS does offer the potential of element specificity. Here the L + M line partial cross-sections from the nanoparticle standards were used to quantify an on-axis nanoparticle. Even though the needle and nanoparticle M lines have a discrepancy, the M line should be consistent between nanoparticles and can be exploited to increase the total x-ray count. Combining x-ray lines in this manner should be done with care, but it is necessary for thin samples to increase counting statistics.

5.2.10.1 Comparison of ADF atom counting with EDS measured cross-sections.

Finally, the nanoparticle EDS atom counts were compared to the atom counts obtained from the ADF quantification, Figure 5.15. The images in Figure 5.15 serve a dual purpose, the ADF images show the damage caused by the electron beam before and after ADF + EDS acquisition using the settings listed in Table 5.2. The column peaks are then overlaid with atom numbers from the ADF quantification on the left image and the EDS quantification on the right image. The total number of atoms between the two quantification techniques are within 10% agreement with one another. It should also be noted that the EDS quantification does not take channelling into account and is therefore expected to overestimate the number of atoms slightly (Allen et al., 2012; MacArthur et al., 2017). If channelling were considered, then the EDS partial cross-section would vary monotonically by atomic column thickness in a similar manner to the ADF cross-section, Figure 5.16.

Additionally, the edge atoms in the EDS quantification seem to have been overestimated significantly when compared to their ADF quantified counterparts. This may be attributed to the sequential multi-pass scan where the nanoparticle may have rotated and restructured over the acquisition period. The error bar on the EDS partial cross-section is also significantly higher than the ADF one. From Poisson-limited ($\sqrt{N}$) counting statistics this error can be up to ±3 atoms (MacArthur et al., 2015) for the EDS quantification plus the errors arising from a non-channelling approximation. For the EDS quantification nanoparticle in Figure 5.15, the error in each atomic column ranges between 2 and 3 atoms depending on the integrated EDS intensity per Voronoi cell. None the less, the total EDS quantification is *accurate*

within 10% for nanoparticles between 2nm and 5nm, but the atom counting *precision* on a column by column basis is quite poor as observed in Figure 5.15. To improve upon this in the future, the author aims to employ a multiframe SI acquisition routine, recently developed at the University of Oxford (Jones et al., 2018).

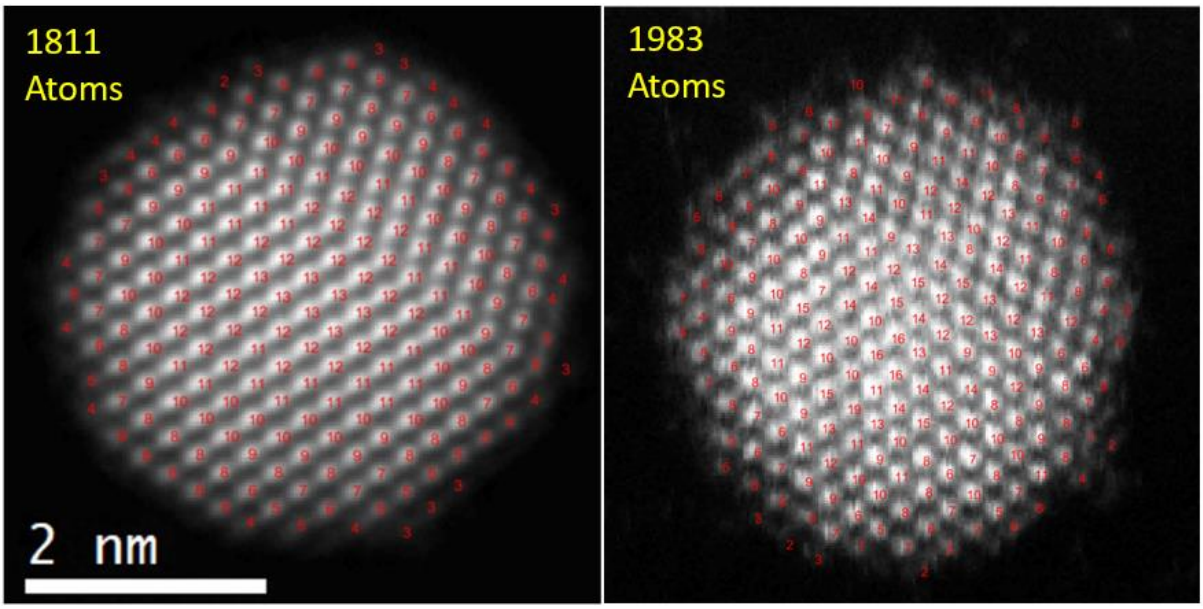

Figure 5.15 A comparison between the ADF(left) and the EDS(right) atom counts for an on-axis pure Pt nanoparticle for each atomic column, obtained from voronoi integration. The Left and right images also display the before and after effects of a SI acquisition at ~85pA beam current and a 50µs × 60 frames pixel dwell time.

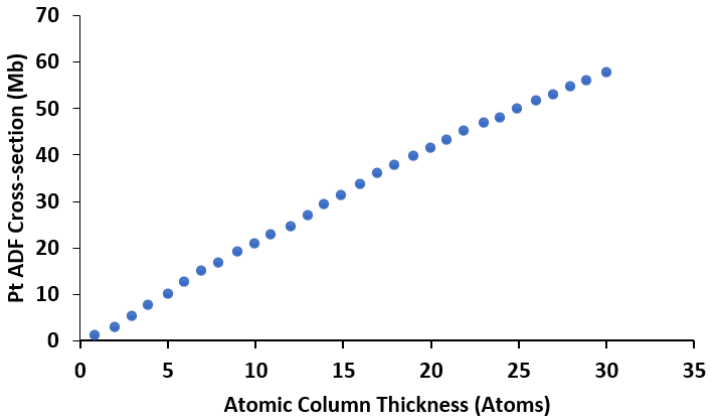

Figure 5.16 the µSTEM simulation library used to quantify the on-axis ADF nanoparticle. The scattering cross-section (in mega-barns, Mb) per atomic column varies monotonically with column thickness due to channelling.

5.2.11 Error analysis

5.2.11.1 EDS partial cross-section error propagation for a single measurement

The error analysis performed here is very similar to the ζ-factor method proposed by (Watanabe and Williams, 2006). Here the error for a function *f*, with *n* uncorrelated variables (i.e. $f = f(p_1, p_2, \ldots, p_n)$) and deviation *d* can be given as

$$d_f^2 = \sum_{j=1}^{n} \left(\frac{\partial f}{\partial p_i}\right)^2 d_{p_j}^2 \qquad 14$$

For the needle samples, in the case of the EDS partial cross-section, the major error contributors from equation 6 would be the number density (*n*), thickness (*t*) and the measured intensity (*I*). The minor errors would be attributed to: the probe current to calculate the dose, giving a relative error of ~0.5% and the pixel dwell time (τ) with a negligible contribution (MacArthur et al., 2015). Therefore, the error ($\Delta\sigma_{EDS}$) from a single EDS partial cross-section (σ_{EDS}) can be derived similarly from(Watanabe and Williams, 2006) using equations 6 and 14 as:

$$\Delta\sigma_{EDS} = \sigma_{EDS}\sqrt{\left[\left(\frac{\Delta n}{n}\right)^2 + \left(\frac{\Delta t}{t}\right)^2 + \left(\frac{\Delta I}{I}\right)^2\right]} \qquad 15$$

Where $\Delta n, \Delta t$, and ΔI, indicate errors in n, t, and I respectively. Here the error in *n* can be negligible if the analysis is performed from the bulk area of the needle to negate surface-oxide effects and the sample stoichiometry is well known. Any errors from the two-window background subtraction method would can be considered minimal compared to the terms listed in equation 10 as well due to the low background signal (Watanabe and Williams, 2006). The ΔI term can have a $\sqrt{I}$ error if the signal obeys a Poisson distribution (Thompson, 2001; Watanabe and Williams, 2006). The Δt term can be derived from the variance of several mean free path measurements.

The errors from equation 15 can be visualised by plotting their error bars and the corresponding partial cross-section as a function of thickness and nominal intensity, Figure 5.17. Both the Pt and Co errors bars decrease as the thickness of the sample increases up to a certain thickness, after which the portion of the error contribution from $\sqrt{I}$ decreases. In Figure 5.5 the EDS Pt show a slight decrease in intensity at higher thicknesses, this could imply a systematic error when determining the thickness. The contribution from such a systematic error should be small compared to the error arising from the counting statistics, as shown by Figure 5.18. In this figure, the counting statistics error shown is 1σ (~65%) of the whole intensity distribution.

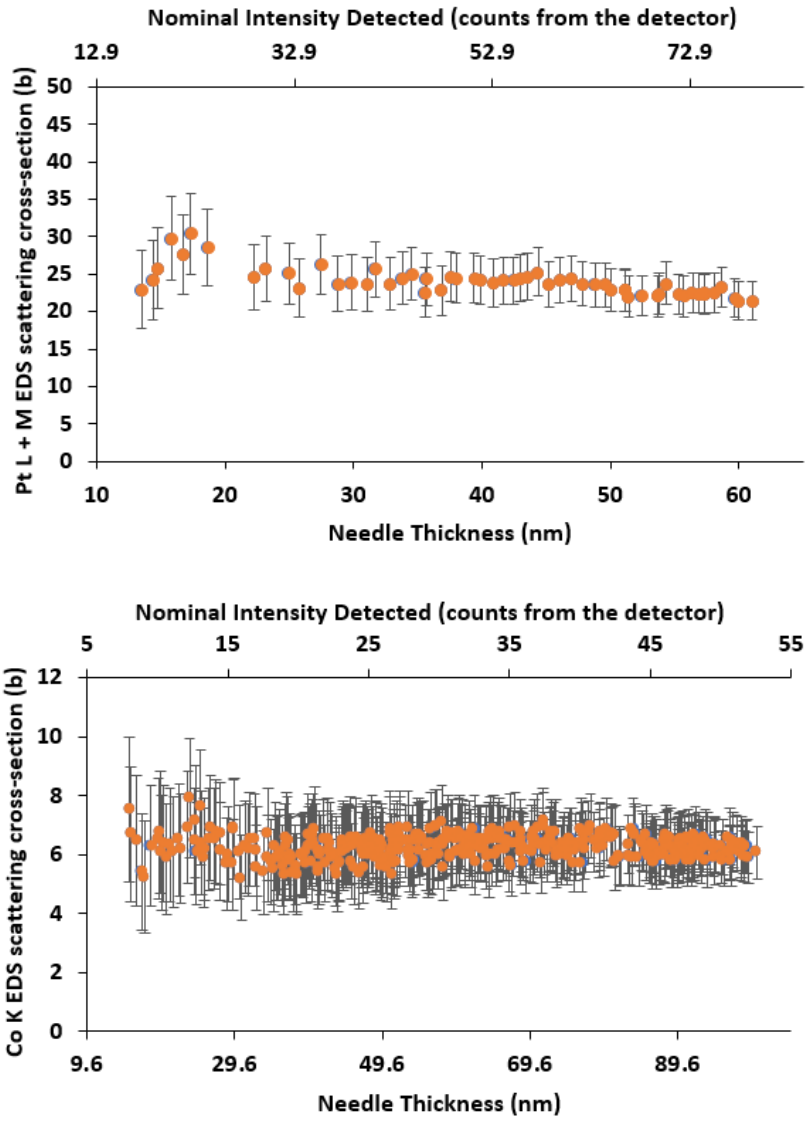

Figure 5.17 The single measurement error in the Pt and Co total EDS partial cross-sections as a function of thickness and nominal intensity (0.001s pixel dwell time, ~74pA beam current) from the line scans in Figure 5.5.

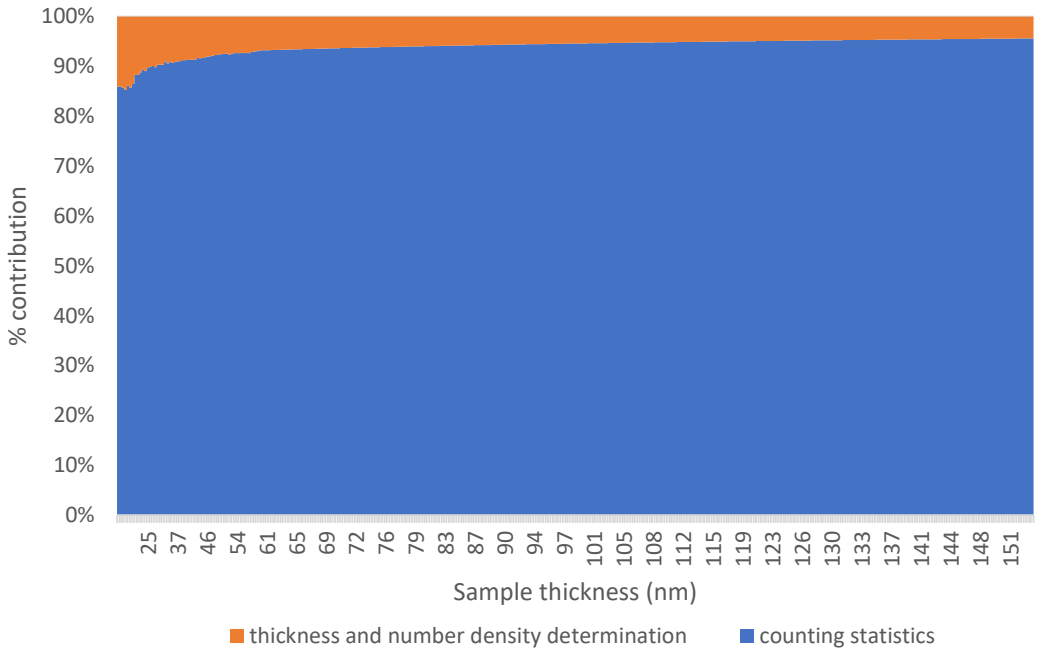

Figure 5.18 counting statistics and thickness error contribution comparison for the terms listed in equation 10 of the Pt needle. The points beyond 60nm have been extrapolated to show how the % error contribution changes at higher thicknesses.

Similarly, for the nanoparticles, the EDS partial cross-section error bars reduce with increasing number of atoms, Figure 5.19. The largest contributions to the error originate from counting statistics. After a certain nanoparticle size, >2000 atoms at the given dose, the $\sqrt{I}$ error becomes more consistent. At larger thicknesses, an increasing portion of the error is dominated by systematic errors such as the magnification calibration. The pixel area errors can vary by up to ±4% (MacArthur et al., 2015) and depends on the magnification calibration. The error in the number of atoms determined for a nanoparticle depends on the thresholding mask resulting in a ±5% deviation.

Since the dominant error propagator for nanoparticles is the counting statistics, the percentage error from this can be plotted as a function of thickness. Figure 5.20 shows this representation for a selected dose of ~74pA from the Pt and Co needle total partial cross-section measurements. The error is clearly dose dependent and therefore limited by counting statistics. However, one should take sample damage into consideration as well. A delicate balance between dose and sample damage is required to achieve enough counting statistics without altering the sample.

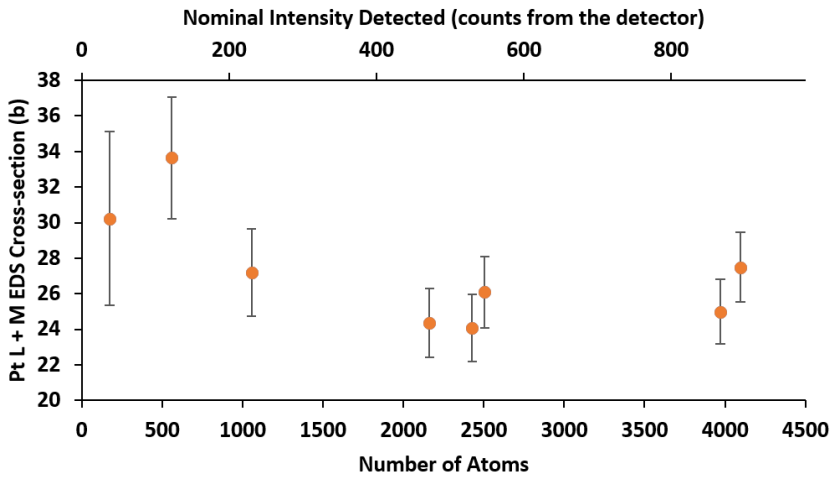

Figure 5.19, Single Pt tot EDS partial cross-section as a function of number of atoms and nominal intensity for a single EDS detector from a single acquired frame (0.001s pixel dwell time, ~186pA beam current).

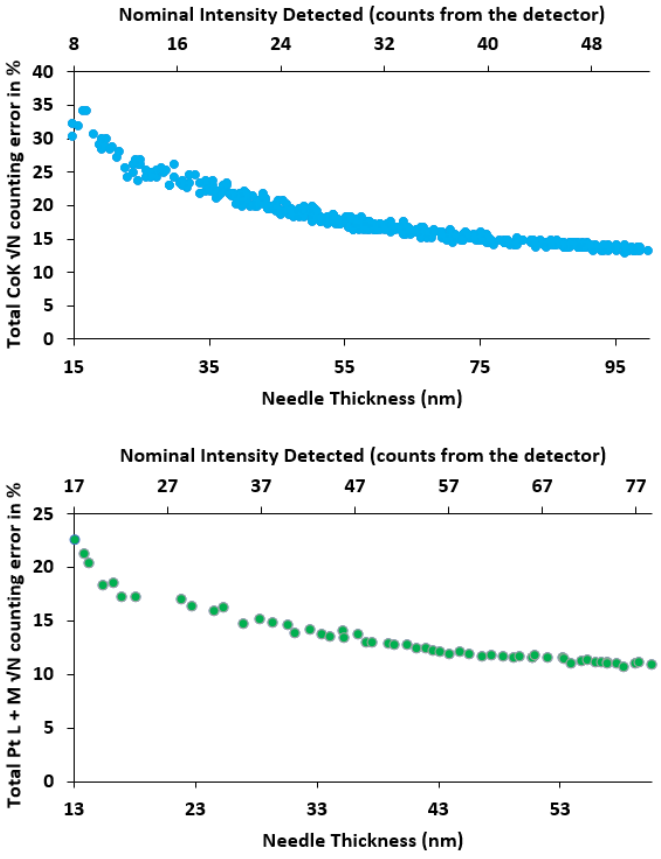

Figure 5.20 Percentage error from counting statistics for the needle samples as a function of thickness and nominal intensity.

5.3 EDS Error Propagation for Several Measurements

There are several sources of error to consider for a single scattering partial cross-section measurement. To improve the statistical accuracy, several EDS measurements need to be taken. Alternatively, as shown by the previous section, the dose could also be increased. For several measurements the error in the partial cross-section determination σ can be expressed as the standard error SE for n measurements with standard deviation s, equation 16.

$$s^2 = \sum_{j=1}^{n} \frac{(\sigma_j - \bar{\sigma})}{n-1}$$

$$SE = \frac{s}{\sqrt{n}} \qquad 16$$

The error measurements in Figure 5.17 and Figure 5.19, show that the individual error remains consistent after a certain sample thickness. This value depends on the dose of course and the largest contributor to this error is the counting statistics. However, since each error is similar, the above equation can be used to evaluate the total error in the process. If the error varies significantly with thickness for a given dose, then a weighted variance approach must be used (Galassi, 2009).

5.4 EELS Error Propagation

In the EELS partial cross-section calculation there are many possible sources of major error contributors. As the EELS signal is not dominated by counting statistics errors at the given 'nanoparticle conditions' dose here, it is not possible to provide the same treatment as the EDS error propagation. The major sources of error in EELS are systematic and the upper bounds of these can be quantified. Thickness, number density and magnification error contributions can be treated in the same manner as the EDS propagation show previously.

Error contributions from the chromatic aberration and collection angle determination are also negligible if the subsequent composition analysis is performed under the same microscope conditions. This error

is effectively minimised by optimising the post specimen optics using a method proposed by (Craven et al., 2017) and directly measuring the collection angle proposed by (Jones et al., 2017).

The error that is difficult to quantify is the CCD gain and dark reference, for this a more detailed study is required. Here independent dark and gain references should be taken and compared to the automated Gatan routines. The error from the gain reference should cancel out in the subsequent fractionation and is expected to be negligible. The error arising from the dark reference correction is much more difficult to quantify as this would depend on several acquisition parameter such as the total SI time, and experiment mode used. This will be explored in a future study using the methods proposed by (Jones et al., 2016).

Surface oxidation and contamination could also potentially contribute to the error, however, these can be effectively minimised during the data processing stage (Craven et al., 2016). The largest source of error in the EELS partial cross-section arises from modelling the EELS background and its subtraction from the SI. In this case an inverse power law background was fit before the element edge. The error arising from this could vary between 1%-10% or greater depending on the signal to noise ratio and the edge/onset windows chosen (Liu and Brown, 1987). This is difficult to generalise if one wants to quantify samples such as nanoparticles, where the signal is very low.

A straightforward approach to calculate the overall error for the EELS partial cross-section could be calculated by checking the linearity of the data and its residuals with respect to the line of best fit and its confidence intervals Figure 5.21. From the standard error of the residuals gives an error of 0.002% for Co and 0.001% for Pt. This error is mostly negligible and therefore the main contribution to the partial cross-section measurement arises from the thickness, number density and magnification.

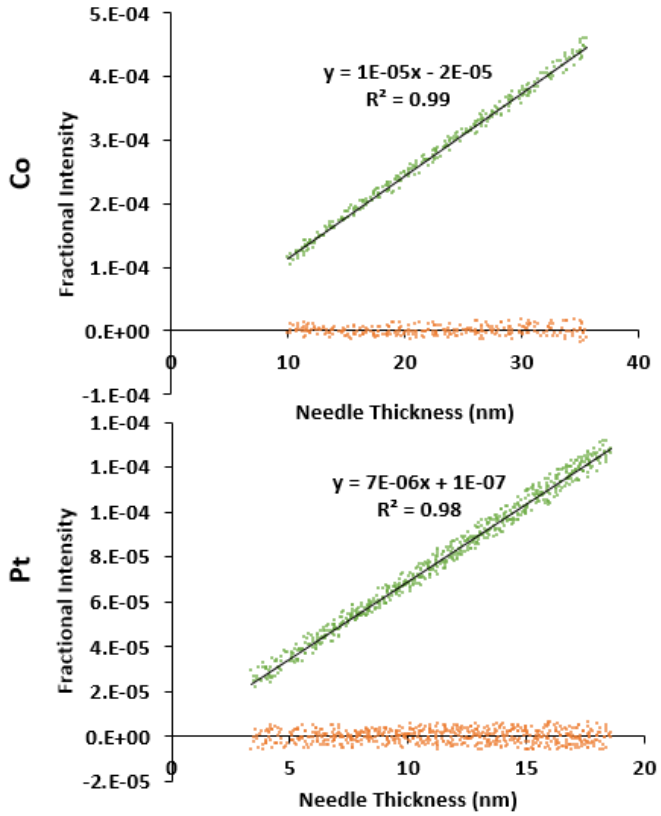

Figure 5.21 EELS fractional intensity plots from Figure 5.5 with their residuals and r-squared values. The green data points show the fractional intensity as a function of thickness, and the orange data points show the corresponding residuals. The 'y' value in the linear fit represents fractional intensity, whereas the 'x' value represents the thickness or number of atoms.

5.5 Percentage Error Summary

The standard errors for the EDS and EELS partial cross-sections are tabulated in percentage, Table 5.7. The tabulated % errors give a good illustration of how the partial cross-section measurements vary between different detectors, sample types, and different beam currents given in Table 5.2. For instance, in the single EDS detector system, the relative Pt Lα and Lβ errors for the needle samples are lower than the nanoparticles due to several measurements adding to the confidence limit of the line fit in Figure 5.5.

None-the-less the EDS nanoparticle % errors show good agreement compared to the needle samples. The nanoparticle % errors are derived from an average of counting statistics, whereas the needle errors were obtained from a standard error of linescans. However, due to absorption effects the error in characterising the Pt Mα+Mβ increases for the needle. In comparison the nanoparticle Pt Mα+Mβ errors for the nanoparticles are much lower.

EDS partial cross-sections errors	Pt EDS relative % error with a single EDS detector					
	EDS lines	Lα	Lβ	Lα + Lβ	Mα+Mβ	L + M
	Needle	3%	4%	3.4%	8%	6%
	Nanoparticles	4%	6%	5%	3%	3%
	Pt EDS relative % error with double EDS detectors					
	EDS lines	Lα	Lβ	Lα + Lβ	Mα+Mβ	L + M
	Nanoparticles	5%	19%	8%	9%	8%
	Co EDS relative % error with a single EDS detector					
	EDS lines	Kα	Kβ	Kα + Kβ		
	Needle	12%	13%	12%		
EELS partial cross-sections errors	Pt EELS relative % error					
	EELS edges	M5, M4 (300eV window)				
	Needle	Measured: 4%		Calculated Hartree Slater: ---		
				Calculated Hydrogenic: ---		
	Co EELs relative % error					
	EELS edges	L3, L2 (30eV window)				
	Needle	Measured: 3.5%		Calculated Hartree Slater: ---		
				Calculated Hydrogenic: ---		

Table 5.7, The % standard errors in the EDS and EELS partial cross-sections, taken from several cross-section measurements.

The largest contributor to the EDS error originates from the electron fluence which affects the signal to noise ratio. For the double EDS detectors, a current of ~67pA was used resulting in a higher relative error due to counting statistics, whereas the single EDS detector measurements had a probe current of ~186pA. This once again highlights the importance of balancing total sample dose against sample damage to obtain reliable quantitative measurements.

As a check on the error arising from nominal solid angle measurements listed by the microscope manufacturers, the EDS cross-section ratios were measured and compared to the relative intensity ratios. The relative x-ray intensity values were obtained from tabulated values in the X-ray data handbook by (Thompson et al., 2001). The relative intensity values are shown alongside the measured cross-sections in Table 5.8. The intensities arising from the subshells encompassing the integration windows used to measure the EDS partial cross-sections are also listed here along with the theoretical peak maxima. The M-line relative intensities are difficult to calculate and measure, and not all subshell values have been tabulated in literature yet, hence only a theoretical estimate has been stated. Due to this the measured M-line ratios were not compared to theory.

The measured EDS partial cross-sections and relative intensity values from Table 5.8 were used to calculate the x-ray line ratios, shown in Table 5.9. For comprehensiveness, a ratio comparison between the needle, nanoparticle, single and double EDS detector was made between all possible ratio measurements in tabulated matrix form in Table 5.9. The ratio comparison shows that most EDS measurements agree with the theoretical ratios and are within the relative error bounds of Table 5.7.

As the measured EDS cross-sections were used as a comparison benchmark against the manufacturer nominal solid angles in 5.2.10, the ratio comparison provides proves some insight into any errors arising from the EDS cross-section measurements. The cross-section ratios in Table 5.9 between the single EDS detector and the double EDS detector configuration are comparable within the error bounds listed in Table 5.7, ruling out any general error in the measurement (although systematic errors could still be present).

It should also be noted that the ratios can vary slightly between the measured and theoretical values due to the integration method and windows used in the experimental measurement. Additionally, oxide samples such as Co can have varied Kβ/Kα ratios ranging from 0.11 to 0.17 (Baltas et al., 2011; Labrecque and Rosales, 1990; Rani et al., 1987). Thus, the relative ratios stated in promotional EDS posters should only be used as guidance. If the cross-section ratio is taken between detectors, i.e. for Pt $^{L\alpha(2Det)}/_{L\alpha(1Det)}$, and compared to the nominal solid angle ratio $^{1.25Sr(2Det)}/_{0.89Sr(1Det)}$, the ratios

do not match. This alludes to earlier discussions in 5.2.1 and 5.2.10 of how the solid angle might not the best benchmark for EDS detector performance due to several factors such as holder geometry, TEM pole-piece gap and location of sample within the TEM grid.

Pt single EDS detector (needle measurement)				
Atomic subshells	*Integration windows (keV) used when measuring σ*	*Theoretical peak maxima (keV)*	*EDS σ (barns)*	*Relative peak intensity*
Pt Lα (1,2)	9.15-9.65	9.44	5.55	111
Pt Lβ (1,2)	10.71-11.43	11.07	3.58	90
Pt Mα + Mβ	1.85-2.24	2.05, 2.12	11.47	>100
Pt single EDS detector (nanoparticle measurement)				
Atomic subshells	*Integration windows (keV) used when measuring σ*	*Theoretical peak maxima (keV)*	*EDS σ (barns)*	*Relative peak intensity*
Pt Lα (1,2)	9.15-9.65	9.44	5.69	111
Pt Lβ (1,2)	10.71-11.43	11.07	3.05	90
Pt Mα + Mβ	1.85-2.24	2.05, 2.12	16.67	>100
Pt double EDS detector (nanoparticle measurement)				
Atomic subshells	*Integration windows (keV) used when measuring σ*	*Theoretical peak maxima (keV)*	*EDS σ (barns)*	*Relative peak intensity*
Pt Lα (1,2)	9.15-9.65	9.44	13.68	111
Pt Lβ (1,2)	10.71-11.43	11.07	7.73	90
Pt Mα + Mβ	1.85-2.24	2.05, 2.12	36.61	>100
Co single EDS detector (needle measurement)				
Atomic subshells	*Integration windows (keV) used when measuring σ*	*Theoretical peak maxima (keV)*	*EDS σ (barns)*	*Relative peak intensity*
Co Kα (1,2)	6.65-7.21	6.93	5.88	151
Co Kβ (1,3)	7.40-7.86	7.65	0.76	17

Table 5.8 Table showing Pt and Co atomic subshells included within the integration windows used for the EDS partial cross-sections in this thesis. The measured EDS cross-section and the relative peak intensities sourced from the X-ray handbook are shown alongside one another. These values were used to in the ratio comparison analysis in Table 5.9.

Pt needle measurement, single EDS detector - 0.89Sr (Theoretical ratio shown in brackets)					
	Kα	*Kβ*	*Lα*	*Lβ*	*Mα + Mβ*
Kα		*Kβ/Kα*	*Lα/Kα*	*Lβ/Kα*	*Mα + Mβ/Kα*
Kβ	*Kα/Kβ*				
Lα	*Kα/Lα*			0.65 (0.81)	6.60
Lβ	*Kα/Lβ*		1.55 (1.23)		10.23
Mα + Mβ	*Kα/Mα+Mβ*		0.15	0.10	
Pt nanoparticle measurement, single EDS detector - 0.89Sr (Theoretical ratio shown in brackets)					
	Kα	*Kβ*	*Lα*	*Lβ*	*Mα + Mβ*
Kα		*Kβ/Kα*	*Lα/Kα*	*Lβ/Kα*	*Mα + Mβ/Kα*
Kβ	*Kα/Kβ*				
Lα	*Kα/Lα*			0.54 (0.81)	2.93
Lβ	*Kα/Lβ*		1.87 (1.23)		5.47
Mα + Mβ	*Kα/Mα+Mβ*		0.34	0.18	
Pt nanoparticle measurement, double EDS detector - 1.25Sr (Theoretical ratio shown in brackets)					
	Kα	*Kβ*	*Lα*	*Lβ*	*Mα + Mβ*
Kα		*Kβ/Kα*	*Lα/Kα*	*Lβ/Kα*	*Mα + Mβ/Kα*
Kβ	*Kα/Kβ*				
Lα	*Kα/Lα*			0.57 (0.81)	2.68
Lβ	*Kα/Lβ*		1.77 (1.23)		4.47
Mα + Mβ	*Kα/Mα+Mβ*		0.37	0.21	
Co needle measurement, single EDS detector - 0.89Sr (Theoretical ratio shown in brackets)					
	Kα	*Kβ*	*Lα*	*Lβ*	*Mα + Mβ*
Kα		0.13 (0.11)	*Lα/Kα*	*Lβ/Kα*	*Mα + Mβ/Kα*
Kβ	7.74 (8.88)				
Lα	*Kα/Lα*				
Lβ	*Kα/Lβ*				
Mα + Mβ	*Kα/Mα+Mβ*				

Table 5.9 Ratio comparisons for Pt and Co for all the measured partial cross-section and relative intensity values listed in Table 5.8. The theoretical values are shown in brackets. In some cases, for oxide samples such as Co, the experimental ratio can vary between 0.11 and 0.17.

To cross-check for further errors, a comparison between the EDS partial cross-sections measured by (MacArthur et al. 2014) and (Varambhia et al. 2018) are shown in Table 5.10. The thickness was determined using the Malis mean free path parametrisation. Both measurements provide comparable results for the Oxford ARM 200CF when identical integration windows are used. This table also provides cross validation of wedge-based and needle-based calibration methods.

Pt (Lα +Lβ) σ (barns)	Pt Integration window (keV)	Co (Kα+Kβ) σ (barns)	Co Integration window (keV)	Publication
8.07	Pt Lα: 9.20-9.62 Pt Lβ: 10.66-11.64	3.90	Co Kα: 6.66-7.08 Co Kβ: 7.40-7.82	MacArthur et al. 2014
9.13	Pt Lα: 9.15-9.65 Pt Lβ: 10.71-11.43	6.64	Co Kα: 6.65-7.21 Co Kβ: 7.40-7.86	Varambhia et al, 2018
7.65	Pt Lα: 9.20-9.62 Pt Lβ: 10.66-11.64	4.40	Co Kα: 6.66-7.08 Co Kβ: 7.40-7.82	

Table 5.10 Comparison of the EDS partial cross-section measured using different integration windows and publications for the Oxford ARM 200CF. When the same integration windows are used the needle calibration by (Varambhia et al, 2018) provide similar results to the wedge-based method by (MacArthur et al, 2014)

As an additional check on the error bounds of the EDS cross-section, a weighted error estimate on the fits shown in Figure 5.5 was performed. The errors from the line fits is shown in Table 5.11, the error values are slightly larger compared to the standard errors in Table 5.7 for the needle measurements. This is due to the needle data in Figure 5.5 varying much more widely than the nanoparticle fits. If these error values are propagated onto the ratio analysis, then all of the ratios agree well with the theoretical emission ratios in Table 5.9.

EDS partial cross-sections errors						
	Pt EDS relative % error with a single EDS detector					
	EDS lines	Lα	Lβ	Lα + Lβ	Mα+Mβ	L + M
	Needle	14.5%	15.7%	14.9%	15.1%	13.6%
	Nanoparticles	5.5%	6.4%	5.6%	2.4%	2.9%
	Pt EDS relative % error with double EDS detectors					
	EDS lines	Lα	Lβ	Lα + Lβ	Mα+Mβ	L + M
	Nanoparticles	5.3%	10.6%	6.8%	4.1%	4.6%
	Co EDS relative % error with a single EDS detector					
	EDS lines	Kα	Kβ	Kα + Kβ		
	Needle	13.6%	13.5%	13.2%		

Table 5.11, The % errors for the EDS line fits in Figure 5.5. This error corresponds to a "single" cross-section measurement i.e. the value derived from the error in the slopes in Figure 5.5.

From the EDS error analysis, it is clear that the largest source of error originates from the counting statistics. Thus, in order to reduce this error, the EDS lines were summed together. This also mitigated

the damage caused to the nanoparticle during acquisition. In comparison, the EELS line fit errors were 0.002% for Co and 0.001% for Pt. For the EELS errors, the largest contributors are systematic, this includes: the determination of sample thickness, number density and magnification. The upper bounds of these errors are quoted in Table 5.7. There can also be an additional error contribution (sometimes 10%, or even more) from the modelling of the background and this error is edge dependent. Higher energy edges would be affected more compared to lower energy edges. Additionally, the signal to noise ratio would also contribute to the background model, especially for nanoparticles where the sample thickness and dose used is low.

5.5.1 Conclusions

A method of measuring and combining EDS and EELS signals using standard needle and nanoparticle standards is presented. The approach describes the intensity measured by the detector in terms of a partial scattering cross-section. These cross-sections are partial cross-sections that depend on several microscope parameters such as spectrum integration-window, detector efficiency, collection-angle and size. By representing the scattering cross-sections in 'barns' allows for an easier benchmarking between different microscopes, which is otherwise not fully realised using the solid angle benchmark.

The spectroscopic partial cross-sections from the needle and nanoparticle standards agree well and both methods could be used as calibration standards provided that the number density of the samples is determined accurately. Error analysis of the individual partial cross-section measurements shows that counting statistics could lead to an error of up to 20% when determining absolute number of atoms. This can be reduced by increasing the dose, however sample damage would also increase. A balance between dose and sample damage is required and would by useful to investigate in another study. This means that for quantifying on axis nanoparticles in the future with the current hardware the error per column count can range from 2 atoms up to 5 atoms.

When comparing the measured EELS partial cross-sections to the HS cross-sections, the agreement between the two is good. It is reassuring that the EELS cross-section calculations using Digital Micrograph provide reasonable values that can be used for quantification. The reliability of the

measured EDS partial cross-sections was verified with an independent ADF quantification. In this comparison, a pure on-axis Pt nanoparticle was atom-counted using both EDS and ADF quantification and the total number of atoms agreed well. The precision in using EDS to count the number of atoms in an individual column was very poor however due to counting statistics. The resolution and SNR can be improved further using multiframe acquisition. In the future this will most likely be the routine approach to quantify spectroscopic signals.

By unifying the ADF, EDS and EELS signals in terms of scattering partial cross-section it is possible to directly compare and switch between the different acquisition modes seamlessly. This method will pave the way for measuring number of atoms for catalyst nanoparticles by exploiting detector efficiencies to atom count bimetallic nanoparticles with high throughput in a future study.

5.6 Case Study: Quantifying Industrial Pt-Co Bi-Metallic Catalysts

5.6.1 The Nanoparticle Ensemble

To enhance and optimise catalyst performance, a secondary alloy metal is often substituted during synthesis. One such example is the Pt-Co system, where catalytic optimisation and stability is achieved by ordering the Pt and Co in such a way that the Pt covers the first 2-3 atomic layers of the nanoparticle. Compositions studied here are the Pt3Co and PtCo3 loadings, both in the "unleached" and "leached" form. Several such nanoparticles have been synthesised before and exhibit superior performance when compared to pure Pt systems (Baldizzone et al., 2015; Gai and Boyes, 2009; Hodnik et al., 2014; Khan et al., 2009; K. E. MacArthur et al., 2016).

Some of these stoichiometries, such as the Pt3Co core-shell system are known to exhibit over 200% increase in mass activity and over 300% increase in specific activity when compared to pure Pt and disordered Pt-Co alloyed systems(Wang et al., 2012). This alone provides enough justification that full three-dimensional structural characterisation is required to understand the ensemble better. For this study, the nanoparticles were grouped into subsets, shown in Figure 5.22.

Previous literature indicates that the leached systems in Figure 5.22 might exhibit the highest catalytic activity (Liu et al., 2012a; Schulenburg et al., 2009; Y. Yu et al., 2012). The activity increase is often correlated to Pt surface enrichment caused by the leaching and induced surface strain. However, most of spectroscopic and strain studies have often measured single or few nanoparticles from an ensemble (Cui et al., 2013; Gan et al., 2012; Goris et al., 2013; Li et al., 2015; MacArthur et al., 2016; Oezaslan and Strasser, 2011; Prabhudev et al., 2013; Slater, 2015; Tran et al., 2011). This means that, sometimes, the conclusions drawn from these studies may not necessarily be representative of the whole ensemble.

Thus far, such a wide-scale study has not yet been conducted and (Liu et al., 2012a) is the closest piece of work that has attempted to characterise nanoparticles ensembles spectroscopically. In (Liu et al., 2012a), PtCo3 leached nanoparticles were characterised using spectroscopy, tomography and electrochemical measurements. However, only one of the systems within the ensemble shown in Figure 5.22 were studied. The problem is complicated further by the Co oxidation state of the samples. Most

of the Co atoms in the Pt-Co nanoparticles are in an oxidised state, which makes it difficult to determine the Co composition accurately. Accurate Co-oxide composition is difficult to determine using pure standards and mapping oxidation states as a function of number of Co atoms is outside the scope of this thesis and will be looked at in the future. Thus, for the Co composition the pure element needle standard cross-section from the previous section was used, hence there is a large error bar associated with the Co measurement.

To understand the effects of strain and composition in this thesis, we focused on characterising the composition in absolute atom counts using spectroscopic and ADF scattering cross-sections. The Co needle cross-section was used for the Co composition quantification, whereas the Pt ADF cross-section was used for determining the Pt composition, this is explained in more detail in the methods section.

Then the measured compositions were linked to strain obtained from the two-dimensional on-axis ADF images. Using automation over 200 off-axis nanoparticles were spectroscopically analysed. Along with this 17 on axis nanoparticles were imaged from the ensembles for strain analysis. Fewer on-axis nanoparticles were imaged because of the lower probability of encountering on-axis nanoparticles compared to off-axis ones during the experiment. A link between peak nanoparticle surface strain and the critical surface composition required is explored and discussed. This analysis was performed for both the leached and unleached systems presented in Figure 5.22.

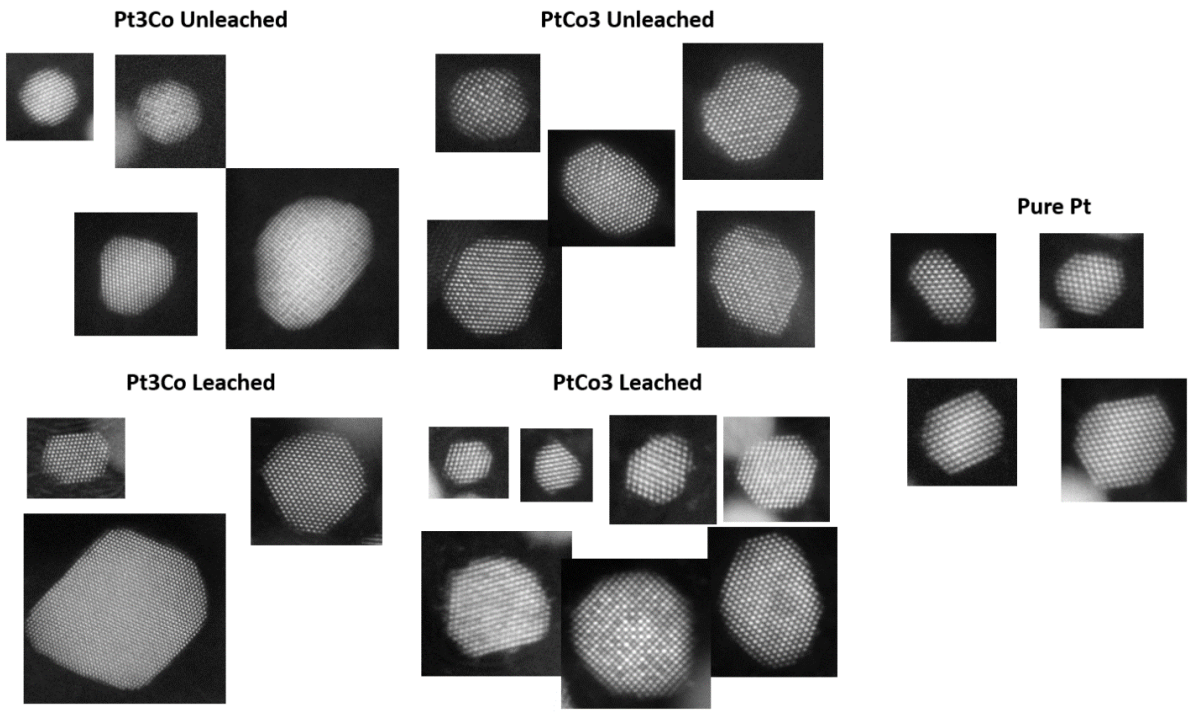

Figure 5.22 The nanoparticle sample overview, on-axis images show how the samples vary and the composition of Pt-Co alloyed nanoparticles were quantified using spectroscopic scattering cross-sections. Results from the pure Pt nanoparticles were discussed in the previous chapter.

5.6.2 Nanoparticle Synthesis

The nanoparticles were supported on carbon-black and synthesised by pre-treatment using an impregnation reduction method at different temperatures under flowing hydrogen or nitrogen gas atmosphere using a similar approach as (Wang et al., 2012). To obtain leached nanoparticles, part of the Pt-Co alloys were exposed to perchloric acid. The acid causes Co to be "leached" off the surface of the nanoparticles. Often this leaves a Pt enriched surface to obtain the "core-shell" effect, and sometimes this leaching process produces porous nanoparticles, Figure 5.23.

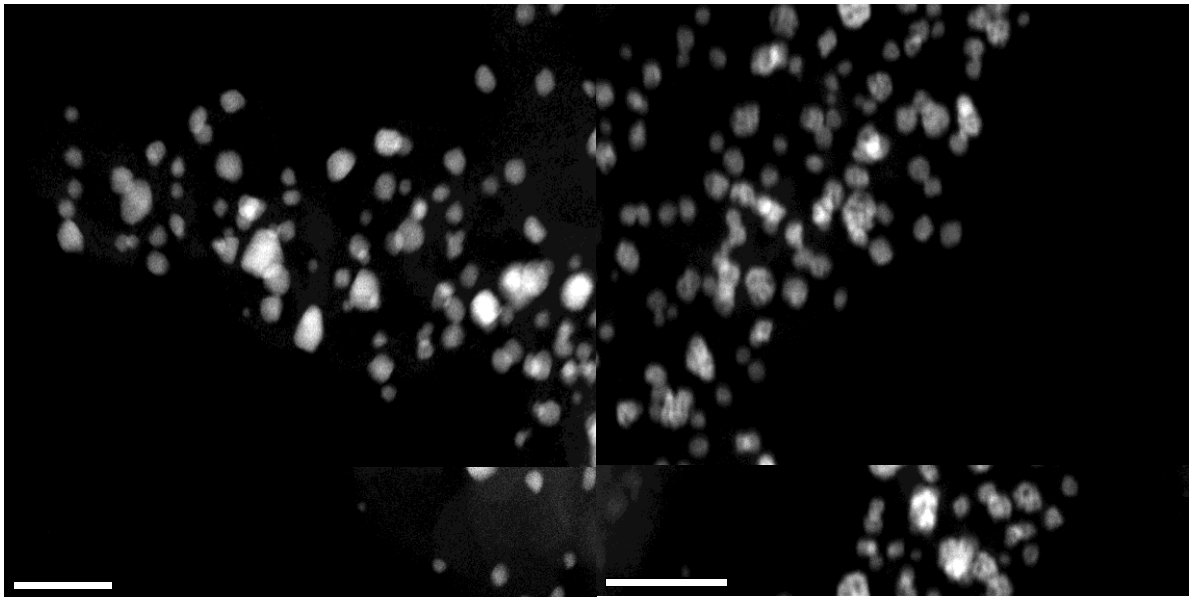

Figure 5.23 Comparison of unleached (left) and leached (right) PtCo3 nanoparticles taken at a lower magnification using a JEOL JEM 3000F microscope. The ADF images show that acid leaching causes some of the nanoparticles to be porous because most of the cobalt has been aggressively leached away from the nanoparticle.

5.6.3 Data Acquisition and Simulation Methods.

All high-resolution images and spectra were recorded on the Oxford Materials JEOL ARM200CF operated at 200kV acceleration voltage. Simultaneously structural and compositional data was recorded using the ADF detector and Gatan EELS GIF Quantum system. On this occasion the EDS detector was not in operation and data could not be recorded using this spectrometer. The ADF detector and the EELS aperture collection angles were mapped using the swung beam technique (Jones et al., 2017). The ADF detector collection angles spanned 77.43-241 mrad, whereas the EELS collection angle was 37.94 mrad. All nanoparticles were recorded using approximately 90pA beam current.

The EELS signal was recorded using a 0.25eV dispersion, and the core-loss spectra were recorded with a pixel dwell time of 0.005s, whereas, the low-loss spectra were recorded with a pixel dwell time of 10μs. The low-loss and high-loss spectra scans were recorded independently using a custom script written in digital micrograph to avoid the EELS bleed through effect (Bobynko et al., 2015). Core-loss spectra were then fractionated using the method described in section 5.2.3. This ensures that the quantification is consistent for atom counting with the measured single atom Pt and Co spectroscopic partial cross-sections from section 5.2.3. Similarly, the ADF image intensities were fractionated using a technique described in chapter 4.2.1.

For the data acquisition, nanoparticles hanging over (or close by) a vacuum region from the carbon support were chosen for analysis, Figure 5.24. This was to minimise the background from the C-edge of the support which is at ~284eV affecting the SNR of the Co L3, L2 edges at 779eV, 794eV respectively. An additional factor that was not investigated was the t/λ of the carbon support around the nanoparticles and its effect on the multiple scattering and reduction of the zero-loss peak intensity (see section, 5.2.9.2). As most nanoparticles are embedded in the carbon support the thickness of the support and its role will be investigated in a future study.

One might argue that by choosing nanoparticles this way, selection bias is introduced within the study. While this is possible, effort was made to ensure that several nanoparticles across the size range were analysed to minimise this.

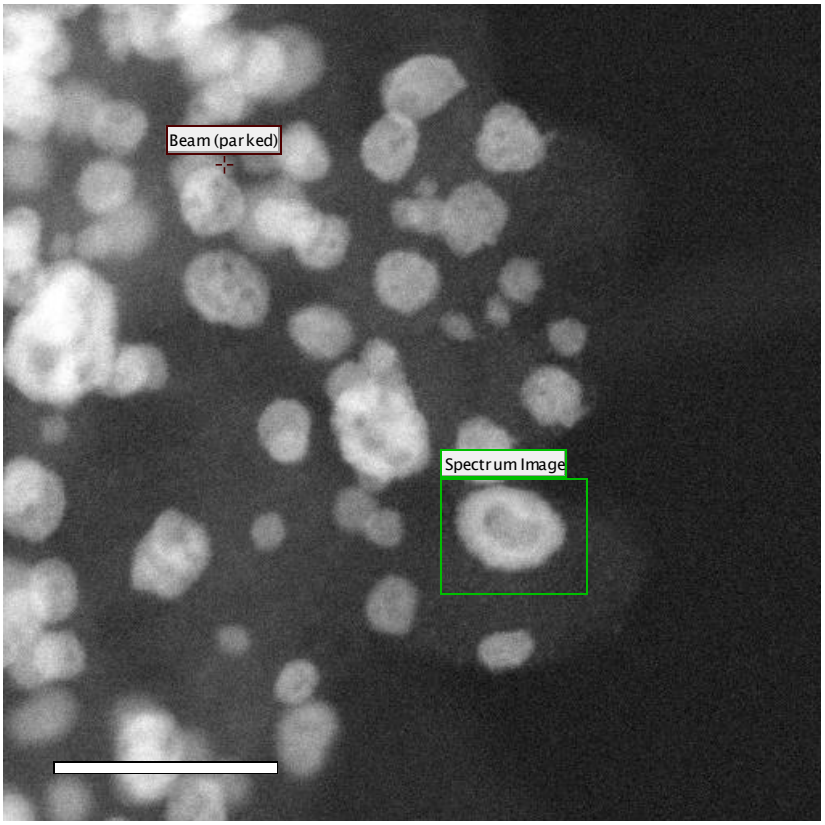

Figure 5.24 Gamma enhanced example image showing nanoparticles overhanging off the carbon support in vacuum were chosen for the spectroscopic quantification.

Due to poor Pt-EELS signal to background ratio for such small nanoparticles, the spectrometer was tuned to record only the Co signal. In principle, a Pt spectrum image can be recorded by increasing the dose. However, this would cause irreversible structural damage to the nanoparticle and change the Pt-

Co distribution. Alternatively, the ADF image contains signal from both Pt and Co atoms that can be decoupled, if the concentration of one of the elements is known.

In this method, we know that the measured experimental cross-section of the nanoparticle in an ADF image is a sum of Pt and Co cross-sections. The Co cross-section in the ADF image corresponds to the same number of Co atoms giving rise to the measured EELS cross-section in the spectrum image. Then by subtracting the ADF (Pt + Co) cross-section by a scaled EELS Co cross-section, a measured Pt cross-section image is obtained. The Co EELS to ADF scaling was obtained from a measured EELS and simulated ADF Co cross-section.

The number of Pt atoms can then be derived by dividing the measured cross-section by a single Pt atom cross-section calculated using multislice simulations. The ADF simulations for the Pt and Co atoms were performed using the same sampling, crystallographic orientation and phonon configuration listed in section 4.6.2. Quantifying in this manner is only valid for off-axis non-channelling nanoparticles, such as Figure 5.24, as stated by chapters 2.6.6 and 5.3.4 of (Egerton, 2008). The processing of the Pt and Co signals is summarised by the figure below.

The ADF image intensity can be expressed as

$$I_{ADF}^{Pt+Co} = I_{ADF}^{Pt} + I_{ADF}^{Co}$$

For thin samples and ignoring channelling we have

$$\frac{I_{ADF}^{Co}}{I_{EELS}^{Co}} = \frac{\sigma_{ADF}^{Co}}{\sigma_{EELS}^{Co}}$$

The total ADF intensity can then be expressed as

$$I_{ADF}^{Pt+Co} = I_{ADF}^{Pt} + \frac{\sigma_{ADF}^{Co} \times I_{EELS}^{Co}}{\sigma_{EELS}^{Co}}$$

Obtained from STEM simulations

Obtained from pure element standards

$$I_{ADF}^{Pt} = I_{ADF}^{Pt+Co} - \frac{\sigma_{ADF}^{Co} \times I_{EELS}^{Co}}{\sigma_{EELS}^{Co}}$$

All intensities are represented as a fraction of the incident beam/ZLP

$$I_{ADF} = \frac{I_{experiment} - I_{vacuum}}{I_{detector} - I_{vacuum}} \left(\frac{i_{detector}}{i_{experiment}} \right)$$

$$I_{EELS} = \frac{I}{I_0}$$

The sample areal density is obtained from

$$areal\ density\ Pt = \frac{I_{ADF}^{Pt} \times\ pixel\ area}{\sigma_{ADF}^{Pt}}$$

Obtained from STEM simulations

$$areal\ density\ Co = \frac{I_{EELS}^{Co} \times\ pixel\ area}{\sigma_{EELS}^{Co}}$$

Figure 5.25 Obtaining the Pt and Co areal densities using a combination of simulated ADF cross-sections and the measured Co EELS cross-section from a pure element needle standard.

In this experiment, spectra were taken for over 200 nanoparticles using this method and spectroscopically quantified. Due to the lower EELS signal collection efficiency compared to the ADF signal, a balance between sampling, beam current, dwell time and nanoparticle damage is required to increase SNR. EELS spectrum images require higher beam currents and longer dwell times; this often means that the nanoparticles suffer irreversible damage when probed. Here it was found that a sampling of less than or equal to 1Å with a dwell time of 0.005s for the Co signal was sufficient to scan nanoparticles above 3nm diameter without causing severe structural damage.

Once the spectra were recorded, a threshold mask used over the nanoparticles for core and shell analysis. From the atomic resolution images, such as Figure 5.22, a ~5Å shell outer shell mask was determined, which covers the first two atomic layers of the nanoparticle. The first two atomic layers exhibit the largest 2D lattice displacements and the mask for these was determined by eroding the threshold mask with the appropriate number of pixels to obtain information from the layers.

For the strain analysis, on-axis atomic resolution nanoparticles were chosen, as this type of analysis only requires the ADF signal. These were fewer in number due to the difficulty in finding nanoparticles along an easy to image low-order crystallographic zone; these are shown in Figure 5.22. The ADF images were recorded using multi-frame acquisition (Jones et al., 2015) with a dwell time of 4µs.

The multi-frame image stacks were non-rigidly aligned (Jones et al., 2015), and the strain analysis was performed by Dr Lewys Jones using a previously published method (Yankovich et al., 2016, 2014). In this method, the two-dimensional strain is measured by fitting two-dimensional Gaussians on the nanoparticle atomic columns, and the peak offsets are compared to a reference lattice, Figure 5.26. It is important to note that this is not the "true three-dimensional" strain of a nanoparticle, but rather a two-dimensional projection of lattice displacements from a bulk reference. None-the-less when coupled with spectroscopic analysis, the strain analysis provides insight towards linking nanoparticle strain to composition and eventually total three-dimensional structural inversion.

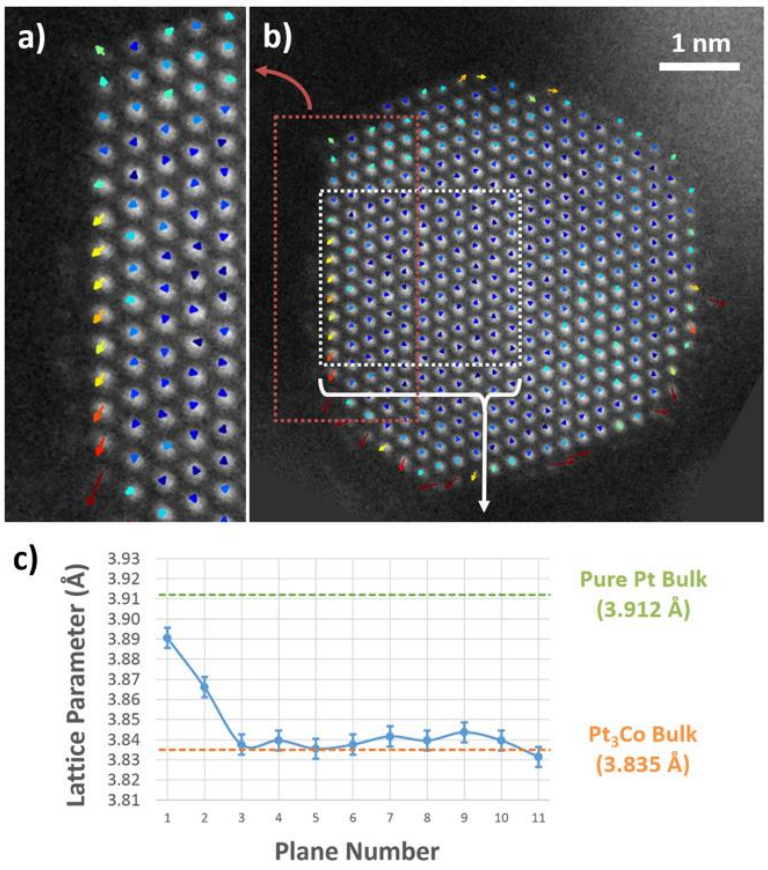

Figure 5.26 Two-dimensional strain mapping by Dr Lewys Jones. The arrow plots give a qualitative visual impression of the magnitude of the differences in the lattice displacements with respect to the bulk. Near the core of the nanoparticle, a bulk-like lattice parameter is overserved. To understand the effects in the first three lattice planes more spectroscopic analysis is required to invert the data to obtain 3D strain information. Figure provided by Dr Lewys Jones.

5.6.4 Results and Discussion

Figure 5.27 and Figure 5.28 show composite elemental maps of the nanoparticle ensembles, obtained from areal density maps which were converted to percentage composition. The Co signal was obtained from the EELS spectrum image maps, and the Pt signal was obtained from the ADF image. Pt is represented in red, whereas Co is represented in blue, and anything in between is a mixture of the two elements (shown by the colour bar).

The leached PtCo3 nanoparticles in Figure 5.27 have multiple dark blue patches within the nanoparticle core. These patches are caused by the acid leaching process, where Co is aggressively leached from the nanoparticle leaving voids, divots or pores within the nanoparticles (Liu et al., 2012b). Furthermore, the size of the Co patches are correlated to nanoparticle size. As the nanoparticle size gets smaller, the size and frequency of the dark Co patches decrease, and a more core-shell-like nanoparticle structure is observed. Additional observations of the nanoparticle show that most of the shell is Pt enriched and some nanoparticles tend to be mostly composed of Pt. This is more noticeable for the smaller nanoparticles in Figure 5.27 andFigure 5.28.

In contrast, the unleached PtCo3 nanoparticles do not exhibit the same dark Co patch-effect, Figure 5.28. The alloyed nature of the unleached nanoparticles means that the Co diffuses within the nanoparticle giving rise to several different composition morphologies, an effect often observed in precursor PtCo3 alloys (Liu et al., 2012b; Schulenburg et al., 2009; Z. Yu et al., 2012). Observations of the shell and core show a mixed distribution of Pt and Co across the nanoparticles in this case.

In the Pt3Co batch, Figure 5.28, both the leached and the unleached nanoparticles are Pt enriched. This is due to higher Pt loading during synthesis. However, the larger unleached nanoparticles show greater Co content compared to the leached nanoparticles. A common observation that can be made across both ensembles (Figure 5.27, PtCo3 leached and Figure 5.28) is that the smaller ~2.5nm nanoparticles are mostly Pt enriched. This can be attributed to a size-dependent thermodynamic limit where it is difficult to form Pt-Co alloyed nanoparticles after a certain nanoparticle size threshold. This trend could not be probed further for nanoparticles <2.5nm without inducing structural damage caused by the electron beam.

To summarise:

The leached PtCo3 nanoparticles between 4nm and 7nm tend to have a Pt-rich shell. Above 7nm most particles have ‘divots’ (Liu et al., 2012b), whereas the smaller nanoparticles below 4nm are mostly Pt rich.

The unleached PtCo3 nanoparticles between 4nm and 10nm have a Pt-rich shell, whereas, the smaller nanoparticles <4nm have some Co composition as well. These smaller nanoparticles are generally in an alloyed form.

The leached Pt3Co nanoparticles are mostly Pt rich across the entire size range, there is no indication of core-shell structure.

The unleached Pt3Co nanoparticles have more Co composition than their leached counterparts, and a few of the nanoparticles have a core-shell like structure.

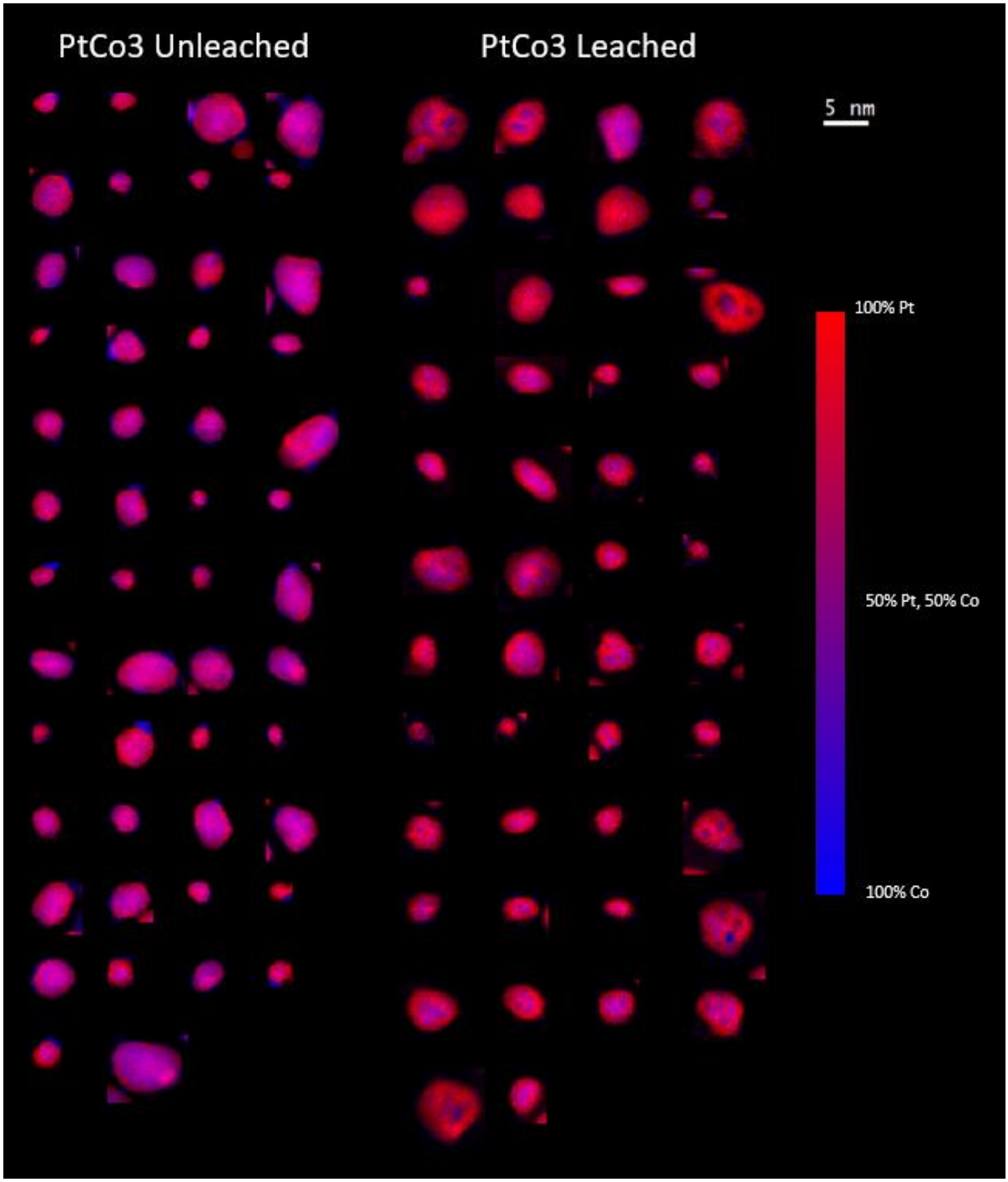

Figure 5.27 % areal density maps, for the PtCo3 ensemble, obtained from the combined ADF and EELS spectrum image data. The elemental distribution of Pt is shown in red, whereas the Co is shown in blue.

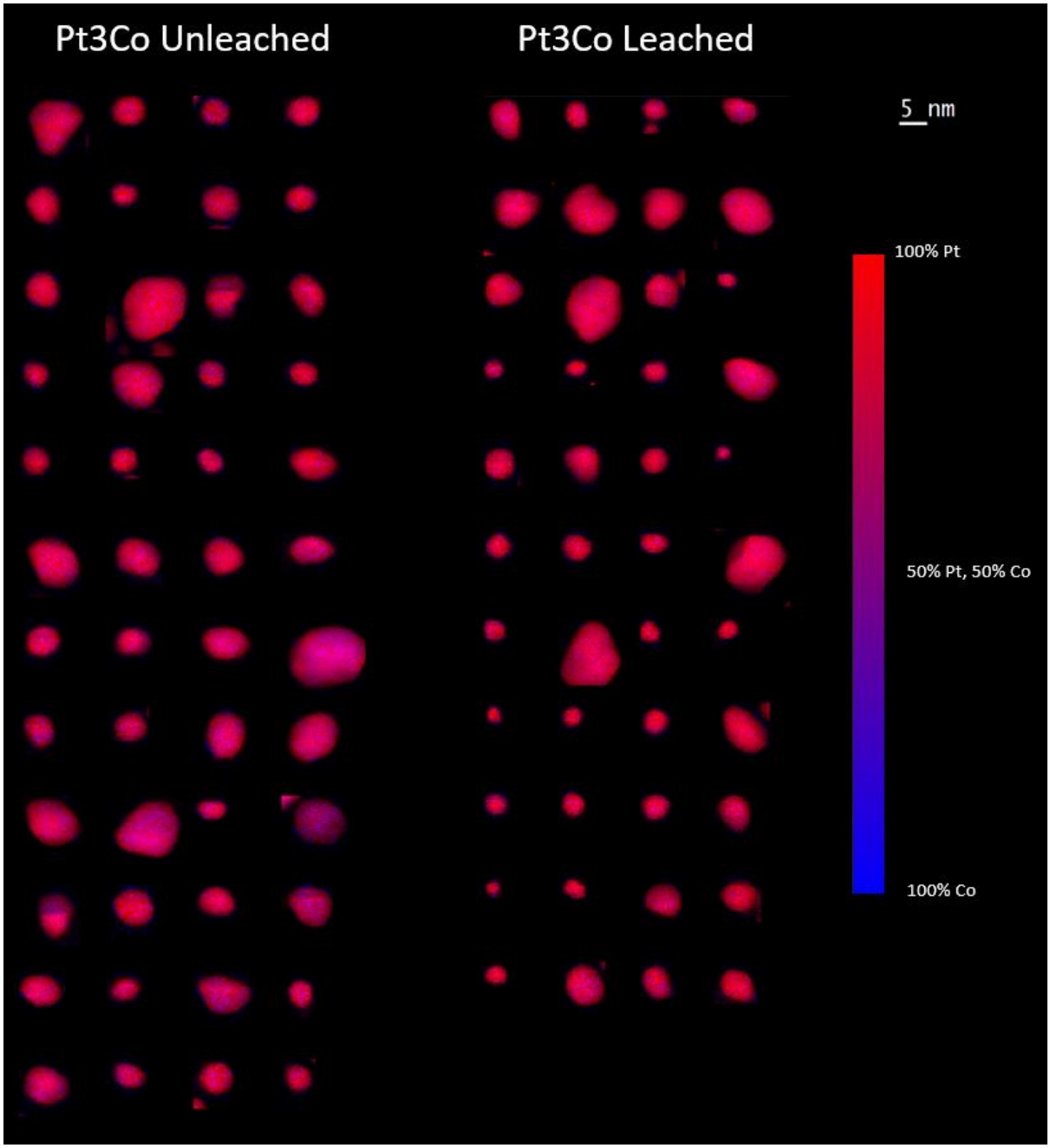

Figure 5.28 % areal density maps, for the Pt3Co ensemble, obtained from the combined ADF and EELS spectrum image data. The elemental distribution of Pt is shown in red, whereas the Co is shown in blue.

To measure core and shell elemental composition quantitatively, the nanoparticle areal density maps were thresholded with masks and plotted as a function of nanoparticle size. The shell masks were ~5Å, which corresponded to the first two atomic layers of the nanoparticle. The mask was obtained by eroding the initial thresholded mask by 2-3pixels depending on the pixel width (giving a ~5Å shell).

Particle size histograms were obtained from over 1000 nanoparticle observations for both the leached and unleached ensembles, upon which the Pt and Co atom counts were overlaid, Figure 5.29.

The nanoparticle size data is represented by the histogram and fitted with a purple line using a log-normal function. The median nanoparticle size is ~3.6nm for Pt3Co and PtCo3 leached ensembles, and ~4.5nm for the PtCo3 unleached ensemble. The average nanoparticle size is ~3.9nm for the Pt3Co leached and unleached ensemble. Whereas, the average particle size for the PtCo3 ensemble is ~3.5nm and ~4.7nm for leached and unleached nanoparticles respectively.

The scatter plots in Figure 5.29 represent the composition in number of atoms as a function of nanoparticle size. These plots have been fitted with a power-law function. The green data points show a hypothetical pure Pt nanoparticle fit as a function of diameter. This green "weighing" fit is the same as Figure 4.14 and, as expected, trends above the alloyed Pt (red) and Co (blue) curves for both ensembles within the size range. For the PtCo3 leached, Pt3Co unleached and leached nanoparticles, the Pt alloy trend is similar and always above the Co alloy curve. However, this is not the case of the PtCo3 unleached nanoparticles, where the Co trend is above the Pt alloy trend.

The total number of Pt+Co atoms for all the ensembles is shown by the black line. Here, in the unleached case the black line trends above the pure Pt line (green), this should be as expected as the unleached alloyed nanoparticles do not have a well defined structure as seen in the areal density maps (Figures 5.25 and 5.26). Whereas after leaching, the black line is closer to the pure Pt line. This is especially noticeable for nanoparticles <5nm, where most of the nanoparticles shown in the areal density maps are pure Pt.

To investigate fractional Pt-Co composition trend as a function of nanoparticle size, the number of atoms were converted into fractional composition plots Figure 5.30. Here a smoothing spline function

was used as a fit to visualise the average trend of how the Pt and Co composition varied with size. In the figure, the blue lines represent changes in Co composition, and the red lines represent changes in the Pt composition. The solid line shows the total composition of the whole nanoparticle, whereas the dashed and double-dashed lines represent the shell and core compositions respectively.

For the PtCo3 unleached sample, the Co composition increases as the nanoparticle size increases. An inversion in the dominant bulk composition can be observed at ~5.6nm nanoparticle size and onwards. This means that after a particular nanoparticle size, less than ~3nm, it is not energetically favourable for Pt to alloy with Co. Hence most of the smaller nanoparticles tend to be pure Pt. This trend can also be visually seen within the composition maps in Figure 5.27. However, in the PtCo3 leached sample, this is not the case. Here Pt enrichment is present across the whole particle size range, Figure 5.30.

In contrast, the composition fraction in Pt3Co samples, for both leached and unleached ensembles, is Pt dominant. In this case, as the nanoparticle size increases, the fraction of Co steadily increases as well. The Co composition is also higher in the unleached nanoparticles, which is expected and the nanoparticle shell is mostly Pt enriched.

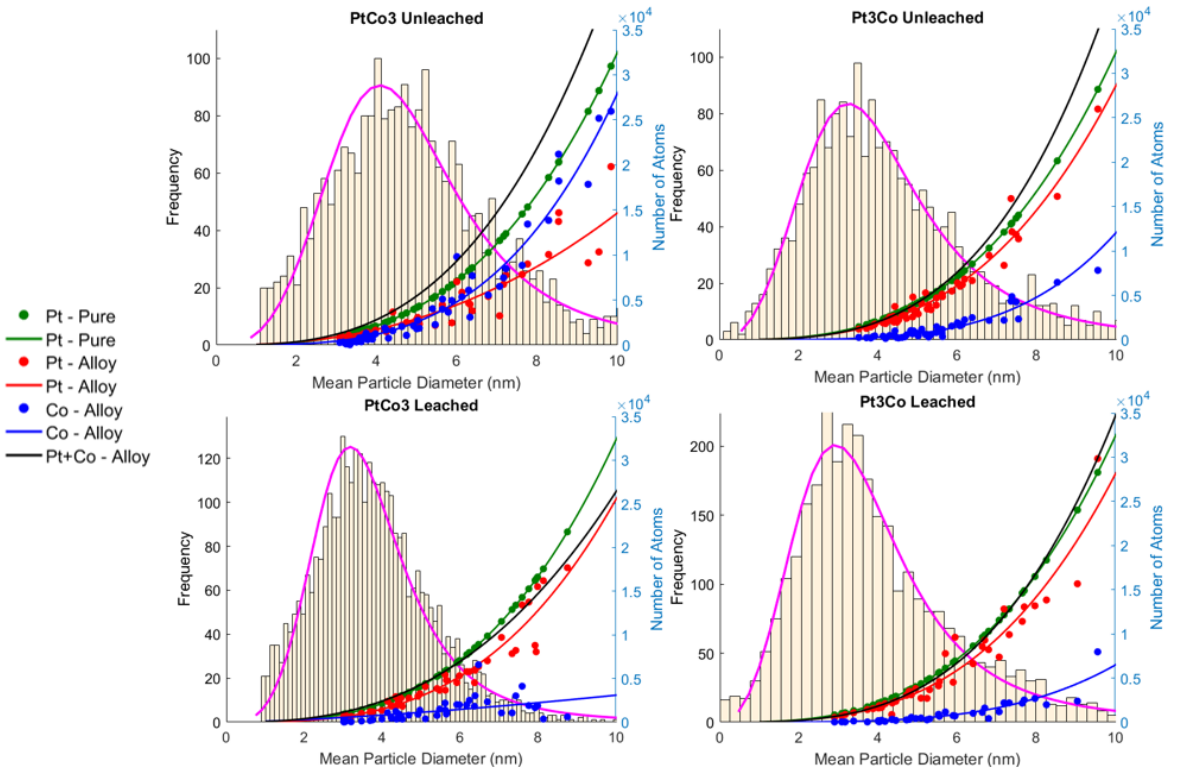

Figure 5.29 nanoparticle size distributions histograms overlaid with scatter plots of number of atoms as a function of mean particle diameter for both, unleached and leached, PtCo3 and Pt3Co ensembles.

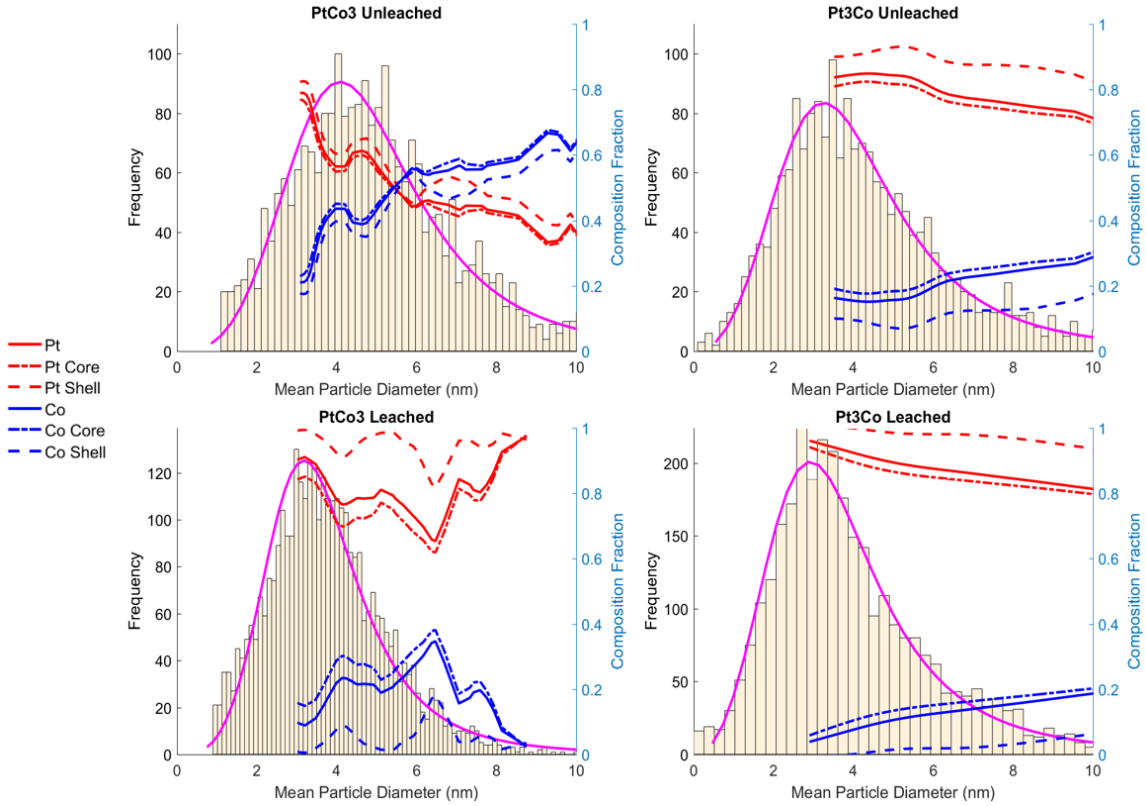

Figure 5.30 nanoparticle size distributions histograms overlaid with fractional composition plots as a function of mean particle diameter for both, unleached and leached, PtCo3 and Pt3Co ensembles.

To link composition to strain, the measured two-dimensional surface strain was plotted as a function of nanoparticle size, Figure 5.31. The surface strain is an average measurement of the first two atomic layers of an on-axis nanoparticle, such as the ones shown in Figure 5.22. There are a fewer number of data points for this plot compared to the composition plots because it is statistically rarer to observe on-axis nanoparticles during an experiment. For this experiment, one on-axis nanoparticle was observed every 2-3hrs of experiment time. Furthermore, this becomes more difficult for PtCo3 samples because the nanoparticles tend to be more disordered.

Thus, drawing decisive claims linking nanoparticle strain and composition to catalytic activity remains future work. None-the-less, trends can be drawn from the available data points. From Figure 5.31, PtCo3 leached nanoparticles peak in strain at a nanoparticle diameter of ~3.9nm. Similarly, within the same size range, the Co shell composition peaks at ~4.1nm as seen in Figure 5.30.

From literature, the PtCo3 leached nanoparticles are known to exhibit the highest catalytic activity (Liu et al., 2012; Wang et al., 2012). The increase in catalytic activity has been attributed to nanoparticle composition and strain (Oezaslan and Strasser, 2011). The hypothesis is that at a critical elemental composition fraction, the nanoparticle surface strain peaks, causing a shift in the nanoparticles electronic d-band centre (Bhattacharjee et al., 2016; Jacobsen et al., 1996) leading to better catalytic activity because of a change in surface binding energy.

Thus from Figure 5.30 and Figure 5.31, a link between the surface composition and strain can be made. Here for PtCo3 leached nanoparticles within 2nm and 5nm, the surface strain is at its highest when a nanoparticle shell is ~90% Pt and ~10% Co, with a standard error of ~6%, for a 3.9nm ± 0.2nm nanoparticle. From the hypothesis mentioned above, the 3.9nm nanoparticles should, exhibit the highest catalytic activity. However, to probe the whole nanoparticle size ranger further, more on-axis strain measurements are required for draw any decisive conclusions. Additionally, the change in the composition also affects nanoparticle stability; this remains an area to explore as well.

To probe surface strain and composition effects, atomic resolution on-axis spectroscopy and strain measurements are required. Here quantitative on-axis techniques such as ADF nanoparticle

quantification mentioned in chapter 4.5 are required for spectroscopy. The three-dimensional models from this could then be used as inputs for DFT calculations to probe the electronic properties of these catalysts. The next chapter looks at how to acquire on-axis atomic resolution ADF and spectroscopic data for nanoparticles. And the future work section (chapter 7) will discuss a proposed method on how to perform three-dimensional structural inversion of bi-metallic nanoparticles.

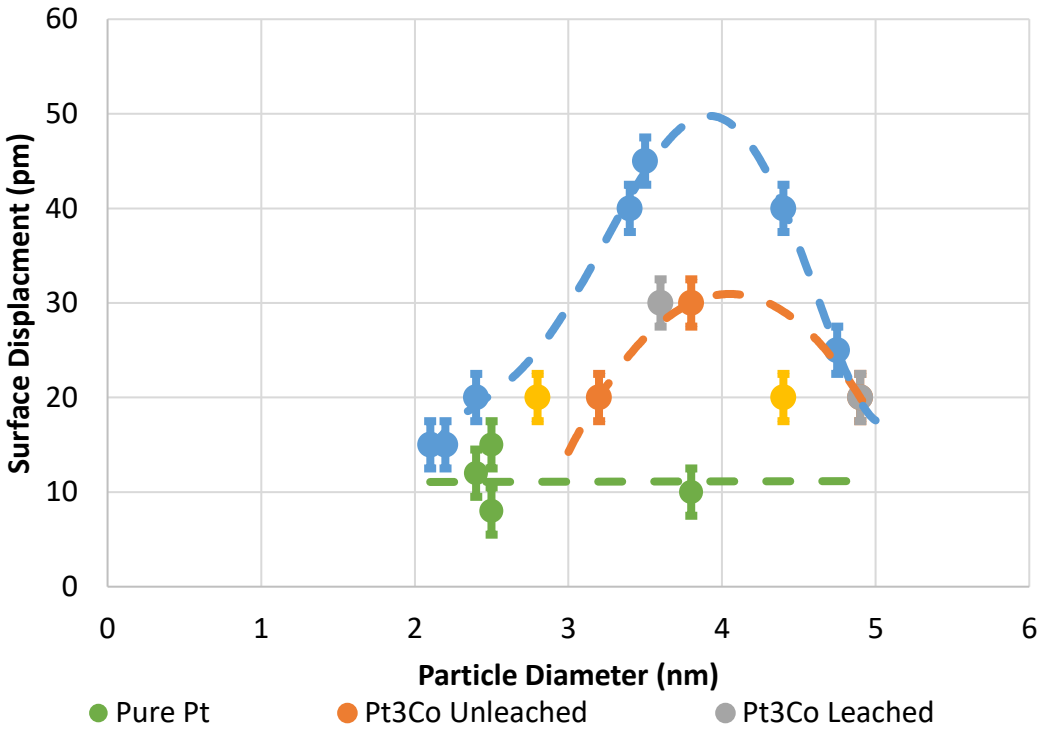

Figure 5.31 Two-dimensional strain as a function of average nanoparticle diameter.

5.6.5 Conclusions

Most nanoparticle ensemble studies, involving spectroscopy have looked at single or few particle analyses. The conclusions drawn from this might not be representative of the whole nanoparticle ensemble, and one of the few studies that has attempted to address this problem is (Liu et al., 2012). However, linking nanoparticle strain, composition and shape to catalytic activity is difficult. Here, a methodology for quantifying several bimetallic Pt3Co and PtCo3 (leached and unleached) ensembles was presented. A total of ~200 spectrum images were acquired from leached and unleached samples across a broad size range.

Alongside this, a total of 17 on-axis nanoparticles were acquired for strain analysis. On-axis nanoparticles are difficult to acquire at high throughput as observations are rare during the experiment. None-the-less there were sufficient statistics to draw trends between composition and two-dimensional strain. Core and shell masks of the nanoparticles indicate that 3.9nm PtCo3 leached nanoparticles exhibit the highest surface strain compared to the other ensembles. This could mean that 3.9nm PtCo3 leached nanoparticles exhibit the highest catalytic activity.

However, more strain observations are required to probe the entire size range to observe any conclusive trends. To link nanoparticle strain and composition to catalytic activity, a study of the particle's electronic structure is required. Here a full three-dimensional inversion of the nanoparticle is required using spectroscopy in a similar manner to ADF quantification shown in chapter 4.5. Chapter 7 discusses how data for this could be acquired at the microscope.

5.7 References

Aarons, J., Jones, L., Varambhia, A., MacArthur, K.E., Ozkaya, D., Sarwar, M., Skylaris, C.K., Nellist, P.D., 2017. Predicting the Oxygen-Binding Properties of Platinum Nanoparticle Ensembles by Combining High-Precision Electron Microscopy and Density Functional Theory. Nano Lett. 17, 4003–4012. doi:10.1021/acs.nanolett.6b04799

Allen, L.J., D'Alfonso, A.J., Freitag, B., Klenov, D.O., 2012. Chemical mapping at atomic resolution using energy-dispersive x-ray spectroscopy. MRS Bull. 37, 47–52. doi:10.1557/mrs.2011.331

Allen, L.J., D′Alfonso, A.J., Findlay, S.D., 2014. Modelling the inelastic scattering of fast electrons. Ultramicroscopy 151, 1–12. doi:10.1016/j.ultramic.2014.10.011

Baldizzone, C., Gan, L., Hodnik, N., Keeley, G.P., Kostka, A., Heggen, M., Strasser, P., Mayrhofer, K.J.J., 2015. Stability of Dealloyed Porous Pt/Ni Nanoparticles. ACS Catal. 5, 5000–5007. doi:10.1021/acscatal.5b01151

Baltas, H., Ertugral, B., Kantar, C., Sasmaz, S., Yılmaz, E., 2011. K β / K α X-Ray Intensity Ratios for Co , Ni , Cu , and Zn in Phthalocyanines Complexes 119, 764–768.

Bhattacharjee, S., Waghmare, U. V., Lee, S.-C., 2016. An improved d-band model of the catalytic activity of magnetic transition metal surfaces. Sci. Rep. 6, 35916. doi:10.1038/srep35916

Bobynko, J., MacLaren, I., Craven, A.J., 2015. Spectrum imaging of complex nanostructures using DualEELS: I. digital extraction replicas. Ultramicroscopy 149, 9–20. doi:10.1016/j.ultramic.2014.10.014

Chen, Z., Weyland, M., Sang, X., Xu, W., Dycus, J.H., LeBeau, J.M., D'Alfonso, A.J., Allen, L.J., Findlay, S.D., 2016. Quantitative atomic resolution elemental mapping via absolute-scale energy dispersive X-ray spectroscopy. Ultramicroscopy 168, 7–16. doi:10.1016/j.ultramic.2016.05.008

Cliff, G., Lorimer, G.W., 1975. The quantitative analysis of thin specimens. J. Microsc. 103, 203–207. doi:10.1111/j.1365-2818.1975.tb03895.x

Craven, A.J., Bobynko, J., Sala, B., MacLaren, I., 2016. Accurate measurement of absolute experimental inelastic mean free paths and EELS differential cross-sections. Ultramicroscopy 170, 113–127. doi:10.1016/j.ultramic.2016.08.012

Cui, C., Gan, L., Heggen, M., Rudi, S., Strasser, P., 2013. Compositional segregation in shaped Pt alloy nanoparticles and their structural behaviour during electrocatalysis. Nat. Mater. 12, 765–71. doi:10.1038/nmat3668

Davey, W.P., 1925. Precision Measurements of the Lattice Constants of Twelve Common Metals. Phys. Rev. 25, 753–761. doi:10.1103/PhysRev.25.753

De Backer, A., Martinez, G.T., Rosenauer, A., Van Aert, S., 2013. Atom counting in HAADF STEM using a statistical model-based approach: Methodology, possibilities, and inherent limitations. Ultramicroscopy 134, 23–33. doi:10.1016/j.ultramic.2013.05.003

De wael, A., De Backer, A., Jones, L., Nellist, P.D., Van Aert, S., 2017. Hybrid statistics-simulations based method for atom-counting from ADF STEM images. Ultramicroscopy 177, 69–77. doi:10.1016/j.ultramic.2017.01.010

E, H., MacArthur, K.E., Pennycook, T.J., Okunishi, E., D'Alfonso, a. J., Lugg, N.R., Allen, L.J., Nellist, P.D., 2013. Probe integrated scattering cross sections in the analysis of atomic resolution HAADF STEM images. Ultramicroscopy 133, 109–119. doi:10.1016/j.ultramic.2013.07.002

Egerton, R.F., 2011. Electron Energy-Loss Spectroscopy in the Electron Microscope, Springer, New York. doi:10.1007/978-1-4419-9583-4

Egerton, R.F., 2008. Electron energy-loss spectroscopy in the TEM. Reports Prog. Phys. 72, 16502. doi:10.1088/0034-4885/72/1/016502

Findlay, S.D., Chen, Z., Weyland, M., Sang, X., Xu, W., Dycus, J.H., LeBeau, J.M., Allen, L.J., 2017. Absolute-Scale Comparison with Simulation for Quantitative Energy-Dispersive X-Ray Spectroscopy in Atomic-Resolution Scanning Transmission Electron Microscopy. Microsc. Microanal. 23, 388–389. doi:10.1017/S1431927617002628

Gai, P.L., Boyes, E.D., 2009. Advances in atomic resolution in situ environmental transmission electron microscopy and la aberration corrected in situ electron microscopy. Microsc. Res. Tech. 72, 153–164. doi:10.1002/jemt.20668

Galassi, M., 2009. GNU scientific library : reference manual. Network Theory.

Gan, L., Heggen, M., Rudi, S., Strasser, P., 2012. Core − Shell Compositional Fine Structures of Dealloyed Pt.

Goris, B., De Backer, A., Van Aert, S., Gómez-Graña, S., Liz-Marzán, L.M., Van Tendeloo, G., Bals, S., 2013. Three-dimensional elemental mapping at the atomic scale in bimetallic nanocrystals. Nano Lett. 13, 4236–4241. doi:10.1021/nl401945b

Gubbens, A., Barfels, M., Trevor, C., Twesten, R., Mooney, P., Thomas, P., Menon, N., Kraus, B., Mao, C., McGinn, B., 2010. The GIF Quantum, a next generation post-column imaging energy filter. Ultramicroscopy 110, 962–970. doi:10.1016/j.ultramic.2010.01.009

Haberfehlner, G., Orthacker, A., Albu, M., Li, J., Kothleitner, G., 2014. Nanoscale voxel spectroscopy by simultaneous EELS and EDS tomography. Nanoscale 6, 14563–14569. doi:10.1039/C4NR04553J

Hodnik, N., Jeyabharathi, C., Meier, J.C., Kostka, A., Phani, K.L., Rečnik, A., Bele, M., Hočevar, S., Gaberšček, M., Mayrhofer, K.J.J., 2014. Effect of ordering of PtCu3 nanoparticle structure on the activity and stability for the oxygen reduction reaction. Phys. Chem. Chem. Phys. 16, 13610–5. doi:10.1039/c4cp00585f

Hofer, F., 1991. Determination of inner-shell cross-sections for EELS-quantification. Microsc. Microanal. Microstruct. 2, 215–230. doi:10.1051/mmm:0199100202-3021500

hyperspy/hyperspy: HyperSpy 1.3, 2017. doi:10.5281/ZENODO.583693

Iakoubovskii, K., Mitsuishi, K., Nakayama, Y., Furuya, K., 2008. Thickness measurements with electron energy loss spectroscopy. Microsc. Res. Tech. 71, 626–631. doi:10.1002/jemt.20597

Jacobsen, K.W., Stoltze, P., Nørskov, J.K., 1996. A semi-empirical effective medium theory for metals and alloys. Surf. Sci. 366, 394–402. doi:10.1016/0039-6028(96)00816-3

Jones, L., MacArthur, K.E., Fauske, V.T., van Helvoort, A.T.J., Nellist, P.D., 2014. Rapid estimation of catalyst nanoparticle morphology and atomic-coordination by high-resolution z-contrast electron microscopy. Nano Lett. 14, 6336–41. doi:10.1021/nl502762m

Jones, L., Varambhia, A., Beanland, R., Kepaptsoglou, D., Griffiths, I., Ishizuka, A., Azough, F., Freer, R., Ishizuka, K., Cherns, D., Ramasse, Q.M., Lozano-Perez, S., Nellist, P.D., 2018. Managing dose-, damage- and data-rates in multi-frame spectrum-imaging. Microscopy. doi:10.1093/JMICRO/DFX125

Jones, L., Varambhia, A., Sawada, H., Nellist, P.D., 2017. An optical configuration for fastidious STEM detector calibration and the effect of the objective lens pre-field Manuscript. J. Microsc. submitted.

Jones, L., Yang, H., Pennycook, T.J., Marshall, M.S.J., Van Aert, S., Browning, N.D., Castell, M.R., Nellist, P.D., 2015. Smart Align—a new tool for robust non-rigid registration of scanning microscope data. Adv. Struct. Chem. Imaging 1, 8. doi:10.1186/s40679-015-0008-4

Khan, A S. A, Ahmed, R., Mirza, M.L., 2009. Evaluation of Catalytic Activity of Pt and Pt-Ru Catalysts for Electro-oxidation of Methanol in Acid Medium by Cyclic Voltammetry. Port. Electrochim. Acta 27, 429–442. doi:10.4152/pea.200904429

Koh, S., Strasser, P., 2007. Electrocatalysis on bimetallic surfaces: Modifying catalytic reactivity for oxygen reduction by voltammetric surface dealloying. J. Am. Chem. Soc. 129, 12624–12625. doi:10.1021/ja0742784

Kothleitner, G., Grogger, W., Dienstleder, M., Hofer, F., 2014. Linking TEM Analytical Spectroscopies for an Assumptionless Compositional Analysis. Microsc. Microanal. 20, 678–86. doi:10.1017/S1431927614000130

Lábár, J.L., Salter, C.J., 1991. Uncertainties in the Analysis of M X-Ray Lines of the Rare-Earth Elements, in: Electron Probe Quantitation. Springer US, Boston, MA, pp. 223–249. doi:10.1007/978-1-4899-2617-3_13

Labrecque, J.J., Rosales, P.A., 1990. (TFltr) (513) 5, 269–271.

Li, Y., Zakharov, D., Zhao, S., Tappero, R., Jung, U., Elsen, A., Baumann, P., Nuzzo, R.G., Stach, E. A., Frenkel, A. I., 2015. Complex structural dynamics of nanocatalysts revealed in Operando conditions by correlated imaging and spectroscopy probes. Nat. Commun. 6, 7583. doi:10.1038/ncomms8583

Liu, D.-R., Brown, L.M., 1987. Influence of some practical factors on background extrapolation in EELS quantification. J. Microsc. 147, 37–49. doi:10.1111/j.1365-2818.1987.tb02816.x

Liu, J., Cowley, J.M., 1990. High-angle ADF and high-resolution SE imaging of supported catalyst clusters. Ultramicroscopy 34, 119–128. doi:10.1016/0304-3991(90)90066-U

Liu, Z., Ma, L., Zhang, J., Hongsirikarn, K., Goodwin, J.G., 2013. Pt Alloy Electrocatalysts for Proton Exchange Membrane Fuel Cells: A Review. Catal. Rev. 55, 255–288. doi:10.1080/01614940.2013.795455

Liu, Z., Xin, H., Yu, Z., Zhu, Y., Zhang, J., Mundy, J. A., Muller, D. A., Wagner, F.T., 2012. Atomic-Scale Compositional Mapping and 3-Dimensional Electron Microscopy of Dealloyed PtCo3 Catalyst Nanoparticles with Spongy Multi-Core/Shell Structures. J. Electrochem. Soc. 159, F554–F559. doi:10.1149/2.051209jes

Lucy, L.B., B., L., 1974. An iterative technique for the rectification of observed distributions. Astron. J. 79, 745. doi:10.1086/111605

MacArthur, K.E., Brown, H.G., Findlay, S.D., Allen, L.J., 2017. Probing the effect of electron channelling on atomic resolution energy dispersive X-ray quantification. Ultramicroscopy 182, 264–275. doi:10.1016/J.ULTRAMIC.2017.07.020

MacArthur, K.E., Slater, T.J.A., Haigh, S.J., Ozkaya, D., Nellist, P.D., Lozano-Perez, S., 2015. Quantitative EDX Analysis of Catalyst Nanoparticles Using a Partial Scattering Cross Section Approach. Microsc. Microanal. In press, 1–23. doi:10.1017/S1431927615015494

MacArthur, K.E., Slater, T.J.A., Haigh, S.J., Ozkaya, D., Nellist, P.D., Lozano-Perez, S., 2016. Compositional quantification of PtCo acid-leached fuel cell catalysts using EDX partial cross sections. Mater. Sci. Technol. 32, 248–253. doi:10.1080/02670836.2015.1133021

Malis, T., Cheng, S.C., Egerton, R.F., 1988. EELS log-ratio technique for specimen-thickness measurement in the TEM. J. Electron Microsc. Tech. 8, 193–200. doi:10.1002/jemt.1060080206

Martinez, G.T., Jones, L., Backer, A. De, Béché, A., Verbeeck, J., Aert, S. Van, Nellist, P.D., 2015. Quantitative STEM normalisation: the importance of the electron flux. Ultramicroscopy. doi:10.1016/j.ultramic.2015.07.010

Miller, M.K., Russell, K.F., 2007. Atom probe specimen preparation with a dual beam SEM/FIB miller. Ultramicroscopy 107, 761–6. doi:10.1016/j.ultramic.2007.02.023

Oezaslan, M., Strasser, P., 2011. Activity of dealloyed PtCo3 and PtCu3 nanoparticle electrocatalyst for oxygen reduction reaction in polymer electrolyte membrane fuel cell. J. Power Sources 196, 5240–5249. doi:10.1016/j.jpowsour.2010.11.016

Ostaševičius, T., de la Peña, F., Midgley, P., 2016. SAMFire - a smart adaptive fitting algorithm for multi-dimensional microscopy, in: European Microscopy Congress 2016: Proceedings. Wiley-VCH Verlag GmbH & Co. KGaA, Weinheim, Germany, pp. 95–96. doi:10.1002/9783527808465.EMC2016.6233

Owen, E.A., Jones, D.M., 1954. Effect of Grain Size on the Crystal Structure of Cobalt. Proc. Phys. Soc. Sect. B 67, 456–466. doi:10.1088/0370-1301/67/6/302

Pennycook, S.J., Nellist, P.D., 2011. Scanning Transmission Electron Microscopy: Imaging and Analysis. Springer. doi:10.100/978-1-4419-7-200-2

Phillips, P.J., Paulauskas, T., Rowlands, N., Nicholls, A.W., Low, K.-B., Bhadare, S., Klie, R.F., 2014. A New Silicon Drift Detector for High Spatial Resolution STEM-XEDS: Performance and Applications. Microsc. Microanal. 20, 1046–52. doi:10.1017/S1431927614001639

Prabhudev, S., Bugnet, M., Bock, C., Botton, G. a., 2013. Strained lattice with persistent atomic order in Pt3Fe 2 intermetallic core-shell nanocatalysts. ACS Nano 7, 6103–6110. doi:10.1021/nn4019009

Rani, A., Chaturvedi, S.N., Nath, N., 1987. K and L Shell X-ray Relative intensity Measurements 2, 2–3.

Retsky, M., 1974. Observed single atom elastic cross sections in a scanning electron microscope. Optik (Stuttg). 41, 127–142. doi:10.2172/4239746

Richardson, W.H., 1972. Bayesian-Based Iterative Method of Image Restoration*. J. Opt. Soc. Am. 62, 55. doi:10.1364/JOSA.62.000055

Rosenauer, A., Gries, K., Müller, K., Pretorius, A., Schowalter, M., Avramescu, A., Engl, K., Lutgen, S., 2009. Measurement of specimen thickness and composition in Alx Ga1 - x N / GaN using high-angle annular dark field images. Ultramicroscopy 109, 1171–1182. doi:10.1016/j.ultramic.2009.05.003

Schulenburg, H., Müller, E., Khelashvili, G., Roser, T., Bönnemann, H., Wokaun, a., Scherer, G.G., 2009. Heat-Treated PtCo3 Nanoparticles as Oxygen Reduction Catalysts. J. Phys. Chem. C 113, 4069–4077. doi:10.1021/jp808134j

Slater, T., 2015. Three Dimensional Chemical Analysis of Nanoparticles Using Energy Dispersive X-ray Spectroscopy.

Thompson, W.J., 2001. Poisson distributions. Comput. Sci. Eng. 3, 78–82. doi:10.1109/5992.919271

Thompson, A.C., Attwood, D.T., Gullikson, E.M., Howells, M.R., Kortright, J.B., Robinson, A.L., Underwood, J.H., Kirz, J., Lindau, I., Pianetta, P., Winick, H., Williams, G.P., Scofield, J.H., Vaughan, D., 2001. X-RAY DATA BOOKLET.

Tran, D.T., Jones, I.P., Preece, J. a., Johnston, R.L., Van Den Brom, C.R., 2011. TEM characterization of chemically synthesized copper-gold nanoparticles. J. Nanoparticle Res. 13, 4229–4237. doi:10.1007/s11051-011-0367-2

Van Aert, S., Batenburg, K.J., Rossell, M.D., Erni, R., Van Tendeloo, G., 2011. Three-dimensional atomic imaging of crystalline nanoparticles. Nature 470, 374–377. doi:10.1038/nature09741

Wang, D., Xin, H.L., Hovden, R., Wang, H., Yu, Y., Muller, D. a., DiSalvo, F.J., Abruña, H.D., 2012. Structurally ordered intermetallic platinum–cobalt core–shell nanoparticles with enhanced activity and stability as oxygen reduction electrocatalysts. Nat. Mater. 12, 81–7. doi:10.1038/nmat3458

Watanabe, M., Horita, Z., Nemoto, M., 1996. Absorption correction and thickness determination using the zeta factor in quantitative X-ray microanalysis. Ultramicroscopy 65, 187–198. doi:10.1016/S0304-3991(96)00070-8

Watanabe, M., Williams, D.B., 2006. The quantitative analysis of thin specimens: A review of progress from the Cliff-Lorimer to the new ζ-factor methods. J. Microsc. 221, 89–109. doi:10.1111/j.1365-2818.2006.01549.x

Watanabe, M., Williams, D.B., Tomokiyo, Y., 2003. Comparison of detectability limits for elemental mapping by EF-TEM and STEM-XEDS. Micron 34, 173–183. doi:10.1016/S0968-4328(03)00028-3

Xin, H.L., Mundy, J.A., Liu, Z., Cabezas, R., Hovden, R., Kourkoutis, L.F., Zhang, J., Subramanian, N.P., Makharia, R., Wagner, F.T., Muller, D.A., 2012. Atomic-resolution spectroscopic imaging of ensembles of nanocatalyst particles across the life of a fuel cell. Nano Lett. 12, 490–497. doi:10.1021/nl203975u

Yankovich, A., Pingel, T., Feng, J., Kvit, A., Slater, T., Haigh, S., Morgan, D., Voyles, P., Olsson, E., 2016. Exposing New Atomic-scale Information about Materials by Improving the Quality and Quantifiability of Aberration-corrected STEM Data, in: European Microscopy Congress 2016: Proceedings. Wiley-VCH Verlag GmbH & Co. KGaA, Weinheim, Germany, pp. 495–496. doi:10.1002/9783527808465.EMC2016.8366

Yankovich, A.B., Berkels, B., Dahmen, W., Binev, P., Sanchez, S.I., Bradley, S.A., Li, A., Szlufarska, I., Voyles, P.M., 2014. Picometre-precision analysis of scanning transmission electron microscopy images of platinum nanocatalysts. Nat. Commun. 5, 4155. doi:10.1038/ncomms5155

Yu, Y., Xin, H.L., Hovden, R., Wang, D., Rus, E.D., Mundy, J.A., Muller, D.A., Abruña, H.D., 2012. Three-dimensional tracking and visualization of hundreds of Pt-Co fuel cell nanocatalysts during electrochemical aging. Nano Lett. 12, 4417–4423. doi:10.1021/nl203920s

Yu, Z., Zhang, J., Liu, Z., Ziegelbauer, J.M., Xin, H., Dutta, I., Muller, D. a., Wagner, F.T., 2012. Comparison between dealloyed PtCo 3 and PtCu 3 cathode catalysts for proton exchange membrane fuel cells. J. Phys. Chem. C 116, 19877–19885. doi:10.1021/jp306107t

Zanaga, D., Altantzis, T., Sanctorum, J., Freitag, B., Bals, S., 2016. An alternative approach for ζ-factor measurement using pure element nanoparticles. Ultramicroscopy 164, 11–16. doi:10.1016/j.ultramic.2016.03.002

Zhang, H.-R., Egerton, R.F., Malac, M., 2012. Local thickness measurement through scattering contrast and electron energy-loss spectroscopy. Micron 43, 8–15. doi:10.1016/j.micron.2011.07.003

6 Conclusions

The main aim of this thesis is to link structure and composition of catalyst nanoparticles to activity for smarter catalyst design. As presented in chapter 1, several studies have shown that to link structure and composition to activity, a detailed characterisation of a catalyst's size, shape, strain and composition at high throughput is required. There are several characterisation methods that can be used to measure some of these properties. Chapter 2 shows that these can be grouped into two categories, "bulk-averaging" (x-ray, CV, IR) or "few particle" (STEM, AFM, APT) methods. An overview of these methods indicates that STEM is the only technique that can probe catalyst structure and composition simultaneously at atomic resolution.

STEM offers a board range of signals which can be used to quantify catalyst nanoparticles at high throughput. This is highlighted in chapter 3, where the ADF signal can be used to obtain structure information, whereas the EDS and EELS signals can be used to obtain composition information. Thus, a workflow using the latest quantification techniques and automation can be implemented to obtain three-dimensional structures of nanoparticles. These models can be used as inputs for electronic structure calculations such as DFT.

Quantitative methods on how to obtain the number of atoms in a catalyst using ADF scattering cross-sections is presented in Chapter 4. The atom counts can be obtained by using either simulation matching, statistical decomposition or a hybrid of the two. Since the statistical method requires a large number of observations (or atomic columns) for accurate atom counting in a sample, and the hybrid method is in its infancy, most work in this thesis used the simulation matching approach. For reliable atom counting with the simulation method, accurate and precise characterisation of the microscope's ADF detector collection angles is required. For accurate and precise determination of the collection angles, a new "swung mapping" method was developed. This method addresses discrepancies present in previously published methods when determining the ADF detector's inner and outer angles.

By utilising the latest quantification techniques two pure element, Ru and Pt, catalysts were analysed as case studies. In the Ru catalyst study, chapter 4.4, the aim was to investigate the crystal structure and

the rafting phenomenon. Ru is commonly known to have a hcp structure in the bulk, however, previous TEM observations inconclusively hinted at a fcc raft-like structure. Thus, determining the crystal structure of Ru nanoparticles was a controversial topic. To investigate this controversy, this thesis quantified a pure Ru catalyst on carbon black under the effects of the electron beam. Atomic resolution imaging and quantification revealed that the catalyst nanoparticles initially started off as amorphous and then formed into a stable fcc raft of up to 6 atoms in thickness. Thus, conclusively demonstrating that it is possible to form stable fcc Ru rafts under the electron beam.

In the Pt catalyst study, the aim was to implement the latest quantification techniques to atom count, obtain 3D structures and use them as inputs for DFT to predict catalytic activity of the Pt nanoparticle ensemble. The 13 three-dimensional models across the entire Pt size distribution presented in chapter 4.5 can be obtained from a single day of microscope time. Then within a few hours of data processing, models of up to 5000 atoms can be created on a standard desktop computer. These models were then used as inputs for DFT calculations to yield their electronic structure.

From the coordination number and nanoparticle shape analysis, it was seen that as the nanoparticle size increased, the roughness increased compared to the Wulff structures. Electronic iso-surface calculations indicated that this leads to more sites with lower electron density and therefore higher O-binding reducing catalytic activity. Using a DFT calibrated master curve, an estimate of the fraction of sites within 0.2eV of the optimum binding energy can be calculated in a few seconds and used to rapidly predict the catalytic activity of experimentally determined structures. This high throughput approach agrees well with experimentally and theoretically determined findings for the pure Pt nanoparticle system.

While quantitative structural inversion of bi-metallic catalysts is difficult with ADF images, the use of quantitative spectroscopic techniques in STEM was explored in chapter 5. In this chapter, a method of measuring and combining EDS and EELS signals using standard needle and nanoparticle standards was presented. The approach describes the intensity measured by the detector in terms of a partial scattering cross-section. These cross-sections are partial cross-sections that depend on several microscope parameters such as spectrum integration-window, detector efficiency, collection-angle and size.

The reliability of the measured EDS partial cross-sections was verified with an independent ADF quantification. In this comparison a pure on-axis Pt nanoparticle was atom-counted using both EDS and ADF quantifications and the total number of atoms agreed well. The precision in using EDS to count the number of atoms in an individual column was very poor however due to counting statistics. The spectroscopic partial cross-sections from the needle and nanoparticle standards agreed well and both methods could be used as calibration standards provided that the number density of the samples is determined accurately. Error analysis of the individual partial cross-section measurements shows that counting statistics could lead to an error of up to 20% when determining absolute number of atoms. This can be reduced by increasing the dose, however sample damage would also increase. A balance between dose and sample damage is required and would be useful to investigate in another study.

By unifying the ADF, EDS and EELS signals in terms of scattering partial cross-section it is possible to directly compare and switch between the different acquisition modes seamlessly. This method was then implemented to quantify bimetallic Pt-Co nanoparticle ensembles in chapter 5. Most nanoparticle ensemble studies, involving spectroscopy have looked at single or few particle analyses. The conclusions drawn from this might not be representative of the whole nanoparticle ensemble. In chapter 5.6, a total of ~ 200 spectrum images were acquired from Pt3Co and PtCo3, leached and unleached, samples across a broad size range. Alongside this an independent ADF strain study was undertaken. Here a total of 17 on-axis nanoparticles were acquired, however on-axis nanoparticles are difficult to acquire at high throughput as observations are rare during the experiment. More strain observations are required to probe the entire size range, and further work is required to understand the link between nanoparticle strain and composition.

To link nanoparticle strain and composition to catalytic activity at the atomic scale, a study of the particle's electronic structure is required. Here a full three-dimensional inversion of the nanoparticle is required using spectroscopy in a similar manner to ADF quantification shown in chapter 4.5. The next chapter presents some preliminary data and proposes approaches on how to perform this.

7 Future Prospects

7.1 Chapter Overview

This chapter covers the author's initial findings and works within the past year of the project. In some cases, preliminary data is presented as a proof of concept. A method of obtaining atomic resolution spectroscopic data from nanoparticles using multiframe acquisition is presented. A concept of mixing EDS and EELS signals as multivariate datasets is explored and discussed. Then a method of acquiring custom EELS gain and dark references is presented with some initial results. A method of obtaining full three-dimensional data inversion of bi-metallic nanoparticles is presented. This method requires a combination of STEM simulations, statistical decomposition and structure searching.

Additionally, a method of automating the electron microscope aimed at increasing throughput is presented. Here the scripting capabilities of Digital Micrograph software are reviewed, and some initial concepts are presented. Finally, an initial look at in-situ and ex-situ microscopy is presented, where the nanoparticles are subject to miniature fuel-cell like environments. Some initial results are presented and future possibilities within this field are discussed.

Currently all the ingredients are present to perform most of the work listed in this chapter. The main hurdle is that codes to piece these concepts together have not been developed adequately to make these tasks routine. Most work presented in this section was performed with several colleagues across different institutions. These contributions are acknowledged in each section respectively.

The results in this chapter present work from the following peer-reviewed publication:

- Second author: "Managing dose-, damage- and data-rates in multi-frame spectrum-imaging",Lewys Jones, Aakash Varambhia, Richard Beanland, Demie Kepaptsoglou, Ian Griffiths, Akimitsu Ishizuka, Feridoon Azough, Robert Freer, Kazuo Ishizuka, David Cherns, Quentin M. Ramasse, Sergio Lozano-Perez, and Peter D. Nellist, *Microscopy*, (2018), DOI:10.1093/jmicro/dfx125.

7.2 On-axis Size, Shape, Strain and Composition Determination using STEM

7.2.1 Section overview

This section covers current capabilities and methods developed during this project to measure simultaneous, size, shape, strain and composition information from catalyst nanoparticles. Firstly, a review of current acquisition methods is presented, and then a proposed multiframe acquisition technique is presented. An example of multiframe spectroscopy on an on-axis PtCo3 leached nanoparticle is presented which highlights the current cutting-edge limitations of what can be achieved with the hardware available.

Here the author performed the experiment and coded most of the multiframe spectra acquisition script, from an initial script written by Prof. Sergio Lozano-Perez. Additionally, useful discussions, suggestions and improvements for the script were provided by Dr Lewys Jones. Dr Lewys Jones performed ADF and EDS data alignment and the author produced the Pt maps.

7.3 Brief Review of Current Acquisition Methods and Multiframe Spectroscopy

The STEM is a versatile instrument that can capture both the structure and chemical variations in materials at atomic resolution. This is made possible due to the scanning configuration and the detectors available in this mode. Data are acquired serially originating simultaneously from the same area of the sample excited by the electron beam.

Currently, there are many hardware manufacturers for different detectors used within the microscope, each have their own proprietary software to acquire and process the data. This is a crucial hurdle for simultaneous spectroscopic acquisition. For example, most STEM-EDS acquisition packages are derivations of SEM microanalysis software and were not designed with the STEM in mind. One clear disadvantage present most EDS software packages is the lack of simultaneous EELS acquisition.

However, recent collaboration between manufacturers has unlocked the capability to acquire all the data, at a fast rate, within the Gatan Microscopy Suite Digital Micrograph software (Haberfehlner et al., 2014; Kothleitner et al., 2014). Furthermore, this capability allows spectroscopic data to be recorded in a multiframe manner (Jones et al., 2018) similar to ADF multiframe imaging (Jones et al., 2015; Yankovich et al., 2014). With this approach is it possible to demonstrate how dose-sharing methods can

help reduce sample damage and improve the signal-to-noise ratio. This is very important for quantifying catalyst nanoparticles as damage and sample alteration can lead to an incorrect analysis.

7.3.1 Why Multi-Frame Spectroscopy is Important.

With the introduction of aberration correction, it is now possible to routinely image materials at atomic resolution. However, using the ADF signal alone to quantify composition in a multielement sample can sometimes be difficult. So for composition quantification, either EDS or EELS is used but the signals are six and three orders of magnitude weaker respectively compared to ADF imaging (MacArthur et al., 2015).

While the spectrometer hardware is improving gradually, little has changed on the data acquisition side. There are three conventional approaches used to increase the SNR of acquired spectra:

1. Increasing the pixel dwell time
2. Increasing the beam current
3. Using more spectrometers

The first two approaches can cause severe sample damage, for example increasing the pixel dwell time risks introducing scanning distortions, stage -drift or focal drift into the frame. Whereas increasing the beam current can cause sample damage or accelerate carbon contamination. The third approach is good, but sometimes not practical within microscopes with small objective pole-piece gaps.

However, with recent developments to robust registration of serially scanned data (Jones et al., 2015), multiframe spectrum-image (MFSI) data can now be equally registered. MFSI experiment design frees the experimentalist from points 1 and 2 above to achieve realistic SNR datasets. The required total signal is built up from a series of individual fast scans at a lower dose. In this configuration, specimen drift is significantly reduced and so is beam damage. Additionally, post-acquisition analysis can be used to determine which frames to keep in case there is damage in the final few frames in the acquisition.

7.4 Methods and Data Processing

A PtCo3 leached on axis nanoparticle was chosen for this study and comes from the same ensemble described in section 5.6.2. The nanoparticle batch was transferred onto a TEM grid by conventional crushing, dusting and drop casting onto a standard carbon grid. The ADF imaging was performed on the Oxford JEOL ARM 200CF microscope operated at 200kV acceleration voltage. EDS mapping of the nanoparticle was performed using a ~20pA beam current, with a 22.48mrad probe semi-angle and a pixel dwell time of 0.001s. 60 spectrum image frames were recorded alongside the ADF images. Unfortunately, no EELS frames could be acquired during this experiment due to hardware failure prior to the experiment.

To maximize throughput and reduce operator burden an interactive graphical script was written in Digital Micrograph where the image and spectra pairs are recorded, numbered and saved to disk automatically, Figure 7.1.

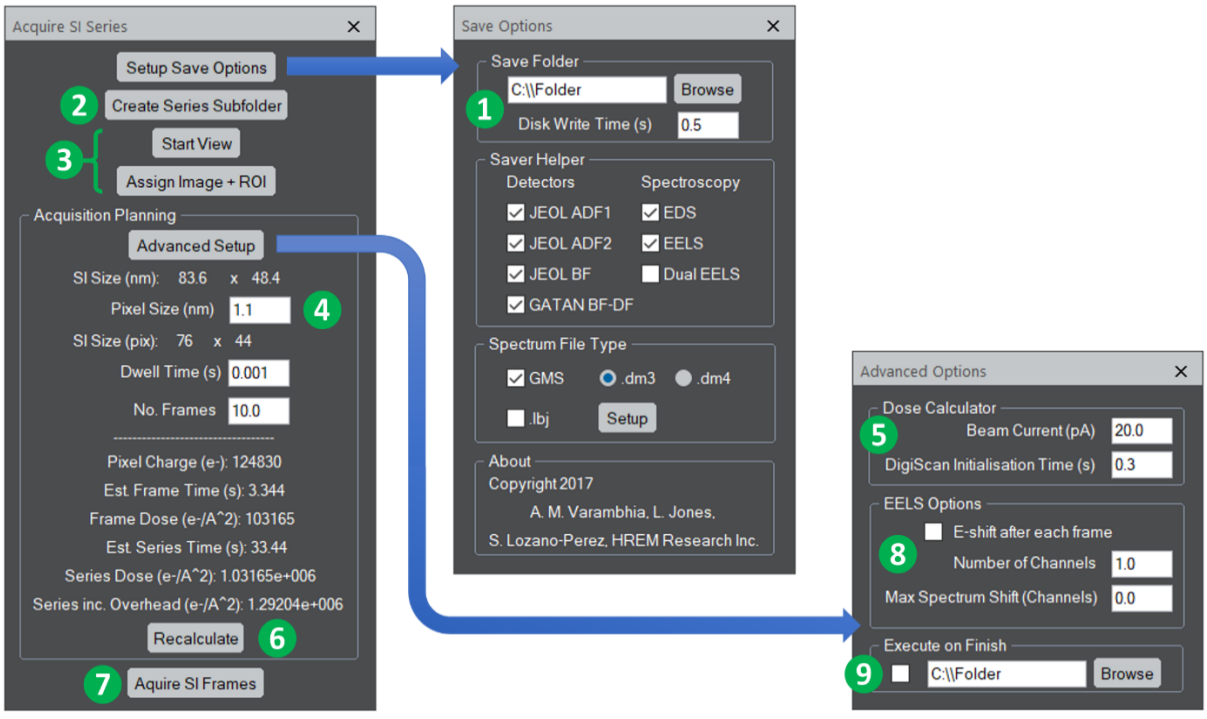

Figure 7.1 The interactive graphical user interface to streamline data acquisition and saving. Reprinted from (Jones et al., 2018).

In this script, the user first indicates the save-path for the microscope session (1), the data writing overhead time, the signals to record and whether advanced options such as data compression and energy

stepping should be used. After this, a new folder may be created for a new region of interest without leaving the main workflow (2). Then the user starts a live image view and specifies the region of interest (3). After this, the user specifies the required pixel step-size (4) which is then fixed and is contrary to the microscope's built-in workflow (Where the pixel step is a free parameter as the field of view is changed). Here the number of pixels is determined automatically from the user input pixel step size. In the advanced setup menu, the user specifies the STEM probe current and the DigiScan unit software-to-hardware overhead communication time.

After the SI parameters are set, the user is presented with a dose and total time calculator. The dose is estimated in electrons/$Å^2$ for the entire series including all communication and fly-black overhead times. The user can also re-evaluate the dose by using the recalculate button (6) if acquisition changes, such as changing the dwell time or region of interest, are made. Therefore, giving the user an indication of practicability before data acquisition is started. More detailed options such as EELS dispersion and energy offset are handled using the usual Gatan menus.

The selected signals are then recorded, saved to disk and closed from memory with (7). If the sample is undamaged after the acquisition, and further frames are required to increase the SNR, the user can simply press the 'acquire SI frames' button again. And further frames will be added to the same subfolder. This process can be repeated as many times until the user selects the 'create series subfolder' to move to the next numbered sub-folder during the session. The user can also select other options such as to step the EELS spectrum along the camera between SI frames by incrementing the drift-tube voltage (8). Further details of this method have been previously used by (Bosman and Keast, 2008) or by (Hou, 2009) to improve EELS dark reference quality. Additionally, a custom script, for example, dropping the magnification by 10,000x or send email to the operator after acquisition or blank the beam, can be executed upon completion (9) (Schaffer, 2017).

Using the simultaneously acquired ADF and EDS images, the image alignment and scan-distortions were corrected using the Smart Align software(Jones and Nellist, 2013). The technical details of the algorithm used and the alignment workflow are provided in more detail by Dr Lewys Jones in the publications (Jones et al., 2018; Jones and Nellist, 2013)

7.5 Results and Discussion

Figure 7.2 shows an on-axis PtCo3 leached nanoparticle with simultaneously acquired ADF and EDS spectra. While the individual ADF frame has good SNR, the same cannot be said about the single EDS frame. There is hardly any signal within the EDS frame, until about 30-40 cumulative frames are added, even then the Pt and Co counts are <5 over a select few pixels.

The number of counts per pixel should improve with better hardware or more detectors, such as the JEOL double EDS detector microscopes. Currently, to achieve lattice resolution EDS maps within realistic experiment time frames, beam currents <20pA with ~0.6Å pixel step size and dwell times of ~0.001s is required. Realistically, for nanoparticles such as Pt-Co, up to 60 frames under 20 minutes can be acquired without causing extensive damage to nanoparticles >6nm.

Additionally, further statistics could be built up using the EELS detector, which is about three orders of magnitude more efficient that then EDS detector (MacArthur et al., 2015). However here additional care must be taken when treating the EELS dark reference. For instance, taking the dark reference between frames or at the end of the acquisition could influence the composition quantified, depending on how long the detector was recording.

None the less collecting multiframe EDS and EELS simultaneously can provide a powerful dataset to decouple elemental compositions within a sample. Since the acquired data is at atomic resolution, two-dimensional strain analysis could also be performed on the same sample. This would be the key to linking surface strain to composition and unlock the first step towards full three-dimensional nanoparticle inversion as input for DFT simulations.

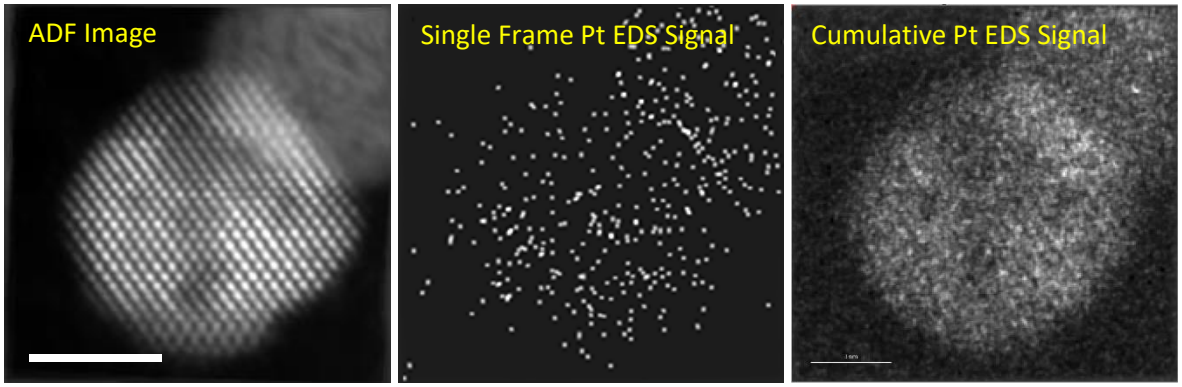

Figure 7.2 On axis PtCo3 nanoparticle with simultaneously acquired ADF and EDS signals. The individual EDS frames have almost no signal, however, when the cumulative frames are added together, lattice resolution can be observed.

7.6 Conclusions

While spectroscopic hardware is gradually improving, little development has been made in how spectroscopic data is collected. In most cases, spectra are recorded independently after an ADF scan as a supplement. With stagnation in software development, simultaneous atomic resolution EDS and EELS spectra acquisition in with ADF imaging is rare.

On-axis atomic resolution spectra acquisition requires a stable sample stage and environment. Creating such an environment is not always possible depending on the location/environment of the lab. Therefore, alternative methods like multiframe spectroscopy are required, where the sample drift, damage and scan coil distortions are corrected post-acquisition. With current hardware capabilities, it is possible to obtain high-quality atomic resolution spectra on stable FIB lamella samples (Jones et al., 2018).

For more beam sensitive samples such as nanoparticles or oxides, lattice resolution images can be obtained. Such spectra are the first stepping stone towards full three-dimensional inversion of bimetallic nanoparticles using scattering cross-sections which incorporate electron channelling. Then with the aid of DFT simulations, the link between nanoparticle composition and strain can be fully realised.

Furthermore, as simultaneous acquisition of multivariate ADF, EDS and EELS datasets become more routine, a whole new field of data analysis is unlocked. One exciting area is multivariate data mixing where all the signals originating from the sample and probe interaction are combined into one big

dataset which is statistically unmixed. Additional improvements would also lead to better routine acquisition methods such as fractional EELS and energy stepping.

7.7 Multivariate Mixing of Datasets

Several upgrades to STEM spectroscopic detectors within the past decade enable collection of good signal to noise ratio of EDS and EELS signals. The new developments have reduced the acquisition time and dose required to probe samples at high spatial resolution for microanalysis. Despite hardware and software improvements, spectroscopic data is usually acquired in a complementary manner. Due to this little development has been made towards mixing multivariate datasets. Recently, (Haberfehlner et al., 2014) demonstrated the potential of such datasets by characterising EELS and EDS data simultaneously.

EDS and EELS datasets are complementary analysis techniques that allow for detection of nearly all elements in the periodic table in a single acquisition. The vast 0-20keV energy range of EDS, and light element with chemical sensitivity, at superior energy resolution, of EELS provides a potent microanalysis dataset. Gradually as the field trends towards large datasets, machine learning libraries such as Hyperspy (de la Peña et al., 2017) have been developed to address these requirements. However, a framework has not been developed to treat mixed multivariate EDS and EELS signals.

To build this framework, one approach is to use multivariate statistical techniques such as principal component analysis (PCA), individual component analysis (ICA) and model fitting. These methods can be used to recast raw spectral data cubes onto new basis sets, denoise data and fit analytical models over them. The strength of such techniques lies in the fact that the data can be well represented by just a few basis factors, rather than thousands of separate sets for each pixel within a large spectrum image(Rossouw et al., 2016).

This area of research has great potential and has largely been unexplored. Since the spectroscopic signal for both EDS and EELS detectors originates from the same electron beam and sample interaction, combining the spectroscopic datasets should be the next natural progression. Current attempts of this have been limited, and recent work by (Haberfehlner et al., 2014; Rossouw et al., 2016) have employed

multivariate statistical methods to decouple signals from simultaneously acquired spectroscopic datasets. However, no attempt has yet been made in the literature to combine the spectra into one data cube, and then analyse it using multivariate statistics.

One of the reasons why such an approach is required is elemental peak overlap in the EDS and EELS spectrum. For example, if one wants to map elements K and Ca in a biological sample using EDS, the Ca-Kα (3.69 keV) and the K-Kβ (3.59 keV) peaks are within 0.2keV of each other and thus overlap in energy. Moreover, if one tries to decouple them using the EELS, then the K and C (284eV) peaks are within 10eV of each other, where the K $L_{3,2}$ (290eV) peaks are located on the background/shoulder of the C edges.

To decouple peak overlap, two approaches could be used. First, an extended energy resolution method proposed by (Craven et al., 2017) can decouple the Ca-Kα and K-Kβ EDS lines using the high energy resolution of the EELS spectrometer tuned to detect electron energies up to 4keV. Here the corresponding EELS edges for Ca-Kα and K-Kβ EDS lines can be resolved using the EELS spectrometer. Alternatively, in the second method, the EDS and EELS datasets can be combined into a single multivariate datacube and unpicked by machine learning.

Here we propose a multivariate data mixing approach with preliminary, simultaneously acquired, EDS and EELS data from a Co sample. The example shown in the next section was from a single spectrum from a pixel from the needle sample discussed in chapter 5.2.2.

7.7.1 Proposed Method, Preliminary Results and Discussion.

The data was acquired using the Oxford JEOL ARM 200CF operated at 200kV equipped with an EDS and EELS fast sync cable, enabling simultaneous acquisition at 1000spectra/s. For a full description of the data acquisition parameters and sample synthesis methods see chapter 5.2.2. The collected spectroscopic signal was normalised in units of fractional beam current, Figure 7.3, using a method described in chapter 5,

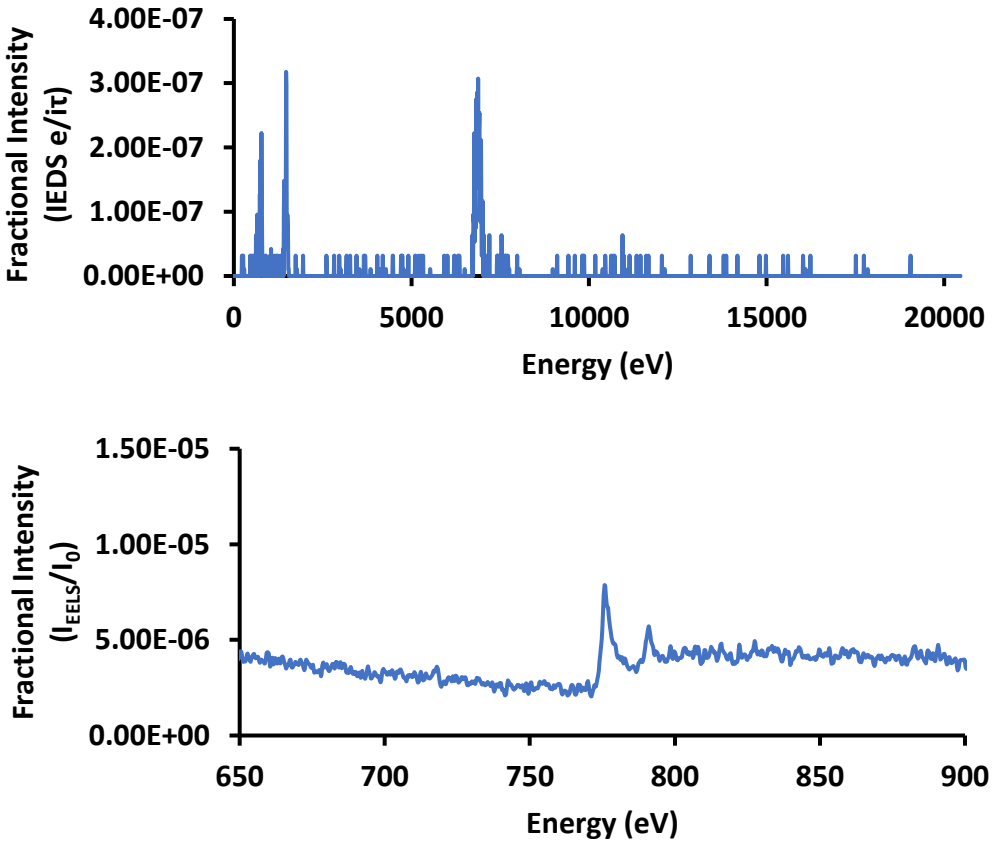

Figure 7.3 Simultaneously acquired Co EELS and EDS data, where the y-axis intensity is represented as a fraction of the incident beam flux, and the x-axis has been converted to eV for both spectra. The EDS Co Kα and Kβ peaks are located at 6930eV and 7650eV respectively. Whereas the EELS L3 and L2 peaks are located at 779eV and 794eV respectively.

By using the partial Co cross-sections from Table 5.6, the EDS and EELS data can be normalised, for example with respect to sample thickness, by rewriting equations *6* and *10* as:

$$t = \frac{I_x e}{i\tau n_x \sigma_x^{EDS}} \qquad (17)$$

$$t = \frac{I_x}{I_0 n_x \sigma_x^{EELS}} \qquad (18)$$

This means that after normalisation, the y-axis in Figure 7.3 can be expressed in units of $[1/n^{-1}b^{-1}]$. Where n is the sample number density in atoms/nm^3 and b is the cross-section units in barns. This can be further simplified to just $[1/nm]^{-1}$ which is just sample thickness, Figure 7.4. Normalising the y-axis in this way (equations *17* and *18*) means that the EDS and EELS signals have intensities with the same order of magnitude and the integral under the element peaks should give sample thickness. For signal integrated and background subtraction, the windows listed in Table 5.3 were used. The peak

integration gave thicknesses of 79.76nm and 68.96nm from the EDS and EELS spectra respectively. Whereas, the thickness obtained from the t/λ Malis parametrisation is 69.98nm. The thickness agreement obtained between the two methods is good and could be improved further for EDS with more counting statistics (by increasing the beam current or pixel dwell time).

A circular argument could be made that getting such a good match between the spectra normalised thickness and the Malis parameterisation is because of a good initial mean free path measurement. While this is true, the method's consistency boils down to accurate calibrations. With careful measurements and characterisation of the microscope, the units of the measured spectra can be simplified to just sample thickness.

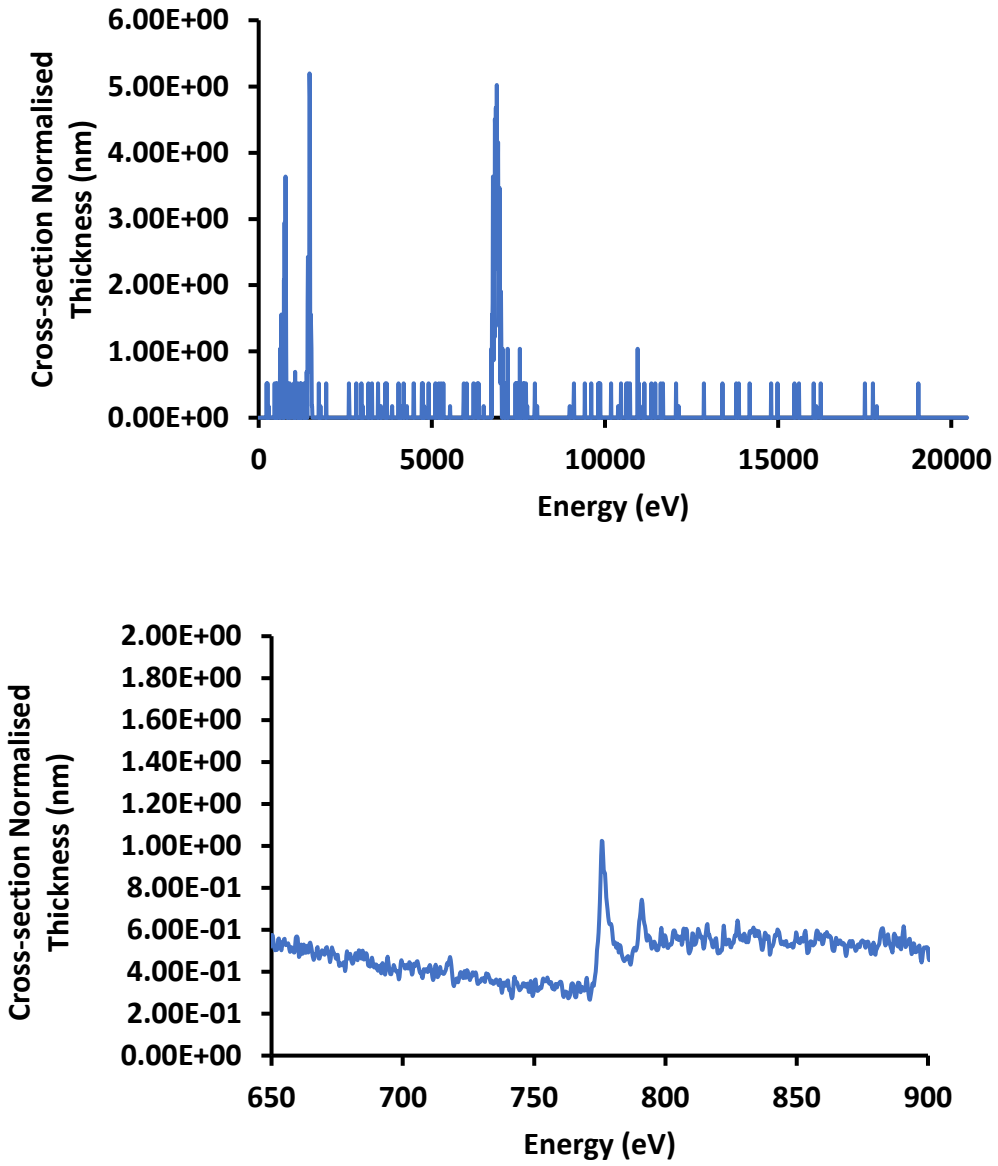

Figure 7.4 EDS and EELS plots from Figure 7.3 normalised using equations 17 *and* 18*, with units nm along the y-axis. The integral under the chemical peaks gives the thickness of the sample in nm.*

By normalising datasets in this manner, it is then possible to deploy machine learning algorithms such as PCA and model fitting to combine the independently acquired EDS and EELS signals into one big dataset. For example, after the cross-section normalisation, the data could be denoised and concatenated as shown in Figure 7.5. After subsequent energy alignment, the data could be model fit with Gaussians using inbuilt libraries within the Hyperspy package, Figure 7.6. The sequences in which the multivariate post-processing is done can vary and remains an area to be investigated in the future.

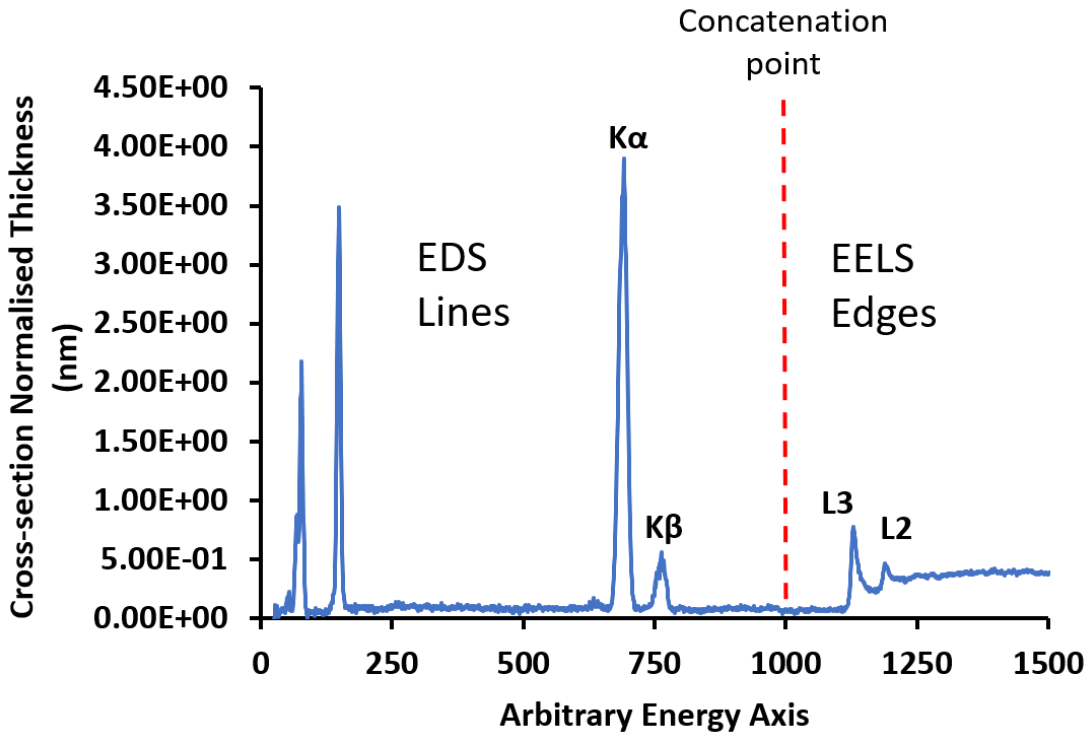

Figure 7.5 Concatenated EDS and EELS spectra which could be processed as a single dataset.

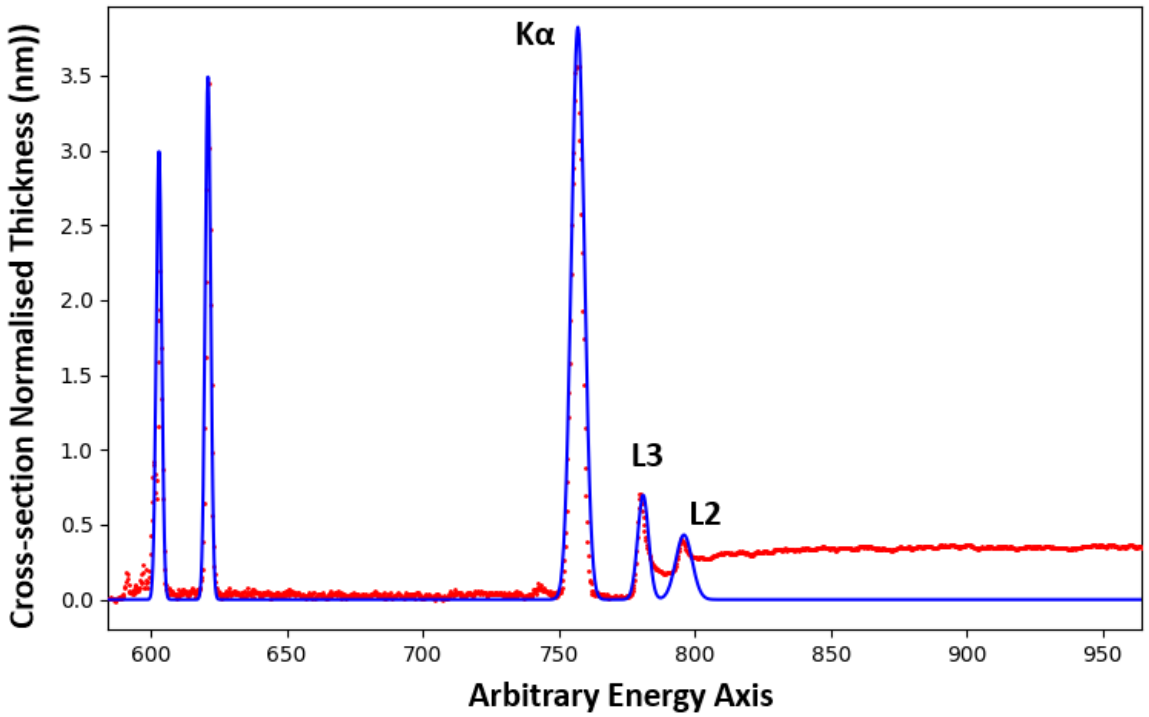

Figure 7.6 Multivariate peaks from the experiment shown in red with Gaussian fits modelled over the ionisation edges in blue, using Hyperspy. This is preliminary data and requires further work, especially in modelling the EELS edges and background effects.

7.8 Fractional EELS

In recent years, great progress has been made in putting ADF STEM on a quantitative scale (Aarons et al., 2017.; E et al., 2013; Jones et al., 2014; Lebeau et al., 2010; G. T. T. Martinez et al., 2015; Rosenauer et al., 2010; Van Aert et al., 2011). These methods aim to fractionate the observed ADF intensity with respect to the incoming electron beam, as shown in chapter 4.2. In principle, something similar can be done during post-processing with the EELS spectra.

EELS fractionation requires a dark' and 'gain' reference from the CCD for use in equation 19. Where the fractionated $EELS_{norm}$ is obtained by ratios of the experimentally measured intensity $EELS_{exp}$ and the CCD gain reference Ref_{Gain}, after a dark reference Ref_{dark} correction. The principle behind this equation is the same as the ADF fractionation equation *5* from chapter 4.2.

$$EELS_{norm} = \frac{EELS_{exp} - Ref_{dark}}{Ref_{Gain} - Ref_{dark}} \qquad (19)$$

Conventionally Ref_{Gain} and Ref_{dark} are recorded using the in-built Gatan Digital Micrograph software procedures. However, these offer little customisation and the values are not easy to obtain during live acquisition. Another point that remains for debate is the validity of a CCD dark reference during a long spectrum image acquisition. For example, the Gatan dark reference acquisition routine measures a dark reference at the end of the acquisition (usually recorded at a speed that is a tenth of the experiment dwell time). A question that remains is whether the same dark reference is valid after an hour long or several minutes long spectra acquisition.

To tackle the dark reference problem, a custom script was developed to record an "in-line" dark reference during the SI acquisition. Dr Lewys Jones developed the bulk of the custom acquisition script and Dr Hidetaka Sawada developed the beam-blanking. Whereas, the author coded parts of the custom script and took part in the experiment with Dr Lewys Jones.

Using the script the relevant dark reference is read out and recorded with exactly the same experimental conditions as the investigation spectrum image. Figure 7.7 shows simultaneously acquired ADF, EDS

and EELS, where the in-line beam-blanking is visible in the ADF and EELS. Although there are a few synchronisation issues with the in-line beam blank control, the result is usable for analysis. Note, unlike the other signals the EDS has no dark noise. Thus the beam blanking region appears the same. In the future, this will be combined with the multiframe acquisition and EELS energy stepping routines (Bosman and Keast, 2008; Jones et al., 2018).

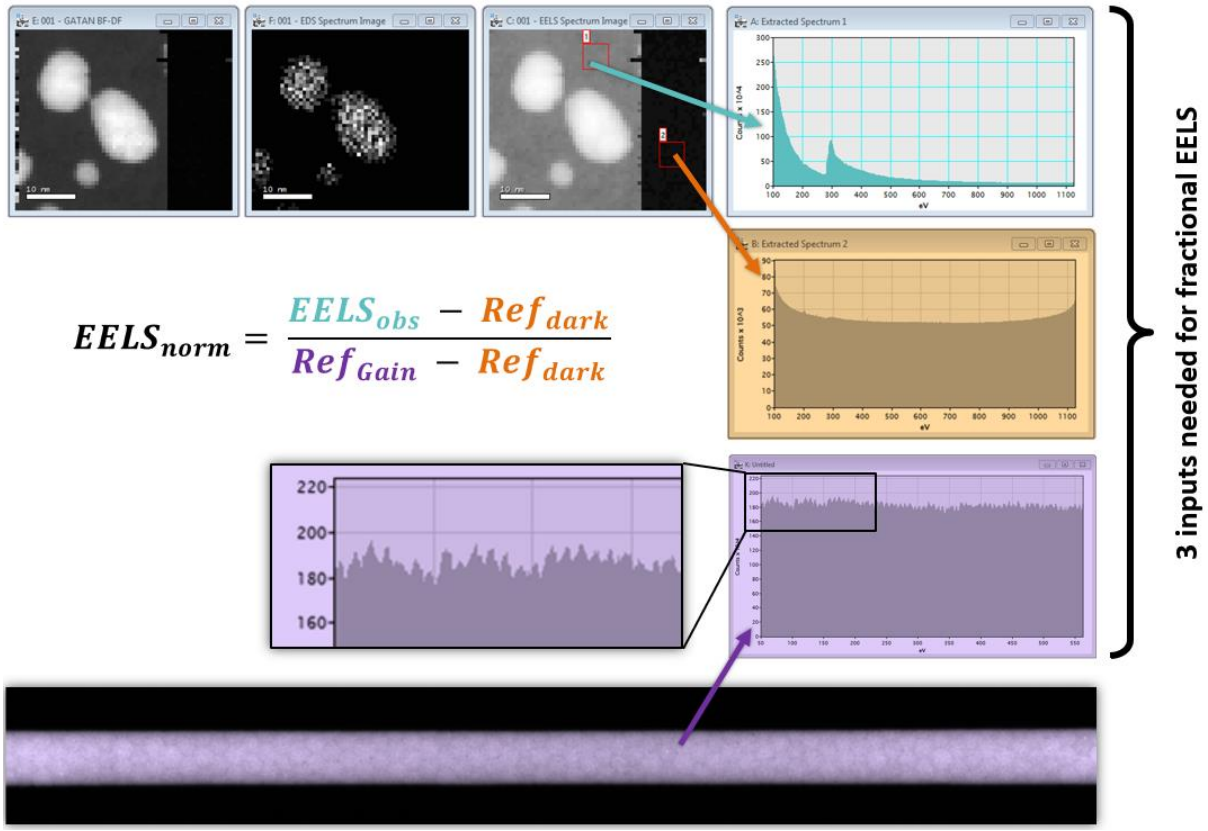

Figure 7.7 Figure by Dr Lewys Jones showing the data required for the calculation of fractional-EELS. The top row shows the custom acquisition incorporating (from left to right) the ADF image signal, the simultaneous EDX signal, and the EELS SI data. In the custom acquisition, blanking of the beam is controlled to yield a dark region on the right-hand side. The EELS SI then natively contains its own dark-reference that can be used in the post-processing (orange). An EELS gain-reference is required and is recorded independently of the experimental acquisition (purple).

7.9 Full Three-Dimensional Data Inversion for Bi-Metallic Nanoparticles

With further improvements to software and hardware for spectroscopic acquisition, obtaining near atomic resolution spectra will be more routine. Intensities from spectra such as Figure 7.2 can be quantified using the same peak fitting methods and integration as the ADF methods shown in chapter 4.2. Using cross-sections measured from pure element standards, shown in chapter 5.2.2 the number of atoms along an atomic column can be determined for bimetallic nanoparticles.

However, for a full three-dimensional inversion not only does one need the number of atoms along a column, but also the ordering of the atoms. To decouple ordering from the measured signals, the electron channelling effect in ADF image could be exploited using simulations. However, as the atomic column thickness increases, the number of simulations increases as well. A typical STEM multislice simulation of up to 20 Pt atoms with 30-phonon configurations can take up to 20 minutes on a typical Nvidia GTX Titan GPU. For a Pt-Co binary system the number of simulations to calculate all the Pt-Co configurations scale by 2^N, where N represents the number of atoms within a column. Thus, to simulate a 20-atom thick Pt-Co column, 1,048,576 simulations are required. Interpreting results from these simulations is further complicated by electron channelling, giving rise to a broad range of scattering cross-sections, Figure 7.8.

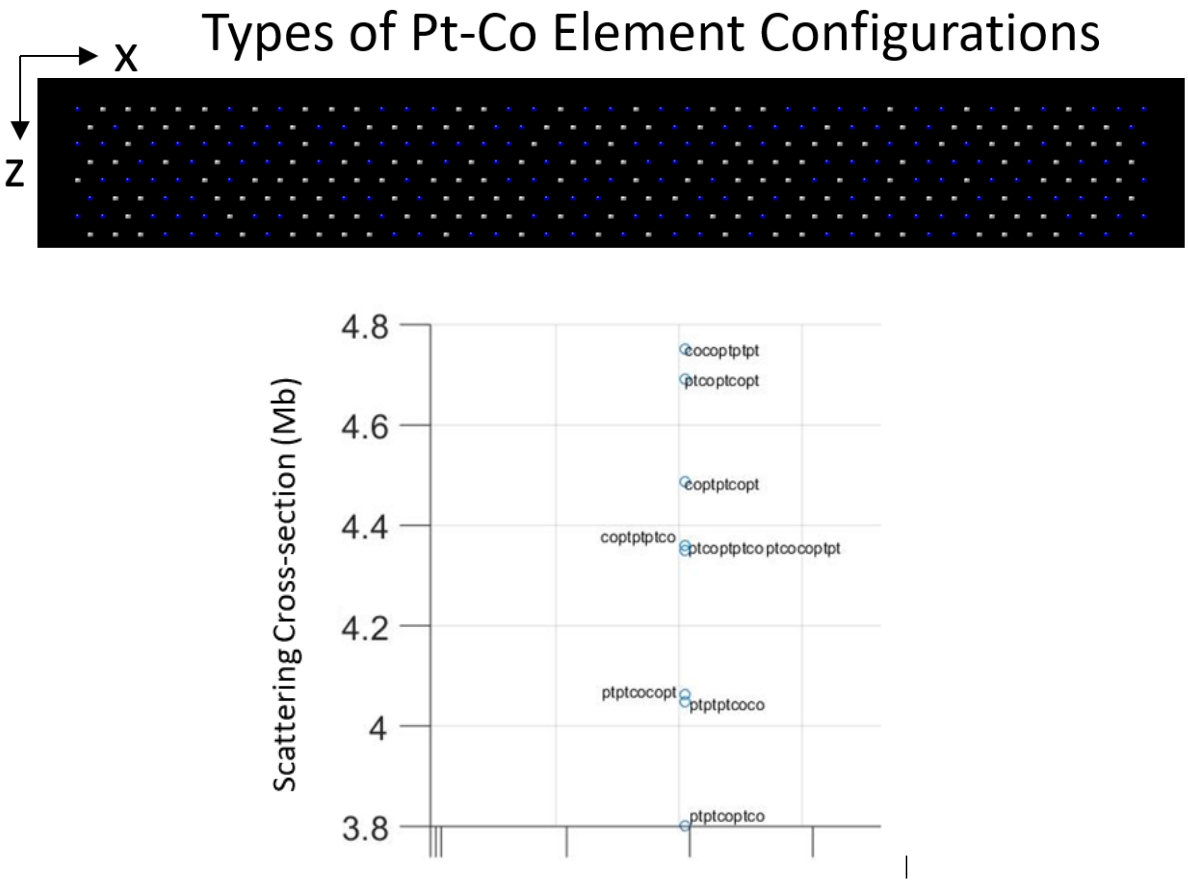

Figure 7.8 Some of the possible Pt-Co atomic configurations and simulated ADF scattering cross-section in units of barns for a 5-atom thick Pt-Co column.

Two promising attempts have tried to address this problem. The first one is a direct simulation matching approach using the PRISM software, where the computationally intensive steps time is reduced drastically by interpolation and careful approximations of the sample and electron wavefunction interactions(Pryor et al., 2017). It was reported that by distributing the workload between four CUDA-enabled GPUs and multicore processors, the simulation time could be accelerated by as high as 30x for multislice simulations.

The second approach employs a statistical decomposition technique, where the channelling of the Pt-Co elements is characterised by a lensing model (van den Bos et al., 2016). The channelling of each Pt and Co atom in a bimetallic configuration can be approximated from prior pure Pt and Co simulated libraries for given column thicknesses. This approach requires only two pure element simulation libraries and drastically reduces the simulation time required to decouple ordering from a Pt-Co ADF image. While this technique has been demonstrated to work well for strain-free samples such as Ag-Au

nanoparticles, it has not yet been demonstrated how the lensing model approximation would hold for strained Pt-Co catalyst nanoparticles shown in section 5.6.2.

Then ideally, for a strained Pt-Co bimetallic system, a combination of approaches would be required as proposed by Figure 7.9. Firstly, the data would be acquired using multiframe imaging and spectroscopy. Then initial atom counting using EDS and EELS partial scattering cross-sections would be performed. Here the ADF image can be used to obtain 2D strain data at the atomic column positions at high precision for peak fitting and Voronoi integration. An initial guess could be made of the Pt-Co ordering along the atom columns of the nanoparticle using prior knowledge. For example, if a nanoparticle was core-shell, with a Pt enriched surface, then most of the Pt atoms would be arranged at the beginning and end positions of the column.

Further refinement could be made by statistical decomposition combined with fast multislice simulations to improve precision. After a few iterations, the structure could be reordered, and an initial three-dimensional structure guess could be made. This structure could be refined further by using a genetic structure search (Yu et al., 2016) and structural relaxation. A follow-up STEM multislice image simulation using the 3D model could be performed and compared to the experimental image. Once convergence is achieved, the most probable solutions could be retrieved as inputs for DFT simulations.

Here Dr Lewys Jones proposed the initial concept for this method during discussions with the author. For this approach to work several quantification methods such as quantitative atom counting, electron lensing model, simulations and genetic structure searching need to be integrated into the workflow. Hence this remains an area to be explored in the future.

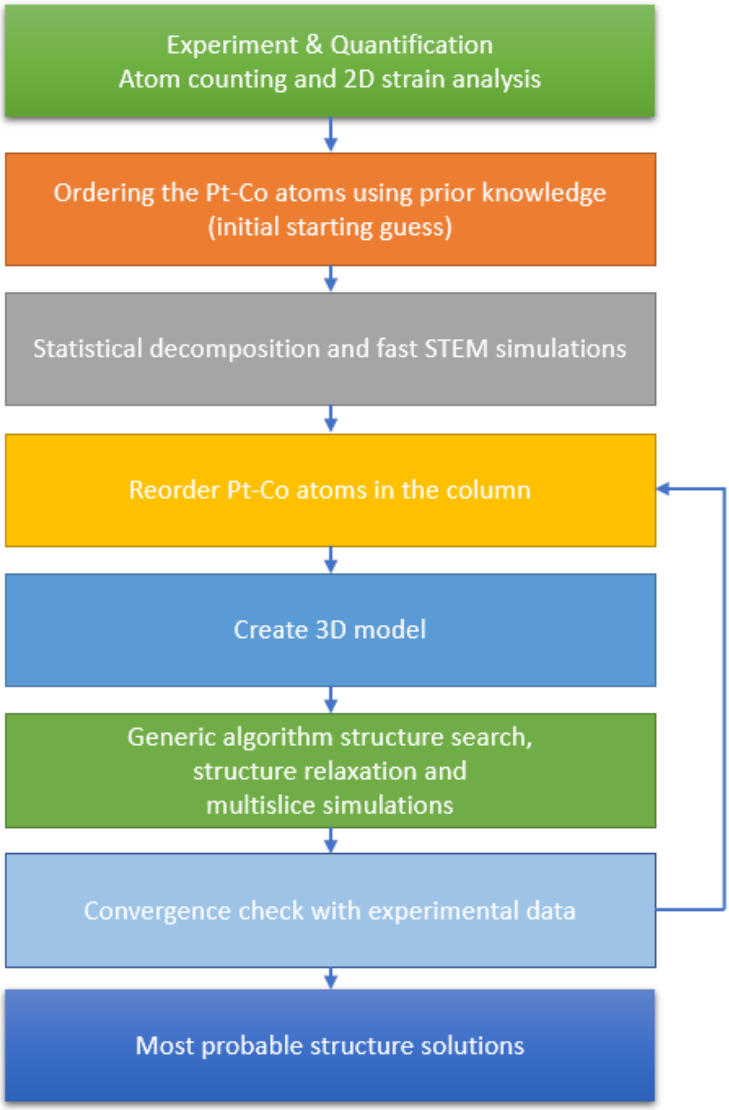

Figure 7.9 A full 3D structure inversion technique proposed for bimetallic nanoparticles using a combination of STEM multislice simulations, statistical decomposition and genetic structure searching.

7.10 Machine Learning Assisted Microscope Operation

While the EM biological fields have routinely automated microscope operation and data acquisition methods (Hu et al., 2010), little progress has been made in the physical sciences towards hardware automation. Commercial catalyst manufacturers produce a large quantity of catalysts daily that need to be characterised rapidly and accurately. To improve the applicability of electron microscopy to characterise industrially relevant samples, high throughput methods are needed. Much of the data analysis has now been automated and generalised for several materials (De Backer et al., 2016; House et al., 2017; Jones et al., 2014). However, a framework for hardware automation has not yet been fully developed.

Some manufacturers have however attempted to automate spectroscopic acquisition and analysis with the use of feature detection and segmentation algorithms (Bruker Nano GmbH, 2015). Such software was initially designed for SEMs and then exported over for electron microscopy and thus has not yet been fully developed. The limitation of proprietary software is that the subsequent analysis is performed using the manufacturer's software and is essentially a black box. One could export the acquired raw data and analyse it independently. However, this significantly reduces throughput, as there is a 'manual data export' bottleneck in the process. Methods of automating data acquisition that directly feeds into the analysis pipeline with open source software can not only increase throughput for nanoparticles, but also generalise the process, extending it to several other materials.

7.10.1 Proposed Method

One ideal candidate for microscope automation is using the Gatan Microscopy Suite (GMS) software, also commonly known as Digital Micrograph. The widespread implementation of GMS means that scripting is generalised and can be potentially used on any (S)TEM with little modification. The ingredients for automation are present but have not yet been implemented fully. However, with cooperation between hardware manufacturers, it is now possible to automate microscopy stage control, spectrometer acquisition, ADF image acquisition and electron beam control.

A user with some scripting experience can piece together an automation routine for a specific task. This is becoming more routine with the emergence of scripting databases such as the Graz University scripting database (Mitchell and Schaffer, 2005). One such script on the database is an automated stage scanning script, Figure 7.10. In this script, the user assigns the start and end positions for the stage, and the script automates stage movement and image acquisition. One could also add simultaneous spectroscopic acquisition and analysis along with this.

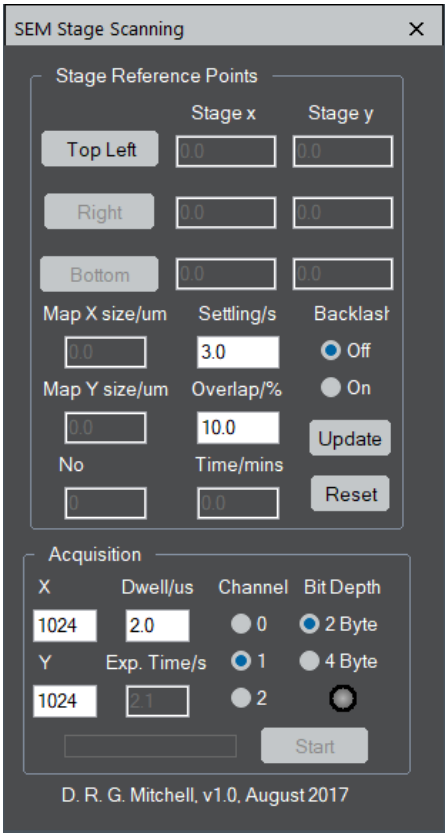

Figure 7.10 Automated SEM stage scanning script by Dr David Mitchell that can was modified for STEM functionality by the author.

For catalyst nanoparticles the workflow would be as follows. First an autofocus routine could be used to focus the probe onto the nanoparticles to obtain a sharp ADF image. Then a stage movement and acquisition script could be run where the images are recorded and saved onto disk. The nanoparticle positions in the images could then be deduced using more advanced libraries using the Python or Matlab programming languages.

Object recognition algorithms could provide the coordinates of where the nanoparticles are located in the image. These coordinates are then fed back into GMS where ROIs are drawn over the nanoparticles, and simultaneous ADF EDS and EELS acquisition routines are called. A proof of concept workflow is shown in Figure 7.11. such a script would drastically reduce operator burden and allow for high throughput data acquisition. In parallel to this, the already developed, automated analysis scripts could be run as well.

Initial Python library source codes for image focusing and segmentation can be found on the OpenCV website (Bradski, 2000). Whereas, creating custom regions of interest from a given set of coordinates

and calling to external scripts from GMS3 can be found in the Digital Micrograph Scripting Handbook by (Schaffer, 2017). This is a concept that shows great promise and much further work is required.

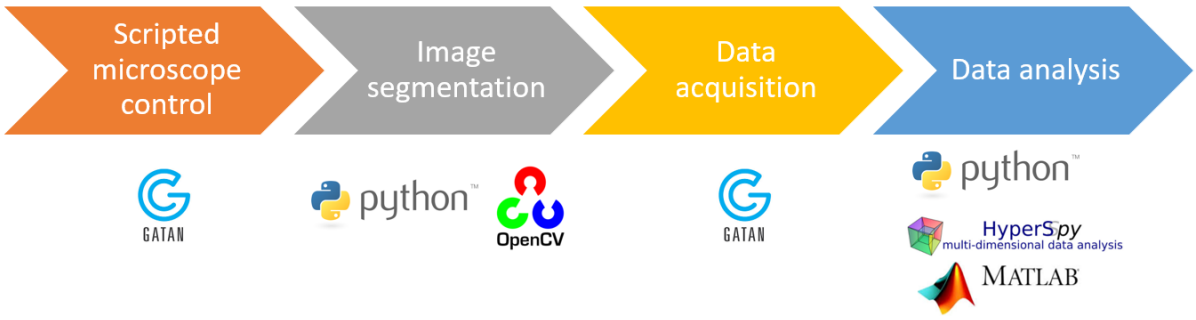

Figure 7.11 Automated microscope acquisition and analysis workflow concept using GMS, Python and Matlab programming languages.

7.11 In-Situ and Ex-Situ Electron Microscopy

Thus far, this project has focused on linking nanoparticle synthesis to catalytic activity using electron microscopy. The aim of this approach is to jump from synthesis to predicting optimal catalyst performance by reducing the design trial and error process. A possible argument against this is that to truly understand the dynamics of a reaction, a more direct approach such as in-situ or ex-situ observation is required. Here miniature reactions emulating the fuel cell are carried out 'in-situ' within the microscope or 'ex-situ' outside the microscope.

7.11.1 Acknowledgements

For this section, the author would like to thank a couple of faculty staff based at the University of Oxford and the University of York. For the In-situ experiments, I would like to thank Dr Leonardo Larii, Prof Edward Boyes and Prof Pratibha Gai for provision of the ETM and inviting Dr Lewys Jones and I to York. For the ex-situ experiments, I would like to thank Dr Lewys Jones for arranging the electrochemical experiment with Prof. Kylie Vincent's group in Oxford University Chemistry department. I would like to thank Dr Ian McPherson and colleagues for performing the ex-situ experiments; Dr Gareth Hughes for operating the SEM and Dr Lewys Jones for operating the TEM.

7.11.2 In-situ Electron Microscopy

In the in-situ approach, the nanoparticles are subjected to a micro-reactor system. One approach uses a MEMS chip where the catalyst nanoparticles are confined between two thin SiN windows, and gas or

liquid is flown through the system (Gai and Boyes, 2009). Figure 7.12 shows a schematic of such a device and a corresponding top-down view of Pt nanoparticles dispersed onto the chip. An alternative approach to this is converting the microscope itself into a microreactor (ETEM) using high-pressure differential pumping(Boyes and Gai, 2014).

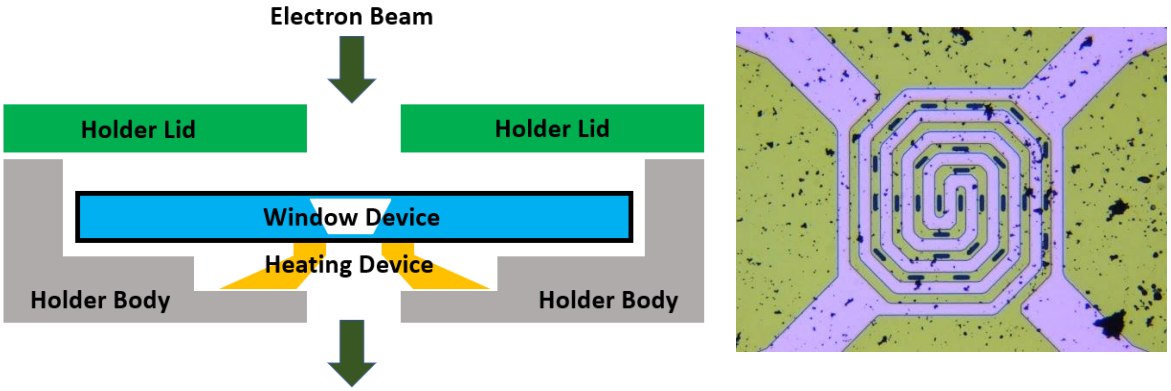

Figure 7.12 In-situ TEM holder schematic (left) and a top-down image of a DENS Solutions in-situ heating holder with Pt nanoparticles (right) taken by Dr Lewys Jones.

One concern that remains with a micro-reactor setup is beam damage and electron-induced reactions. Several studies have been published on how to tackle this; one popular method is to reduce the electron beam dose. Alternatively, the beam is switched off during the reaction, and the effects are observed after the reaction is over. Insitu microscopy remains a promising area of investigation, but due to sample damage, drift, stability and holder design, quantitative in-situ STEM using ADF imaging and spectroscopy is difficult. As an initial observation, this project looked at a batch of Pt nanoparticles subjected to PEMFC-like environments at the University of York.

7.11.2.1 Experimental Methods, Preliminary Results and Discussion

The experiment was performed on a JEOL JEM 2200 ETEM electron microscope, with a 24mrad probe convergence angle and a 88mrad ADF detector inner collection angle. The nanoparticles were ground and dusted onto a DEN Solutions MEMS chip heating holder and inserted into the electron microscope. Fresh batches of Pt nanoparticles, used in chapter 4.5, were subjected to H_2 and O_2 gases in two independent experiments at 80°C emulating PEMFC reaction temperatures.

For this initial test, the aim was to see whether it was possible to observe stable nanoparticles at atomic resolution with in-situ STEM. Figure 7.13 shows Pt nanoparticles subjected to a H_2 gas at atomic

resolution to emulate anode hydrogen exchange dynamics. From images such as these, two-dimensional strain analysis could be performed as a function of size. Alternatively, in the future, it could also be possible to probe these samples using multiframe acquisition spectroscopically.

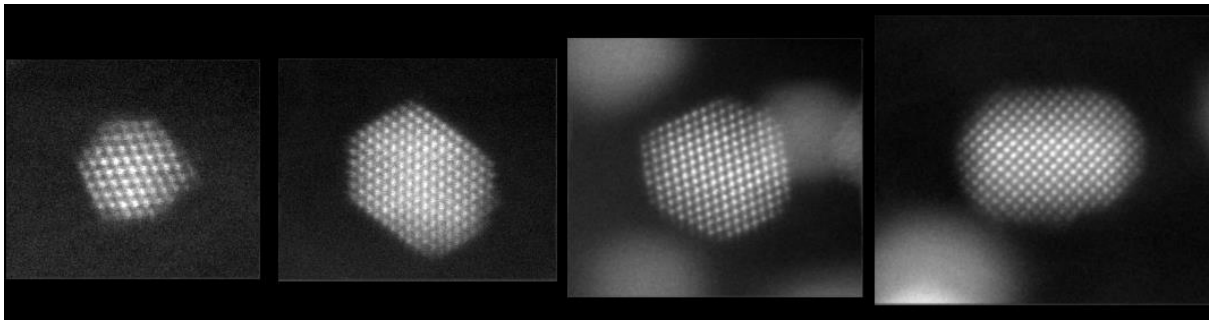

Figure 7.13 Pt nanoparticles subjected to H_2 gas at 80°C using the University of York JEOL 2100 ETEM

As a comparison, the Pt nanoparticles were also subject to O_2 gas to emulate cathode oxygen reduction dynamics, Figure 7.14. Here, although the sample size is small, the larger nanoparticles appear to be more rounded when subjected to gas. Another interesting observation was that the overall morphology and core structure of the nanoparticle did not change during the reaction. Although individual atom-hopping at the surface probably occurred at a fast-enough rate that could not be observed live.

A useful comparison that remains future work is measuring the two-dimensional strain before and after exposure to gas. Bulk material x-ray experiments and simulations indicate that the first two Pt atomic layers expand by a fraction of an Angstrom (Friebel et al., 2011). Strain analysis coupled with quantitative ADF structure inversion also remains a field to be investigated. Here the primary challenge would be quantifying the observed nanoparticles through a silicon nitride window.

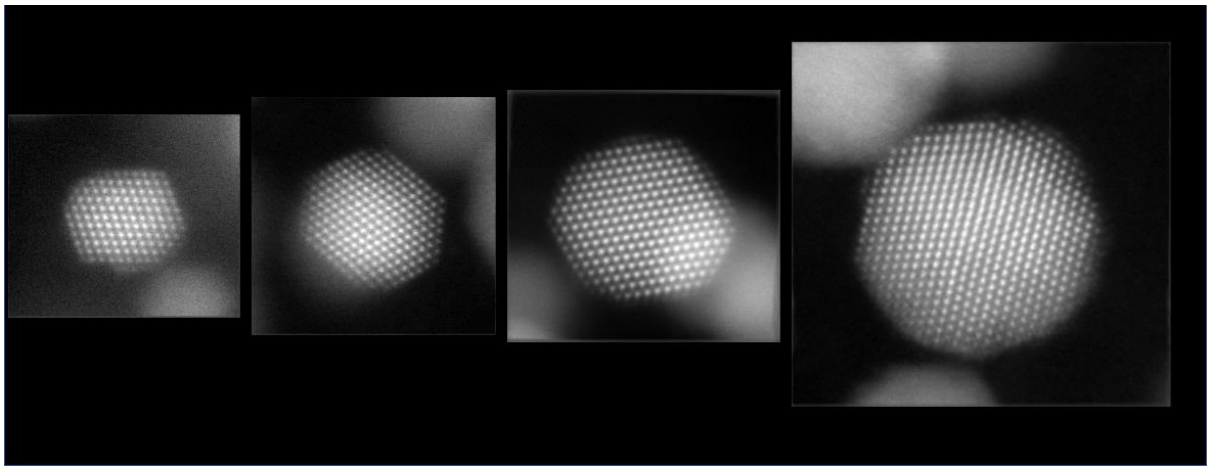

Figure 7.14 Pt nanoparticles subjected to O_2 gas at 80°C using the University of York JEOL 2100 ETEM

7.11.3 Ex-situ Electron Microscopy

In this approach, the sample is subjected to reaction conditions outside of the microscope and then, after the reaction, transferred into an electron microscope for analysis. A fixed bed reaction with a similar setup as a PEMFC is designed, where a TEM grid with the catalyst sample is housed (Kliewer et al., 2006). This set-up exposes the whole TEM grid to actual process conditions such as pressure, gas, and temperature without having to modify the electron microscope.

7.11.3.1 Experimental Methods, Preliminary Results and Discussion

For ex-situ testing, electrochemical experiments were performed in a spectrochemical flow cell. In this approach the TEM grid is attached to a surface electrode element, using a set up similar to cyclic voltammetry experiments (McPherson et al., 2017). However, only one electrochemical cycle was performed as the aim of the experiment was to see whether the same cluster of nanoparticles could be observed again. Pt nanoparticles were ground, sonicated and drop cast onto a TEM finder grid. A finder grid allows for easier tracking of nanoparticle ensembles before and after the ex-situ experiment. The gird was scanned using an SEM and a suitable area with a broad dispersion of nanoparticles was chosen for STEM analysis, Figure 7.15.

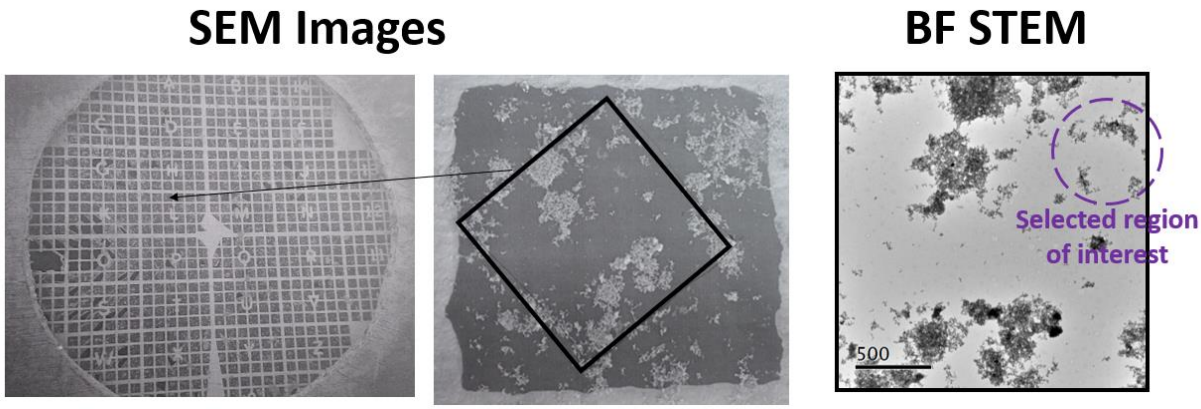

Figure 7.15 SEM and low-magnification STEM images of catalyst nanoparticles from the same area using a finder grid. A region of interest was selected from the BF STEM image for a before and after ex-situ comparison at higher magnification.

The grid was then subject to O_2 gas for about 20 minutes. The before and after effects from the experiment were observed using the Oxford JEOL ARM 200CF microscope operated at 200kV voltage. Initial low magnification ADF images showed that the TEM grid was slightly damaged, fortunately the

analysis area was intact, Figure 7.16. Medium magnification images of the selected region of interest from Figure 7.15 show that several contaminants had dispersed around the grid after the ex-situ experiment, Figure 7.16. Subsequent EDS analysis showed that these were mostly Au and Si from the electrode contact material. However, when a higher magnification image was taken from a selected zone, the Pt cluster distribution was mostly undispersed and intact. Further investigations of what would happen after more electrochemical cycles remains to be investigated, along with quantitative structural inversion before and after ex-situ experiments.

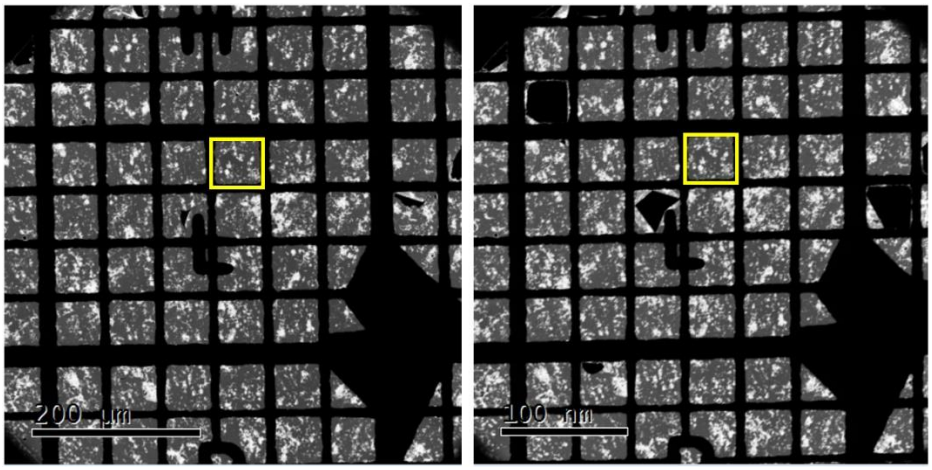

Figure 7.16 Low magnification ADF STEM images of a finder grid before (left) and after (right) the ex-situ experiment.

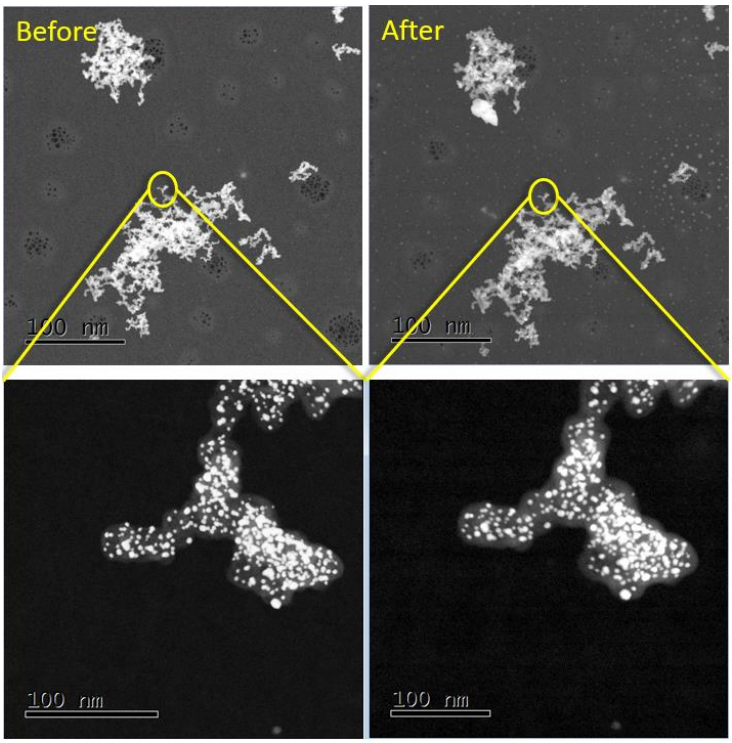

Figure 7.17 Medium and high magnification ADF images showing that the Pt clusters have not changed drastically. Additional contaminants were observed after ex-situ experiments originating from the electrode contact

7.12 References

Aarons, J., Jones, L., Varambhia, A., MacArthur, K.E., Ozkaya, D., Sarwar, M., Skylaris, C.K., Nellist, P.D., 2017. Predicting the Oxygen-Binding Properties of Platinum Nanoparticle Ensembles by Combining High-Precision Electron Microscopy and Density Functional Theory. Nano Lett. 17, 4003–4012. doi:10.1021/acs.nanolett.6b04799

Bosman, M., Keast, V.J., 2008. Optimizing EELS acquisition. Ultramicroscopy 108, 837–846. doi:10.1016/j.ultramic.2008.02.003

Boyes, E.D., Gai, P.L., 2014. Aberration corrected environmental STEM (AC ESTEM) for dynamic in-situ gas reaction studies of nanoparticle catalysts. J. Phys. Conf. Ser. 522, 12004. doi:10.1088/1742-6596/522/1/012004

Bradski, G., 2000. The OpenCV Library.

Bruker Nano GmbH, 2015. Particle Analysis - QUANTAX for SEM - Applications, X-ray spectrometer for scanning electron microscopes | Bruker [WWW Document]. URL https://www.bruker.com/products/x-ray-diffraction-and-elemental-analysis/eds-wds-ebsd-sem-micro-xrf-and-sem-micro-ct/quantax-eds-for-sem/applications/particle-analysis.html (accessed 2.14.18).

Craven, A.J., Sawada, H., McFadzean, S., MacLaren, I., 2017. Getting the most out of a post-column EELS spectrometer on a TEM/STEM by optimising the optical coupling. Ultramicroscopy 180, 66–80. doi:10.1016/j.ultramic.2017.03.017

De Backer, A., van den Bos, K.H.W., Van den Broek, W., Sijbers, J., Van Aert, S., 2016. StatSTEM: An efficient approach for accurate and precise model-based quantification of atomic resolution electron microscopy images. Ultramicroscopy 171, 104–116. doi:10.1016/J.ULTRAMIC.2016.08.018

E, H., MacArthur, K.E., Pennycook, T.J., Okunishi, E., D'Alfonso, A. J., Lugg, N.R., Allen, L.J., Nellist, P.D., 2013. Probe integrated scattering cross sections in the analysis of atomic resolution HAADF STEM images. Ultramicroscopy 133, 109–119. doi:10.1016/j.ultramic.2013.07.002

Francisco de la Peña; Tomas Ostasevicius; Vidar Tonaas Fauske; Pierre Burdet; Petras Jokubauskas; Magnus Nord; Mike Sarahan; Duncan N. Johnstone; Eric Prestat; Joshua Taillon; Jan Caron; Tom Furnival; Katherine E. MacArthur; Alberto Eljarrat; Stefano Mazz, 2017. Hyperspy. doi:10.5281/zenodo.345099

Friebel, D., Miller, D.J., O'Grady, C.P., Anniyev, T., Bargar, J., Bergmann, U., Ogasawara, H., Wikfeldt, K.T., Pettersson, L.G.M., Nilsson, A., 2011. In situ X-ray probing reveals fingerprints of surface platinum oxide. Phys. Chem. Chem. Phys. 13, 262–266. doi:10.1039/C0CP01434F

Gai, P.L., Boyes, E.D., 2009. Advances in atomic resolution in situ environmental transmission electron microscopy and la aberration corrected in situ electron microscopy. Microsc. Res. Tech. 72, 153–164. doi:10.1002/jemt.20668

Haberfehlner, G., Orthacker, A., Albu, M., Li, J., Kothleitner, G., 2014. Nanoscale voxel spectroscopy by simultaneous EELS and EDS tomography. Nanoscale 6, 14563–14569. doi:10.1039/C4NR04553J

Hou, V. D., 2009. Reduce Correlated Noise in EELS Spectrum with High Quality Dark Reference. Microsc. Microanal. 15, 226–227. doi:10.1017/S1431927609093283

House, S.D., Chen, Y., Jin, R., Yang, J.C., 2017. High-throughput, semi-automated quantitative STEM mass measurement of supported metal nanoparticles using a conventional TEM/STEM. Ultramicroscopy 182, 145–155. doi:10.1016/j.ultramic.2017.07.004

Hu, M., Vink, M., Kim, C., Derr, K., Koss, J., D'Amico, K., Cheng, A., Pulokas, J., Ubarretxena-Belandia, I., Stokes, D., 2010. Automated electron microscopy for evaluating two-dimensional crystallization of membrane proteins. J. Struct. Biol. 171, 102–110. doi:10.1016/j.jsb.2010.02.018

Jones, L., MacArthur, K.E., Fauske, V.T., van Helvoort, A.T.J., Nellist, P.D., 2014. Rapid estimation of catalyst nanoparticle morphology and atomic-coordination by high-resolution z-contrast electron microscopy. Nano Lett. 14, 6336–41. doi:10.1021/nl502762m

Jones, L., Nellist, P.D., 2013. Identifying and correcting scan noise and drift in the scanning transmission electron microscope. Microsc. Microanal. 19, 1050–60. doi:10.1017/S1431927613001402

Jones, L., Varambhia, A., Beanland, R., Kepaptsoglou, D., Griffiths, I., Ishizuka, A., Azough, F., Freer, R., Ishizuka, K., Cherns, D., Ramasse, Q.M., Lozano-Perez, S., Nellist, P.D., 2018. Managing dose-, damage- and data-rates in multi-frame spectrum-imaging. Microscopy. doi:10.1093/JMICRO/DFX125

Jones, L., Yang, H., Pennycook, T.J., Marshall, M.S.J., Van Aert, S., Browning, N.D., Castell, M.R., Nellist, P.D., 2015. Smart Align—a new tool for robust non-rigid registration of scanning microscope data. Adv. Struct. Chem. Imaging 1, 8. doi:10.1186/s40679-015-0008-4

Kliewer, C.E., Kiss, G., DeMartin, G.J., 2006. Ex Situ Transmission Electron Microscopy: A Fixed-Bed Reactor Approach. Microsc. Microanal. 12, 135–144. doi:10.1017/S1431927606060077

Kothleitner, G., Grogger, W., Dienstleder, M., Hofer, F., 2014. Linking TEM Analytical Spectroscopies for an Assumptionless Compositional Analysis. Microsc. Microanal. 20, 678–86. doi:10.1017/S1431927614000130

Lebeau, J.M., Findlay, S.D., Allen, L.J., Stemmer, S., 2010. Standardless atom counting in scanning transmission electron microscopy. Nano Lett. 10, 4405–4408. doi:10.1021/nl102025s

MacArthur, K.E., Slater, T.J.A., Haigh, S.J., Ozkaya, D., Nellist, P.D., Lozano-perez, S., 2015. Quantitative EDX Analysis of Catalyst Nanoparticles Using a Partial Scattering Cross Section Approach. Microsc. Microanal. In press, 1–23. doi:10.1017/S1431927615015494

Martinez, G.T.T., Jones, L., Backer, A. De, Béché, A., Verbeeck, J., Aert, S. Van, Nellist, P.D.D., De Backer, A., Béché, A., Verbeeck, J., Van Aert, S., Nellist, P.D.D., Backer, A. De, 2015. Quantitative STEM normalisation: the importance of the electron flux. Ultramicroscopy 159, 46–58. doi:10.1016/j.ultramic.2015.07.010

McPherson, I.J., Ash, P.A., Jones, L., Varambhia, A., Jacobs, R.M.J., Vincent, K.A., 2017. Electrochemical CO Oxidation at Platinum on Carbon Studied through Analysis of Anomalous in Situ IR Spectra. J. Phys. Chem. C 121, 17176–17187. doi:10.1021/acs.jpcc.7b02166

Mitchell, D.R.G., Schaffer, B., 2005. Scripting-customised microscopy tools for Digital MicrographTM. Ultramicroscopy 103, 319–332. doi:10.1016/j.ultramic.2005.02.003

Pryor, A., Ophus, C., Miao, J., 2017. A Streaming Multi-GPU Implementation of Image Simulation Algorithms for Scanning Transmission Electron Microscopy.

Rosenauer, A, Gries, K., Müller, K., Schowalter, M., Pretorius, A, Avramescu, a, Engl, K., Lutgen, S., 2010. Measurement of composition profiles in III-nitrides by quantitative scanning transmission electron microscopy. J. Phys. Conf. Ser. 209, 12009. doi:10.1088/1742-6596/209/1/012009

Rossouw, D., Knappett, B.R., Wheatley, A.E.H., Midgley, P.A., 2016. A New Method for Determining the Composition of Core-Shell Nanoparticles via Dual-EDX+EELS Spectrum Imaging. Part. Part. Syst. Charact. 33, 749–755. doi:10.1002/ppsc.201600096

Schaffer, B., 2017. How to script... Digital Micrograph Scripting Handbook.

Van Aert, S., Batenburg, K.J., Rossell, M.D., Erni, R., Van Tendeloo, G., 2011. Three-dimensional atomic imaging of crystalline nanoparticles. Nature 470, 374–377. doi:10.1038/nature09741

van den Bos, K.H.W., De Backer, A., Martinez, G.T., Winckelmans, N., Bals, S., Nellist, P.D., Van Aert, S., 2016. Unscrambling Mixed Elements using High Angle Annular Dark Field Scanning Transmission Electron Microscopy. Phys. Rev. Lett. 116, 246101. doi:10.1103/PhysRevLett.116.246101

Yankovich, A.B., Berkels, B., Dahmen, W., Binev, P., Sanchez, S.I., Bradley, S.A., Li, A., Szlufarska, I., Voyles, P.M., 2014. Picometre-precision analysis of scanning transmission electron microscopy images of platinum nanocatalysts. Nat. Commun. 5, 4155. doi:10.1038/ncomms5155

Yu, M., Yankovich, A.B., Kaczmarowski, A., Morgan, D., Voyles, P.M., 2016. Integrated Computational and Experimental Structure Refinement for Nanoparticles. ACS Nano 10, 4031–4038. doi:10.1021/acsnano.5b05722

8 Appendix

8.1 Angle-Space Detector Mapping Procedure for the ARM200 and Grand ARM

Manual written by A. M. Varambhia and Dr Lewys Jones, following the procedure in (Jones et al., 2017)

(Demonstration tested at 12cm camera length)

8.1.1 Pre-experiment setup

Key parameters to optimise: gun tilt, image shift, apertures, camera length, GIF tuning, detector gain and level.

1. Insert a test specimen that yields approximately the same amount of dark field scattering (similar mass & thickness) as the planned quantitative ADF experiment. For this example a Au-test specimen sample was used as an analogue for platinum nanoparticles.

2. Adjust Gun Tilt using the Anode Wobbler checking for only homocentric dilation of the ronchigram texture.

3. Align the microscope for normal imaging conditions. Choose the desired **camera length** and **spot size**. Correct for **coma** and **astigmatism** appropriately. Insert the **same aperture** that you plan to use for the **imaging experiment**. Note: the aperture could drift, it is recommended to wait for it to stabilise and verify its position before going to the next step. At this step you should feel free to adjust PLA if necessary.

4. **Optional** (GIF calibrations): for GIF aperture calibrations; Set up and tune the GIF at the optimal EELS camera length.

5. Find an area of the grid where it is easy to alternate between the vacuum (hole) and specimen (particles) on the grid

6. Using a thick part of the sample or a grid bar to generate a significant amount of high-angle scattering, observe the high-angle scattering cut-off (red circle below) using the CCD and verify the centring of the objective aperture. To correct the centring use Beam Align (using the shift knobs). Note that this both moves the cut-off and the aperture positions so you may need to converge gradually.

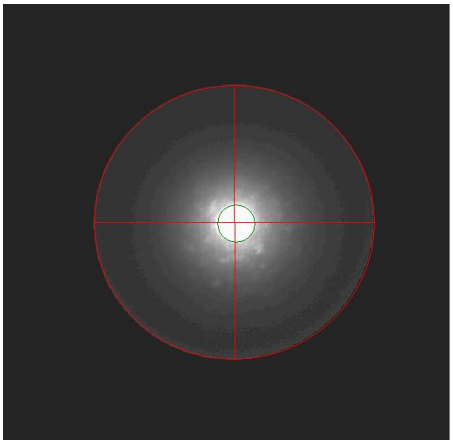

Figure 8.1. High-angle flux distribution within the cut-off.

7. Having changed image shift you will need to retune coma (perhaps significantly). Iterate steps 3 and 5 until both are converged. Image should not be adjusted for the rest of the experiment now.

8. Insert the relevant detectors to be scanned (release ronchigram mode)
9. Adjust the amplifier **gain** and **level** settings appropriately using the live waveform in DM. The data range should be entirely within the linear regime of the amplifiers (generally between 20% and 80%). **Record the detector "Level" and "Gain" values**. These **MUST** not be changed throughout the rest of the mapping procedure nor the imaging experiment.

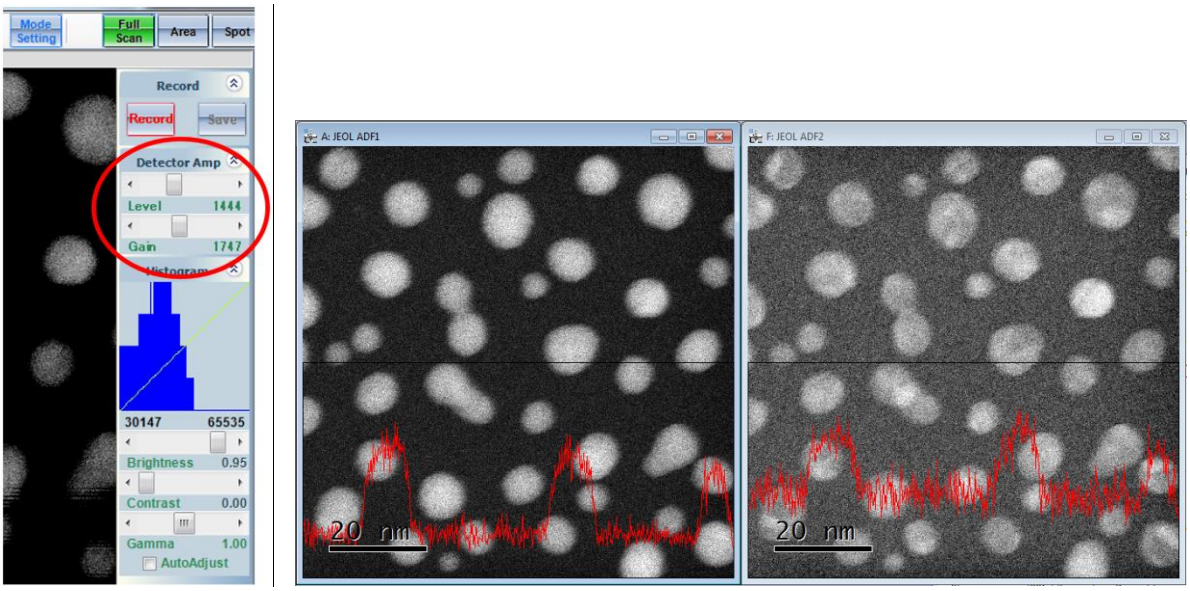

Figure 8.2. JEOL gain and level settings adjust accordingly with the help of the DM waveform. Ignore JEOL brightness, contrast and gamma settings.

8.1.2 Getting a Diffraction Pattern

Key parameters to optimise: diffraction pattern using CM in alignment mode, CL3 in MAG mode.

1. Starting from STEM Mag mode, select 20k magnification (Figure 8.3):

Figure 8.3 Mag mode selection in main menu.

2. Navigate to a region of vacuum (such as a large hole in the sample).

3. Retract all detectors by selecting Ronchigram mode.
4. Go to control>free lens control and select manual control of CL3 (CL2 on Grand ARM)(Figure 8.4).

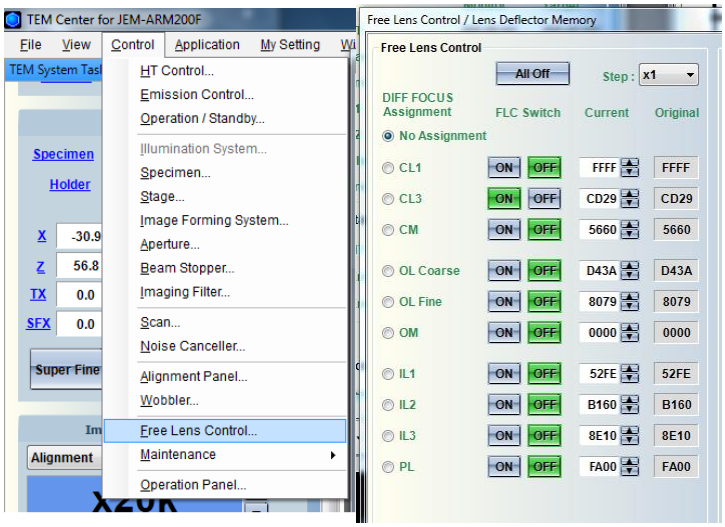

Figure 8.4 free lens control

5. Select alignment mode (Figure 8.5)

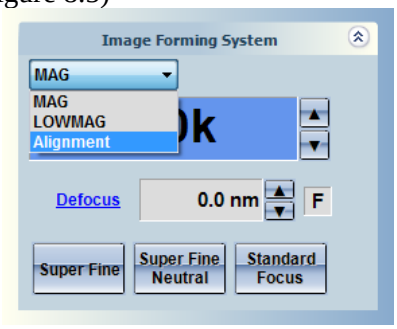

Figure 8.5 alignment mode can be selected from a dropdown menu

6. Switch on CM (Figure 8.6)

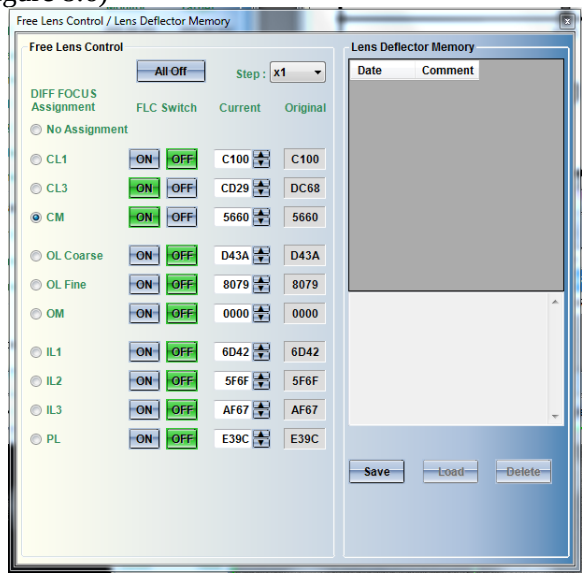

Figure 8.6 Free Lens Control (FLC), Cl3 should be switched on in mag mode, whereas Cm should be switched on in alignment mode.

7. Go to control>maintenance>scan maintenance and switch off scan coil 2(Figure 8.7)

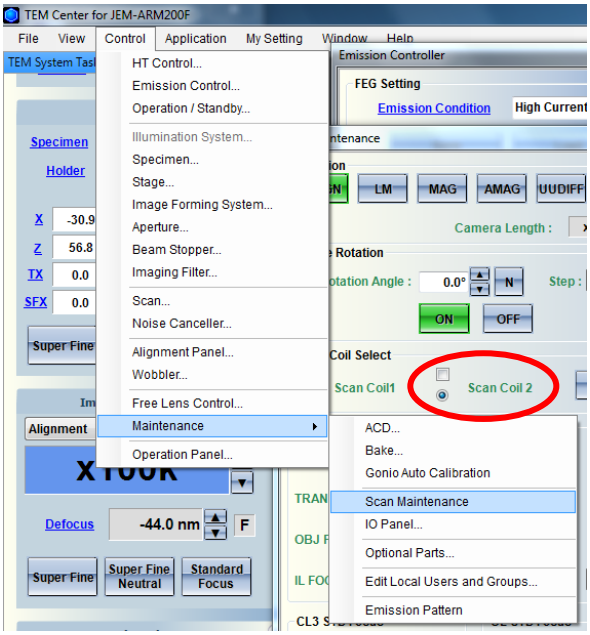

Figure 8.7 scan maintenance

8. View the pencil-beam defining aperture on the CCD. Correct obj-stig using OBJ STIG knob. The aperture position should be centred relative to the bright spot, use the aperture controls to correctly position the aperture. Use PL to adjust view if necessary. **Aperture may drift.**

9. Go to mag mode and adjust the stage height to bring the ronchigram to sweet spot (Figure 8.8). Make sure that you're at **0 defocus**.

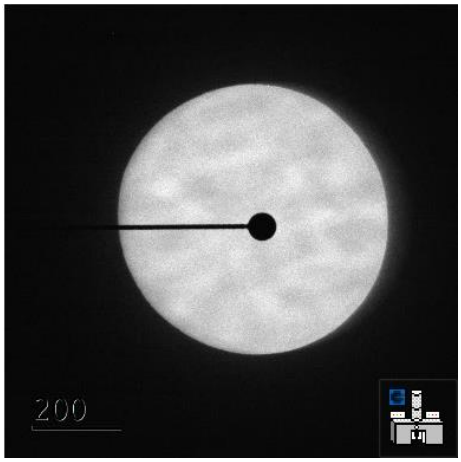

Figure 8.8 ronchigram on CCD camera

10. Correct coma and stig using the corrector.
    On the Grand ARM: While viewing the ronchigram with no aperture, vary objective focus and the pattern should have 6-fold symmetry. Use the corrector panel in TEM mode and use 2-fold stig and coma to correct the circularity.

11. Go to MAG mode. Create a small spot by changing the strength of **CL3(CL2 on Grand ARM)**. As you increase the excitation of **CL3(3)** the appearance of the texture enlarges and contracts concentrically, and eventually you will obtain a diffraction pattern. If you notice streaking, adjust GUN TILT and COND STIG (will change the shape of the circle/diffraction pattern). Also you may need to re-adjust aperture position using step 8. The focus of the diffraction pattern may change with camera length. To focus the DP use IL1 in the maintenance panel (you will have to use the mouse to adjust the setting).

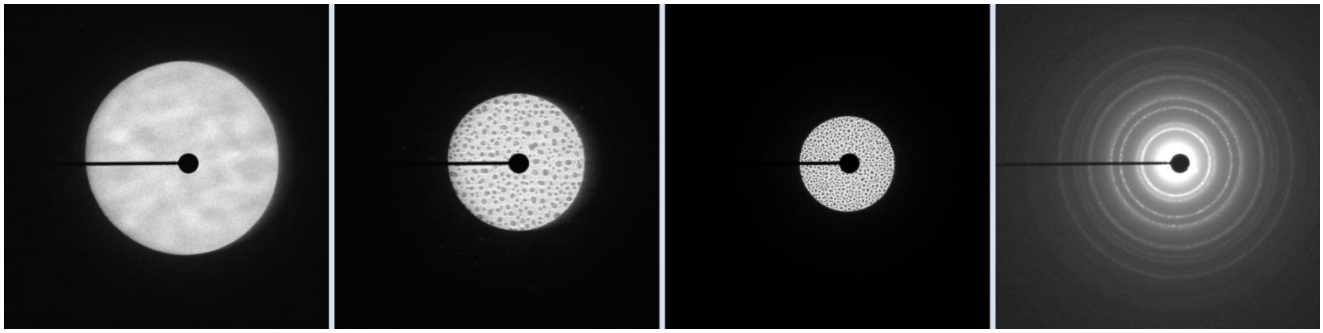

12. Figure 8.9 Au diffraction pattern, use PL to centre the pattern.

13. Select a high mag e.g. 200kx and start scanning. Use the table below to iterate between **CM** in alignment mode (DM should be scanning) and **CL3(CL2 on the Grand ARM)** in mag mode (no DM scanning) to make spot stationary and smallest size. Ignore flyback.

Mode	Alignment	MAG
Scanning	Yes	No
Adjust	CM	CL3(2)
Metric	Least movement	Sharpness

14. Insert CCD and lift the screen. Don't forget to use the beam stopper! (optional)
15. Take an image of the diffraction pattern. This will later be used to calibrate the angles of the ADF detectors at the selected camera length
16. Stop the CCD camera and unselect camera inserted.

8.1.3 Obtaining a Detector scan

1. During this procedure you must make sure that no optics apart from PL align are used, **in FLC select no assignment for the diffraction focused knob**
2. Find a hole in the sample
3. Insert detectors by releasing ronchigram mode. Start Scanning on DM. If the detectors are obscured by the bore, centre them using PL align. If the intensity on the detectors is high, then drop the emission current (use DM waveform for help).

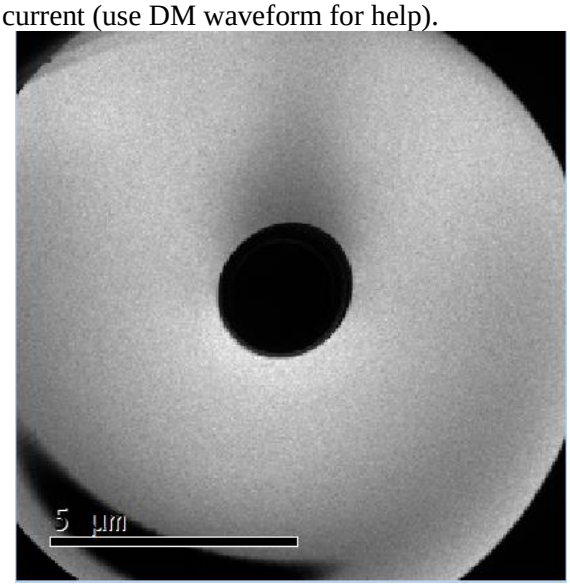

Figure 8.10 ADF1 centred using Pl align

4. Reduce the emission current so that the detector doesn't saturate.
5. To change to field of view; in DM go to Digiscan settings > advanced settings (Figure 8.11)

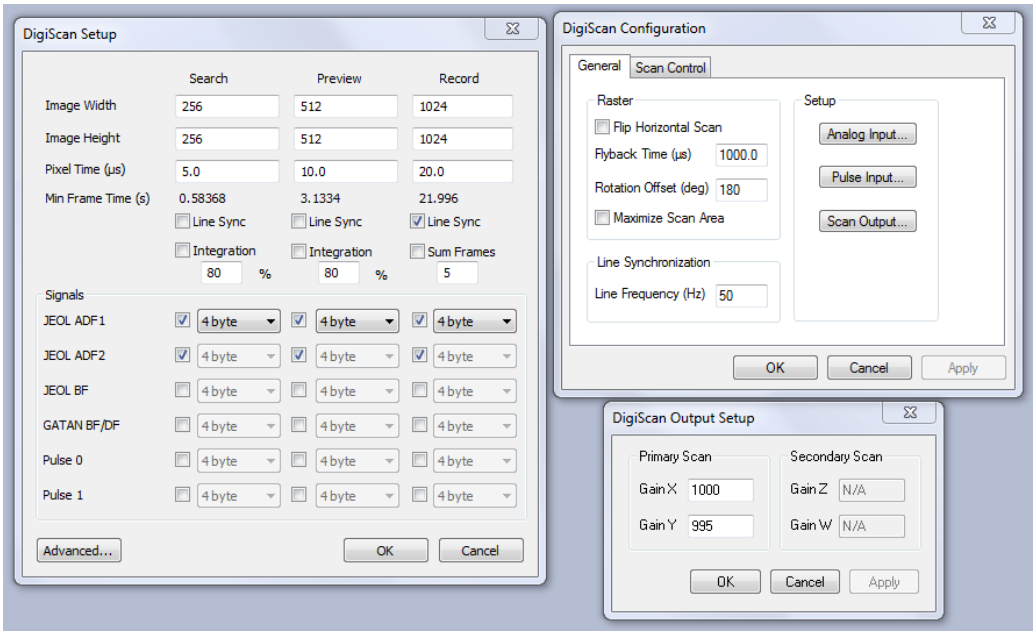

Figure 8.11 in Digiscan Setup, click on advanced and go to the general tab and select scan output.the default values for gainX and gainY are shown in the figure

6. In Digiscan output setup change (usually reduce) the gainX and gainY to values (Figure 8.11) (1300, 1294, are good gainX and gainY values for 12cm camera length) that allow the whole detector to be imaged in the whole field of view (Figure 8.11). Do not change the gain values more than x2 from their defaults (defaults shown in Figure 8.11). Alternatively just tick the maximise scan area box.

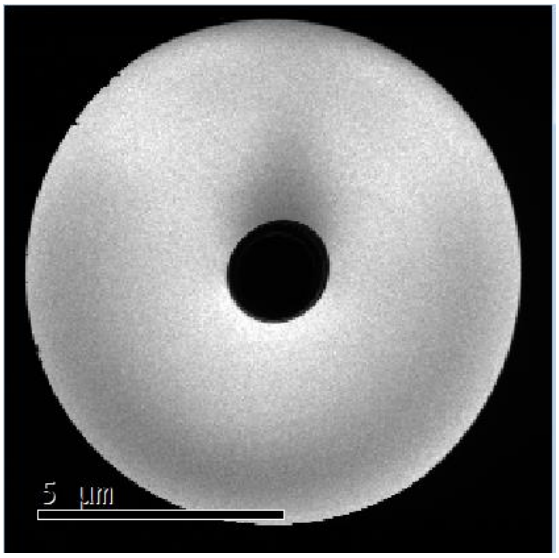

Figure 8.12 ADF 1 in the entire field of view after adjusting Digiscan gain settings

7. If detector scan is mis-aligned, IMAGE SHIFT translates both detector and OL cutoff, PL ALIGN translates only the detector. Centre the cutoff wrt the scan area with IMG SHIFT, centre the detector with PL ALIGN
8. Record an image of the detector. Record the current, gain and level settings for quantification. The ellipticity of the detector will vary with pixel time because of flyback (in Digiscan, e.g. 10us will remove flyback at 8cm)
9. Hierarchical height sequence of the detectors within the microscope are: ADF 1, ADF 2, BF, Gatan DF.

8.1.4 Imaging the probe scan.

1. Retract the detectors by initiating ronchigram mode.
2. Insert the CCD (note: when “camera inserted checkbox” is checked the electrostatic shutter takes the view on the ADF detector away).
3. You will now see the probe swinging in angle space.
4. Cut the folding/aberrations of the probe by inserting an aperture. E.g. OL L1 for 12 cm camera length (Figure 8.13)
5. Record and image of the scanning probe at 0° and 90° settings from the Digiscan (Figure 8.13).

Figure 8.13 two orthogonal probe scan images

8.1.5 Returning the microscope to standard conditions.

1. Retract the detectors and the CCD
2. In DM change scan output gain X and Y values to their defaults (Figure 8.11). Get out of service user as well.
3. Deselect maximise scan area in DM scan output advances settings.
4. Restart scan coil 2 (control>maintenance>scan maintenance (Figure 8.7))
5. Release free lens control
6. Remove apertures
7. Pl align the beam to the centre
8. Reset emission to its default value (if emission current was dropped during detector scan), set emission to auto.

8.2 Definition of a Watershed Transform.

In the segmentation method used in chapter 5, a binary image is segmented using a combination of local intensity maxima obtained from the original image, a binary Euclidian distance transform and a gradient image. The local maxima of the image mark the location of the features. Image intensities are then “flooded” (integrated) outwards from the local maxima. This flooding is performed on the gradient image, where the edges should appear along a shared minimum between two “blobbed” features. The overlapping image features are then segmented along this boundary.